

# **Chemical shift tensors as a direct probe in metal-carbon bonding**

Christopher Andrew Goult

Doctor of Philosophy

The University of York

Chemistry

September 2021

## Abstract

Chemical shift tensors, the three-dimensional representation of chemical shift, have been recovered for a range of organometallic complexes through the collection of solid-state (SS) nuclear magnetic resonance (NMR) spectroscopy. Quantum chemical calculations using density functional theory (DFT) have also been performed to predict the chemical shift tensors. The chemical shift interaction is encoded with electronic information and can be decomposed into two contributions: diamagnetic shielding ( $\delta^{\text{dia}}$ ) and paramagnetic shielding ( $\delta^{\text{para}}$ ).  $\delta^{\text{para}}$  dominates the observed change in shielding in large nuclei and is associated with magnetically coupled transitions between frontier molecular orbitals (FMOs).

In this thesis, chemical shift tensors have been used to analyse the FMOs of organometallic compounds with a focus on metal-carbon bonding. The fluorine effect has been explored on ruthenium alkynyl and vinylidene moieties. The metal-bound carbon ( $C_{\alpha}$ ) undergoes a large change in isotropic chemical shift between fluorinated and non-fluorinated moieties:  $\delta_C \approx 380$  vs  $\delta_C \approx 350$ . This has been shown to be a 236 ppm deshielding shift in the  $\delta_z$  tensor associated with the HOMO $\rightarrow$ LUMO transition. The increased deshielding arises from the contraction of the HOMO $\rightarrow$ LUMO energy and an improved magnetic coupling. The opposite trend has been explored in  $C_{\alpha}$  between fluorinated and non-fluorinated alkynyl moieties:  $\delta_C \approx 36$  vs  $\delta_C \approx 120$ . A 100 ppm shielding shift in the  $\delta_x$  and  $\delta_y$  tensors is responsible. Inclusion of fluorine decreases the energy of the  $\sigma$ -bonding orbital reducing the deshielding.

High resolution  $^{195}\text{Pt}$  SS NMR spectra have been recorded.  $^{103}\text{Rh}$  solid-state NMR spectra were too technically demanding to record. Platinum chemical shift tensors have been used as a model for exploring the FMOs of metal complexes directly at the metal. This has been expanded to study a range of rhodium complexes relevant to hydroformylation looking at the effect of pnictogen and phosphine bite angle on  $^{103}\text{Rh}$  tensors.

# List of Contents

Abstract .....	2
List of Contents .....	3
List of Tables.....	10
List of Figures .....	13
Acknowledgements.....	24
Author's Declaration .....	25
Chapter 1. Introduction .....	26
1.1 Fundamentals of NMR spectroscopy .....	28
1.1.1 Nuclear spin.....	28
1.1.2 The NMR Hamiltonian.....	28
1.1.3 The interaction of nuclear spin with an external magnetic field (Zeeman) . .....	29
1.2 Basics of Solid-State Nuclear Magnetic Resonance Spectroscopy.....	29
1.2.1 Dipolar and quadrupolar interactions.....	31
1.2.2 Magic Angle Spinning (MAS) .....	32
1.3 Introduction to computational chemistry.....	34
1.3.1 The Schrödinger equation.....	35
1.3.2 Application of the Born-Oppenheimer approximation to the Schrödinger equation.....	35
1.3.3 Hartree-Fock method.....	37
1.3.4 Basis sets .....	37
1.3.5 Effective Core Potential (ECP) .....	38
1.3.6 Relativistic methods.....	38
1.3.7 Density functional theory (DFT).....	39
1.4 Metal-ligand bonding .....	39

1.5	Probing metal ligand bonding .....	42
1.5.1	Direct methods for probing M-L bonding .....	42
1.5.2	Indirect methods of probing M-L bonding.....	43
1.5.3	Analysis of alkene metathesis by SS NMR spectroscopy .....	45
1.5.4	Use of SS NMR in the analysis of example catalytic systems .....	50
1.5.5	Project aims.....	57
Chapter 2.	Methodology.....	58
2.1	Aims .....	58
2.2	Selection of SS NMR pulse sequences and SS NMR spectroscopic methodology testing on representative compounds. ....	59
2.2.1	SS NMR pulse programs .....	59
2.2.2	Spectral optimisation: $^{13}\text{C}\{^1\text{H}\}$ CP MAS. ....	61
2.2.3	Optimisation of $^{31}\text{P}\{^1\text{H}\}$ Solid-State NMR spectra .....	65
2.2.4	Optimisation $^{19}\text{F}$ Solid-State NMR spectra.....	66
2.2.5	Fitting optimisation of TopSpin Solid-State line shape analysis tool.....	69
2.3	Optimisation of computational methodology for the calculation of chemical shift tensors.....	73
2.3.1	Geometry optimisation of $[\text{2a}]^+$ , basis set and functional tolerance.....	73
2.3.2	Comparison of calculated geometry of $[\text{2a}]^+$ to the crystal structure geometry of $[\text{2a}]\text{BF}_4$ .....	75
2.3.3	Optimisation of NMR calculations of complex $[\text{2a}]^+$ .....	78
2.3.4	Dependence of chemical shielding on geometry.....	83
2.4	Referencing of chemical shift calculations.....	84
2.4.1	Selection of an appropriate reference compound .....	84
2.5	Benchmark calculation of chemical shift tensors for simple molecule examples.....	86
2.6	Visualisation of chemical shift tensors.....	87

2.6.1	Example of tensor visualisation .....	87
2.7	Analysis of ethane, ethene, and ethyne FMOs .....	89
2.7.1	Step-by-step orbital analysis and correlation to chemical shift tensors of ethene [37] .....	89
2.7.2	Step by step orbital analysis and correlation to chemical shift tensors of ethyne [38].....	92
2.7.3	Step by step orbital analysis and correlation to chemical shift tensors of ethane .....	95
2.8	Conclusions.....	96
Chapter 3.	Investigation of fluorine effect on chemical shift in ruthenium vinylidene and alkynyl complexes .....	99
3.1	Introduction.....	99
3.1.1	Carbon-fluorine bonds .....	100
3.1.2	Effect of fluorine on structure and bonding – The gauche effect .....	100
3.1.3	Fluorobenzene complexes .....	102
3.1.4	C-H and C-F activation of fluoroarenes.....	104
3.1.5	Stable fluoro-vinylidene and -alkynyl complexes .....	108
3.1.6	Aims.....	111
3.2	Synthesis and characterisation of complexes .....	113
3.2.1	Characterisation of [1d], [2d]OTf, and [3d]PF <sub>6</sub> .....	116
3.3	Recording of Solid-state NMR spectra of complexes [1a] – [10]PF <sub>6</sub> .....	124
3.3.1	Example of SS characterisation of <sup>13</sup> C{ <sup>1</sup> H} CP MAS spectra, showing <sup>13</sup> C{ <sup>1</sup> H} CP MAS spectra of [2a]BF <sub>4</sub> ·Et <sub>2</sub> O.....	124
3.3.2	Example of SS characterisation of <sup>31</sup> P{ <sup>1</sup> H} CP MAS SS NMR spectra, showing <sup>31</sup> C{ <sup>1</sup> H} CP MAS spectra of [2a]BF <sub>4</sub> ·Et <sub>2</sub> O .....	127
3.3.3	Example SS characterisation of <sup>19</sup> F MAS SS NMR spectra, showing <sup>19</sup> F MAS spectra of [3a]PF <sub>6</sub> .....	129
3.3.4	Effect of crystallinity on SS NMR Spectra.....	131

3.3.5	Summary of chemical shift tensors of ruthenium organometallics .....	133
3.3.6	SS NMR spectroscopy of fluoroalkynyl complex, [7] .....	135
3.4	Calculation of chemical shift tensors for ruthenium vinylidene- and alkynyl- complexes.....	140
3.4.1	Calculation of chemical shift tensors (coordinated) .....	140
3.4.2	Visualisation of chemical shift tensors.....	144
3.5	Interpretation of vinylidene tensors .....	144
3.5.1	Identification of FMO transitions using simple uncoordinated vinylidene complex models .....	144
3.5.2	Identification of FMO transitions using simple allene and vinyliminium compounds as vinylidene models.....	152
3.5.3	Explanation of the changes in deshielding of coordinated vinylidene complexes .....	158
3.5.4	Discussion of vinylidene tensors .....	159
3.6	Interpretation of alkynyl tensors.....	167
3.6.1	Identification of FMO transitions using simple alkyne models.....	167
3.6.2	Coordinated alkynyl complexes .....	170
3.6.3	Discussion of alkynyl tensors .....	170
3.7	Correlation of chemical shift tensors and first excitation energy.....	171
3.8	Discussion of differences in tensors between metal fragments.....	174
3.9	Discussion of differences in C $\alpha$ chemical shift tensors in metal vinylidene- and alkynyl- complexes on changing remote conjugated substituents (R groups) .....	175
3.10	Conclusions.....	177
Chapter 4.	Exploration of metal chemical shift tensors .....	179
4.1	Introduction.....	179
4.1.1	The hydroformylation reaction (oxo process) .....	180
4.1.2	Hydroformylation using rhodium catalysts.....	182

4.1.3	Effect of diphosphine bite angle on linear:branched (l:b) ratio .....	182
4.1.4	Heterogeneous Rh-catalysed hydroformylation.....	184
4.1.5	Aims.....	185
4.2	Synthesis and characterisation of rhodium carbonyl chloride complexes ....	187
4.2.1	Identification and synthesis of target Rh complexes.....	187
4.3	Recording of $^{103}\text{Rh}$ and $^{195}\text{Pt}$ metal SS NMR spectra .....	187
4.3.1	SS NMR spectrum of $\text{K}_2\text{PtCl}_6$ .....	189
4.3.2	SS NMR spectrum of $\text{K}_2\text{PtCl}_4$ .....	190
4.3.3	Attempted recording of $^{195}\text{Pt}$ SS NMR spectra of $[\text{Pt}(\text{ppyH})(\text{ppy})\text{Cl}]$ and $[\text{Pt}(\text{ppy})_2\text{Cl}_2]$ .....	193
4.3.4	Attempts to record $^{103}\text{Rh}$ SS NMR spectra.....	194
4.4	Computational methodology for the calculation of geometries and NMR properties of metal nuclei .....	197
4.4.1	Geometry optimisation of simple Pt species $[\text{72}]^{2-}$ .....	197
4.4.2	Inclusion of solvent corrections in geometry optimisation of $[\text{72}]^{2-}$ .....	199
4.4.3	Dependence of chemical shielding of $[\text{72}]^{2-}$ on geometry.....	201
4.5	Calculation of metal chemical shift tensors .....	202
4.6	Analysis of metal complex FMOs .....	204
4.6.1	Analysis of $\text{K}_2[\text{PtCl}_6]^{2-}$ chemical shift tensors and FMOs .....	204
4.6.2	Analysis of $\text{K}_2[\text{PtCl}_4]^{2-}$ chemical shift tensors and FMOs .....	206
4.6.3	Analysis of <i>cis</i> - $[\text{PtCl}_2(\text{NH}_3)_2]$ chemical shift tensors and FMOs.....	208
4.6.4	Analysis of <i>cis</i> - $[\text{PtCl}_2(\text{PH}_3)_2]$ chemical shift tensors and FMOs .....	210
4.6.5	Analysis of <i>cis</i> - $[\text{Rh}(\text{Cl})(\text{CO})(\text{PH}_3)_2]$ chemical shift tensors and FMOs .....	211
4.6.6	Analysis of <i>trans</i> - $[\text{Rh}(\text{Cl})(\text{CO})(\text{PH}_3)_2]$ chemical shift tensors and FMOs ..	213
4.7	Discussion .....	215
4.7.1	Effect of pnictogen on $^{103}\text{Rh}$ chemical shift tensors in <i>trans</i> -rhodium Vaska-type complexes .....	215

4.7.2	Effect of L-Rh-L bite angle on $^{103}\text{Rh}$ chemical shift tensors in <i>cis</i> -rhodium Vaska-type complexes .....	217
4.8	Conclusions and future work.....	220
Chapter 5.	Conclusions and future work .....	221
Chapter 6.	Experimental .....	223
6.1	General considerations .....	223
6.2	Synthesis of $[\text{Ru}(\text{Cl})(\eta^5\text{-C}_5\text{H}_5)(\text{PPh}_3)_2]$ , [35] .....	226
6.3	Synthesis of $[\text{Ru}(\eta^5\text{-C}_5\text{H}_5)(\text{-C}\equiv\text{C-Ph})(\text{PPh}_3)_2]$ , [1a] .....	228
6.4	Synthesis of $[\text{Ru}(\eta^5\text{-C}_5\text{H}_5)(\text{-C}\equiv\text{C-(C}_6\text{H}_4\text{-}p\text{-OMe)})(\text{PPh}_3)_2]$ , [1b] .....	229
6.5	Synthesis of $[\text{Ru}(\eta^5\text{-C}_5\text{H}_5)(\text{-C}\equiv\text{C-(C}_6\text{H}_4\text{-}p\text{-CF}_3)})(\text{PPh}_3)_2]$ , [1c] .....	231
6.6	Synthesis of $[\text{Ru}(\eta^5\text{-C}_5\text{H}_5)(\text{-C}\equiv\text{C-}^t\text{Bu})(\text{PPh}_3)_2]$ , [1d] .....	232
6.7	Synthesis of $[\text{Ru}(\eta^5\text{-C}_5\text{H}_5)(\text{PPh}_3)_2(=\text{CHPh})]\text{BF}_4$ [2a] $\text{BF}_4$ .....	233
6.8	Synthesis of $[\text{Ru}(\eta^5\text{-C}_5\text{H}_5)(\text{PPh}_3)_2(=\text{CH(C}_6\text{H}_4\text{-}p\text{-OMe)})]\text{OTf}$ [2b] $\text{OTf}$ .....	234
6.9	Synthesis of $[\text{Ru}(\eta^5\text{-C}_5\text{H}_5)(\text{PPh}_3)_2(=\text{CH(C}_6\text{H}_4\text{-}p\text{-CF}_3))]\text{OTf}$ [2c] $\text{OTf}$ .....	235
6.10	Synthesis of $[\text{Ru}(\eta^5\text{-C}_5\text{H}_5)(\text{PPh}_3)_2(=\text{CH}^t\text{Bu})]\text{BF}_4$ [2d] $\text{BF}_4$ .....	236
6.11	Synthesis of $[\text{Ru}(\eta^5\text{-C}_5\text{H}_5)(\text{PPh}_3)_2(=\text{CFPh})]\text{PF}_6$ [3a] $\text{PF}_6$ .....	237
6.12	Synthesis of $[\text{Ru}(\eta^5\text{-C}_5\text{H}_5)(\text{PPh}_3)_2(=\text{CF(C}_6\text{H}_4\text{-}p\text{-OMe)})]\text{BF}_4$ [3b] $\text{BF}_4$ .....	239
6.13	Synthesis of $[\text{Ru}(\eta^5\text{-C}_5\text{H}_5)(\text{PPh}_3)_2(=\text{CF(C}_6\text{H}_4\text{-}p\text{-CF}_3))]\text{PF}_6$ [3c] $\text{PF}_6$ .....	241
6.14	Synthesis of $[\text{Ru}(\eta^5\text{-C}_5\text{H}_5)(\text{PPh}_3)_2(=\text{CF}^t\text{Bu})]\text{PF}_6$ [3d] $\text{PF}_6$ .....	242
6.15	Synthesis of $[\text{Ru}(\eta^5\text{-C}_5\text{H}_5)(\text{PPh}_3)_2(=\text{C(CF}_3)\text{Ph})]\text{BF}_4$ [9] $\text{BF}_4$ .....	244
6.16	Synthesis of $[\text{Ru}(\eta^5\text{-C}_5\text{H}_5)(\text{PPh}_3)_2(\text{CO})]\text{PF}_6$ [10] $\text{PF}_6$ .....	246
6.17	Synthesis of $[\text{Ru}(\text{Cl})_2(\text{PPh}_3)_3]$ .....	247
6.18	Synthesis of <i>trans</i> - $[\text{Ru}(\text{Cl})_2(\text{dppe})_2]$ .....	248
6.19	Synthesis of $[\text{Ru}(\text{Cl})(\text{dppe})_2]\text{OTf}$ .....	249
6.20	Synthesis of $\text{LiN}(\text{SiMe}_3)_2$ .....	250
6.21	Synthesis of <i>trans</i> - $[\text{Ru}(\text{Cl})(\text{-C}\equiv\text{C-Ph})(\text{dppe})_2]$ [1a]' .....	251

6.22	Synthesis of <i>trans</i> -[Ru(Cl)(dppe) <sub>2</sub> (=·=CHPh)]OTf [2a]'OTf.....	252
6.23	Synthesis of <i>trans</i> -[Ru(Cl)(dppe) <sub>2</sub> (=·=CFPh)]PF <sub>6</sub> [3a]'PF <sub>6</sub> .....	253
6.24	Synthesis of <i>trans</i> -[Ru(Cl)(dppe) <sub>2</sub> (=·=CH <sub>2</sub> )]OTf [5]'OTf .....	255
6.25	Synthesis of <i>trans</i> -[Ru(Cl)(dppe) <sub>2</sub> (-C≡C-H)] [4]' .....	256
6.26	Synthesis of <i>trans</i> -[Ru(Cl)(dppe) <sub>2</sub> (=·=CHF)]OTf [6]'BF <sub>4</sub> .....	257
6.27	Synthesis of <i>trans</i> -[Ru(Cl)(-C≡C-F)(dppe) <sub>2</sub> ] [7]' .....	258
6.28	Synthesis of [Pt(Cl)(ppy)(ppyH)] [73].....	259
6.29	Synthesis of [Pt(Cl) <sub>2</sub> (ppy) <sub>2</sub> ] [74].....	260
6.30	Synthesis of [Rh(CO)Cl(PPh <sub>3</sub> ) <sub>2</sub> ] <i>trans</i> -[15] .....	261
6.31	Synthesis of [Rh(CO)Cl(AsPh <sub>3</sub> ) <sub>2</sub> ] [16] .....	262
6.32	Synthesis of [Rh(CO)Cl(SbPh <sub>3</sub> ) <sub>3</sub> ] [70] .....	263
6.33	Synthesis of [Rh(CO)Cl(dppe)] [19].....	264
6.34	X-Ray Data for [Ru(η <sup>5</sup> -C <sub>5</sub> H <sub>5</sub> )(PPh <sub>3</sub> ) <sub>2</sub> (=·=CHPh)]BF <sub>4</sub> ·CH <sub>2</sub> Cl <sub>2</sub> [2a]BF <sub>4</sub> .....	265
6.35	X-Ray Data for [Ru(η <sup>5</sup> -C <sub>5</sub> H <sub>5</sub> )(PPh <sub>3</sub> ) <sub>2</sub> (=·=CH(C <sub>6</sub> H <sub>4</sub> - <i>p</i> -CF <sub>3</sub> ))]OTf·CH <sub>2</sub> Cl <sub>2</sub> [2c]OTf .....	267
6.36	X-Ray Data for [Ru(η <sup>5</sup> -C <sub>5</sub> H <sub>5</sub> )(PPh <sub>3</sub> ) <sub>2</sub> (=·=CH( <sup>t</sup> Bu))]OTf [2d]OTf .....	270
	Table of Abbreviations .....	272
	References.....	275

## List of Tables

Table 1. Relative peak height of D1 optimisation spectra of complex <b>[35]</b> recorded at 101 MHz at a spinning speed of 10 kHz. Spectra collected with 16 scans. Time denotes total experiment time. The maximum peak height of the aromatic resonance of experiment 4 was set to 10 and the intensity represents the relative peak height in 1-3 compared to this value. ....	64
Table 2. Relative intensity vs D1 of complex <b>[3a]</b> PF <sub>6</sub> recorded at 376 MHz at a spinning speed of 10 kHz. Spectra collected with N <sub>s</sub> = 16. Time denotes total experiment time. The maximum peak height of the PF <sub>6</sub> <sup>-</sup> anion of experiment 4 was set to 10 and the intensity represents the relative peak height in 1-3 compared to this value. ....	68
Table 3. Methodologies tested for geometry optimisation of <b>[2a]</b> <sup>+</sup> , all starting from the same input structure obtained from crystal coordinates. Time for job completion includes geometry optimisation and calculation of vibrational frequencies at the same level of theory. ....	75
Table 4. Comparison of key geometries around Ru of <b>[2a]</b> <sup>+</sup> after geometry optimisation in Turbomole to values obtained from the X-ray diffraction crystal structure, estimated standard deviations are shown in square brackets [ ]. Absolute differences are shown in brackets ( ). ....	76
Table 5. Chemical shift calculation results for the alpha carbon of <b>[2a]</b> <sup>+</sup> . The chemical shielding tensors recovered from the quantum chemical calculations were converted to chemical shift using the experimental isotropic shift of $\delta^{\text{iso}} = 353.7$ ppm....	78
Table 6. Chemical shift calculation results for an aromatic carbon of <b>[2a]</b> <sup>+</sup> . The calculations were converted using the same conversion factor as in Table 5. ....	80
Table 7. Chemical shift tensors calculated in Orca with ZORA corrections for the vinylidene C <sub><math>\alpha</math></sub> (C <sub>1</sub> ) and a representative aromatic environment (C <sub>84</sub> ) of <b>[2a]</b> <sup>+</sup> . Each method is internally referenced so that the vinylidene carbon C <sub>1</sub> has a chemical shift of $\delta^{\text{iso}} = 353.7$ . Experimental results recovered from the <sup>13</sup> C{ <sup>1</sup> H} Cp MAS SS NMR spectrum of <b>[2a]</b> BF <sub>4</sub> ·OEt <sub>2</sub> . ....	82

Table 8.	$^{13}\text{C}$ Chemical shielding tensors recovered from single point DFT calculations in Orca at the PBE0/def2_TZVPP level of theory with ZORA corrections.....	83
Table 9.	$^{13}\text{C}$ Chemical shift tensors for compounds <b>[35]</b> , <b>[36]</b> and <b>[37]</b> calculated in Orca at the PBE0/def2_TZVPP level of theory with ZORA. Experimental values reported by Zuschneid <i>et al.</i> in $d_2$ -dichloromethane. <sup>72</sup> .....	87
Table 10.	Energies of MOs of <b>[38]</b> and transitions relevant to chemical shift, calculated in Orca at the PBE0/def2_TZVPP level of theory with ZORA corrections. ....	94
Table 11.	Yields of alkynyl, vinylidene, and fluorovinylidene synthesis recovered as crystalline material.....	116
Table 12.	Comparison of solid and solution phase $^{13}\text{C}$ resonances of <b>[2a]X</b> . Solid-phase resonances recorded at 101 MHz at 10 kHz on a sample of <b>[2a]BF<sub>4</sub></b> . Literature solution-phase resonances of <b>[2a]PF<sub>6</sub></b> recorded at 123 MHz in $d_1$ -chloroform. <sup>123</sup> .....	126
Table 13.	Chemical shift tensors recovered from $^{13}\text{C}\{^1\text{H}\}$ CP MAS SS NMR spectra recorded at 101 MHz. ....	134
Table 14.	Chemical shift tensors of ruthenium alkynyl and vinylidene species. Optimized in Turbomole at the BP86/def2_SV(P) level of theory, NMR calculations performed in Orca at the PBE0/def2_TZVPP level of theory with ZORA corrections. .	141
Table 15.	Chemical shift tensors of complexes possessing a <i>pseudo</i> - $\infty$ rotational axis. Calculated values are shown in brackets, calculated at the PBE0/def2_TZVPP level of theory with the ZORA correction.....	143
Table 16.	Characteristic deshielding patterns observed in ruthenium vinylidene complexes for $\text{C}_\alpha$ .....	145
Table 17.	Chemical shift tensors of allene and vinyliminium compounds calculated in Orca at the PBE0/ def2_TZVPP level of theory with ZORA corrections. Literature experimental shifts shown in brackets. ....	153
Table 18.	Chemical shift tensors of halogen vinylidene complexes $\text{C}_\alpha$ calculated in Orca at the PBE0/def2_TZVPP level of theory with ZORA corrections. Numbers in parentheses are experimental results reported by Slattery and Lynam. <sup>112</sup> .....	165
Table 19.	Chemical shift tensors of halogen vinylidene complexes $\text{C}_\beta$ calculated in Orca at the PBE0/def2_TZVPP level of theory with ZORA corrections.....	165

Table 20.	Calculated chemical shift tensors along the M-C bond axis ( $\delta_{M-C}$ ) and calculated wavelength and wavenumber of the first excitation of ruthenium organometallics. Both calculated at the PBE0/def2_TZVPP level of theory with ZORA corrections. ....	173
Table 21.	Tabulated Pt-Cl bond lengths from geometry optimisation calculations for <b>[72]</b> <sup>2-</sup> calculated in Turbomole and Orca. Mean values are denoted by an asterisk (*). Experimental value obtained from literature crystal structure. <sup>152</sup> .....	198
Table 22.	Tabulated Pt-Cl bond lengths from geometry optimisation calculations for <b>[72]</b> <sup>2-</sup> calculated in Turbomole and Orca with COSMO and CPCM implemented. ....	200
Table 23.	Chemical shift tensors of <b>[72]</b> <sup>2-</sup> against Pt-Cl bond length. Tensors calculated in Orca at the PBE0/def2_TZVPP level of theory with ZORA corrections. The Basis functions of Pt were represented by the SARC_TZVPP basis set. ....	201
Table 24.	Platinum and rhodium chemical shift tensor calculate in Orca at the PBE0/def2_TZVPP level of theory with ZORA corrections. The Basis functions of Pt were represented by the SARC_TZVPP basis set. ....	203
Table 25.	Chemical shift tensors of rhodium Vaska-type complexes calculated at the PBE0/def2_TZVPP. ....	215
Table 26.	Chemical shift tensors and P-Rh-P angles of rhodium Vaska-type complexes calculated at the PBE0/def2_TZVPP. ....	217

## List of Figures

Figure 1. Complexes <b>[1]</b> – <b>[13]</b> <sup>+</sup> , which have been studied in chapter 3. For complexes <b>[1]</b> – <b>[13]</b> <sup>+</sup> , the absence of diacritical marks denotes the ruthenium centre: [Ru( $\eta^5$ -C <sub>5</sub> H <sub>5</sub> )(PPh <sub>3</sub> ) <sub>2</sub> ) <sup>+</sup> . A single diacritical mark denotes the ruthenium centre: <i>trans</i> -[Ru(Cl)(dppe) <sub>2</sub> ) <sup>+</sup> . Two diacritical marks denote the ruthenium centre: [Ru( $\eta^5$ -C <sub>5</sub> Me <sub>5</sub> )(dppe) <sub>2</sub> ) <sup>+</sup> .....	26
Figure 2. Complexes <b>[14]</b> – <b>[20]</b> studied in chapter 4. ....	26
Figure 3. Spherical harmonic representation of a rank 2 tensor (left) and SS NMR spinning at the magic angle with respect to <i>B</i> <sub>0</sub> (right). ....	34
Figure 4. Breaking the degeneracy of the d orbitals. In the octahedral geometry, the orbitals split into <i>T</i> <sub>2g</sub> and <i>E</i> <sub>g</sub> subsets. ....	40
Figure 5. Dewar-Chatt-Duncanson model for the synergic bonding of a general M-X bond (left) and of an alkene to a metal (right) through donation and back-donation interactions. ....	41
Figure 6. Schematic representation of the Tolman cone angle (left) and the TEP (right). ....	44
Figure 7. Catalytic ring closing metathesis of <b>[22]</b> to form <b>[23]</b> using <b>[21]</b> as demonstrated by Fürstner <i>et al.</i> R = Ph, Cy. ....	44
Figure 8. Fischer, Schrock, and ruthenium carbene complexes studied by Yamamoto <i>et al.</i> .....	46
Figure 9. Trigonal bipyramidal (left) and square pyramidal (right) geometry of metallocyclobutane rings relevant to catalyst deactivation of alkene metathesis catalysts. The metallocyclobutane ring loses planarity when the metal adopts a square pyramidal geometry.....	46
Figure 10. Immobilised alkylidene complexes studied by Blanc.....	48
Figure 11. Transitions responsible for $\delta_{11}$ deshielding in ethene (Middle) and a metathesis carbene (Bottom) shown by Halbert <i>et al.</i> .....	49
Figure 12. The effect of decreasing M-C $\pi$ -bond character directs the reactivity from alkene metathesis to alkene insertion to $\sigma$ -bond metathesis.....	51
Figure 13. CO coordination modes on ruthenium nanoparticles calculated by Foppa <i>et al.</i> , the $\eta^2$ - $\mu_4$ coordination mode is suggested to be key in C-O bond cleavage. ....	52

Figure 14. Gem-hydrogenation of alkynes resulting in carbene <b>[26]</b> . The electronics of the M=C bond are tuneable based on the electronic nature of the Cp ring. ....	52
Figure 15. Catalytic ring opening of epoxides by pinacolborane and organolanthanum-decorated silica nanoparticles. ....	53
Figure 16. Hydroaminoalkylation of oct-1-ene by dimethylamine, catalysed by titanium complex supported by silica. ....	55
Figure 17. General formula of disubstituted tellurium compounds studied by SS NMR spectroscopy for fluorine transfer. ....	56
Figure 18. Schematic of a $^{13}\text{C}\{^1\text{H}\}$ CP experiment. ....	60
Figure 19. CP MAS $^{13}\text{C}\{^1\text{H}\}$ spectrum of complex <b>[35]</b> recorded at 101 MHz at a spinning speed of 10 kHz. Isotropic resonances are denoted by an arrow. Number of scans (Ns) = 16. Carbon environments have been labelled 1-4. ....	62
Figure 20. Single-crystal XRD asymmetric unit structure of complex <b>[35]</b> . Coordinates obtained from the Cambridge Crystallographic Data Centre entry CPDRUA. <sup>66</sup> Hydrogen atoms have been omitted for clarity. ....	63
Figure 21. D1 optimisation performed on complex <b>[35]</b> recorded at 101 MHz at a spinning speed of 10 kHz from top to bottom: D1 = 3, 5, 10 and 20 s. Ns = 16. Increasing values of D1 lead to a higher signal:noise ratio. ....	64
Figure 22. $^{31}\text{P}\{^1\text{H}\}$ CP MAS SS NMR spectra of PPh <sub>3</sub> recorded at 162 MHz at a spinning speed of 10 kHz, Ns = 16. CP contact time from bottom to top: P15 = 1000, 2000, 3000, 5000 and 8000 $\mu\text{s}$ . ....	66
Figure 23. Structure of <b>[3a]</b> PF <sub>6</sub> . ....	67
Figure 24. $^{19}\text{F}$ MAS SS NMR spectra of complex <b>[3a]</b> PF <sub>6</sub> recorded at 376 MHz at a spinning speed of 10 kHz. Isotropic resonances are denoted with an arrow. A contaminant was also observed at $\delta_{\text{F}} = -147$ and is denoted by an asterisk. ....	68
Figure 25. $^{13}\text{C}\{^1\text{H}\}$ CP MAS SS NMR spectra of complex <b>[35]</b> recorded at 101 MHz at a spinning speed of 10 kHz (bottom), 4 kHz (middle), 2 kHz (top). Ns = 256. The effect of decreasing MAS rotation speed, $\nu^{\text{rot}}$ on the intensity of the sidebands is shown. ....	70
Figure 26. $^{31}\text{P}\{^1\text{H}\}$ CP MAS SS NMR spectra of PPh <sub>3</sub> recorded at 162 MHz at a spinning speed of 10 kHz (bottom), 4 kHz (middle), and 2 kHz (top). Ns = 32. The effect of decreasing MAS rotation speed, $\nu^{\text{rot}}$ on the intensity of the sidebands is shown. ....	71
Figure 27. Structure of <b>[2a]</b> <sup>+</sup> used for methodology optimisation. ....	74

Figure 28. Single crystal XRD structure of [CpRu(PPh <sub>3</sub> ) <sub>2</sub> (=·=CHPh)]BF <sub>4</sub> , <b>[2a]</b> BF <sub>4</sub> , tetrafluoroborate counterion and solvent of crystallisation omitted for clarity. Selected bond lengths and angles are shown in Table 4.....	77
Figure 29. CP MAS SS <sup>13</sup> C{ <sup>1</sup> H} spectra of complex <b>[10]</b> PF <sub>6</sub> recorded at 101 MHz at a spinning speed of 10 kHz. Ns = 256. Isotropic resonances are denoted by an arrow....	85
Figure 30. Simple molecules that were selected for benchmarking chemical shift tensor calculations calculated using the previously developed methodology.....	86
Figure 31. Top: Visualised chemical shift tensors left to right: ethane, ethene, ethyne. Bottom: Visualised tensors in a pictorial representation, chemical shift reported in ppm. ....	89
Figure 32. Selected frontier molecular orbitals of ethene and key transitions identified using group theory, calculated in Orca at the PBE0/TZVPP level of theory with ZORA corrections and visualised in gOpenMol (left). Chemical shift tensor for ethene calculated in Orca at the PBE0/TZVPP level of theory with ZORA corrections and visualised in Wolfram Mathematica with pictorial representations (right). ....	91
Figure 33. Selected FMOs of ethyne and key transitions identified using group theory, calculated in Orca at the PBE0/def2_TZVPP level of theory with ZORA corrections and visualised in gOpenMol (left). Chemical shift tensors for ethyne calculated in Orca at the PBE0/def2_TZVPP level of theory with ZORA corrections and visualised in Wolfram Mathematica with pictorial representations (right). ....	93
Figure 34. Orbital transitions responsible for deshielding along the x and y axes....	94
Figure 35. Orbital transitions responsible for deshielding along the z axis.....	95
Figure 36. Energy profile for butane (R = Me) on rotation of the C-C bond. Two local minima are observed, antiperiplanar (A) and gauche (G). ....	101
Figure 37. Hyperconjugation interaction between the C-H σ and the C-F σ* orbitals in 1,2-difluoroethane. ....	101
Figure 38. Hydrogenation of alkynes using a rhodium fluorobenzene complex....	102
Figure 39. Examples of Rh <sup>I</sup> fluoroarene complex reactivity. ....	103
Figure 40. Fluoroarene sandwich complexes of Ga and In (left) and the polymerisation of <i>iso</i> -butene catalysed by Ga <sup>I</sup> (right).....	103
Figure 41. Forced η <sup>2</sup> -coordinated fluoroarene complex coordination modes show clear preference for coordination <i>ortho</i> - to C-F bonds. ....	104

Figure 42. Thermal C-H activation of fluorobenzenes by a 16 electron Rh <sup>I</sup> complex....	105
Figure 43. Photochemical C-H activation of fluorobenzenes by a 16 electron Rh complex and further C-F oxidative addition of hexafluorobenzene by Rh <sup>I</sup> .....	106
Figure 44. C-H activation of <b>[45]</b> , forming <b>[46]</b> and <b>[47]</b> . <b>[47]</b> is only observed when <i>o</i> -difluorobenzene is used.....	107
Figure 45. Outer-sphere electrophilic fluorination of ruthenium organometallics in the synthesis of fluorinated organometallic complexes. i. CH <sub>2</sub> Cl <sub>2</sub> , 20 °C, 16 h. ii. CH <sub>2</sub> Cl <sub>2</sub> , 20 °C, 1 h. iii. Toluene, -78 °C → RT. iv. THF, LiN(SiMe <sub>3</sub> ) <sub>2</sub> , -78 °C → RT.....	109
Figure 46. Fluorovinylidene (Bottom left) and fluoroalkynyl (Bottom right) complexes show significant changes to deshielding at C <sub>α</sub> compared to proteo-equivalents (Top). .....	109
Figure 47. (Top) Synthesis of fluoroethyne, <b>[53]</b> , and (Bottom) difluoroethyne, <b>[54]</b> , by pyrolysis. Degradation of the fluoroalkyne occurs even at low temperatures. ....	111
Figure 48. Formation of ruthenium alkynyl complex, overreaction of the intermediate vinylidene leads to carbene <b>[58]</b> <sup>+</sup> and phosphinovinyl <b>[59]</b> <sup>+</sup> species. ....	113
Figure 49. Formation of ruthenium alkynyl complex without heat or chloride abstraction agent using an organic base 1,8-diazobicyclo[5.4.0]undec-7-ene (DBU). <b>[2a]BF<sub>4</sub></b> can be formed by reacting <b>[1a]</b> with an acid in DCM. ....	114
Figure 50. <sup>1</sup> H NMR spectra recorded at 400 MHz of the vinylidene and Cp region of <b>[2a]BF<sub>4</sub></b> , (a), recorded after addition of tetrafluoroboric acid etherate to <b>[1a]</b> , (b). The diagnostic vinylidene proton resonance is observed after protonation at δ <sub>H</sub> = 5.44. <sup>31</sup> P{ <sup>1</sup> H} NMR spectra recorded at 162 MHz of <b>[2a]BF<sub>4</sub></b> , (c), and <b>[1a]</b> , (d). All spectra recorded in <i>d</i> <sub>2</sub> -dichloromethane.....	115
Figure 51. <sup>1</sup> H NMR Spectrum of complex <b>[1d]</b> recorded at 400 MHz. The spectrum was recorded in <i>d</i> <sub>2</sub> -dichloromethane, the residual <i>d</i> <sub>1</sub> -dichloromethane was referenced to δ <sub>H</sub> = 5.32 and is denoted by *.....	117
Figure 52. <sup>1</sup> H NMR Spectrum of complex <b>[2d]OTf</b> recorded at 400 MHz. The spectrum was recorded in <i>d</i> <sub>2</sub> -dichloromethane, the residual <i>d</i> <sub>1</sub> -dichloromethane was referenced to δ <sub>H</sub> = 5.32 and is denoted by *.....	118

Figure 53. $^1\text{H}$ NMR Spectrum of <b>[3d]</b> PF <sub>6</sub> recorded at 400 MHz. The spectrum was recorded in <i>d</i> <sub>2</sub> -dichloromethane. Residual <i>d</i> <sub>2</sub> -dichloromethane resonance obscured with the Cp resonance and is denoted by *.	120
Figure 54. $^1\text{H}\{^{31}\text{P}\}$ NMR spectrum of the aromatic resonances of complex <b>[3d]</b> PF <sub>6</sub> in <i>d</i> <sub>2</sub> -dichloromethane (Top) and $^1\text{H}$ NMR spectrum of the aromatic resonances of <b>[3d]</b> PF <sub>6</sub> in <i>d</i> <sub>2</sub> -dichloromethane (Bottom) recorded at 500 MHz. Coupling to phosphorus is observed in the <i>ortho</i> - and <i>meta</i> -positions.	121
Figure 55. $^{19}\text{F}$ spectra of <b>[3d]</b> PF <sub>6</sub> recorded in <i>d</i> <sub>2</sub> -dichloromethane at 376 MHz showing the fluorovinylidene resonance at $\delta_{\text{F}} = -216$ .	122
Figure 56. $^{31}\text{P}\{^1\text{H}\}$ NMR spectra of <b>[1d]</b> (Bottom), <b>[2d]</b> OTf (Middle), and <b>[3d]</b> PF <sub>6</sub> (Top) recorded at 162 MHz in <i>d</i> <sub>2</sub> -dichloromethane.	123
Figure 57. Ruthenium organometallic complexes studied by SS NMR spectroscopy ...	124
Figure 58. $^{13}\text{C}\{^1\text{H}\}$ CP MAS SS NMR spectra of <b>[2a]</b> BF <sub>4</sub> ·Et <sub>2</sub> O recorded at 101 MHz at a spinning speed of 10 kHz. Isotropic resonances are denoted by an arrow. Resonance associated with the ether of crystallisation are denoted by asterisks (*).	125
Figure 59. A (Top) $^{31}\text{P}\{^1\text{H}\}$ CP MAS SS NMR spectra of <b>[2a]</b> BF <sub>4</sub> recorded at 162 MHz recorded at a spinning speed of 10 kHz. Isotropic resonances denoted by an arrow. B (Bottom) $^{31}\text{P}\{^1\text{H}\}$ NMR spectra of <b>[2a]</b> BF <sub>4</sub> recorded at 162 MHz.	128
Figure 60. A (Top) $^{19}\text{F}$ MAS SS NMR spectrum of complex <b>[3a]</b> PF <sub>6</sub> recorded at 376 MHz recorded at a spinning speed of 10 kHz. Isotropic resonances denoted by an arrow. B (Bottom) $^{19}\text{F}$ NMR spectrum of complex <b>[3a]</b> BF <sub>4</sub> recorded in <i>d</i> <sub>2</sub> -dichloromethane at 376 MHz.	130
Figure 61. $^{13}\text{C}\{^1\text{H}\}$ CP MAS SS NMR Spectra of complex <b>[3a]</b> BF <sub>4</sub> (A, Top) and <b>[3a]</b> PF <sub>6</sub> (orange polymorph) (B, Bottom) recorded at 101 MHz at a spinning speed of 10 kHz. Isotropic resonances are denoted by an arrow. B (Bottom) Isotropic resonances are denoted by an arrow.	132
Figure 62. CP MAS SS NMR spectrum of complex <b>[7]</b> recorded at 101 MHz at a spinning speed of 10 kHz. The resonance for C <sub>α</sub> is observed at 44.7 ppm.	136
Figure 63. HPDEC MAS SS NMR spectrum of complex <b>[7]</b> recorded at recorded at 101 MHz at a spinning speed of 10 kHz. The intensity of the C <sub>α</sub> is still low, but the resonance is observed.	137

Figure 64. Proton-carbon (Top) and fluorine-carbon (Bottom) CP MAS SS NMR spectra of <b>[3a]</b> PF <sub>6</sub> recorded at recorded at 101 MHz at a spinning speed of 10 kHz.. The intensity of the beta carbon shows a large increase in relative intensity. ....	138
Figure 65. Proton-carbon (Top) and fluorine-carbon (Bottom) CP MAS SS NMR spectrum of <b>[7]</b> recorded at recorded at 101 MHz at a spinning speed of 10 kHz.. The intensity of C <sub>β</sub> (112.8 ppm) shows a large increase in relative intensity.....	139
Figure 66. Ruthenium organometallic complexes studied by quantum chemical calculations using DFT. ....	140
Figure 67. Fit between computationally- and experimentally- derived chemical shift tensors. The calculated values and trends match those observed experimentally. ....	143
Figure 68. Visualised chemical shift tensors of key ruthenium organometallics. From top left going clockwise: <b>[2a]</b> <sup>+</sup> , <b>[3a]</b> <sup>+</sup> , <b>[1a]</b> , <b>[4]</b> , <b>[7]</b> , <b>[10]</b> <sup>+</sup> . ....	144
Figure 69. Structure of <b>[60]</b> and <b>[61]</b> , which are used as simple electronic models of vinylidene and fluorovinylidene complexes. ....	145
Figure 70. FMO diagram of <b>[60]</b> with selected orbitals visualised in gOpenMol (left). Key transitions identified using group theory. <b>[60]</b> optimised in Turbomole at the BP86/def2_SV(P) level of theory, chemical shift tensors calculated in Orca at the PBE0/def2_TZVPP level of theory with ZORA corrections and visualised in Wolfram Mathematica with pictorial representations (right). The Barycentre is represented by the dotted line.....	147
Figure 71. FMOs diagram of fluorovinylidene <b>[61]</b> with selected orbitals visualised in gOpenMol (left). Orbitals and transitions that do not contribute to deshielding are shown in grey. Key transitions identified using group theory. <b>[61]</b> optimised in Turbomole at the BP86/def2_SV(P) level of theory, chemical shift tensors calculated in Orca at the PBE0/def2_TZVPP level of theory with ZORA corrections and visualised in Wolfram Mathematica with pictorial representations (right). The Barycentre is represented by the dotted line. ....	150
Figure 72. Key transitions responsible for deshielding along the z axes of <b>[60]</b> and <b>[61]</b> calculated in Orca at the PBE0/def2_TZVPP level of theory with ZORA corrections. Constructive interactions are represented by green arrows and deconstructive interactions by red arrows. ....	151

Figure 73. Allene and vinyliminium species <b>[62]</b> – <b>[67]</b> <sup>+</sup> identified as simple models for <b>[2a]</b> <sup>+</sup> and <b>[3a]</b> <sup>+</sup> . .....	152
Figure 74. Effect of fluorination on the chemical shift tensors for allene, vinyliminium, and coordinated vinylidenes optimised in Turbomole at the BP86/def2_SV(P) level of theory, chemical shift tensors calculated in Orca at the PBE0/def2_TZVPP level of theory with ZORA corrections and visualised in Wolfram Mathematica with pictorial representations. ....	154
Figure 75. FMO diagram of <b>[62]</b> with selected orbitals visualised in gOpenMol (left). Key transitions identified using group theory. <b>[62]</b> optimised in Turbomole at the BP86/def2_SV(P) level of theory, chemical shift tensors calculated in Orca at the PBE0/def2_TZVPP level of theory with ZORA corrections and visualised in Wolfram Mathematica with pictorial representations (right). The barycentre is represented by the dotted line.....	155
Figure 76. FMO diagram of <b>[66]</b> <sup>+</sup> with selected orbitals visualised in gOpenMol (left). Key transitions identified using group theory. <b>[66]</b> <sup>+</sup> optimised in Turbomole at the BP86/def2_SV(P) level of theory, chemical shift tensors calculated in Orca at the PBE0/def2_TZVPP level of theory with ZORA corrections and visualised in Wolfram Mathematica with pictorial representations (right). The barycentre is represented by the dotted line.....	157
Figure 77. HOMO (top) and LUMO (bottom) of <b>[2a]</b> <sup>+</sup> (left) and <b>[3a]</b> <sup>+</sup> (right) showing the change in bonding character on fluorination. This transition dominates the changes to $\delta^{\text{para}}$ along the z axis.....	159
Figure 78. <sup>13</sup> C{ <sup>1</sup> H} CP MAS SS NMR Spectra of <b>[2a]</b> BF <sub>4</sub> (Top) and <b>[3a]</b> PF <sub>6</sub> (Bottom) recorded at 101 MHz at a spinning speed of 10 kHz showing changes to $\delta^{\text{iso}}$ . The intensity of the vinylidene resonances has been increased to aid identification. ....	161
Figure 79. <sup>13</sup> C{ <sup>1</sup> H} CP MAS SS NMR Spectra of <b>[2a]</b> BF <sub>4</sub> (Top) and <b>[3a]</b> PF <sub>6</sub> (Bottom) recorded at a spinning speed of 4 kHz showing changes to CSA. The intensity of the vinylidene resonances has been increased to aid identification. ....	162
Figure 80. Key orbitals of <b>[60]</b> and <b>[61]</b> responsible for deshielding with orbital energies, calculated in Orca at the PBE0/def2_TZVPP level of theory with ZORA corrections. ....	163

Figure 81. Structure of halogenovinylidene complexes synthesized by Lynam and Slattery. ....	164
Figure 82. Pictorial (left) and visualised chemical shift tensors ( $C_{\alpha}$ , middle) ( $C_{\beta}$ , right) of halogenovinylidene complexes. ....	166
Figure 83. Pictorial (Top) and visualised (bottom) chemical shift tensors of <b>[38]</b> and <b>[4]</b> . ....	168
Figure 84. FMO diagram of fluoroethyne <b>[53]</b> with selected orbitals visualised in gOpenMol (left). Key transitions identified using group theory. <b>[53]</b> optimised in Turbomole at the BP86/def2_SV(P) level of theory, chemical shift tensors calculated in Orca at the PBE0/def2_TZVPP level of theory with ZORA corrections and visualised in Wolfram Mathematica with pictorial representations (right). The barycentre is represented by the dotted line. ....	169
Figure 85. Ruthenium organometallic complexes studied by quantum chemical calculations using DFT and TD TDF. ....	172
Figure 86. Correlation of the first excitation energy calculated using TD DFT and chemical shift tensors pointing along the M-C bond axis. Both calculated in Orca at the PBE0/def2_TZVPP level of theory with ZORA corrections. ....	172
Figure 87. Structure of different ruthenium fragments used to study the effect of metal fragment on alkynyl- and vinylidene $C_{\alpha}$ chemical shift. The chemical shift of $C_{\alpha}$ was largely invariant on changing metal fragment. ....	175
Figure 88. General scheme for the hydroformylation of an alkene to produce aldehydes. The transition metal catalyst used is typically a group 9 hydridecarbonyl complex of Co or Rh. ....	180
Figure 89. Key side products in hydroformylation of terminal alkenes. Aldol condensation products not shown. ....	180
Figure 90. Mechanism of cobalt-catalysed hydroformylation as described by Heck and Breslow. ....	181
Figure 91. Hydroformylation of a terminal alkene. The subscript l and b denote the proto-linear and proto-branched pathways. ....	183
Figure 92. Equilibrium between EE and EA for <b>[A]</b> . ....	184
Figure 93. Schematic examples of heterogeneous rhodium hydroformylation catalysts as summarized by Schunk; supported Rh complexes where L = phosphine or	

CO (left), supported metallic Rh nanoparticles (middle), and supported single atom Rh catalysts (right).....	185
Figure 94. Target Vaska-type complexes identified for SS NMR analysis.....	187
Figure 95. SS $^{195}\text{Pt}$ NMR spectrum of $\text{K}_2\text{PtCl}_6$ recorded at 86 MHz at a spinning speed of 10 kHz. ....	190
Figure 96. SS NMR MAS $^{195}\text{Pt}$ spectra recorded at 86 MHz between -1000 and -2300 ppm at a spinning speed of 10 kHz. $N_s = 4096$ . ....	191
Figure 97. SS NMR MAS $^{195}\text{Pt}$ spectra of $\text{K}_2$ [ <b>72</b> ] recorded at 86 MHz between 6000 and -6000 ppm at a spinning speed of 10 kHz. ....	192
Figure 98. Structure of $[\text{Pt}(\text{ppyH})(\text{ppy})\text{Cl}]$ ( <b>[73]</b> ), and $[\text{Pt}(\text{ppy})_2\text{Cl}_2]$ ( <b>[74]</b> ). ppyH = 2-phenylpyridine. ....	193
Figure 99. Solution phase $^{31}\text{P}\{^1\text{H}\}$ NMR spectra of <i>trans</i> - <b>[15]</b> recorded at 162 MHz in $d_2$ -dichloromethane. ....	195
Figure 100. $^{103}\text{Rh}\{^1\text{H}\}$ NMR spectra of <i>trans</i> - <b>[16]</b> recorded in $d_1$ -chloroform at 27 MHz. ....	196
Figure 101. Platinum and rhodium complexes studied in this chapter.....	202
Figure 102. Visualised FMOs of <b>[71]</b> $^{2-}$ with d character. Transitions are allowed between $T_{2g}$ and $E_g$ orbitals. <b>[71]</b> $^{2-}$ optimised in Turbomole at the PBE0/def2_TZVPP level of theory with a water COSMO implemented. Chemical shift tensors calculated in Orca at the PBE0/def2_TZVPP level of theory with ZORA corrections. The platinum was represented with the SARC_TZVPP basis set. Ligand-based orbitals are shown in grey....	204
Figure 103. FMO diagram of <b>[72]</b> $^{2-}$ with selected orbitals visualised in gOpenMol (left). Key transitions identified using group theory. <b>[72]</b> $^{2-}$ optimised in Turbomole at the PBE0/def2_TZVPP level of theory with a water COSMO implemented. Chemical shift tensors calculated in Orca at the PBE0/def2_TZVPP level of theory with ZORA corrections. The platinum was represented with the SARC_TZVPP basis set. Chemical shift tensors visualised in Wolfram Mathematica with pictorial representations (right). The barycentre is represented by the dotted line. Ligand-based orbitals are shown in grey. ....	206
Figure 104. FMO diagram of <i>cis</i> - <b>[75]</b> with selected orbitals visualised in gOpenMol (left). Key transitions identified using group theory. <i>cis</i> - <b>[75]</b> optimised in Turbomole at	

the PBE0/def2\_TZVPP level of theory with a water COSMO implemented. Chemical shift tensors calculated in Orca at the PBE0/def2\_TZVPP level of theory with ZORA corrections. The platinum was represented with the SARC\_TZVPP basis set. Chemical shift tensors visualised in Wolfram Mathematica with pictorial representations (right). The barycentre is represented by the dotted line. Ligand-based orbitals are shown in grey. ....208

Figure 105. FMO diagram of *cis*-[76] with selected orbitals visualised in gOpenMol (left). Key transitions identified using group theory. *cis*-[76] optimised in Turbomole at the PBE0/def2\_TZVPP level of theory with a water COSMO implemented. Chemical shift tensors calculated in Orca at the PBE0/def2\_TZVPP level of theory with ZORA corrections. The platinum was represented with the SARC\_TZVPP basis set. Chemical shift tensors visualised in Wolfram Mathematica with pictorial representations (right). The barycentre is represented by the dotted line. Ligand-based orbitals are shown in grey. ....210

Figure 106. FMO diagram of *cis*-[14] with selected orbitals visualised in gOpenMol (left). Key transitions identified using group theory. *cis*-[14] optimised in Turbomole at the PBE0/def2\_TZVPP level of theory with a water COSMO implemented. Chemical shift tensors calculated in Orca at the PBE0/def2\_TZVPP level of theory with ZORA corrections. Chemical shift tensors visualised in Wolfram Mathematica with pictorial representations (right).....212

Figure 107. FMO diagram of *trans*-[14] with selected orbitals visualised in gOpenMol (left). Key transitions identified using group theory. *trans*-[14] optimised in Turbomole at the PBE0/def2\_TZVPP level of theory with a water COSMO implemented. Chemical shift tensors calculated in Orca at the PBE0/def2\_TZVPP level of theory with ZORA corrections. Chemical shift tensors visualised in Wolfram Mathematica with pictorial representations (right).....214

Figure 108. <sup>103</sup>Rh chemical shift tensors of rhodium Vaska-type complexes in pictorial (Top) and visualized (Bottom) forms. Chemical shift tensors visualised in Wolfram Mathematica.....216

Figure 109. <sup>103</sup>Rh chemical shift tensors of rhodium Vaska-type complexes in pictorial (Top) and visualized (Middle) forms. Chemical shift tensors visualised in Wolfram

Mathematica. Angular dependence of NMR parameters based on P-Rh-P angle (Bottom). .....	218
Figure 110. Solid-state structure of <b>[2a]</b> BF <sub>4</sub> , hydrogen atoms, solvent of crystallisation, and counter ion omitted for clarity. Selected bond lengths / Å Ru1-C1 1.848, C1-C2 1.314, C2-C3 1.476. Selected bond angles / ° Ru1-C1-C2 165.68, C1-C2-C3 131.74. ....	266
Figure 111. Solid-state structure of <b>[2c]</b> OTf, hydrogen atoms and counter ion omitted for clarity. Selected bond lengths / Å Ru1-C1 1.836, C1-C2 1.317, C2-C3 1.470. Selected bond angles / ° Ru1-C1-C2 174.23, C1-C2-C3 124.04. ....	269
Figure 112. Solid-state structure of <b>[2d]</b> OTf, hydrogen atoms and counter ion omitted for clarity. Selected bond lengths / Å Ru1-C6 1.861, C6-C7 1.307, C7-C8 1.521. Selected bond angles / ° Ru1-C6-C7 169.41, C6-C7-C8 130.35.....	271

## Acknowledgements

I would like to thank my supervisors, John Slattery and Jason Lynam, for all your support and feedback throughout my PhD which never faltered, even during a pandemic. Your support has been invaluable in my development as an, apparently, professional chemist. I couldn't have asked for better supervisors, even if you could've asked for a better student!

I would also like to thank Heather Fish, Karl Heaton, and Adrian Whitwood for all your technical support keeping departmental NMR, Mass Spec, and crystallography services running without fail.

To the SLUG group, past and present, I have thoroughly enjoyed working, socializing and Zoom calling all of you. I reiterate the words of Lewis Hall, "may all your NMR spectra be clean, and your reactions catalytic", I'll add may all your crystals be single.

A special shoutout to Nina, Will, and Ben for listening to 5 years of rants and bad jokes. But more importantly, for being your unadulterated selves.

I thank my parents for all your help and encouragement for getting to this point in my life. Thank you to all my family who have supported and nodded politely after asking what I do for work.

Thank you, Katherine, for always being there. I couldn't have done it without you.

## **Author's Declaration**

I declare that this thesis is a presentation of original work and I am the sole author. This work has not been presented for an award at this, or any other, university. All sources are acknowledged as references.

## Chapter 1. Introduction

In this thesis, the bonding in organometallic complexes has been interpreted and correlated to the chemical shift tensors, which are the three-dimensional representations of the chemical shift interaction. The tensors have been recovered from solid-state NMR spectra and predicted using quantum chemical calculations using DFT. The complexes **[1]** – **[13]**<sup>+</sup> studied in chapter 3 are shown in Figure 1. The complexes **[14]** – **[20]**, studied in chapter 4 are shown in Figure 2.

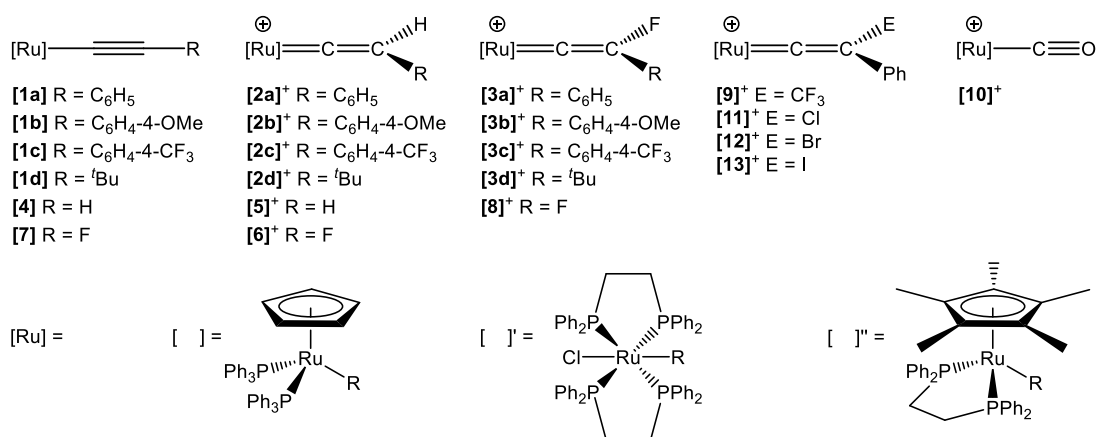


Figure 1. Complexes **[1]** – **[13]**<sup>+</sup>, which have been studied in chapter 3. For complexes **[1]** – **[13]**<sup>+</sup>, the absence of diacritical marks denotes the ruthenium centre:  $[Ru(\eta^5-C_5H_5)(PPh_3)_2]^+$ . A single diacritical mark denotes the ruthenium centre: *trans*- $[Ru(Cl)(dppe)_2]^+$ . Two diacritical marks denote the ruthenium centre:  $[Ru(\eta^5-C_5Me_5)(dppe)]^+$ .

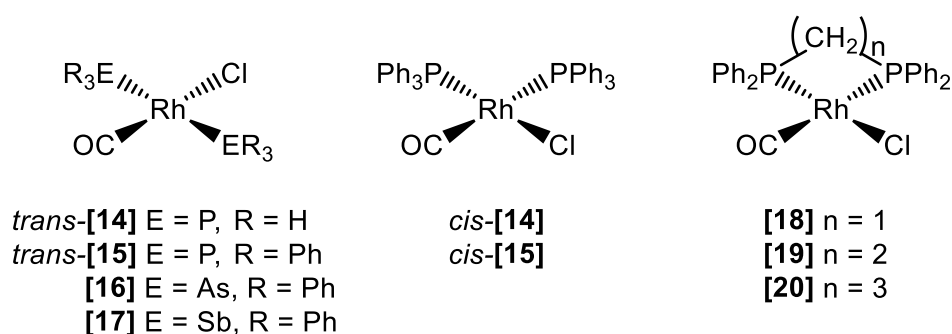


Figure 2. Complexes **[14]** – **[20]** studied in chapter 4.

In this introduction, the fundamentals of NMR spectroscopy will be discussed including the key interactions experienced by the nuclear spin. How the key concepts

are applied in SS NMR spectroscopy will then be discussed. As quantum chemical calculations are a key part of this work, a brief introduction to computational chemistry has been included, focusing on the Schrödinger equation and the key approximations that are required for solving a multi-electron system. The bonding between metals and ligands will be described.

The literature has been reviewed on the analysis of metal-ligand bonding and how understanding of bonding may be utilised to improve function. A brief summary of some direct spectroscopic and indirect techniques is included with examples of their use in structure/function determination. SS NMR spectroscopy has been used extensively in the study of alkene metathesis catalysts, which is described along with other systems that have benefited from SS NMR spectroscopic analysis.

## 1.1 Fundamentals of NMR spectroscopy

### 1.1.1 Nuclear spin

Elementary particles exhibit the quantum property known as spin ( $I$ ). Elemental nuclei are comprised of protons and neutrons, which are both spin  $\frac{1}{2}$  particles. In the nucleus of an atom, the magnetic dipoles align against each other, cancelling each other out. This means that for an atomic nucleus that contains an even number of protons and neutrons, the total spin must equal zero,  $I = 0$ . A nucleus with  $I = 0$  will not exhibit different spin states. Several key isotopes possess  $I = 0$  such as  $^4\text{He}$ ,  $^{16}\text{O}$ , and  $^{32}\text{S}$ , but the most important with respect to synthetic organic chemistry is  $^{12}\text{C}$ . As  $I = 0$  nuclei cannot occupy different spin states, they are unobservable by NMR spectroscopy.

If the total number of nucleons is odd, the total spin will be a half-integer value,  $I = \frac{1}{2}, \frac{3}{2}, \frac{5}{2}$  etc. If both the number of protons and neutrons are odd, the total spin will be an integer value,  $I = 1, 2, 3$  etc. A nucleus that has  $I = \frac{1}{2}$  acts like a magnetic dipole and is therefore referred to as a dipole. Nuclei with  $I > \frac{1}{2}$  are called quadrupolar..

### 1.1.2 The NMR Hamiltonian

The overall spin dynamics of a given system can be represented as a sum of the individual interactions of the spin with the local and global environments. The Hamiltonian for the NMR signal can also be deconvoluted into individual components as shown in Equation 1:

$$\hat{H} = \hat{H}_Z + \hat{H}_{CS} + \hat{H}_{rf} + \hat{H}_{ID} + \hat{H}_{DD} + \hat{H}_Q \quad \text{Equation 1}$$

Each Hamiltonian operator represents the interaction with a nuclear spin. The Zeeman interaction, which is described by  $\hat{H}_Z$ , is the interaction of  $I$  with an external magnetic field,  $B_0$ .  $\hat{H}_{CS}$  is the chemical shielding, also known as chemical shift, Hamiltonian and represents changes in the local magnetic field due to the interaction of  $I$  with the local electron cloud.  $\hat{H}_{rf}$  arises from the interaction of  $I$  with the applied

radiofrequency (*rf*) pulse.  $\hat{H}_{ID}$  is the indirect dipolar-coupling interaction between spins  $I_j$  and  $I_k$ , mediated by electrons. This is known as the *J* coupling interaction.  $\hat{H}_{DD}$  is the direct dipolar through space coupling interaction between spins  $I_j$  and  $I_k$ .  $\hat{H}_Q$  is the coupling interaction between  $I$  and the local electric field. This is called the quadrupolar interaction.

### 1.1.3 The interaction of nuclear spin with an external magnetic field (Zeeman)

In any given sample, the spins of the nuclei point in random directions. However, in the presence of an external field, the degeneracy between spin states is disrupted and spins reorient themselves into discrete energy levels. This interaction is called the Zeeman effect. Considering a  $I = 1/2$  nuclei such as  $^1\text{H}$ , rather than being randomly oriented, the spins can now occupy two discrete spin states with the spins aligned with the external magnetic field or opposing the field. As the size of  $B_0$  increases, so does the energy gap between aligned and opposing spins.<sup>1</sup> This relationship is represented in Equation 2 where  $\gamma$  is the gyromagnetic ratio,  $\hbar$  is the reduced Planck's constant, and  $B_0$  is the external magnetic field in Tesla. The energy gap between the two states is very small, corresponding to light in the *rf* region.

$$\Delta E = \gamma \hbar B_0 \quad \text{Equation 2}$$

As the energy gap between the high and low energy states increases, so does the population difference. The ratio of the population difference can be calculated using the Boltzmann equation (Equation 3) where  $k$  is the Boltzmann constant and  $T$  is the absolute temperature. Using Equation 3, it can be shown that the population difference is only very small. Most spins in the system cancel each other out and the only spins that can be recorded are a tiny proportion of the system. This leads to the poor sensitivity observed in NMR spectroscopy.

$$\frac{N_{Upper}}{N_{Lower}} = e^{\left(\frac{-\Delta E}{kT}\right)} \quad \text{Equation 3}$$

## 1.2 Basics of Solid-State Nuclear Magnetic Resonance Spectroscopy

Resonances in solution exhibit a single chemical shift value, corresponding to the magnetic field. However, the nucleus responds differently depending on its orientation with respect to the magnetic field. The single value observed is comprised of nine individual chemical shift values. These values have a specific direction to them and are therefore rank 2 tensor quantities and can be better represented as a 3 by 3 matrix.<sup>2</sup>

Only one value of chemical shift is observed due to rapid sampling of all orientations as the nuclei is tumbling rapidly in solution. This rotation averages the anisotropy in the system giving the isotropic chemical shift ( $\delta^{\text{iso}}$ ), which has a non-zero average. A 3 by 3 matrix of chemical shift tensors contains nine individual tensor components. The eigenvalues of the matrix can be calculated and multiplied by a 3 by 3 identity matrix to give the diagonal tensor components corresponding to the 3 cardinal axes:  $\delta_{11}$ ,  $\delta_{22}$ ,  $\delta_{33}$ . These tensors are called the principal components and are orthogonal.

$$\begin{pmatrix} \delta_{11} & \delta_{12} & \delta_{13} \\ \delta_{21} & \delta_{22} & \delta_{23} \\ \delta_{31} & \delta_{32} & \delta_{33} \end{pmatrix} \rightarrow \begin{pmatrix} \delta_{11} & 0 & 0 \\ 0 & \delta_{22} & 0 \\ 0 & 0 & \delta_{33} \end{pmatrix} \quad \text{Equation 4}$$

In a solid, as molecules are no longer tumbling and are in defined positions, the anisotropy in the system is no longer averaged out. This is observed as a broadening of the resonance. NMR spectroscopic experiments on a solid sample can be performed to obtain the chemical shift tensors:  $\delta_{11}$ ,  $\delta_{22}$ ,  $\delta_{33}$ .<sup>3</sup>

In a solid rotating at the magic angle, which is equal to an angle of  $\theta_m = 54.74^\circ$  for an  $l = \frac{1}{2}$  particle, a resonance is observed as a series of sharp bands rather than a broad resonance. Spinning at  $\theta_m$  averages the chemical shift interaction to its non-zero average. More detail on the magic angle is described in section 1.2.2. If the spinning speed is greater than the chemical shift anisotropy, then most of the signal intensity is accounted for in the isotropic band. Small portions of signal then trail from  $\delta^{\text{iso}}$  as spinning side echoes, which are periodic. The separation between the side bands and  $\delta^{\text{iso}}$  is related to the spinning speed ( $\nu^{\text{rot}}$ ) in Hertz with side bands occurring at  $\pm n\nu^{\text{rot}}$ . Information on the anisotropy in the system is not encoded into the side echoes. As the spinning speed is reduced, the side bands move closer to the centre

band. When the side band occurs in the span of the SS NMR spectrum, they begin to have significant intensity. This is because the side band now has a contribution from the chemical shift tensors. The spinning side band intensities give a distinctive line shape which correlates to the shape observed in a non-rotating “static” powder SS NMR spectrum.<sup>4</sup> Chemical shift tensors can be extracted directly from the static SS NMR spectrum based on the breadth of the resonance and the location of the most intense peak in the broad resonance. Chemical shift tensors can also be extracted from spinning samples based on the intensities of the spinning side bands. This can be done graphically or by iterative simulation.<sup>4-6</sup>

### 1.2.1 Dipolar and quadrupolar interactions

Each nucleus with  $I = 1/2$  acts as a magnetic dipole. Magnetic dipoles may interact with each other. The magnetic resonance Hamiltonian is a sum of several interactions as described in section 1.1.2 of which  $H_{ID}$  and  $H_{DD}$  are due to dipolar coupling.

Unlike the  $J$  coupling interaction  $H_{ID}$ , the through space coupling between spins is not mediated by electrons. The magnitude of the direct-dipole coupling can be expressed by the Equation 5 below:

$$b_{jk} = - \left( \frac{\mu_0}{4\pi} \right) \frac{\hbar \gamma_j \gamma_k}{r_{jk}^3} \quad \text{Equation 5}$$

$b_{jk}$  is the dipole-dipole coupling constant in  $\text{rad s}^{-1}$  (division by  $2\pi$  gives  $b_{jk}$  in Hz),  $\mu_0$  is the magnetic vacuum permeability constant,  $\gamma$  is the gyromagnetic ratio of nuclei  $j$  and  $k$ , and  $r_{jk}$  is the vector distance between the spins. The magnitude of  $b_{jk}$  is dependent on the gyromagnetic ratios of the coupling spins and is inversely proportional to the cube of the distance between them.

Strong coupling occurs when the distance between spins is low and leads to splitting of the SS NMR trace into a Pake doublet.<sup>7</sup> Direct-dipole coupling is particularly important in the analysis of SS systems both directly and indirectly. The direct-dipole coupling constant has been used to measure the interatomic distances directly

between the H atoms in hydrated Gypsum, this would be challenging using other analytical techniques.<sup>7</sup> In more complicated systems, direct-dipole coupling leads to significant broadening and complication of the spectra. This interaction is more commonly exploited for transferring polarisation from high  $\gamma$  nuclei to low  $\gamma$  nuclei in the process known as cross polarisation (CP), further described in section 2.2.1.

Direct-dipole coupling is orientation dependent and has an average of 0. Due to this, the effect of direct-dipole coupling cannot be observed directly in solution due to rapid sampling of all orientation from molecular tumbling. However, the effects of direct-dipole coupling can be observed indirectly through the Nuclear Overhauser Effect (NOE).

### 1.2.2 Magic Angle Spinning (MAS)

As previously mentioned in section 1.2.1, direct-dipole interactions and chemical shift anisotropy lead to significant broadening of each magnetic environment in the solid state. Spectra of even small molecules become convoluted due to the overlap of chemical shift anisotropy and Pake doublets.<sup>7</sup>

In a rotating solid, the magnetic resonance signal is profoundly affected by the local magnetic environment as the sample is rotating. This can be represented by the time-dependent Hamiltonian (Equation 6), where  $I$  and  $J$  are the spins in the system, and  $\lambda$  represents the interactions experienced in the system (such as dipolar interactions and chemical shift).<sup>4</sup>

$$H^{td} = \sum_{i \neq j} \sum_{\lambda} H^{(i,j; \lambda)} \quad \text{Equation 6}$$

This Hamiltonian can be expressed in a coordinate system fixed in the sample holder, called the rotor.  $C$  contains physical constants such as the gyromagnetic ratio. The symbols  $r$  and  $\tau$  are tensor quantities that denote the spatial and spin dependence of the Hamiltonian with respect to the rotating coordinate system.  $\Theta$  is the angle between the rotor and the magnetic field,  $\beta$  and  $\gamma$  are about the rotating frame of reference. This is shown in Equation 7. The indices have been omitted for clarity ( $i, j ; \lambda$ ).

$$H_0 = C\rho\tau_{00} + \sqrt{3/2} C\delta\tau_{20} \left[ \frac{1}{2}(3\cos^2\theta - 1) \right] \left[ \frac{1}{2}(3\cos^2\beta - 1) + \left(\frac{\eta}{2}\right) \sin^2\beta \cos^2\gamma \right] + \sqrt{3/2} C\delta\tau_{20} \zeta(t) \quad \text{Equation 7}$$

The time-dependent Hamiltonian can be substituted for a time-independent Hamiltonian by integration due to the periodic nature of the rotation as shown in Equation 8.<sup>4</sup>

$$H_{00}^{tid} = \frac{\omega_r}{2\pi} \int_0^{2\pi} \sum_{i \neq j} \sum_{\lambda} H^{(i,j;\lambda)}$$

$$H_{00}^{tid} = C\rho\tau_{00} + \sqrt{3/2} C\delta\tau_{20} \left[ \frac{1}{2}(3\cos^2\theta - 1) \right] \left[ \frac{1}{2}(3\cos^2\beta - 1) + \left(\frac{\eta}{2}\right) \sin^2\beta \cos^2\gamma \right] \quad \text{Equation 8}$$

The second term of the integral can be reduced to 0 if:

$$(3\cos^2\theta - 1) = 0$$

$$\therefore \cos^2\theta = \frac{1}{3}$$

$$\theta = \tan^{-1}(\sqrt{2}) = 54.74^\circ$$

$$\theta_m = 54.74^\circ$$

This value,  $\theta_m$ , is known as the magic angle. At  $\theta_m$  the chemical shift interaction become averaged as the Hamiltonian collapses to the isotropically averaged form observed in solution. Direct-dipole coupling and chemical shielding are both rank 2 tensors. Direct-dipole coupling has a zero average and is therefore completely removed from the spectrum. The chemical shielding interaction has a non-zero average, meaning that partial averaging occurs and each magnetic environment will correspond to a sharp isotropic resonance with a unique chemical shift.

Another way to visualise the effect of the magic angle is by visualising a rank 2 tensor as a spherical harmonic, as shown in Figure 3. A line can be drawn bisecting the positive and negative phases of the tensor where the value is 0. The angle of this line with respect to the principal axis is  $\theta_m = 54.74^\circ$ .

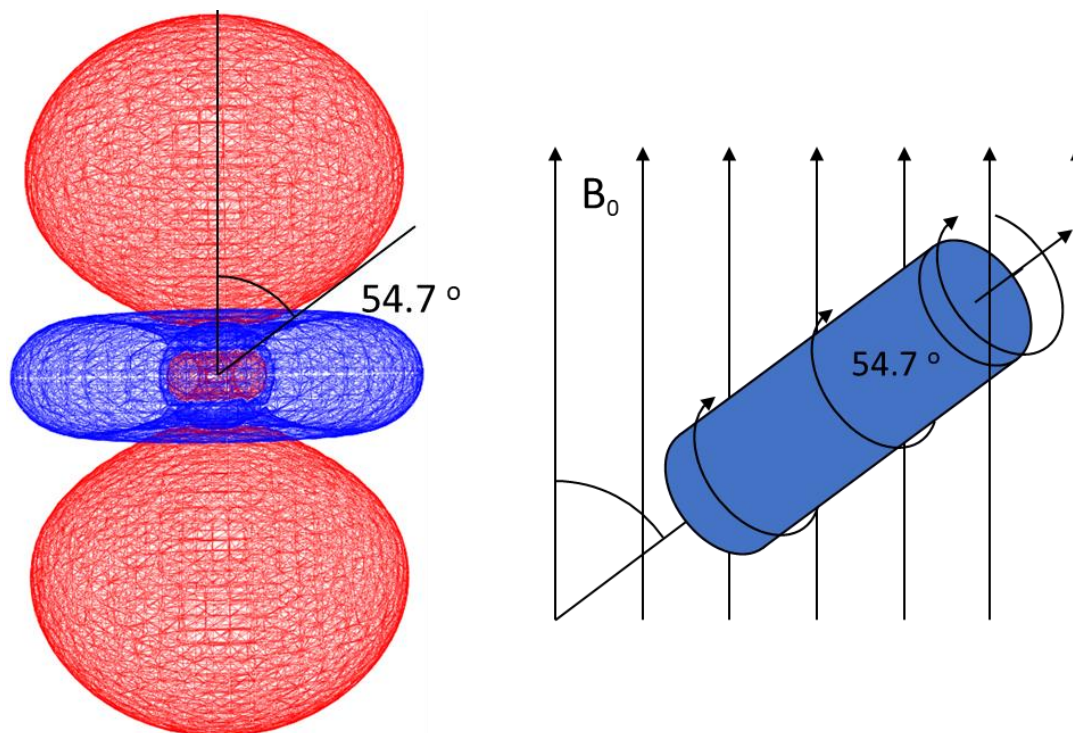


Figure 3. Spherical harmonic representation of a rank 2 tensor (left) and SS NMR spinning at the magic angle with respect to  $B_0$  (right).

The intensities of the side bands can be expressed mathematically. This has been shown by Herzfeld and Berger, but will not be further described in this thesis.<sup>4</sup>

### 1.3 Introduction to computational chemistry

Chemical systems are small and are poorly described using classical, or Newtonian, mechanics because of their small scales. Chemical systems, being on the atomic scale, are better described using quantum mechanics. The main difference between classical and quantum mechanics is that in quantum mechanics, the quantities of the system are restricted to discrete quantized values. In classical mechanics, the quantities of the system are described by a continuum.<sup>8</sup>

### 1.3.1 The Schrödinger equation

As mentioned previously, the qualities of an atomic system are described by discrete values. The energy of a given system is described by the Schrödinger equation below (Equation 9).<sup>8-10</sup>

$$\hat{H}\Psi = E\Psi \quad \text{Equation 9}$$

Equation 9 is the time-independent form of the Schrödinger equation and describes the energy of a stationary state.  $\Psi$  is the wavefunction of the system and is a mathematical descriptor of the stationary state.  $E$  is the energy of the state and  $\hat{H}$  is a Hamiltonian operator that describes the allowed states of the system. The eigenvalues of  $\hat{H}$  give the possible outcomes in the calculation of the energy of the system. As  $\hat{H}$  gives the values of  $E$  for the system when applied to the given wavefunction,  $\hat{H}$  can be degraded into a series of Hamiltonians to represent each interaction that contributes to the total energy of the system. The eigenvalues of each Hamiltonian give rise to observable values.

A time-independent Schrödinger equation may only describe a stationary point and does not describe a system with any temporal resolution. To calculate the energy of a system that changes with time, the time-dependent Schrödinger equation must be applied instead.

The Schrödinger equation allows for the calculation of the energy states that are allowed in a system. However, the limiting factor is that the Schrödinger equation is only solvable in a system that contains one electron, such as the hydrogen atom. This is because  $\Psi$  becomes too complex to be solved explicitly in larger systems due to Coulomb repulsion interactions between electrons. Instead, the wavefunction must be approximated for the Schrödinger equation to be solved in large systems.

### 1.3.2 Application of the Born-Oppenheimer approximation to the Schrödinger equation

The many factors that make up the wavefunction mean that the Schrödinger equation cannot be solved for large systems. However, if the wavefunction is

approximated, the Schrödinger equation can be solved taking the approximation into account. Nuclei are much larger and heavier than electrons. This means that the motion of the nuclei is much slower than the motions of the electrons and therefore electronic motion should be independent of nuclear motion. If the two properties are independent, the wavefunctions may be considered separately.<sup>8</sup>

As the nuclei appear to be stationary from the electronic point of view, the kinetic energy must be zero and any repulsions are fixed. Coordinates are no longer a variable parameter, simplifying the calculation of the energy states. The Born-Oppenheimer approximation allows the degradation of the Hamiltonian to an electronic Hamiltonian and a nuclear Hamiltonian. Application of the electronic Hamiltonian to the wavefunction gives the electronic energy only. Application of the nuclear Hamiltonian gives the kinetic energy. The solution to the electronic energy can be used to generate a potential energy surface (PES), which can be in turn be used to calculate nuclear motion.

The Born-Oppenheimer approximation allows for the simplification of the Schrödinger equation into electronic and nuclear components, allowing for separate energy calculation. To gain meaningful solutions to the Schrödinger equation, the electron coordinates are determined by only considering how a single electron responds to the average field of the other electrons. The electron is moved to give the lowest energy. This is repeated for all the electrons until movement of the electrons no longer reduces the energy of the system. The electron field is then consistent and the process is iterative. It is referred to as the self-consistent field (SCF) procedure.

The Born-Oppenheimer approximation holds when electronic motion and nuclear motion do not influence each other greatly. However, when this is no longer the case, the approximation breaks down.

Electrons are indistinguishable from one another, however, the probability of finding an electron is dependent on the location of the other electrons due to electron repulsion interactions. The wavefunction of a multi electron system may be described

using Slater determinants. Electrons may not have the same quantum numbers, as stated by the Pauli exclusion principle. A Slater determinant satisfies this principle by assigning all electrons to a spin orbital with a location and a spin. If two electrons are assigned the same spin and location, the wavefunction would be zero in all locations. Slater determinants allow multi-electron systems to be handled in a way that satisfies the Pauli exclusion principle.

### 1.3.3 Hartree-Fock method

The Hartree-Fock method uses a single Slater determinant and the SCF may be used to approximate the wavefunction and the energy of a system with many bodies, such as a chemical system. For a body with  $N$  particles,  $N - 1$  electron spin orbitals may be generated.<sup>8</sup> The SCF method allows for the iterative solving of the variational energy of the system by solving a Hartree-Fock equation for each electron iteratively. This method gives an approximate solution to the Schrödinger equation. The molecular orbitals (MOs) that are used in the SCF method may be comprised of linear combinations of Slater-type orbitals or Gaussian-type orbitals. Gaussian-type orbitals are more commonly used in quantum chemical calculations as they can be represented using polar coordinates, reducing the number of components that require calculating.<sup>8</sup> This means that, for the same time, a larger number of basis functions may be used to describe the orbitals.

### 1.3.4 Basis sets

In computational quantum chemical calculations, parameters for the electronic wavefunctions must be supplied in order to solve the Schrödinger equation.<sup>8</sup> The form these wavefunctions take in the calculations is as the basis set. A basis set is a collection of basis functions that correspond to the atomic orbitals. The individual atomic orbitals may be combined to yield linear combinations of atomic orbitals. As the number of basis functions increases, the accuracy of the description of the system increases towards infinity where the Schrödinger equation

would be solved explicitly. Increasing the number of basis functions also increases the computational demand, which is why very large basis sets are not always the best choice for quantum chemical calculations.

### **1.3.5 Effective Core Potential (ECP)**

There is a large computational cost associated with increasing the size of a system by increasing the number of electrons. The extra computational demand may be incurred by including a larger number of atoms or by including increasingly heavier elements. As well as the associated computational cost of including more electrons, relativistic effects must also be considered. Relativistic effects arise from electron speed increasing in heavy elements becoming appreciable compared to the speed of light ( $c$ ). Given that many of the parameters that dictate structure are best described by the valence electrons, core electrons often do not participate in bonding interactions.

To improve the speed of the calculation, an effective core potential (ECP), or pseudopotential, may be employed to replace the core electrons.<sup>8</sup> The valence electrons may then be treated independently. Using an appropriate ECP function will not only improve calculation times, but also may take some relativistic effects into account while still describing the system well.

### **1.3.6 Relativistic methods**

Although a pseudopotential may be used to account for some relativistic effects, other methods are available that provide better modelling of the system. These methods are all-electron methods. Examples of this are calculations using the Zero-Order Regular Approximation (ZORA) or by using explicit two-component Hamiltonians.<sup>11</sup> The Schrödinger equation can be converted into a form that accounts for relativistic effects, but the Hamiltonian becomes more complicated being described by four components.<sup>8</sup> In calculations where ZORA is applied, the energies of the valence orbitals are well represented, including relativistic effects.

### 1.3.7 Density functional theory (DFT)

Any quantum chemical calculation method that relies on the *ab initio* determination of the wavefunction is computationally demanding due to the dimensionality of the wavefunction. Meaning that large systems may only be studied at low levels of theory and small systems at high levels of theory. The ground state energy of the system can be calculated from the electron density using a functional.<sup>8</sup> Quantum chemical calculation of the energy, or related properties, using electron density and a functional is known as DFT. DFT scales much better than *ab initio* methods. The wavefunction is described by three spatial coordinates and electron spin for each electron,  $4N$  descriptors in an  $N$  electron system. Electron density can be described by three spatial coordinates only, regardless of the size of  $N$ . The integration of the electron density defines the number of electrons in the system and can be used to determine nuclear positions and charges based on electron peaks.

True DFT methods scale well with system size, but do not give good approximations of kinetic energy. Kohn-Sham DFT methods are also known as hybrid-DFT methods as they are a hybridisation of density functional approximations with Hartree-Fock exchange.<sup>8</sup> The exact calculation of the exchange-correlation term improves the prediction of molecular properties that are useful in interpreting a chemical system such as bond lengths, kinetic energy, and vibrational frequencies.<sup>12</sup> Kohn-Sham DFT improves on DFT by including an exchange-correlation term and is more widely used than non-Kohn-Sham methods.

## 1.4 Metal-ligand bonding

Organometallic complexes are of particular interest in chemistry due to their prevalence in industrial transformations and catalysis and rely on the bonding of the metal nuclei with carbon. Understanding of the structure and bonding of organometallics may be translated towards understanding and predicting reactivity. Metals have access to many orbitals that may be used for bonding interactions. The

frontier metal orbitals of transition metal complexes will be dominated by the highest energy orbitals which are from the d subset.

The d orbitals of the metal are degenerate when the metal is uncoordinated. However, through the introduction of ligands to the metal, the degeneracy of the orbitals is perturbed. This effect was originally described as crystal field theory by Bethe and van Vleck and used to describe the differences in electronic spectra of metal complexes.<sup>13-15</sup> Crystal field theory has been developed further with molecular orbital theory and is described as ligand field theory.<sup>16</sup> Orbitals that are angled directly towards the ligands become higher in energy as they are repulsed by the ligand. This breaks the degeneracy of the d orbitals used in bond formation.

The three-dimensional arrangement of ligands around a transition metal core influences the energy of the frontier d orbitals with respect to each other. The number of and spatial arrangement of the ligands lead to splitting of the degeneracy of the d orbitals. In an example octahedral complex, the six equivalent ligands lying on each of the three coordinate axes would coordinate to the metal, equally spaced around the metal centre with bond angles of 90°. The  $d_{xz}$ ,  $d_{yz}$ , and  $d_{xy}$  orbitals do not have orbital character that points along the M-L bond, the orbital lobes straddle the M-L bond axis. The lobes of the quadratic d functions,  $d_{x^2-y^2}$  and  $d_{z^2}$ , point directly along the molecular axes. This leads to the breaking of the d functions into two distinct orbital subsets. The subsets can be described by their irreducible representation in the  $O_h$  point group shown in Figure 4:  $T_{2g}$  and  $E_g$ .

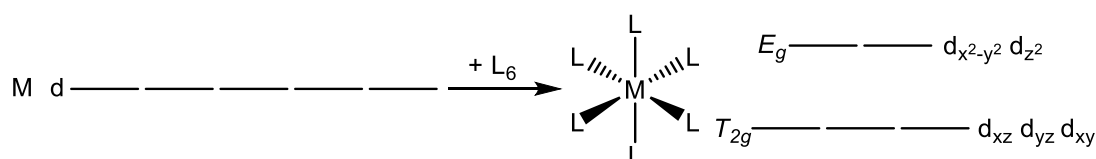


Figure 4. Breaking the degeneracy of the d orbitals. In the octahedral geometry, the orbitals split into  $T_{2g}$  and  $E_g$  subsets.

This means that the  $T_{2g}$  d orbitals fill first and are occupied, provided that the metal possesses d electrons. The presence of orbitals that are filled and vacant dominates the bonding modes that are available for the metal with ligands. An example of the bonding can be described using the Dewar-Chatt-Duncanson model.<sup>17</sup> An example is

shown in Figure 5 for a general M-X bond and the bonding of a metal to ethene, given the importance of ethene complexes in processes such as hydrogenation and hydroformylation.<sup>18</sup>

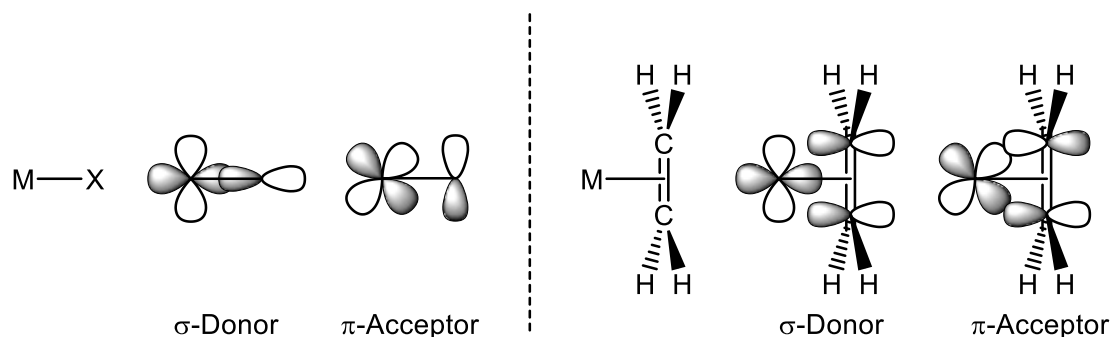


Figure 5. Dewar-Chatt-Duncanson model for the synergic bonding of a general M-X bond (left) and of an alkene to a metal (right) through donation and back-donation interactions.

A generalized X ligand may possess an orthogonal set of filled and vacant orbitals, shown in Figure 5 as p orbitals. The filled p orbital may overlap with the  $E_g$  metal d orbitals which are higher in energy than the  $T_{2g}$  subset and therefore filled last and likely to be unfilled provided the metal is not  $d^{10}$ . This leads to a bonding interaction between M and X and is called  $\sigma$ -donation. At the same time, the orthogonal unfilled p orbital is the correct symmetry to overlap with the  $T_{2g}$  d orbitals which fill first in an octahedral metal complex. The overlap leads to a bonding interaction between M and X and is called  $\pi$ -accepting.

Another example that will be described is the interaction between a metal and an alkene, Figure 5. The filled  $\pi$  orbital of the alkene is the correct symmetry to overlap with the  $E_g$  metal d orbitals which are higher in energy than the  $T_{2g}$  subset and therefore filled last. This leads to electron donation from the  $\pi$  system of the alkene to the metal in a bonding interaction. At the same time, the filled  $T_{2g}$  d orbitals of the metal are the correct symmetry to overlap with the  $\pi^*$  orbital of the alkene. This leads to a back-bonding interaction as electron density from the metal is donated in another bonding interaction. In the case of alkenes, donation of metal electron density into the antibonding C-C orbitals weakens the C-C bonding interaction and

reduces the  $sp^2$  character of the alkene. The extent of this bond weakening is dependent on the strength of the back-bonding interaction.

## **1.5 Probing metal ligand bonding**

### **1.5.1 Direct methods for probing M-L bonding**

The energy of molecular vibration is on the order of the energy of light with infrared (IR) wavelengths.<sup>19</sup> Vibrational modes can be excited on absorption of IR frequency light, the resonant frequency. The energy of the absorption is dependent on the potential energy surface and the masses of the atoms in motion, as well as the coupling of vibrational and electronic motion. Practically, IR spectroscopy can be used as a probe for structure and bond strength and is a sensitive technique requiring only small amounts of sample with very fast sampling times. Because of the effect of synergic bonding described in section 1.4 earlier, the IR stretching frequencies can be correlated to changes in M-X bond strengths. Stretching modes may be associated with the movement of many atoms, meaning that the energy does not necessarily correlate to changes in a single bond strength, but in many. In theory, the stretching frequency of M-X bonds can be directly analysed, but practically, the frequencies of more synthetically relevant M-C modes are too low and insensitive for analysis.

A molecule can undergo an electronic transition on absorption of light in the ultra-violet and visible range (UV-vis). UV-vis spectroscopy can be used to calculate the energy of strong low energy absorptions, which are typically transitions between the highest occupied molecular (HOMO) and lowest unoccupied molecular orbital (LUMO). Although UV-vis spectroscopy can give the energy of FMO transitions, it is typically limited to molecules with small FMO energy gaps and is limited on the number of orbitals that can be studied in a given system.

Another method for directly probing metal ligand bonding is NMR spectroscopy. NMR spectroscopy is element specific meaning that particular nuclei can be probed separate from other elements, for example in probing just the carbon nuclei in a molecule. One major advantage is that all carbon environments can be observed to

give diagnostic chemical shifts and  $J$  coupling values that are indicative of position and electronics, as long as the complex is diamagnetic. NMR spectroscopy is a less sensitive technique than other spectroscopic methods, such as UV-vis and IR spectroscopy, due to the relative energy gap between ground and excited states being low. Another disadvantage of NMR spectroscopy is that some of the three-dimensional information in the NMR signal is lost when analysis is performed in solution due to rapid averaging through molecular motion.

Information on molecular structure and bonding can be obtained through the collection of X-ray diffraction (XRD) patterns of single crystals or powders. The diffraction pattern of a single crystal can be used to generate an electron density map to recover the atomic coordinates of the unit cell. However, only geometric information is recovered which does not directly correlate to specific frontier molecular orbital energies and a single crystal is required for full three-dimensional information.

### 1.5.2 Indirect methods of probing M-L bonding

Many methods have been used to probe and understand M-C bonding. The electronic and steric properties of ligands bound to the metal have a profound effect on the bonding in organometallic complexes. Tolman *et al.* created two parameters to describe the indirect effects that ligands impart on the other metal bond atoms including M-C bonds: the Tolman cone angle and the Tolman electronic parameter (TEP).<sup>20</sup>

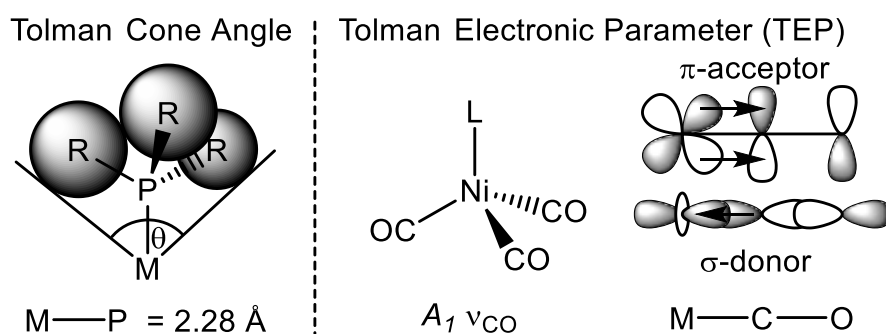


Figure 6. Schematic representation of the Tolman cone angle (left) and the TEP (right).<sup>20</sup>

The Tolman cone angle was developed using physical models of phosphines.<sup>21</sup> It is defined as the angle formed by drawing a cone between the outermost point of the Van der Waals radii of the phosphine substituents with the metal as the vertex point. The M-P bond length is fixed at 2.28 Å, Figure 6. The cone angle represents the approximate size of the ligand at the metal centre. It works directly for symmetrical phosphine ligands, but approximations can be also made for asymmetric phosphines. The Tolman cone angle can be used to explain the differences in reactivity in organometallic systems based on changes to M-L bond strengths. shown by ring closing metathesis of diene **[22]** to form 3-pyrroline **[23]** by ruthenium indenylidene **[21]** shown in Figure 7.<sup>22</sup> Precatalyst **[21]** can be prepared with different phosphine ligands, PR<sub>3</sub> = PPh<sub>3</sub>, PCy<sub>3</sub>. However, precatalyst **[21]** only forms an active ring closing metathesis catalyst with PCy<sub>3</sub> ligands. This difference in reactivity is associated with the activation of the precatalyst during phosphine dissociation and requires. The Tolman cone angle can explain the change in reactivity as the presence of two, high  $\theta$ , PCy<sub>3</sub> ligands lead to weaker Ru-P bonding and accelerated phosphine loss, providing a route into the catalytic cycle.

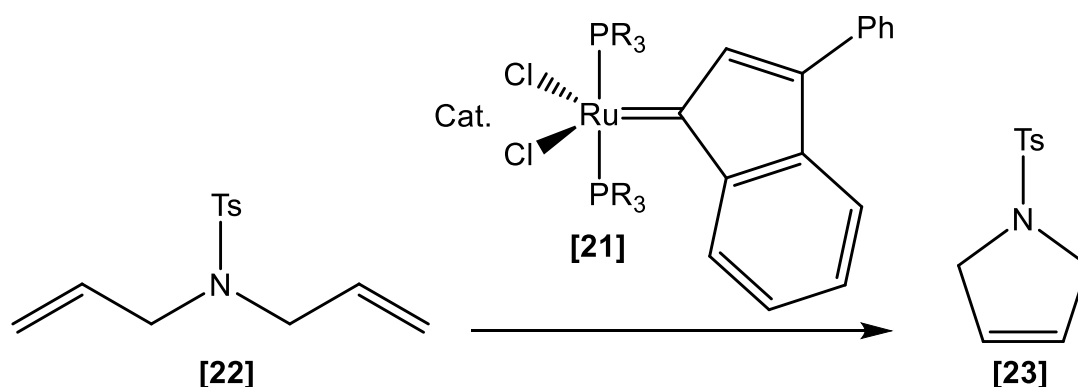


Figure 7. Catalytic ring closing metathesis of **[22]** to form **[23]** using **[21]** as demonstrated by Fürstner *et al.* R = Ph, Cy.<sup>22</sup>

The TEP, also shown in Figure 6, is a measure of the electron donating/withdrawing effects of a phosphine on the A<sub>1</sub> stretching frequency ( $\nu_{CO}$ ) of [Ni(CO)<sub>3</sub>L] as described by Tolman.<sup>23</sup> The TEP relies on the synergic bonding experienced by ligands

coordinated to metals. Strong donation from the ligand L into the metal d orbitals leads to greater donation of electron density into the M-C-O  $\pi$  orbitals and stronger M-C-O  $\pi$  bonding. As the M-C-O  $\pi$  bond has  $\pi^*$  character between the carbon and oxygen atoms, stronger M-C-O  $\pi$  bonding leads to weakening of the C-O bond. The reduced C-O bond strength is observed as a reduction of  $\nu_{CO}$  meaning that phosphines can be ranked based on their electron donating power.

Other methods have been subsequently developed, both experimentally and theoretically, to allow the comparison of other ligands as well as phosphines. Notable examples are methods for comparing the electronic properties of N-heterocyclic carbene (NHC) ligands shown by Nonnenmacher and Gusev based on rhodium and nickel complexes, respectively.<sup>24, 25</sup>

Both the cone angle and TEP ligand parameters provide indirect understanding of the system in question and have their disadvantages. However, they are useful concepts that can be used to help explain the reactivity and activity of initiators and catalysts.<sup>20</sup> A more direct parameter may be able to provide more detailed information about the nature of M-C bonding in a given system.

### 1.5.3 Analysis of alkene metathesis by SS NMR spectroscopy

SS NMR spectroscopy has been used extensively in the study of alkene metathesis catalysts.<sup>26-29</sup> Alkene metathesis is mediated by metal carbene complexes.<sup>30</sup> The chemical shift of the carbene carbon of Fischer and Schrock type carbenes, Figure 8, are distinctly deshielded ( $C_{\alpha} \delta^{iso} > 250$  ppm) and the differences observed in the chemical shift of the carbene carbon have been investigated by Yamamoto *et al.* Fischer and Schrock carbenes, which can be identified by the presence of the stabilizing E group, Figure 8, can also be identified by changes to  $\delta_{11}$ , induced by a lower lying M=C  $\pi^*$  orbital in Fischer carbenes and is associated with the presence of strong  $\pi$  acceptor ligands.<sup>26, 31, 32</sup> Ruthenium systems display deshielding that reflects both Fischer and Schrock carbenes.

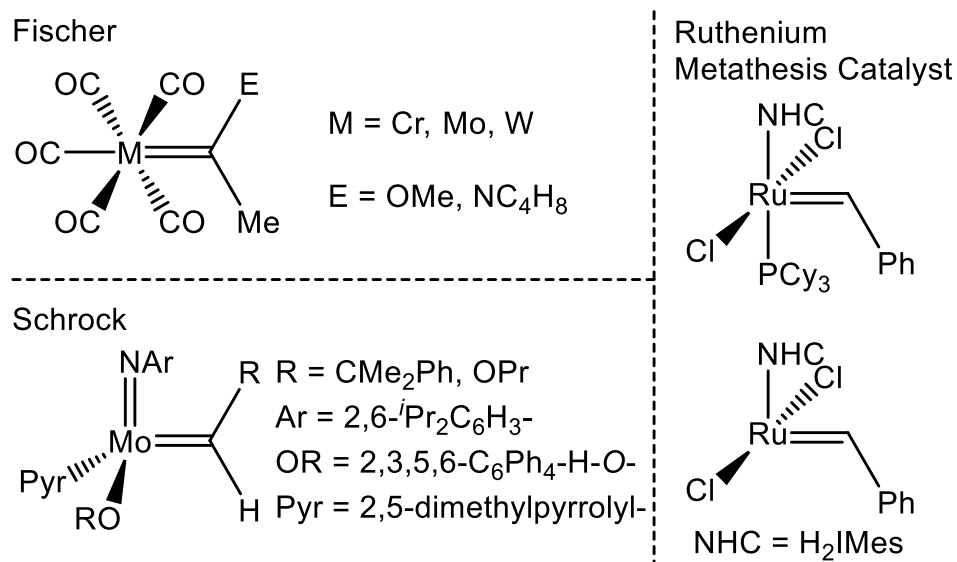


Figure 8. Fischer, Schrock, and ruthenium carbene complexes studied by Yamamoto *et al.*<sup>26, 29, 31</sup>

A key intermediate in the alkene metathesis reaction using Grubbs-type catalysts is the metallocyclobutane ring.<sup>33</sup> The metallocyclobutane ring may adopt a trigonal bipyramidal structure or a square pyramidal geometry at the metal, Figure 9. The interconversion between the geometries impacts catalysis.

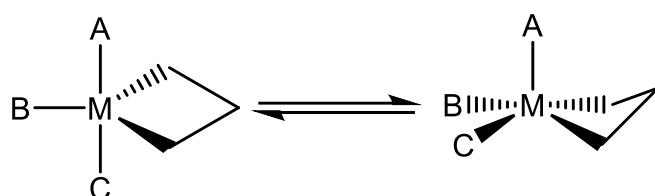


Figure 9. Trigonal bipyramidal (left) and square pyramidal (right) geometry of metallocyclobutane rings relevant to catalyst deactivation of alkene metathesis catalysts. The metallocyclobutane ring loses planarity when the metal adopts a square pyramidal geometry.

Square pyramidal geometry leads to catalyst deactivation and trigonal bipyramidal geometry leads to metathesis.<sup>33</sup> The chemical shift of the C<sub>α</sub> and C<sub>β</sub> in the trigonal bipyramidal complex have been used to determine the preference for interconversion to square pyramidal geometry, which is a catalytic resting state, by Solans-Monfort *et al.*<sup>28</sup> Complexes that prefer adopting the trigonal bipyramidal geometry show less deactivation and higher activity. This effect can be probed

computationally and experimentally. Increased planarity in the metallocyclobutane is linked to a low lying  $\pi^*$  orbital with alkylidene character, leading to increased differences in shielding between the  $C_\alpha$  and  $C_\beta$  carbons as shown by Gordon *et al.*<sup>29</sup> Metathesis active rings show  $\delta^{iso}$  of  $\sim 100$  ppm ( $C_\alpha$ ) and  $\sim 0$  ppm ( $C_\beta$ ). Inactive rings show  $\delta^{iso}$  of  $\sim 50$  ppm ( $C_\alpha$ ) and  $\sim 20$  ppm ( $C_\beta$ ).<sup>29</sup>

Another example of NMR spectroscopy being used in the analysis of the metathesis reaction is the study of the dynamics of metathesis catalysts of the type  $[(\sim SiO)M(ER)(=CH^tBu)(R')]$ , Figure 10, supported on solid surfaces by Blanc *et al.*<sup>34</sup> Calculated chemical shift anisotropies were larger than the experimentally recovered tensors, but varied based on the alkylidene. The variance between the experimental static limit, obtained from low temperature measurements of the immobilised initiators, and the recorded spectra was shown to be dependent on the range of motion of the immobilised catalysts. It is thought that the dynamics may be used to relate the activity and stability of silica supported catalysts. Here, SS NMR spectroscopy has given insight into the flexibility of immobilised/supported catalysts and suggests that mobility is associated with the presence of bulky ligands and the use of heavier metals (5d over 4d). Time averaged anisotropies suggest that the range of motion exhibited by the supported alkylidene catalysts is non-isotropic. However, the exact nature of the motion is unclear and may be associated with site-hopping or a restricted range of motion.

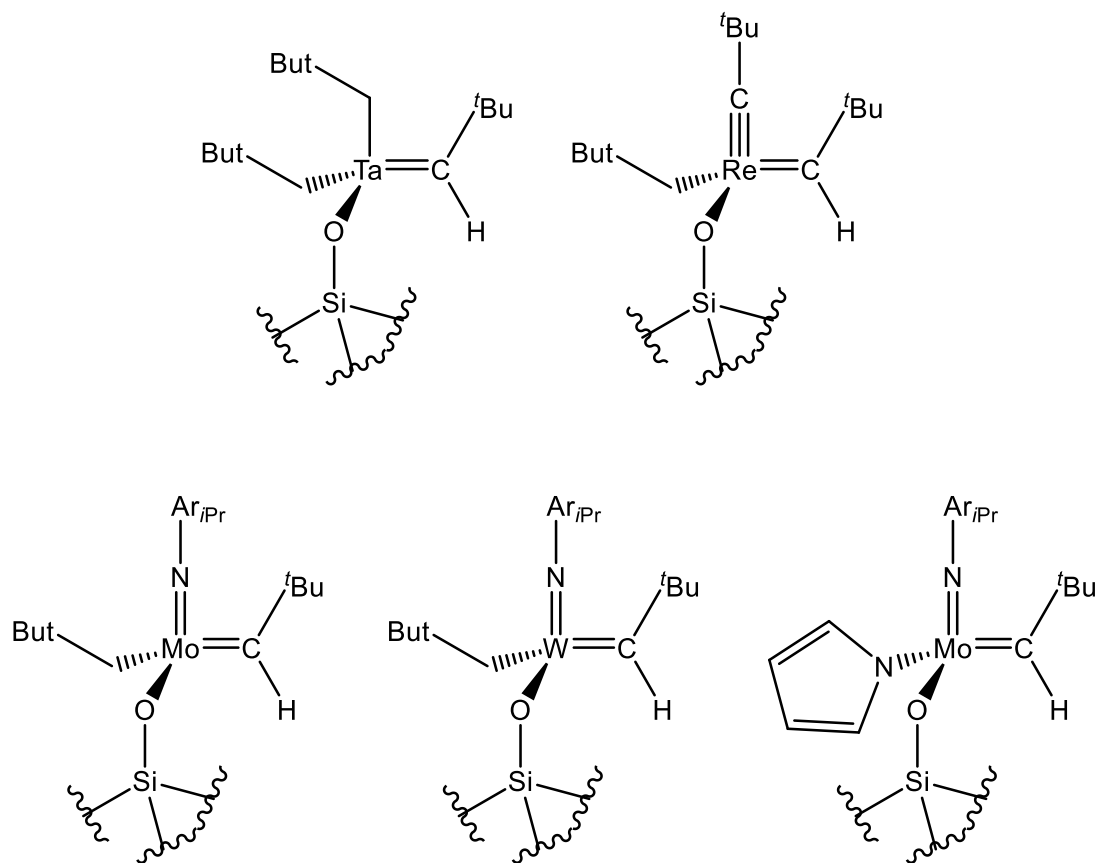


Figure 10. Immobilised alkylidene complexes studied by Blanc.<sup>34</sup>

$\text{Re}_2\text{O}_7$  supported on  $\gamma$ -alumina is another alkene metathesis catalyst that shows functional group tolerance and activity at room temperature.  $\text{Re}_2\text{O}_7$  is inactive in metathesis when supported on silica.<sup>35</sup> A proposed structure of the catalytic site was elucidated using SS NMR spectroscopy and quantum chemical calculations using DFT.<sup>36</sup> Several types of active site were observed by SS NMR spectroscopy, as well as metallocycles by titration of the sample with  $^{13}\text{C}$  labelled ethene. It was shown that high activation temperatures of the alumina were required to reduce the number of surface hydroxyl groups, freeing up space for the interaction of  $\text{Al}^{\text{III}}$  with the rhenium oxide.<sup>36</sup>

As well as linking the dynamics to the chemical shift anisotropy, the chemical shift tensors have also been linked to the electronic structure of the alkylidene complexes by Halbert *et al.*, Figure 10.<sup>27</sup> The chemical shift of carbene  $\text{C}_\alpha$  is highly deshielded, 100 to 200 ppm more deshielded than an alkene carbon which resonates at  $\sim 120$  ppm. This large deshielding shift can be linked directly to the frontier orbitals.

Narrowing of the energy gap between the metal-carbon  $\sigma$  orbital and metal-carbon  $\pi^*$  orbital compared, Figure 11 (bottom), to the alkene C-C  $\sigma$  and C-C  $\pi^*$ , Figure 11 (Top), lead to this large contribution to the paramagnetic shift and therefore deshielding of the  $C_\alpha$ . This is summarised in Figure 10.

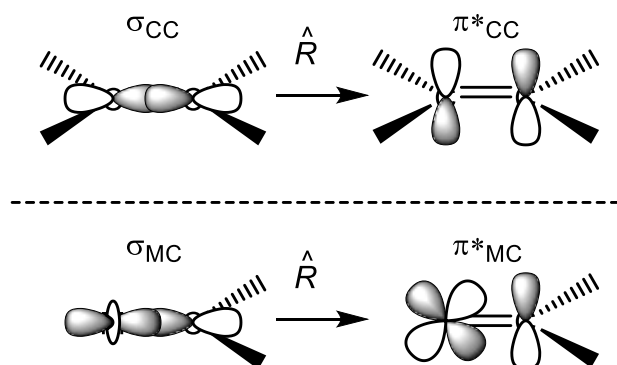


Figure 11. Transitions responsible for  $\delta_{11}$  deshielding in ethene (Top) and a metathesis carbene (Bottom) shown by Halbert *et al.*<sup>27</sup>

The energy gap between the M-C orbitals is reduced compared to the C-C equivalent leading to the large shift in deshielding between carbene chemical shift and alkene chemical shift.  $\hat{R}$  denotes the rotational operator. Both  $^{13}\text{C}$  and  $^{31}\text{P}$  chemical shift tensors were analysed on ruthenium Grubbs metathesis carbene complexes of the type  $[\text{RuCl}_2(\text{L})(\text{PCy}_3)(=\text{CHR})]$ .<sup>37</sup> Larger  $^{31}\text{P}$  chemical shift tensors are linked to stronger Ru-P orbital interactions and reduced lability of the phosphine in methyldiene complexes of ruthenium compared to benzylidene complexes.

The process of alkene metathesis has been studied in detail, alkyne metathesis catalysts are less well developed. The SS NMR spectra and chemical shift tensors have been studied for a range of molybdenum mesityl (Mes, 2,4,6-trimethylphenyl) carbyne complexes,  $[(\text{MesC}\equiv)\text{Mo}(\text{OC}(\text{CH}_3)_{3-x}(\text{CF}_3)_x)_3]$  by Estes *et al.*<sup>38</sup> Increasing the number of  $\text{CF}_3$  groups increases the deshielding at the  $C_\alpha$  from 280 ppm when  $x = 0$ , to 330 ppm when  $x = 3$ . This increased deshielding is associated with a lowering of energy of the  $\text{M}\equiv\text{C}$   $\pi^*$  orbital and increased metathesis activity. However, the totally fluorinated equivalent shows a large drop in activity, this is then associated with increased stability of the metallocyclobutadiene intermediate. Immobilisation of the carbyne complexes onto silica leads to reduced deshielding and reduced metathesis

activity. Study of the grafting of molybdenum carbynes to silica by Estes *et al.* has shown that the  $^{13}\text{C}$  SS NMR signal of the carbyne  $\text{C}_\alpha$  of the molecular complex is conserved on grafting to silica.<sup>39, 40</sup> This suggests conservation of the catalyst structure even when supported by the silica. The use of SS NMR as a probe for alkyne metathesis complexes has helped the development of Mo catalysts with high functional group tolerance, the wealth of SS NMR data on Mo alkyne metathesis catalysts means that new tripodal catalyst designs can be benchmarked against existing catalysts, maintaining the electronics of known active catalysts.<sup>41</sup>

#### 1.5.4 Use of SS NMR in the analysis of example catalytic systems

SS NMR spectroscopy has been utilized in analysing and interpreting several other catalytic systems as well as in the understanding of electronics. There has been success for SS NMR as a technique with a large number of heterogenous catalysts being used for industrial transformations with the catalyst being in the solid phase, for example in characterising ruthenium containing nanoparticles for hydrogenation,<sup>42</sup> or characterising metal speciation of zeolites in the methanol-to-aromatics reaction.<sup>43</sup> Some other examples of SS NMR spectroscopy being used in probing heterogeneous reaction mechanisms have been covered by Blasco.<sup>44</sup>

Work by Gordon *et al.* suggests a link between  $\sigma$ -bond metathesis, alkene insertion, and alkene metathesis reactions based on the extent of  $\pi$ -bond character in metal alkyl complexes, Figure 12.<sup>45-47</sup> Higher  $\pi$  character is required for alkene insertion and metathesis but is still necessary in  $\sigma$ -bond metathesis. The chemical shift tensors indicate that  $\sigma$ -bond metathesis can be classified formally as a [2+2] cycloaddition.

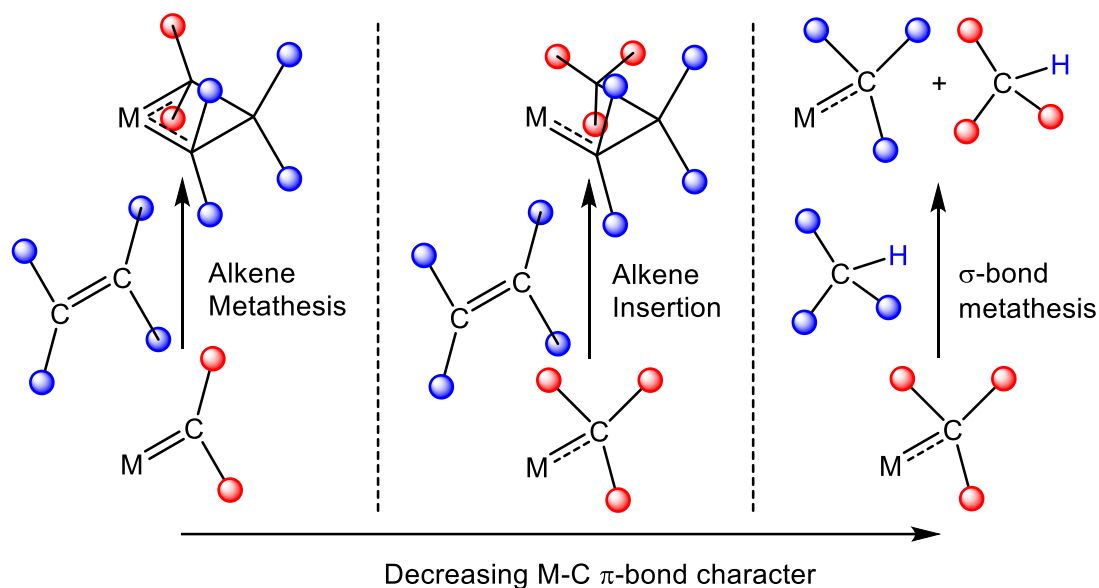


Figure 12. The effect of decreasing M-C  $\pi$ -bond character directs the reactivity from alkene metathesis to alkene insertion to  $\sigma$ -bond metathesis.<sup>45-47</sup>

Other than metathesis reactions, SS NMR spectroscopy has been used to give insight into the surface structure of ruthenium nanoparticles, which are active in the Fischer-Tropsch and Haber-Bosch Processes.<sup>48</sup> The chemical shift tensors of a ruthenium carbonyl has been shown to be sensitive to coordination mode by Foppa *et al.*, Figure 13. Carbonyl ligands coordinating  $\eta^2$ - $\mu_4$  along the step edges of the nanoparticle exhibit the largest deshielding, associated with a partially filled low lying C-O  $\pi^*$  orbital. The population in this orbital correlates well to C-O bond length and explains the ease of C-O cleavage at step edge sites.

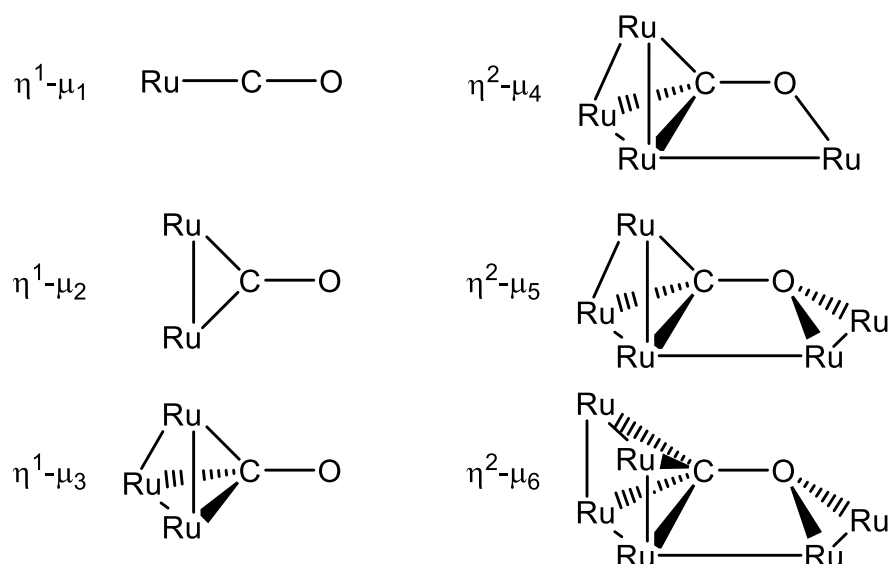


Figure 13. CO coordination modes on ruthenium nanoparticles calculated by Foppa *et al.*<sup>48</sup>, the  $\eta^2\text{-}\mu_4$  coordination mode is suggested to be key in C-O bond cleavage.<sup>48</sup>

Variation in  $^{13}\text{C}$  chemical shift tensors have been studied in the *gem*-hydrogenation of alkynes using ruthenium piano stool complexes by Biberger *et al.*, shown in Figure 14.<sup>49, 50</sup> Alkynes undergo *gem*-hydrogenation when in the presence of  $\text{H}_2$  and a ruthenium half-sandwich complex. The resulting carbene complex **[26]** has shown to have a tuneable M=C bond based on the nature of the  $\eta^5$ -cyclopentadienyl (Cp) ring. The tuneable electronics of the M=C bond may be useful in cyclopropanation or metathesis reactions.<sup>49, 50</sup>

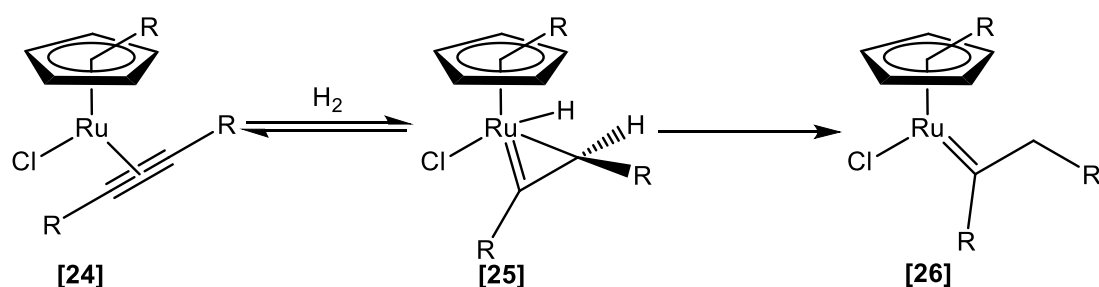


Figure 14. *Gem*-hydrogenation of alkynes resulting in carbene **[26]**. The electronics of the M=C bond are tuneable based on the electronic nature of the Cp ring.<sup>49, 50</sup>

A combination of  $^{11}\text{B}$  and  $^{29}\text{Si}$  SS NMR spectroscopy has been used by Wang *et al.* in the analysis of mesoporous silica-supported organolanthanum catalysts [27] for reductive cleavage of epoxides by pinacolborane forming compound [31], Figure 15.<sup>51</sup>

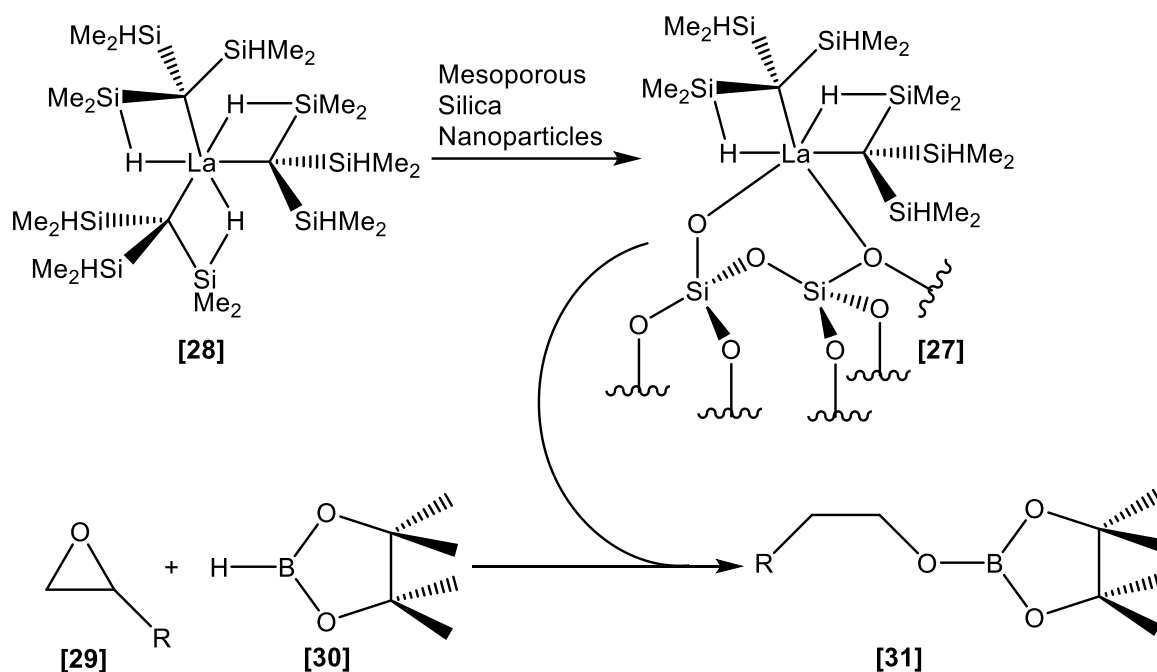


Figure 15. Catalytic ring opening of epoxides by pinacolborane and organolanthanum-decorated silica nanoparticles.

Treatment of the mesoporous silica at 500 °C before decoration by  $[\text{La}(\text{C}(\text{SiHMe}_2)_3)_3]$  [28] resulted in several coordination sites being observed in the  $^{29}\text{Si}$  SS NMR spectra. However, treatment of the mesoporous silica at 700 °C before decoration by compound [28] resulted in only a single site being observed which showed higher activity, suggesting a link between the surface decoration of the silica to catalytic function.<sup>51</sup>

SS NMR spectroscopy has been used as a probe for a range of other solid systems with far reaching consequences, for example;  $^{15}\text{N}$  SS NMR spectroscopy has been used to provide insight into the N-N cleavage of hydrazine by tantalum hydride species supported on silica,<sup>52</sup> and analysis of  $^{35}\text{Cl}$  chemical shift tensors and electric field tensors in metal chloride species.<sup>53, 54</sup>  $^{35}\text{Cl}$  chemical shift tensors can be applied to the study of systems that contain chlorides such as  $\text{MgCl}_2$  in Ziegler-Natta catalysts,

exploring the difference in SS line shape on bulk and ball milled supports linking structure to activity.<sup>55</sup>

As well as in the study of Ziegler-Natta catalysts, <sup>35</sup>Cl SS NMR spectroscopy has been used in tandem with <sup>91</sup>Zr SS NMR spectroscopy in the study of homogeneous and heterogeneous zirconocene catalysts which show activity in polymerisation reactions of alkenes, shown by Rossini *et al.*<sup>56</sup> SS NMR spectroscopy provides a link in the comparison of structure between the heterogeneous zirconocene catalysts that are tethered to a support by comparison to free catalysts through the magnitudes and orientations of electric field gradient and chemical shift tensors. Conservation of the electric field gradient and chemical shift tensors on the supported catalysts indicate that the support does not perturb the electronics of the free catalyst.

The hydroaminoalkylation, first described by Maspero and Nugent,<sup>57, 58</sup> of alkenes and amines catalysed by titanium-containing complex on silica has been investigated by Yaacoub *et al.*<sup>59</sup> SS NMR spectroscopy of the supported catalyst **[32]** provides evidence for the formation of a 5-membered metallocycle **[33]** on addition of the alkene. This is summarized in Figure 16.



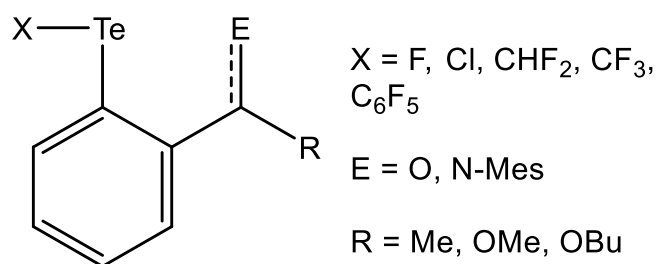


Figure 17. General formula of disubstituted tellurium compounds studied by SS NMR spectroscopy for fluorine transfer.<sup>60</sup>

Given the prevalence of  $^1H$  nuclei in chemical systems, the  $^1H$  is not frequently used as a probe in SS NMR spectroscopy due to the difficulty of observing  $^1H$  nuclei in the solid-state. More recently, the chemical shift anisotropy of  $^1H$  nuclei has been made more accessible even for weaker interactions through the use of heteronuclear recoupling from  $^{13}C$ . This breakthrough may be possible to utilise the chemical shift anisotropy of  $^1H$  nuclei as a probe for the dynamics in chemical and biological systems where the anisotropy is small, giving SS NMR spectroscopy another probe into solid-phase or macroscopic reactivity.<sup>61</sup>

### 1.5.5 Project aims

This project looks at developing new ways of characterising and interpreting the FMO interactions of metals and their coordinating atoms, with a particular focus of the interactions between metals and carbon in M-C bonds. By using SS NMR spectroscopy and the chemical shift interaction, new ways of describing and understanding changes to M-C bonding can be explored for organometallic systems. There is currently a lack of direct methods for interpreting FMOs. Some methods, such as UV-*vis* spectroscopy, may be used to probe FMO interactions of specific compounds. SS NMR spectroscopy may provide information in cases where traditional spectroscopy cannot and complementary information in cases when FMOs can be interpreted by another form of spectroscopy.

In chapter 2, the experimental and computational methodologies that have been used in data acquisition and interpretation are described. Chemical shift tensor analysis of known literature compounds has been included as examples of the analysis performed later in this work.

In chapter 3, the differences in FMO structure and bonding of conjugated organometallic ruthenium species have been investigated with a focus on the effect of fluorine incorporation into the conjugated organic fragment. The effect that fluorine has on the FMO structure of organometallics, as well as the nature of metal-carbon bonding in vinylidene and alkynyl species have been described. The changes in energy or localisation of the FMOs that dictate the chemical shift tensors have been used to explain the observed changes in  $^{13}\text{C}$  chemical shift tensors of metal bound carbons.

In chapter 4, we have used metal-based tensors to explore bonding in platinum and rhodium complexes. We have also included attempts to record high resolution SS NMR spectra of  $^{103}\text{Rh}$  and  $^{195}\text{Pt}$  nuclei. The  $^{103}\text{Rh}$  tensors have been explored in complexes relevant to hydroformylation of alkenes, looking at the effect of pnictogen and phosphine bite angle on the chemical shift tensors.

## Chapter 2. Methodology

### 2.1 Aims

As outlined in chapter 1, the principal aim of the work in this thesis is to use NMR spectroscopy to rationalise the bonding in organometallic complexes. The main tool to do this will be analysis of the principal chemical shift tensors for a range of metal-containing molecules that, as described in Chapter 1, provide insight into the nature and symmetry of the FMOs. Orbital energy gaps and localisations are encoded into chemical shift. Thus, SS NMR can be combined with quantum chemical calculations to give insight into structure and bonding. The chemical shift tensors give spatially encoded information, which is complimentary to information derived from other analytical techniques.

Before any detailed analysis of the chemical shift tensors of chemically relevant species was performed, a general methodology to acquire and interpret the data was developed. The aims of this chapter are to outline the general parameters and pulse programs selected for the recording of  $^{13}\text{C}$ ,  $^{31}\text{P}$ , and  $^{19}\text{F}$  SS NMR spectra that will be analysed further in this thesis. As well as the general recording of SS NMR spectra, the recovery of the principal components  $\delta_{11}$ ,  $\delta_{22}$ , and  $\delta_{33}$  from SS NMR spectra recorded spinning at the magic angle will be outlined.

Alongside SS NMR studies, quantum chemical calculations using DFT have been explored in the calculation of chemical shift tensors for organometallic compounds. A general computational methodology has been developed for further use in the thesis, comparing the simulated chemical shift tensors to experimentally derived results. The chemical shift tensors recovered from calculations using DFT have been correlated to the molecular frame of reference using visualisation techniques. The magnitudes of deshielding in the chemical shift tensors for ethene and ethyne will be correlated with MO energies and localisations as test cases for the analysis performed in this work.

## 2.2 Selection of SS NMR pulse sequences and SS NMR spectroscopic methodology testing on representative compounds.

The work in this thesis relies on the acquisition of  $^{13}\text{C}$  SS NMR spectra, as well as the characterisation of relevant materials by SS NMR spectroscopy. The methods needed for the recording of SS NMR spectra are described below.

### 2.2.1 SS NMR pulse programs

High-power decoupling:

Direct-dipole coupling is the direct through-space coupling interaction between two spins. The magnitude of the interaction between the two spins A and B can be calculated as shown in Equation 10.

$$b_{jk} = - \left( \frac{\mu_0}{4\pi} \right) \frac{\hbar \gamma_j \gamma_k}{r_{jk}^3} \quad \text{Equation 10}$$

$b_{jk}$  is the direct-dipolar coupling constant,  $\mu_0$  is the vacuum permeability constant,  $\hbar$  is the reduced Planck's constant,  $\gamma_j$  and  $\gamma_k$  are the gyromagnetic ratios of spins j and k respectively and  $r_{jk}$  is the distance between them. The magnitude of the coupling constant is therefore proportional to the product of the gyromagnetic ratios of the spins, but is inversely proportional to the cube of the vector distance between them. This means that direct-dipolar coupling constants are very large when the sample contains high  $\gamma$  nuclei with high abundance. As  $^{13}\text{C}$  is a spin dilute nucleus with only 1.109 % abundance, the average distance over which homonuclear couplings may occur is typically large. Large values of  $r$  lead to low values of  $^{13}\text{C}$ - $^{13}\text{C}$  couplings and very little broadening of resonances. However, as  $^1\text{H}$  nuclei possess both a large gyromagnetic ratio and a high abundance, the magnitude of  $^{13}\text{C}$ - $^1\text{H}$  couplings is large. The coupling interaction leads to broadening of the resonances in the  $^{13}\text{C}$  spectra. To counter this, when acquiring SS  $^{13}\text{C}$  NMR spectra, a high-power decoupling field (60 kHz) must be applied over the proton channel to decouple the  $^{13}\text{C}$ - $^1\text{H}$  direct-dipolar coupling interaction, leading to sharp resonances.

## Cross-Polarisation

Cross-Polarisation (CP) is a double resonance experiment and refers to the translation of spin polarisation from high  $\gamma$  nuclei to low  $\gamma$  nuclei. This technique is commonly employed in SS NMR spectroscopy to enhance the sensitivity of  $^{13}\text{C}$  nuclei. As  $^{13}\text{C}$  has a low natural abundance (1.109 %) and a relatively low gyromagnetic ratio ( $\gamma_{\text{C}} = 67.2828 \times 10^6 \text{ rad s}^{-1} \text{ T}^{-1}$ ),  $^{13}\text{C}$  spectra are insensitive.<sup>62</sup> Polarisation of  $^1\text{H}$  nuclei is more intense due to higher natural abundance,  $^1\text{H}$  (99.98 % abundant) and a high gyromagnetic ratio ( $\gamma_{\text{H}} = 267.5222 \times 10^6 \text{ rad s}^{-1} \text{ T}^{-1}$ ).<sup>62</sup> The combined effect of gyromagnetic ratio and natural abundance can be observed by using relative receptivity compared to  $^1\text{H}$ ,  $R_{\text{H}}(\text{X})$ , as described by the Equation 11 below:

$$R_{\text{H}}(\text{X}) = \left| \frac{\gamma_{\text{X}}}{\gamma_{\text{H}}} \right|^3 \cdot \frac{I_{\text{X}}(I_{\text{X}}+1)}{I_{\text{H}}(I_{\text{H}}+1)} \cdot \frac{N_{\text{abundanceX}}}{N_{\text{abundanceH}}} \quad \text{Equation 11}$$

Where  $\gamma_{\text{X}}$  is the gyromagnetic ratio of isotope X,  $I_{\text{X}}$  the spin of isotope X, and  $N_{\text{abundanceX}}$  the natural abundance of isotope X. From Equation 11, the receptivity of  $^{13}\text{C}$  relative to  $^1\text{H}$  is  $R_{\text{H}}(\text{C}) = 1.70 \times 10^{-4}$ . A general CP pulse sequence is shown in Figure 18.

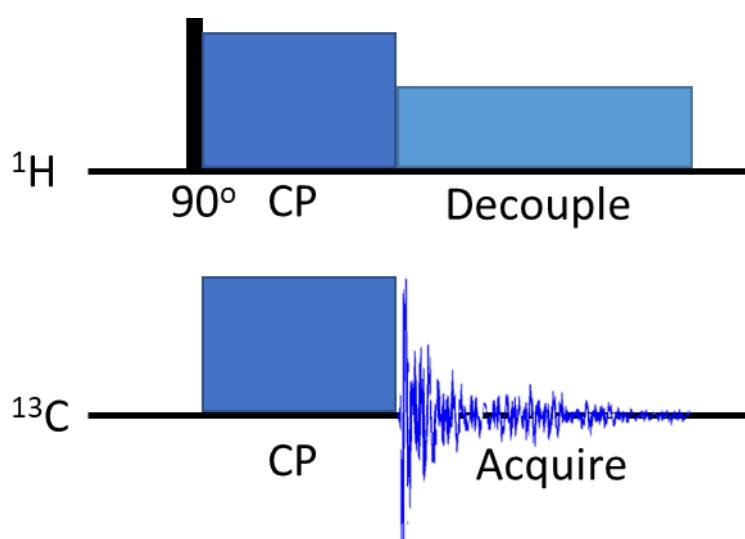


Figure 18. Schematic of a  $^{13}\text{C}\{^1\text{H}\}$  CP experiment.

A CP experiment facilitates polarisation transfer by initially applying a  $90^\circ$  pulse to the indirect nuclei channel, for example  $^1\text{H}$  in Figure 18. During the CP phase, the

nuclei are then spin-locked and a strong pulse applied to the  $^{13}\text{C}$  channel. The magnitude of this pulse can be calculated as shown in Equation 12 so that the precession rate of both  $^1\text{H}$  and  $^{13}\text{C}$  nuclei is the same, as described by Hartmann and Hahn.<sup>63</sup>

$$\gamma_{1\text{H}}B_{1\text{H}} = \gamma_{13\text{C}}B_{13\text{C}} \quad \text{Equation 12}$$

When the nuclei precess at the same rate, polarisation transfer can occur from the high  $\gamma$  nuclei to the low  $\gamma$  nuclei. As well as an increase in polarisation, the spin-lattice relaxation,  $T_1$ , is associated with the  $^1\text{H}$  nuclei rather than the  $^{13}\text{C}$  nuclei. The spin-lattice relaxation of a proton is much faster than carbon due to the gyromagnetic ratio for  $^1\text{H}$  being approximately four times larger than for  $^{13}\text{C}$ , further increasing sensitivity. The  $T_1$  values for slowly relaxing  $^{13}\text{C}$  nuclei may be up to 300 s, whereas even long relaxing  $^1\text{H}$  nuclei typically relax faster by an order of magnitude.<sup>64</sup> A lower  $T_1$  value increases the apparent sensitivity as it reduces the time needed between pulses, allowing for more scans to be performed in the same time frame.

After polarisation transfer has occurred for a given contact time, a decoupling sequence is applied to the  $^1\text{H}$  channel. At the same time, the  $^{13}\text{C}$  channel acquires the NMR signal, the free induction decay (FID). The only difference between a high-power decoupling and CP sequence is the addition of the spin locking and frequency matching phase, CP. Both sequences rely on a powerful decoupling field being applied to the  $^1\text{H}$  channel over acquisition to remove the large direct-dipolar coupling between  $^1\text{H}$  and  $^{13}\text{C}$  nuclei in the solid state as described in section 1.2.1.

### 2.2.2 Spectral optimisation: $^{13}\text{C}\{^1\text{H}\}$ CP MAS.

Initial test spectra were collected on a 4 mm  $\text{ZrO}_2$  rotor packed with  $[\text{RuCl}(\eta^5\text{-C}_5\text{H}_5)(\text{PPh}_3)_2]$  **[35]** and fitted with a Kel-F cap. The structure of complex **[35]** is shown in Figures 19 and 20. The 4 mm rotors have both high sample capacity and a moderate maximum spinning speed  $\nu^{\text{rot}} = 12,500$  Hz. External referencing of the field was achieved as described in the literature using a crystalline sample of adamantane and setting the high frequency resonance to 38.4 ppm.<sup>65</sup>

The synthesis of complex **[35]** is described section 5.2.<sup>66</sup> Complex **[35]** was selected for study because it is a simple organometallic complex with a well-defined metal centre and being representative of the complexes that will be studied in Chapter 3, previously shown in Figure 1. An initial  $^{13}\text{C}\{^1\text{H}\}$  CP MAS spectrum was recorded and is shown in Figure 19. The CP contact time, P15, was set to 2000  $\mu\text{s}$ .

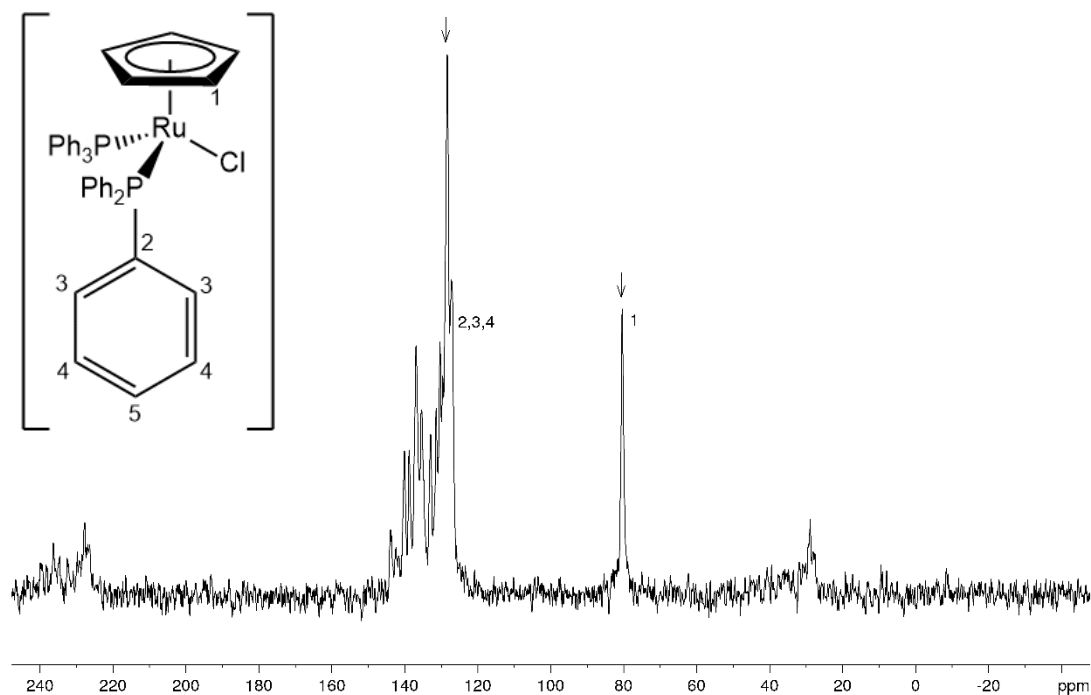


Figure 19. CP MAS  $^{13}\text{C}\{^1\text{H}\}$  spectrum of complex **[35]** recorded at 101 MHz at a spinning speed of 10 kHz. Isotropic resonances are denoted by an arrow. Number of scans (Ns) = 16. Carbon environments have been labelled 1-4.

In the  $^{13}\text{C}$  NMR spectrum on complex **[35]** (figure 19), two clear environments are observed,  $\delta_{\text{C}} = 80$  and  $\delta_{\text{C}} = 120 - 145$ . These resonances are from the Cp and the triphenylphosphine ( $\text{PPh}_3$ )  $^{13}\text{C}$  nuclei, respectively. The single-crystal XRD structure of Complex **[35]** has been described by Bruce *et al.* and is shown in Figure 20.<sup>66</sup>

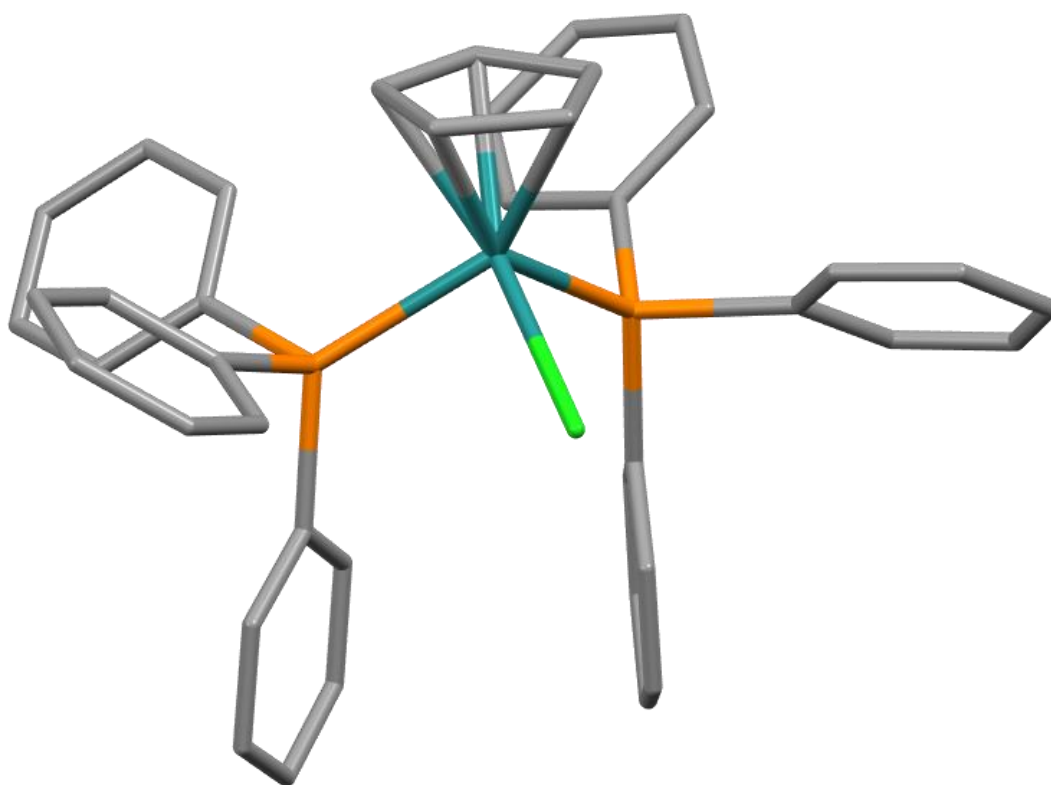


Figure 20. Single-crystal XRD asymmetric unit structure of complex **[35]**. Coordinates obtained from the Cambridge Crystallographic Data Centre entry CPDRUA.<sup>66</sup> Hydrogen atoms have been omitted for clarity.

Each carbon of the PPh<sub>3</sub> ligands is in a different crystallographic environment as there is one molecule in the asymmetric unit. Therefore, each <sup>13</sup>C environment is magnetically inequivalent. The overlap of the 36 environments gives the line shape seen in the <sup>13</sup>C NMR spectrum presented in Figure 19. The resonances for the Cp <sup>13</sup>C nuclei appear as a sharp singlet as they are rotationally averaged on the timescale of the NMR spectroscopic experiment (figure 19). Small spin echoes are also observed for the aromatic resonances at a distance of 10 kHz precessing from the isotropic resonances that have been labelled with arrows.

An initial sweep of the recycle delay (D1) was performed. D1 is the time between the NMR pulse sequences allowing for transverse relaxation. Increasing D1 from 10 to 30s led to an increase of the signal. Although longer values of D1 give more intense signals, a D1 of 20 s was selected as a compromise between full relaxation and

permitting the acquisition of more scans in a given time period. The effect of increasing the time between pulses is highlighted in Table 1 and Figure 21.

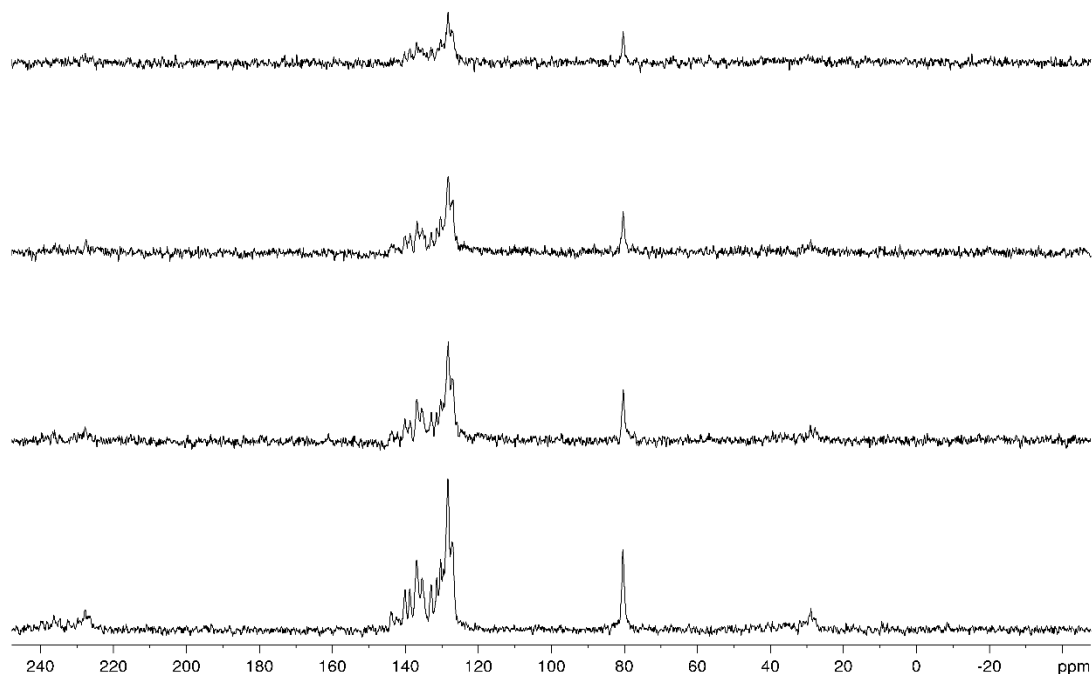


Figure 21. D1 optimisation performed on complex **[35]** recorded at 101 MHz at a spinning speed of 10 kHz from top to bottom: D1 = 3, 5, 10 and 20 s. Ns = 16. Increasing values of D1 lead to a higher signal:noise ratio.

Table 1. Relative peak height of D1 optimisation spectra of complex **[35]** recorded at 101 MHz at a spinning speed of 10 kHz. Spectra collected with 16 scans. Time denotes total experiment time. The maximum peak height of the aromatic resonance of experiment 4 was set to 10 and the intensity represents the relative peak height in 1-3 compared to this value.

Experiment	D1 / s	Relative peak height	Time / s
1	10	3.33	160
2	15	5.04	240
3	20	6.44	320

4	30	10.00	480
---	----	-------	-----

Setting D1 to 20 s gives an opportunity for any slowly relaxing  $^1\text{H}$  nuclei to relax, allowing the whole quanta of signal to be recorded. This is important due to the nature of the NMR spectroscopic experiments, when the spinning speed is reduced the signal will be diluted. Even though multiple scans will improve the signal-to-noise ratio, the more signal in each scan, the lower the signal-to-noise ratio on each individual side band.

The other factor in selection of D1 was the time taken for each experiment. Although the change in D1 is small from 10 to 30 s, the individual contributions begin to vastly increase the total spectra time when large numbers of scans are used. For example, if  $N_s = 4096$ . Sharp resonances were observed indicating that good relaxation was occurring. This methodology was carried forward for the recording of all carbon spectra.

### 2.2.3 Optimisation of $^{31}\text{P}\{^1\text{H}\}$ Solid-State NMR spectra

CP techniques can be used to enhance the sensitivity of low  $\gamma$  nuclei by utilising spin transfer from neighbouring high  $\gamma$  nuclei. As described in section 2.2.1, the effectiveness of polarisation enhancement is proportional to the dipole-dipole interaction. This interaction is dependent on the gyromagnetic ratios of the two spins and is inversely proportional to the cube of the distance between them. For  $^{13}\text{C}$  spectra, the prevalence of C-H bonds and short C-H interatomic distances leads to enhancement of the spin dilute system. As P-H bonds are less common in organometallic chemistry, phosphorus nuclei are more commonly bonded directly to carbon, such as in the archetypal phosphorus ligand  $\text{PPh}_3$ .  $\gamma_{\text{H}}$  is approximately 4 times greater than  $\gamma_{\text{C}}$  meaning that the dipole-dipole interaction is weaker between  $^{31}\text{P}\text{-}^{13}\text{C}$  than  $^{13}\text{C}\text{-}^1\text{H}$  and  $^{31}\text{P}\text{-}^1\text{H}$ . Extended bond lengths and the low natural abundance of  $^{13}\text{C}$ , 1.109 % also contribute to the reduced dipole-dipole interaction between  $^{31}\text{P}\text{-}^{13}\text{C}$ .

To test the application of CP MAS to acquire  $^{31}\text{P}\{^1\text{H}\}$  SS NMR spectra,  $\text{PPh}_3$  was freshly crystallised, ground, and packed into a  $\text{ZrO}_2$  rotor fitted with a Kel-F cap. An initial

sweep on the cross-polarisation contact time, P15, was performed between 1000 and 8000  $\mu\text{s}$ . The spectra are displayed in Figure 22.

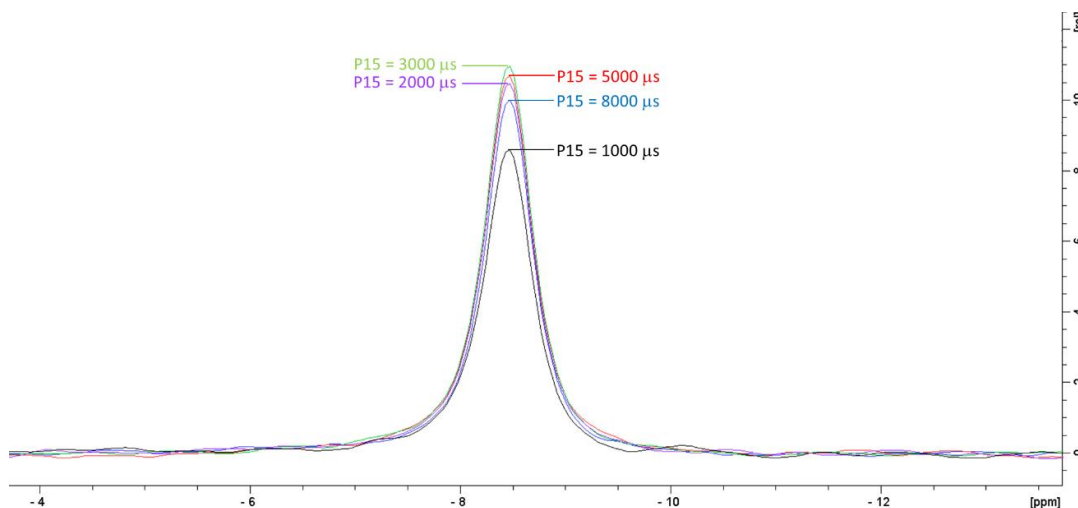


Figure 22.  $^{31}\text{P}\{^1\text{H}\}$  CP MAS SS NMR spectra of  $\text{PPh}_3$  recorded at 162 MHz at a spinning speed of 10 kHz,  $N_s = 16$ . CP contact time from bottom to top: P15 = 1000, 2000, 3000, 5000 and 8000  $\mu\text{s}$ .

Figure 22 shows that signal enhancement of the  $\text{PPh}_3$   $^{31}\text{P}$  resonance occurs as contact time is increased from 1000 to 3000  $\mu\text{s}$ , but very little enhancement occurs with contact times longer than 3000  $\mu\text{s}$ . For this reason, P15 = 3000  $\mu\text{s}$  was selected and sharp  $^{31}\text{P}$  resonances were observed. Longer contact times increase the amount of power supplied to the sample and should be minimised. This methodology was carried forward for the recording of all  $^{31}\text{P}\{^1\text{H}\}$  NMR spectra in this thesis.

#### 2.2.4 Optimisation $^{19}\text{F}$ Solid-State NMR spectra

Like  $^{31}\text{P}$ ,  $^{19}\text{F}$  is a spin-abundant nucleus with  $I = \frac{1}{2}$ . Unlike  $^{13}\text{C}$  and  $^{31}\text{P}$ ,  $^{19}\text{F}$  has a large gyromagnetic ratio,  $\gamma_{\text{F}} = 251.815 \text{ rad s}^{-1} \text{ T}^{-1}$ .<sup>62</sup> Therefore, it has a high Larmor frequency. The Bruker AVANCEIII HD solids spectrometer that was used for the SS NMR spectroscopy in this thesis has a single proton-fluorine probe. This means that CP or proton decoupling pulse sequences cannot be used for the recording of  $^{19}\text{F}$  spectra as the probe must be tuned to fluorine and cannot be simultaneously tuned

to proton. Instead, a 90° pulse sequence was selected for the analysis of  $^{19}\text{F}$ -containing samples.

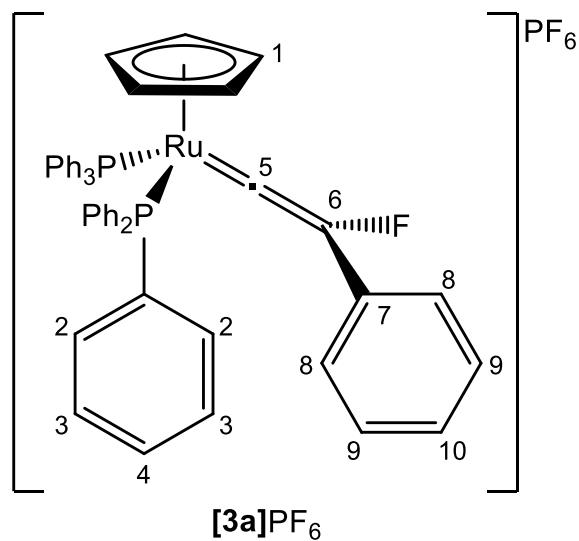


Figure 23. Structure of  $[\mathbf{3a}]\text{PF}_6$ .

Initial spectra were collected on a sample of complex  $[\mathbf{3a}]\text{PF}_6$  due to its relevance to the study in Chapter 3. The synthesis of complex  $[\mathbf{3a}]\text{PF}_6$  is described in section 5.11 and the structure of  $[\mathbf{3a}]\text{PF}_6$  is shown in Figure 23. Changes in signal intensity against longer recycle delay values are summarized in Table 2. A representative spectrum of complex  $[\mathbf{3a}]\text{PF}_6$  is shown in Figure 24.

Table 2. Relative intensity vs D1 of complex **[3a]**PF<sub>6</sub> recorded at 376 MHz at a spinning speed of 10 kHz. Spectra collected with Ns = 16. Time denotes total experiment time. The maximum peak height of the PF<sub>6</sub><sup>-</sup> anion of experiment 4 was set to 10 and the intensity represents the relative peak height in 1-3 compared to this value.

Experiment	D1 / s	Intensity	Time / s
1	1	7.8	16
2	2	8.9	32
3	3	9.4	48
4	5	10.0	80

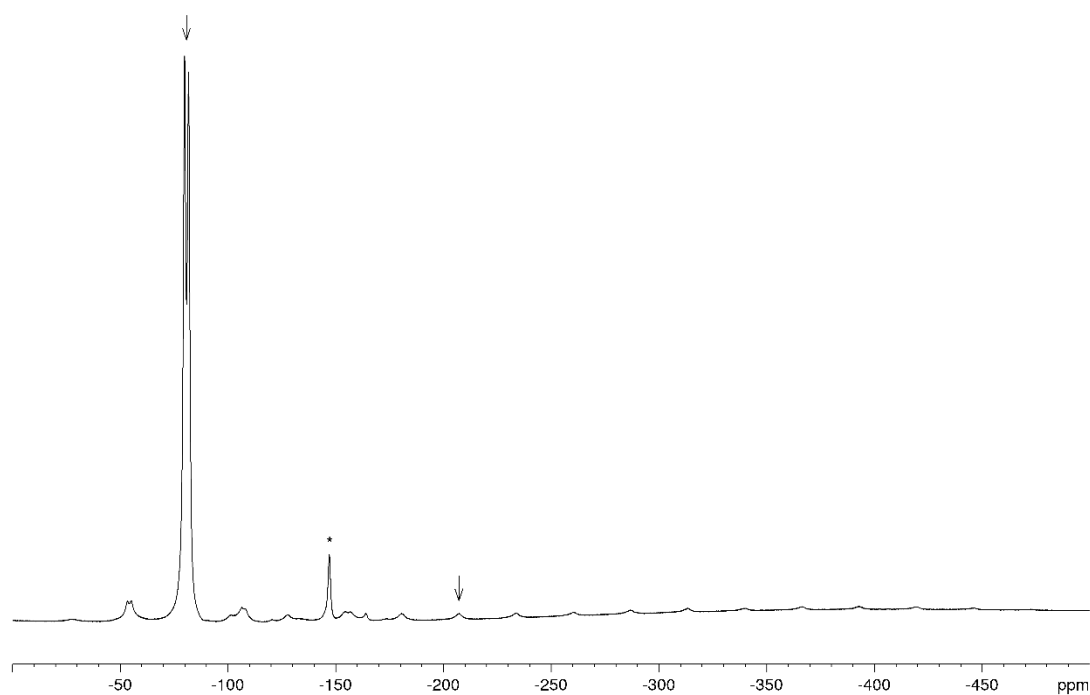


Figure 24. <sup>19</sup>F MAS SS NMR spectra of complex **[3a]**PF<sub>6</sub> recorded at 376 MHz at a spinning speed of 10 kHz. Isotropic resonances are denoted with an arrow. A contaminant was also observed at  $\delta_F = -147$  and is denoted by an asterisk.

The data in table 2 shows that much smaller enhancements are observed on lengthening D1 values. Because of this, the recycle delay was set to 5 s for all  $^{19}\text{F}$  NMR spectra recorded in this thesis. Figure 24 shows the presence of a contaminant at  $\delta_{\text{F}} = -147$ , which is likely to be from fluoroborosilicates in the glass of the probe of the spectrometer. This signal will therefore be present in all SS  $^{19}\text{F}$  NMR spectra. The two other  $^{19}\text{F}$  environments in complex **[3a]** $\text{PF}_6$  are clearly observable in Figure 24 in the spectrum, the  $\text{PF}_6^-$  anion resonance observed as a doublet at  $\sim -80$  ppm and the fluorovinylidene resonance at  $\sim -210$  ppm. As the  $^{19}\text{F}$  nuclei has a much larger gyromagnetic ratio than  $^{13}\text{C}$  or  $^{31}\text{P}$ , as well as a large chemical shift range, large values of chemical shift anisotropy are observed for  $^{19}\text{F}$  nuclei. Because of the large ranges  $\nu^{\text{rot}} < \text{chemical shift anisotropy}$  even when  $\nu^{\text{rot}}$  is large (10 kHz). Spectra do not need recording at much slower spinning speeds as the chemical shift anisotropy is well represented by the spinning side bands at 10 kHz. Slower speeds can be used for the identification of  $\delta^{\text{iso}}$ .

### 2.2.5 Fitting optimisation of TopSpin Solid-State line shape analysis tool

Recording SS NMR spectra with high spinning speeds allows spectra to be recovered that closely resemble the isotropic spectra obtained in solution phase NMR spectroscopy. When the spinning speed is 10 kHz, chemical shift anisotropy is largely averaged out in  $^{13}\text{C}\{^1\text{H}\}$  and  $^{31}\text{P}\{^1\text{H}\}$  spectra, as the magnitude of the anisotropy is typically on a lower scale than the speed of rotation. Consequently, resonances are observed as sharp, intense peaks. Because chemical shift anisotropy is averaged out at 10 kHz, the chemical shift tensors cannot be recovered from spectra obtained at fast spinning speeds. As the spinning speed is reduced, chemical shift anisotropy becomes the dominant feature on the spectra and the intensity of the spinning side bands represents the anisotropy of each environment. This has the side effect that the signal to noise ratio decreases due to signal dilution. This relationship is shown for  $^{13}\text{C}$  in Figure 25 and  $^{31}\text{P}$  in Figure 26. The intensity of the sidebands correlates directly to the static spectrum and the relation is explained in section 1.2.2.

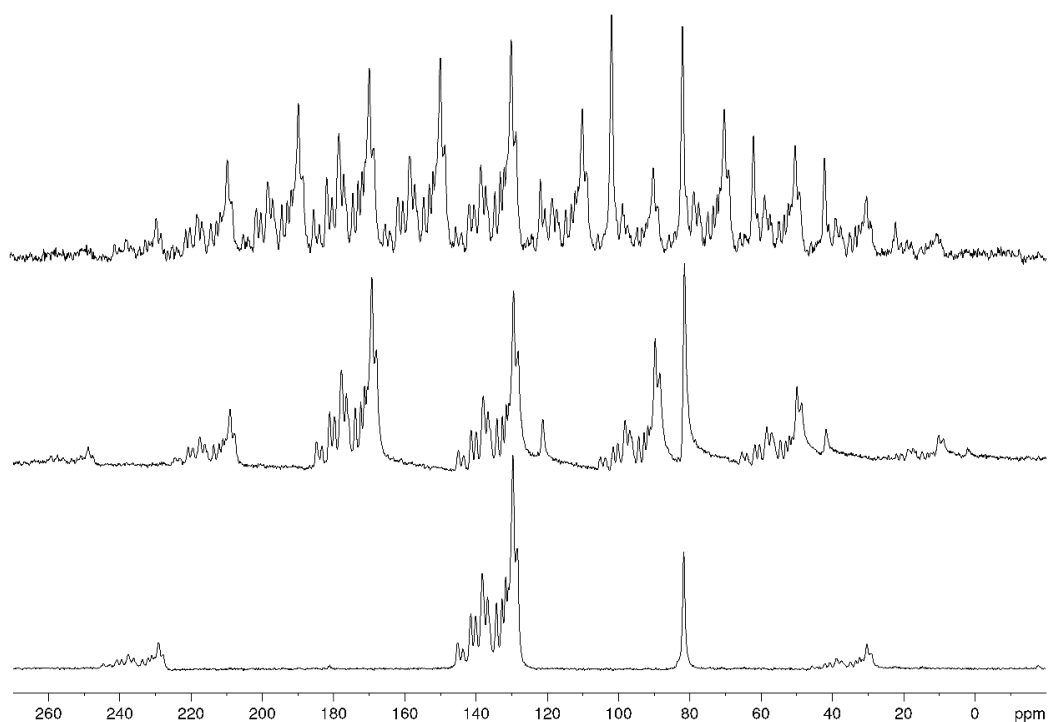


Figure 25.  $^{13}\text{C}\{^1\text{H}\}$  CP MAS SS NMR spectra of complex **[35]** recorded at 101 MHz at a spinning speed of 10 kHz (bottom), 4 kHz (middle), 2 kHz (top).  $N_s = 256$ . The effect of decreasing MAS rotation speed,  $\nu^{\text{rot}}$  on the intensity of the sidebands is shown.

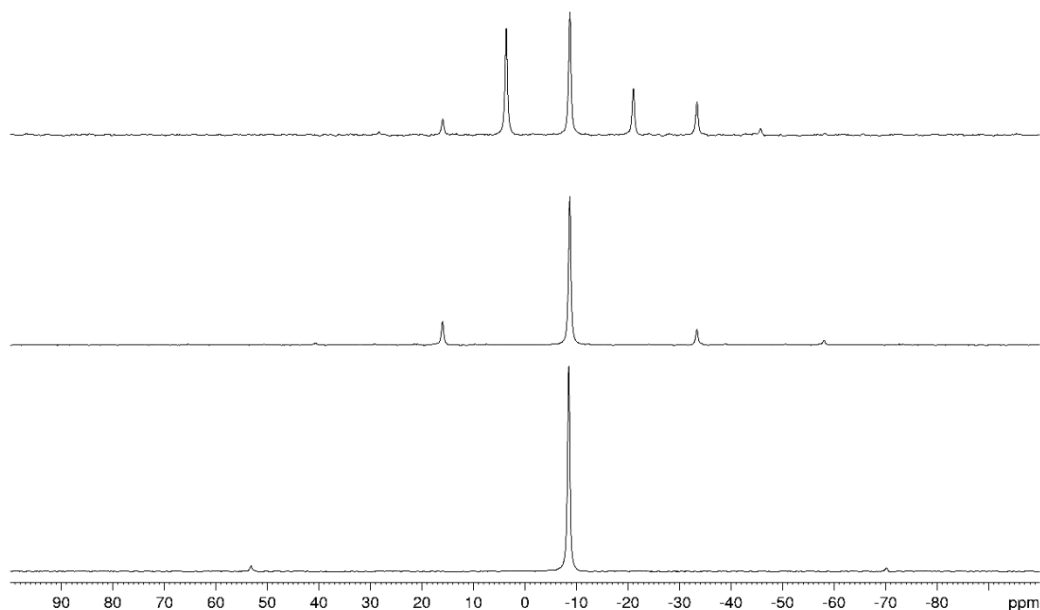


Figure 26.  $^{31}\text{P}\{^1\text{H}\}$  CP MAS SS NMR spectra of  $\text{PPh}_3$  recorded at 162 MHz at a spinning speed of 10 kHz (bottom), 4 kHz (middle), and 2 kHz (top).  $N_s = 32$ . The effect of decreasing MAS rotation speed,  $\nu^{\text{rot}}$  on the intensity of the sidebands is shown.

To obtain the most accurate value of chemical shift anisotropy, the lowest spinning speed must be used. For a system with a single environment this would be from the static spectrum. For more complex systems there must be a compromise between slow spinning speeds to give accurate values of the chemical shift tensors and fast spinning speeds to give increased signal and reduction of sideband overlap (also represented in Figure 25). Complex **[35]** is a simple molecule with two distinct  $^{13}\text{C}$  signals in the solid-state, the aromatic resonances associated with the  $\text{PPh}_3$  ligands and the cyclopentadienyl resonances. In systems with more unique environments, each environment will give different chemical shifts and possesses a unique chemical shift anisotropy. If the spinning speed is not carefully selected, the resonance of interest may become obscured by spinning side bands from other nuclei, preventing effective tensor recovery.

The effect of spinning speed is shown in Figure 25 and Figure 26. The shape of the side bands for the aromatic resonances changes as the spinning speed is reduced

from 10 kHz to 4 kHz. The overall shape of the spinning side bands becomes more detailed as the spinning speed is further reduced to 2 kHz, further representing the chemical shift anisotropy. For all the aromatic resonances, the 4 kHz spectrum has enough information to recover the tensors as chemical shift anisotropy  $> \nu^{\text{rot}}$ , but the resonance for the Cp carbons still has most intensity in the isotropic band at 4 kHz. A spinning speed of 2 kHz is required to calculate the chemical shift anisotropy for this environment as the span of the chemical shift anisotropy is much narrower for this environment.

To recover the chemical shift tensors from the SS NMR spectra, fitting software must be used. The NMR processing software TopSpin (Version 3.6.1 pl7) has been used in this work. TopSpin has an inbuilt SS NMR line shape fitting function that can be called up with the SOLA command. This software iteratively uses the integration of the simulated resonance to match to the recorded sideband intensity.

When using the SOLA fitting software, it was found that the simulated spectra matched the experimental spectra better when the isotropic shift and the line broadening were fixed. This was determined visually, as well as by allowing one round of iteration in the software. For all the complexes that were studied in this thesis, the resonances of interest are typically weak signals in the spectrum from the single metal-coordinated carbon. Without fixing the values of isotropic chemical shift and line broadening, the fitting software will typically drift to the most intense resonance or broaden to match the noise. Because spectra were recorded at fast (10 kHz) spinning speeds as well as slower spinning speeds (4 kHz), the isotropic chemical shifts were easily identifiable as the central resonance does not change chemical shift on altering the spinning speed. The sidebands extend from the isotropic resonance at regular intervals of the MAS spinning speed and therefore change position depending on spinning speed.

In general, the fitting iterations give the most reliable results when provided with good estimates of the chemical shift anisotropy and the asymmetry parameter. This was done by visually estimating the anisotropy and asymmetry based on the sideband intensities. Estimates of the chemical shift tensors could be obtained

visually from the SS NMR spectra by from the chemical shift of the highest and lowest frequency sidebands, setting these to  $\delta_{11}$  and  $\delta_{33}$ . The value of  $\delta_{22}$  was then set as the chemical shift of the most intense sideband. The approximate values of the chemical shift tensors were used as starting points for the iteration software, which was used to finalise the values of the chemical shift tensors.

## 2.3 Optimisation of computational methodology for the calculation of chemical shift tensors

As well as the study of SS NMR spectra of organometallic complexes, detailed analysis of the chemical shift tensors was performed. To relate the chemical shift tensors to FMOs, the chemical shift tensors must be related to the molecular frame. The orientations of the chemical shift tensors with respect to the molecular frame can be calculated in two ways. One such way is by mounting a single crystal on a goniometer and relating the tensors to the unit cell. The second way is by using quantum chemical calculations using DFT. For this thesis, the latter approach has been explored. To do this, a computational methodology has been explored in both the optimisation of molecular geometry and the prediction of chemical shift tensors.

### 2.3.1 Geometry optimisation of $[2a]^+$ , basis set and functional tolerance.

Initial testing of geometry optimisation using quantum chemical calculations using DFT was performed on  $[2a]^+$  shown in Figure 27. Cation  $[2a]^+$  was selected as a test molecule for geometry optimisation, due to its relevance to molecules of interest in Chapter 3, as well as a good quality XRD structure being available as a starting point for the geometry optimisation. Cation  $[2a]^+$  can also be used as a testbed for testing the calculation of the chemical shift tensors. It is critical that the methodology holds for organometallic systems alongside more traditional organic environments. Poor estimations of chemical shift for the metal bound carbons would correlate directly with incorrect orbital energies and localisations.

Geometry optimisations were performed using the quantum chemical package Turbomole Version 6.40 and are surmised in Table 3.<sup>67</sup> Two basis sets were trialled for the geometry optimisations: def2\_SV(P) and def2\_TZVPP. Both basis sets are Karlsruhe-type basis sets, with def2\_TZVPP having more basis functions to describe the orbitals. Both def2\_SV(P) and def2\_TZVPP use a pseudopotential to represent the 28 core electrons of ruthenium. This simplifies the calculation, as fewer electrons are dealt with explicitly and is often a reasonable approximation, as the core electrons do not participate in bonding.<sup>8</sup> As well as two basis sets, two GGA functionals were tested: BP86 and PBE0. PBE0 is a hybrid GGA functional that also includes part of the exchange energy calculated using Hartree-Fock theory.

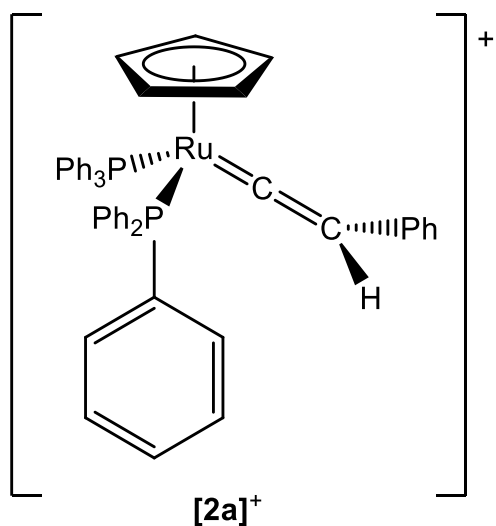


Figure 27. Structure of [2a]<sup>+</sup> used for methodology optimisation.

Table 3. Methodologies tested for geometry optimisation of **[2a]<sup>+</sup>**, all starting from the same input structure obtained from crystal coordinates. Time for job completion includes geometry optimisation and calculation of vibrational frequencies at the same level of theory.

Functional	Basis Set	Job Time / h
BP86	def2_SV(P)	25
BP86	def2_TZVPP	265
PBE0	def2_SV(P)	77
PBE0	def2_TZVPP	2100

After the geometry optimisation in Turbomole, the minima were identified by single point frequency calculations of the vibrational modes. The absence of imaginary frequencies, vibrational modes with negative energy, confirmed the identity of the minima.

As seen in Table 3, the double- $\zeta$  basis set def2\_SV(P) leads to faster completion of the job than triple- $\zeta$  basis set def2\_TZVPP. As def2\_TZVPP is a larger basis set than def2\_SV(P) and has more functions to describe the electrons of the molecule, the difference in job time is expected. The differences in optimised geometries were then compared.

### 2.3.2 Comparison of calculated geometry of **[2a]<sup>+</sup>** to the crystal structure geometry of **[2a]BF<sub>4</sub>**

The key bond lengths and angles for **[2a]<sup>+</sup>** are shown in Table 4, determined from the single-crystal X-ray structure of **[2a]BF<sub>4</sub>**, Figure 28. In general, all methods used for geometry optimisation converged to structures that were in close agreement to the experimental values. As well as this, the values of bond lengths and

bond angles around the metal core were within relatively close agreement to each other.

Table 4. Comparison of key geometries around Ru of **[2a]<sup>+</sup>** after geometry optimisation in Turbomole to values obtained from the X-ray diffraction crystal structure, estimated standard deviations are shown in square brackets [ ]. Absolute differences are shown in brackets ( ).

Property	Crystal	BP86		PBE0	
		def2_SV(P)	def2_TZVPP	def2_SV(P)	def2_TZVPP
Ru <sub>1</sub> -C <sub>1</sub> / Å	1.8479[18]	1.844 (0.004)	1.839 (0.090)	1.844 (0.004)	1.830 (0.018)
C <sub>1</sub> -C <sub>2</sub> / Å	1.3138[25]	1.338 (0.024)	1.328 (0.014)	1.338 (0.024)	1.315 (0.001)
Ru <sub>1</sub> -P <sub>1</sub> / Å	2.3309[5]	2.379 (0.048)	2.367 (0.037)	2.379 (0.048)	2.348 (0.017)
Ru <sub>1</sub> -P <sub>2</sub> / Å	2.3585[7]	2.397 (0.069)	2.387 (0.059)	2.396 (0.068)	2.369 (0.041)
Ru <sub>1</sub> -C <sub>cp</sub>	2.2675[41]	2.316 (0.049)	2.300 (0.033)	2.316 (0.049)	2.262 (0.005)
Average / Å					
Ru <sub>1</sub> -C <sub>1</sub> -C <sub>2</sub> / °	165.685	168.09 (2.41)	167.91 (2.23)	168.11 (2.43)	168.62 (2.94)
P <sub>1</sub> -Ru <sub>1</sub> -P <sub>2</sub> / °	97.689	97.93 (0.24)	98.48 (0.79)	97.93 (0.24)	98.09 (0.40)

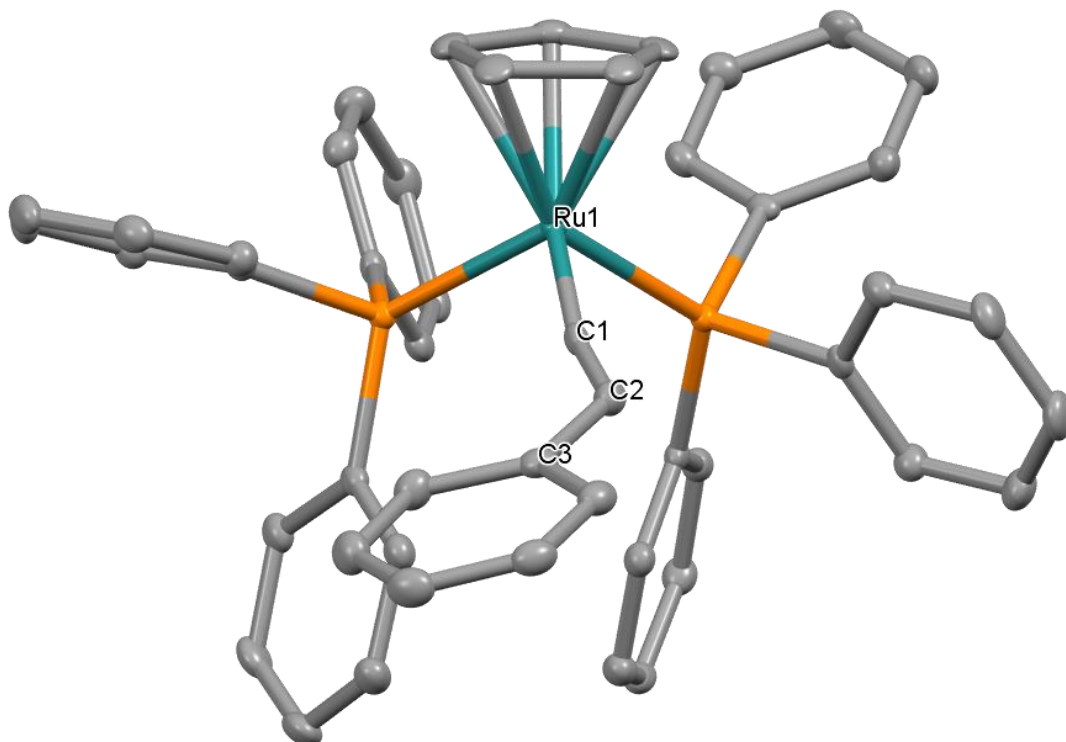


Figure 28. Single crystal XRD structure of  $[\text{CpRu}(\text{PPh}_3)_2(=\text{CHPh})]\text{BF}_4$ , **[2a]** $\text{BF}_4$ , tetrafluoroborate counterion and solvent of crystallisation omitted for clarity. Selected bond lengths and angles are shown in Table 4.

The method that provided the best approximation of bond lengths with the smallest deviation from those determined in the crystal structure values was PBE0/def2\_TZVPP, particularly with the prediction of  $\text{C}_1\text{-C}_2$ ,  $\text{Ru}_1\text{-P}_{1/2}$  and  $\text{Ru}_1\text{-C}_{\text{Cp}}$  showing small differences from the crystal structure. However, the accurate prediction of  $\text{C}_1\text{-C}_2$ ,  $\text{Ru}_1\text{-P}_{1/2}$  and  $\text{Ru}_1\text{-C}_{\text{Cp}}$  bonds was accompanied with extension of the  $\text{Ru}_1\text{-C}_1$  bond and a slightly poorer prediction of bond angles. Some differences in bond angle and lengths between the optimised and solid-state structures would be expected as the gas-phase calculations are being directly compared to the condensed-phase experimental values and the environment around the ions is different. Although PBE0/def2\_TZVPP does provide good approximation of bond length, the time taken for geometry convergence and the calculation of the vibrational spectra vastly outweighs any advantages for use. BP86/def2\_TZVPP was also ruled out as a general method for geometry optimisation for the same reason.

The double- $\zeta$  methodologies BP86/def2\_SV(P) and PBE0/def2\_SV(P) both converge to give nearly identical values for the key bond angles and lengths, for example the Ru-C<sub>1</sub> bond length of 1.844 Å, which is only 0.004 Å shorter from the value obtained from the crystal structure. As BP86/def2\_SV(P) has been used in the literature for the calculation of similar organometallics, this was selected as the methodology for geometry optimisation due to good predictions of bond lengths/angles and quick run times.

### 2.3.3 Optimisation of NMR calculations of complex [2a]<sup>+</sup>

After obtaining optimised coordinates using the accepted optimisation methodology, BP86/def2\_SV(P), a methodology needed to be developed for the calculation of NMR parameters. Initial trialling of chemical shift calculations was performed using two different programs, Gaussian and Orca.<sup>68-70</sup> Two functionals were selected for the NMR chemical shift calculations, BP86 and the hybrid functional PBE0. As with the geometry optimisation, both functionals have been used for calculations on similar compounds in the literature. Three basis sets were selected for the calculations. Def2\_SV(P) and def2\_TZVPP can be implemented in both Orca and Gaussian. Def2\_TZVPP has a larger number of basis functions than def2\_SV(P) and therefore should represent the electronic structure more flexibly. The IGLOIII basis set was also tested as it has been designed specifically for use in the calculation of NMR parameters, however it may only be implemented in Gaussian. The tensors from the calculations were internally referenced in the conversion of chemical shielding to chemical shift following Equation 13 using the experimental  $\delta^{\text{iso}}$  and calculated  $\sigma^{\text{iso}}$  of C <sub>$\alpha$</sub>  to calculate the conversion factor  $\sigma_{\text{iso}}^{\text{ref}}$ .

$$\delta_{\text{iso}} = \sigma_{\text{iso}}^{\text{ref}} - \sigma_{\text{iso}} \quad \text{Equation 13}$$

$$\sigma_{\text{iso}}^{\text{ref}} = \delta_{\text{iso}} + \sigma_{\text{iso}}$$

Table 5. Chemical shift calculation results for the alpha carbon of [2a]<sup>+</sup>. The chemical shielding tensors recovered from the quantum chemical calculations were

converted to chemical shift using the experimental isotropic shift of  $\delta^{\text{iso}} = 353.7$  ppm.

Program	Functional	Basis Set	$\delta_{11}$ / ppm	$\delta_{22}$ / ppm	$\delta_{33}$ / ppm
Experimental	N/A	N/A	558	289	214
Orca	BP86	def2_SV(P)	549	275	237
Orca	BP86	def2_TZVPP	771	293	-3
Orca	PBE0	def2_SV(P)	572	254	236
Orca	PBE0	def2_TZVPP	744	325	-7
Gaussian	BP86	def2_SV(P)	380	380	302
Gaussian	BP86	def2_TZVPP	414	323	323
Gaussian	PBE0	def2_SV(P)	379	379	303
Gaussian	PBE0	def2_TZVPP	421	320	320
Gaussian	PBE0	IGLOIII	426	318	318

Table 6. Chemical shift calculation results for an aromatic carbon of **[2a]<sup>+</sup>**. The calculations were converted using the same conversion factor as in Table 5.

Program	Functional	Basis Set	$\delta^{iso}$ / ppm	$\delta_{11}$ / ppm	$\delta_{22}$ / ppm	$\delta_{33}$ / ppm
Experimental	N/A	N/A	134.0	241	148	13
Orca	BP86	def2_SV(P)	154	244	178	41
Orca	BP86	def2_TZVPP	-150	-48	-132	-269
Orca	PBE0	def2_SV(P)	124	216	152	3
Orca	PBE0	def2_TZVPP	-165	-58	-146	-290
Gaussian	BP86	def2_SV(P)	339	434	364	219
Gaussian	BP86	def2_TZVPP	258	363	276	134
Gaussian	PBE0	def2_SV(P)	334	435	360	208
Gaussian	PBE0	def2_TZVPP	257	368	276	128
Gaussian	PBE0	IGLOIII	255	368	274	123

As seen from the data in Tables 5 and 6, the results obtained from the chemical shift calculations are varied. The Gaussian calculations consistently produced results that showed a small chemical shift anisotropy. As well as this, the data in Table 6 shows that Gaussian was unable to distinguish the large chemical shift difference between a typical aromatic carbon and the highly deshielded vinylidene carbon. Because the calculations in Gaussian yield similar chemical shift values for the vinylidene  $C_{\alpha}$  and an aromatic resonance, it suggests that the interactions responsible for chemical shift are being poorly represented. No further calculations were performed using Gaussian. The large changes in  $\delta^{iso}$  for the aromatic carbon are an artefact of the internal referencing to  $C_{\alpha}$  of **[2a]<sup>+</sup>**.

Unusually, the Orca calculations with the smaller basis set provide results that are closer to the experimental values. Typically, it would be expected that the larger number of basis functions should improve the description of the atomic orbital wavefunctions and should tend towards a limiting value.<sup>8</sup> However, the value that the larger description tends towards is further from the experimental values. This suggests that a larger description of the orbital set represents electronic structure of the experimental system worse.

The chemical shift is a parameter that is affected by many factors, but one key factor when considering organometallic complexes of the transition metals is typically the relativistic effects on chemical shift which arise from the speed of electrons approaching the speed of light.<sup>8</sup> The methodology selected uses a pseudopotential to represent the core electrons of ruthenium. This gives some approximation for relativistic effects. Given the proximity of the metal-bound carbons to a large nucleus, relativistic effects need to be considered more explicitly. To rectify this, the ZORA was applied to the calculations. This is not implemented in Gaussian, so methodology development was moved to Orca only. The chemical shift calculations were repeated in Orca with a ZORA and the results are shown in Table 7. As well as implementing the ZORA in the calculation, a ZORA-compatible basis set must be used so the basis sets chosen before were switched for their ZORA equivalents.

Table 7. Chemical shift tensors calculated in Orca with ZORA corrections for the vinylidene  $C_\alpha$  ( $C_1$ ) and a representative aromatic environment ( $C_{84}$ ) of **[2a]**<sup>+</sup>. Each method is internally referenced so that the vinylidene carbon  $C_1$  has a chemical shift of  $\delta^{iso} = 353.7$ . Experimental results recovered from the  $^{13}\text{C}\{^1\text{H}\}$  Cp MAS SS NMR spectrum of **[2a]**BF<sub>4</sub>·OEt<sub>2</sub>.

Functional	Basis Set	Carbon	$\delta^{iso}$ / ppm	$\delta_{11}$ / ppm	$\delta_{22}$ / ppm	$\delta_{33}$ / ppm
Experimental	N/A	$C_1$	353.7	558	289	214
Experimental	N/A	$C_{Ar}$	134.0	241	148	13
BP86	def2_SV(P) ZORA	$C_1$	354	516	292	253
BP86	def2_SV(P) ZORA	$C_{84}$	148	238	170	35
BP86	def2_TZVPP ZORA	$C_1$	353	528	295	238
BP86	def2_TZVPP ZORA	$C_{84}$	136	237	154	16
PBE0	def2_SV(P) ZORA	$C_1$	354	538	286	237
PBE0	def2_SV(P) ZORA	$C_{84}$	124	219	148	4
PBE0	def2_TZVPP ZORA	$C_1$	354	548	292	221
PBE0	def2_TZVPP ZORA	$C_{84}$	112	219	131	-13

The chemical shift tensors obtained from the ZORA calculations are, in general, in better agreement with experimental values. Particularly with the chemical shift difference between the vinylidene and aromatic carbons as the aromatic carbons now appear consistently in the aromatic region of the spectrum in all calculations,  $\delta_c = 110 - 150$ . The most obvious result of the calculations is that inclusion of relativistic effects appears to bring consistency to the weighting of the chemical shift tensors. The calculated chemical shift anisotropy of the vinylidene is closest to experiment using the PBE0/def2\_TZVPP level of theory with ZORA. As the chemical shift tensor values calculated using the PBE0/def2\_TZVPP level of theory with ZORA best

represent the experimental results, it suggests that any analysis performed on the calculations would give good insight into the structure and bonding of organometallic complexes.

#### 2.3.4 Dependence of chemical shielding on geometry

Computationally-optimised geometries will differ from the geometry obtained from a crystal structure because the calculation is of a single molecule in the gas phase. Solid-state structures possess a close contact network, the energy of the system in the condensed phase is stabilized by maximizing the stabilising interactions between neighbouring contacts. The stabilising interactions are not available in the gas phase. Differences in geometry may occur because of the change in phase and inclusion of close contacts, as well as the level of theory. Chemical shift is dependent on geometry. The geometry of neighbouring atoms determines the overlap of molecular orbitals and therefore the energy and localisations of molecular orbitals responsible for chemical shift. To test the tolerance of the computational methodology to deviations from crystal geometry, NMR single point calculations were performed on crystal coordinates to compare to the computationally optimised coordinates to the crystal coordinates. The results are shown in Table 8, note the value are in chemical shielding not shift.

Table 8.  $^{13}\text{C}$  Chemical shielding tensors recovered from single point DFT calculations in Orca at the PBE0/def2\_TZVPP level of theory with ZORA corrections.

Geometry	$\sigma_{\text{iso}}$	$\sigma_{11}$	$\sigma_{22}$	$\sigma_{33}$
Crystal	-187	-394	-116	-52
BP86/def2_SV(P)	-191	-386	-129	-59

The values of isotropic chemical shielding of the vinylidene  $\text{C}_\alpha$  of **[2a]**<sup>+</sup> only vary by a small amount, 4 ppm between entry 1 and 2 in Table 8 representing different geometries of **[2a]**<sup>+</sup> obtained from single crystal XRD and quantum chemical

geometry optimisations using DFT. The magnitude of variance is small compared to the magnitude of the span of chemical shielding. The largest difference is observed in  $\delta_{22}$  and is a 13 ppm shift. This change in shielding is associated with the small changes to geometry observed between the XRD crystal structure and the structure obtained using DFT calculations. The calculation is of a single ion in the gas phase and is therefore lacking the counter ion and any crystal contacts providing stabilisation to the condensed phase geometry.

The methodology shows a level of tolerance in the calculation of chemical shift with respect to small changes to geometry when calculating  $^{13}\text{C}$  chemical shift tensors. It also suggests that any chemical shift tensors derived from purely computational methods should still give good representations of chemical shift.

## 2.4 Referencing of chemical shift calculations

### 2.4.1 Selection of an appropriate reference compound

In section 2.3, the results of the chemical shielding calculations were converted to chemical shift using Equation 13 but were internally referenced to the vinylidene  $\text{C}_\alpha$  chemical shift. This is a useful tool for optimising the chemical shift calculations and testing accuracy but is not appropriate for comparing between multiple complexes. To get results that are comparable between molecules, the interconversion between chemical shift and shielding is reliant on the selection of an appropriate reference value.

In principle, any  $^{13}\text{C}$  nucleus, regardless of chemical environment, could be used as the reference. For this work, the reference selected for the conversion of  $^{13}\text{C}$  NMR shielding tensors was the experimental  $^{13}\text{C}$  carbonyl resonance of  $[\text{Ru}(\eta^5\text{-C}_5\text{H}_5)(\text{PPh}_3)_2(\text{CO})]\text{PF}_6$ , **[10]** $\text{PF}_6$ . This complex is similar to the systems that are being studied in chapter 3 and has a single well defined  $^{13}\text{C}$  environment that is bonded to the metal. The  $^{13}\text{C}\{^1\text{H}\}$  CP MAS SS NMR spectra of complex **[10]** $\text{PF}_6$  is shown in Figure 29. The carbonyl carbon of **[10]** $\text{PF}_6$  has a chemical shift of  $\delta^{\text{iso}} = 202.7$  in the solid state. This resonance appears in a region of the spectrum that is clear of any other

resonances, as well as being midway between the highly deshielded resonances of vinylidene  $C_\alpha$  ( $\sim 350$  ppm) and many typical organic environments (alkane  $\sim -10 - 40$  ppm, alkyne  $\sim 60 - 80$  ppm, alkene and aromatic  $\sim 100 - 160$  ppm). The sharp carbonyl resonance of **[10]**PF<sub>6</sub> is an ideal reference for these reasons due to the chemical similarity to the vinylidene and alkynyl complexes being studied, as well as being easy to synthesise purely and selectively by stirring complex **[35]** and NH<sub>4</sub>PF<sub>6</sub> together under an atmosphere of CO further described in section 5.16.

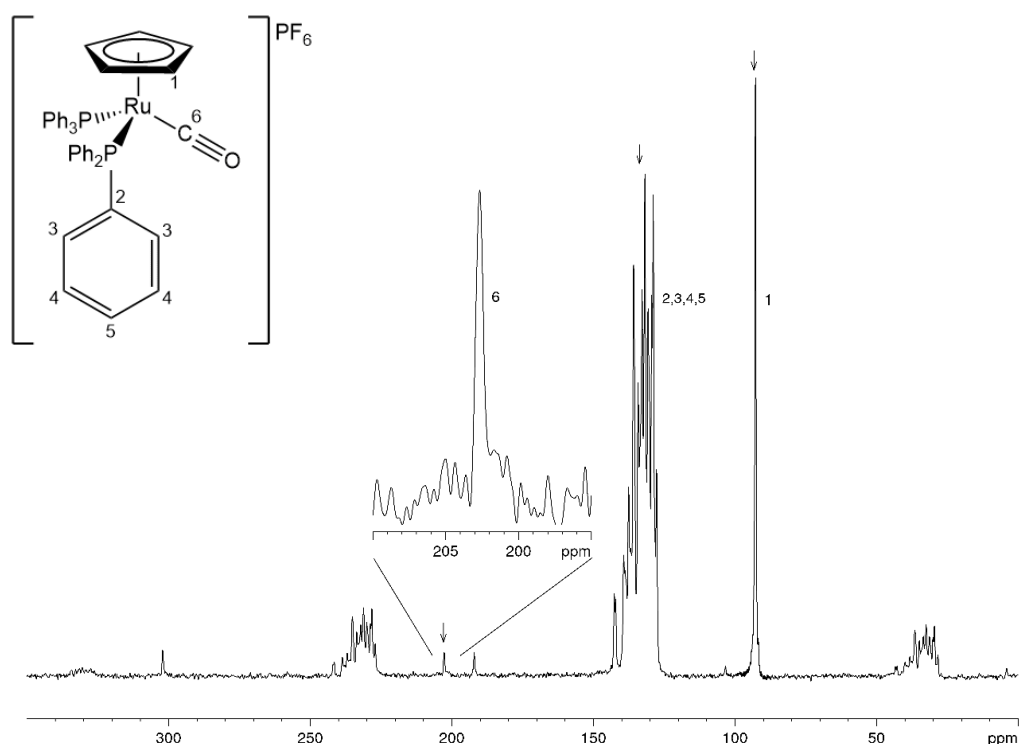


Figure 29. CP MAS SS  $^{13}\text{C}\{^1\text{H}\}$  spectra of complex **[10]**PF<sub>6</sub> recorded at 101 MHz at a spinning speed of 10 kHz.  $N_s = 256$ . Isotropic resonances are denoted by an arrow.

From the SS NMR spectrum in Figure 29, the experimental isotropic chemical shift for the carbonyl carbon of complex **[10]**PF<sub>6</sub> was found to be 202.7 ppm, a value that was then substituted into Equation 13. The absolute isotropic shielding for complex **[10]**<sup>+</sup> was calculated to be -36.8 ppm at the PBE0/def2\_TZVPP level of theory with ZORA corrections and can also be substituted into Equation 13, shown here again. The conversion factor  $\sigma_{iso}^{ref}$  can be calculated for  $^{13}\text{C}$ :

$$\delta_{iso} = \sigma_{iso}^{ref} - \sigma_{iso} \quad \text{Equation 13}$$

$$\delta_{iso} = 202.7, \sigma_{iso} = -36.8$$

$$\sigma_{iso}^{ref} = 202.7 + (-36.8)$$

$$\sigma_{iso}^{ref} = 165.9$$

This value of  $\sigma_{iso}^{ref}$  was then used to convert the calculated chemical shielding tensors into chemical shift by using the modified equation:

$$\begin{pmatrix} \delta_{11} & 0 & 0 \\ 0 & \delta_{22} & 0 \\ 0 & 0 & \delta_{33} \end{pmatrix} = \sigma_{iso}^{ref} \begin{pmatrix} 1 & 0 & 0 \\ 0 & 1 & 0 \\ 0 & 0 & 1 \end{pmatrix} - \begin{pmatrix} \sigma_{11} & 0 & 0 \\ 0 & \sigma_{22} & 0 \\ 0 & 0 & \sigma_{33} \end{pmatrix}$$

## 2.5 Benchmark calculation of chemical shift tensors for simple molecule examples.

Using the optimised methodology described in the previous section, it was decided that a series of simple molecules would be investigated to benchmark the calculations and analysis. In the literature, the  $^{13}\text{C}$  chemical shift tensors of ethene [37] been studied in detail.<sup>71</sup> Given that ethene has a small number of orbitals (9 Occupied MOs: 2 Core MOs, 7 FMOs), the analysis is relatively simple. Ethane [36] and ethyne [38] were analysed in the same way. These compounds are displayed in Figure 30.

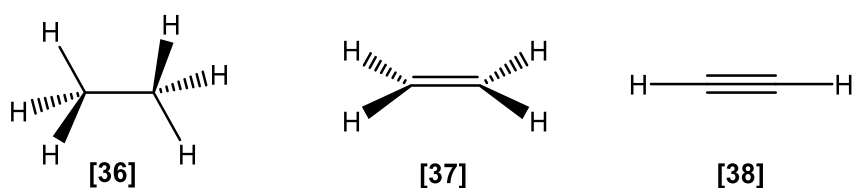


Figure 30. Simple molecules that were selected for benchmarking chemical shift tensor calculations calculated using the previously developed methodology.

The structures of compounds [36], [37], and [38] were optimised in Turbomole at the BP86/def2\_SV(P) level of theory. The resulting coordinates were then used for a single point calculation in Orca at the PBE0/def2\_TZVPP level of theory with ZORA

corrections. The chemical shift tensor magnitudes are displayed in Table 9, with, the calculated values of  $\delta^{iso}$  in line with experimental values. All values are more shielded than the experimental values by up to 20 ppm, which is likely an error that arises from the choice of reference. The magnitudes of the chemical shift tensors are clearly weighted differently to each other as unsaturation increases. Compound [36] shows deshielding values along all three axes that only vary by 15 ppm, which is nearly an isotropic situation. Compound [37] shows the largest anisotropy with a span of 239 ppm between  $\delta_{11}$  and  $\delta_{33}$  with different deshielding along all axes. Compound [38] shows rotational symmetry in its tensors with the values of  $\delta_{11}$  and  $\delta_{22}$  both exhibiting deshielding of 138 ppm,  $\delta_{33}$  is shielding in nature. To understand this fully, the direction of the tensors must also be known. To find out the orientation of the chemical shift tensors, visualisation software was trialled.

Table 9.  $^{13}\text{C}$  Chemical shift tensors for compounds [35], [36] and [37] calculated in Orca at the PBE0/def2\_TZVPP level of theory with ZORA. Experimental values reported by Zuschneid *et al.* in  $d_2$ -dichloromethane.<sup>72</sup>

	$\delta_{iso}$	$\delta_{iso} \text{ lit}$	$\delta_{11}$	$\delta_{22}$	$\delta_{33}$
Ethane	-8	7	-4	-4	-19
Ethene	113	124	237	102	-2
Ethyne	55	72	138	138	-113

## 2.6 Visualisation of chemical shift tensors

### 2.6.1 Example of tensor visualisation

The chemical shift tensor matrix is related to the molecular frame of reference as directional chemical shift is directly associated with transitions between molecular orbitals and rotational operators.<sup>71</sup> However, only the principal components, which are the eigenvalues of the chemical shift tensor matrix, are observable by MAS SS NMR spectroscopy. As the chemical shielding tensors have been calculated using *ab*

*initio* DFT methods in section 2.3, the chemical shielding tensor matrix can be correlated back to the molecular axes.

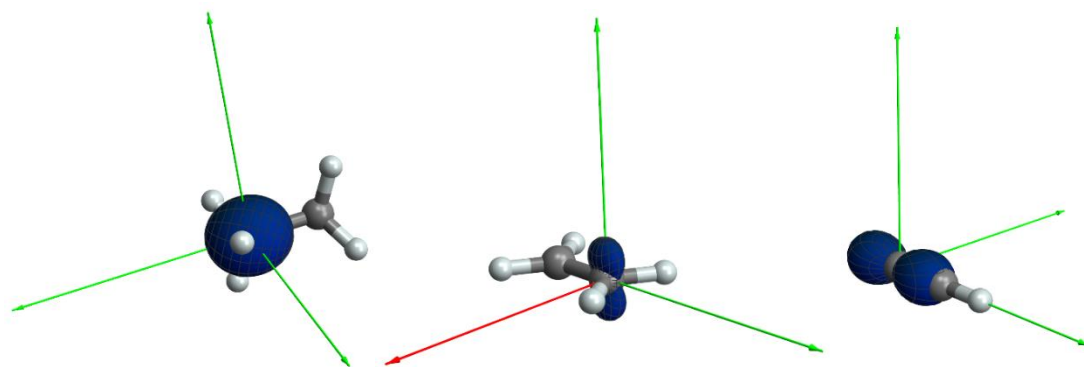
Work by Autschbach *et al.* shows that the chemical shift tensor matrix of a  $^{13}\text{C}$  nucleus of a single-walled nanotube can be represented by an isosurface after converting the chemical shift matrix into polar coordinates.<sup>73, 74</sup> The chemical shielding rank 2 tensor can be represented by Equation 14. Where  $s$  is a scaling factor and  $\sigma_{ij}^A, r$  are the cartesian chemical shielding tensor components of atom A  $r = (r_1, r_2, r_3) = (x, y, z)$ .

$$f(r) = s \sum_{i,j} r_i \sigma_{ij}^A r_j \quad \text{Equation 14}$$

Equation 14 can be written in polar coordinates rather than cartesian coordinates, with the origin of the polar coordinates being located at the centre of atom A where  $g$  is the angular dependence. The isosurface can be represented by Equation 15:

$$r = sg(\theta, \Phi) \quad \text{Equation 15}$$

Building on the work by Autschbach *et al.* in this area, Wolfram Mathematica was used for all visualisation of tensors in this thesis using a prewritten script.<sup>73, 74</sup> All that was needed to create a plot of the angular dependence of chemical shielding were the coordinates of the molecule of interest, as well as the chemical shielding tensor matrix, both obtained from quantum chemical calculations. Two separate surfaces are used to represent positive and negative shielding contributions. Orange represents deshielding and blue represents shielding with the magnitude being represented by the distance of the isosurface from the origin. Following this, the chemical shift tensors for ethane, ethene, and ethyne were visualised. The isosurfaces are shown in Figure 31.



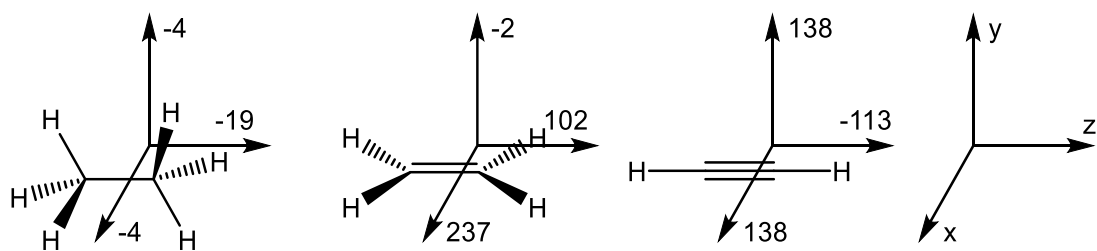


Figure 31. Top: Visualised chemical shift tensors left to right: ethane, ethene, ethyne. Bottom: Visualised tensors in a pictorial representation, chemical shift reported in ppm.

The tensors all have very different shapes. The chemical shielding around the carbon atoms of ethane is roughly spherical and highly shielded, therefore must be dominated by the diamagnetic contribution to chemical shielding,  $\sigma^{\text{dia}}$ , which provides a constant isotropic deshielding to all  $^{13}\text{C}$  nuclei. Small contributions of  $\sigma^{\text{para}}$  lead to the small deviations from isotropy observed meaning that  $\delta_{11} = \delta_{22} \approx \delta_{33}$ . Ethyne exhibits symmetrical shielding around the  $\text{C}\equiv\text{C}$  bond axis. This would be expected due to the symmetry of the  $\pi$  system and  $\delta_{11} = \delta_{22} \neq \delta_{33}$ . Ethene exhibits different shielding in all three axes and is fully anisotropic where  $\delta_{11} \neq \delta_{22} \neq \delta_{33}$ . Ethane exhibit isotropy where  $\delta_{11} = \delta_{22} = \delta_{33}$ .

## 2.7 Analysis of ethane, ethene, and ethyne FMOs

### 2.7.1 Step-by-step orbital analysis and correlation to chemical shift tensors of ethene [37]

As mentioned in section 2.5.1, ethene [37] shows large differences in the chemical shift tensors along each axis. Deshielding along each of these directions is associated with molecular orbitals being coupled by a rotational operator. The chemical shift tensors of ethene have been described in the literature.<sup>71</sup> The identification of the molecular orbitals and rotations can be simplified using group theory. Ethene belongs to the  $D_{2h}$  point group. By assigning the axes as shown in Figure 31, the irreducible representations of the frontier molecular orbitals can be assigned. To calculate the symmetry-allowed transitions, the rotational operators  $\hat{R}_x$ ,

$\hat{R}_y$ , and  $\hat{R}_z$  must be used. The rotation functions in the  $D_{2h}$  point group are described as  $B_{1g}$  ( $\hat{R}_z$ ),  $B_{2g}$  ( $\hat{R}_y$ ), and  $B_{3g}$  ( $\hat{R}_x$ ). Any symmetry-allowed transition with non-zero overlap can be identified if the product of the irreducible representations of the acceptor orbital, donor orbital, and rotation function is equal to the totally symmetrical representation of that group. In the  $D_{2h}$  point group, this is  $A_g$ . The  $\sigma_x$  bonding orbital of ethene possesses  $A_g$  symmetry. Mixing of this orbital with  $\pi_z^*$ , which is  $B_{2g}$ , via  $\hat{R}_y$  is symmetry allowed.

$$\Gamma_{\pi_z^*} \times \Gamma_{\hat{R}_n} \times \Gamma_{\sigma_x} = B_{2g} \times \begin{bmatrix} \Gamma_{\hat{R}_z} \\ \Gamma_{\hat{R}_y} \\ \Gamma_{\hat{R}_x} \end{bmatrix} \times A_g = B_{2g} \times \begin{bmatrix} B_{1g} \\ B_{2g} \\ B_{3g} \end{bmatrix} \times A_g = \begin{bmatrix} B_{3g} \\ A_g \\ B_{1g} \end{bmatrix}$$

This overlap can be visualised as a rotation of the p orbitals about the y axis. The rotation is positive and therefore anticlockwise. After rotation, the interaction between the two p orbitals can be either constructive or destructive. A constructive interaction would be where the overlap is in phase and leads to a shielding interaction. This allowed interaction is destructive, where the overlap is out of phase and therefore is deshielding in nature.  $\sigma_x \xrightarrow{\hat{R}_y} \pi_z^*$ , Y1, has very good overlap and a relatively small energy gap, leading to the majority of the deshielding along  $\delta_{11}$ . The same treatment of the other orbitals can be used to identify the other key transitions, this is shown Figure 32.

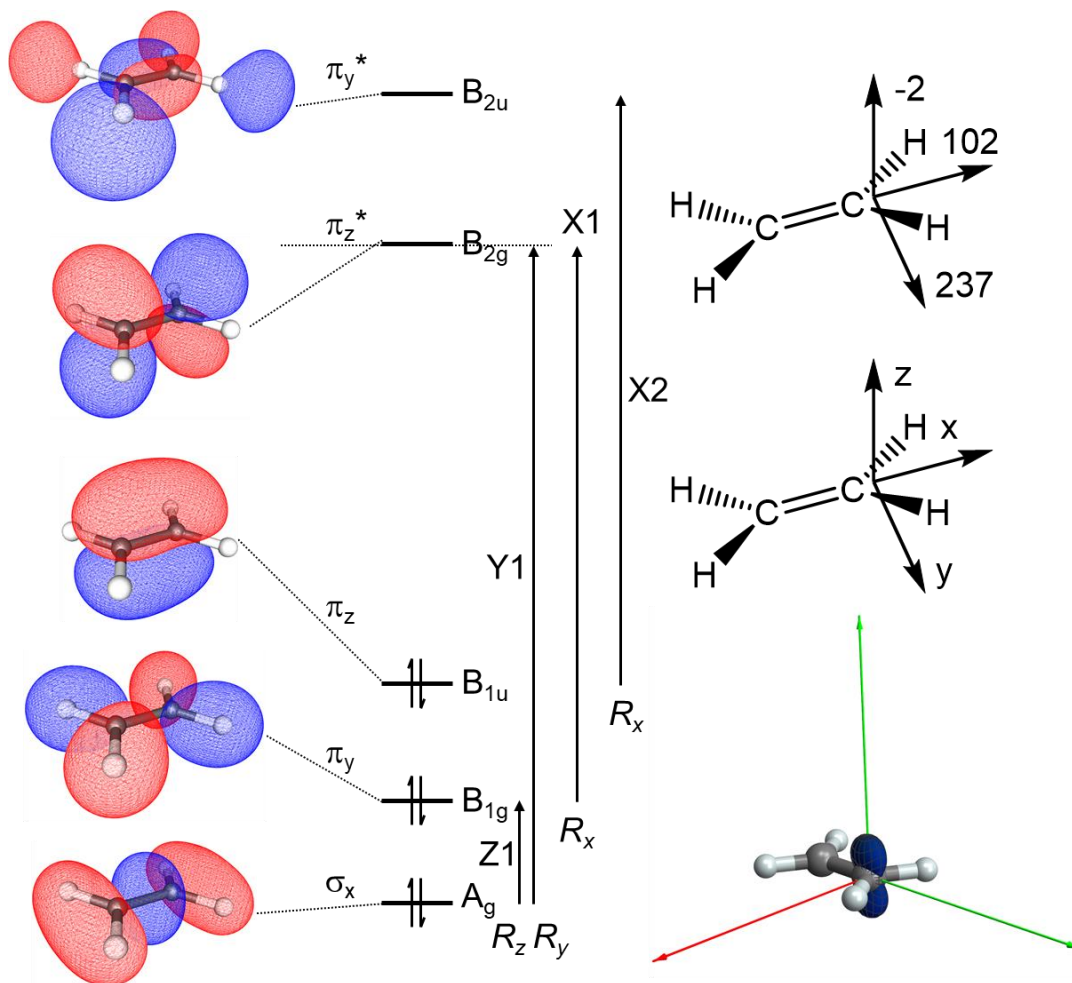


Figure 32. Selected frontier molecular orbitals of ethene and key transitions identified using group theory, calculated in Orca at the PBE0/TZVPP level of theory with ZORA corrections and visualised in gOpenMol (left). Chemical shift tensor for ethene calculated in Orca at the PBE0/TZVPP level of theory with ZORA corrections and visualised in Wolfram Mathematica with pictorial representations (right).

The greatest shielding in ethene is along the z axis. Any deshielding along this axis must be associated with orbitals that are coupled by the rotational operator  $\hat{R}_z$ . Using the same approach, one transition is observed:  $\sigma_x \xrightarrow{\hat{R}_z} \pi_y$ , Z1.

$$\Gamma_{\pi_y} \times \Gamma_{\hat{R}_n} \times \Gamma_{\sigma_x} = B_{1g} \times \begin{bmatrix} \Gamma_{\hat{R}_z} \\ \Gamma_{\hat{R}_y} \\ \Gamma_{\hat{R}_x} \end{bmatrix} \times A_g = B_{2g} \times \begin{bmatrix} B_{1g} \\ B_{2g} \\ B_{3g} \end{bmatrix} \times A_g = \begin{bmatrix} B_{3g} \\ A_g \\ B_{1g} \end{bmatrix}$$

The energy gap is low and the interaction constructive, leading to shielding along the z axis. The significant C–H bonding interaction reduces the effective overlap of the

orbitals due to large amounts of hydrogen orbital character in the MO. The transitions that are symmetry-allowed and that affect deshielding along the z axis are small, so much so that  $\delta_{33}$  is dominated by the diamagnetic shielding contribution  $\delta^{\text{dia}}$ .

Two transitions are symmetry-allowed to contribute to deshielding along x:  $\pi_y \xrightarrow{\hat{R}_x} \pi_z^*$ , X1, and  $\pi_z \xrightarrow{\hat{R}_x} \pi_y^*$ , X2. X2 has a very poor overlap and is constructive in nature so is not a significant contributor to deshielding. All the deshielding is dominated by X1, leading to the moderate deshielding observed in  $\delta_{22}$ .

### 2.7.2 Step by step orbital analysis and correlation to chemical shift tensors of ethyne [38]

The chemical shift anisotropy of ethyne [38] has been studied both experimentally and computationally, making it a good test system for our calculations and interpretation.<sup>75-77</sup> The experimental  $^{13}\text{C}$  chemical shift tensor for ethyne was recorded by trapping acetylene in an argon matrix and is shown to have a large span of ~240 ppm. The tensors also show axial symmetry, with the  $\delta_{11}$  and  $\delta_{22}$  tensors being equal and deshielded, with no deshielding along the  $\delta_{33}$  tensor. Ethyne is a highly symmetric molecule, possessing  $D_{\infty h}$  symmetry.

As mentioned in section 2.5.1, compound [38], ethyne, shows symmetrical deshielding orthogonal to the  $\text{C}\equiv\text{C}$  bond axis (x and y axes), with maximum shielding along the bond axis (z axis). To understand the differences in shielding along the axes, the orbitals that can contribute to  $\sigma^{\text{para}}$  must be identified. Any molecular orbitals that possess large p character and low s character may contribute to deshielding. The FMOs of ethyne were generated following the previously described methodology. A simple FMO diagram of the orbitals with high p character is shown in Figure 33, the energies of the orbitals are shown in Table 10.

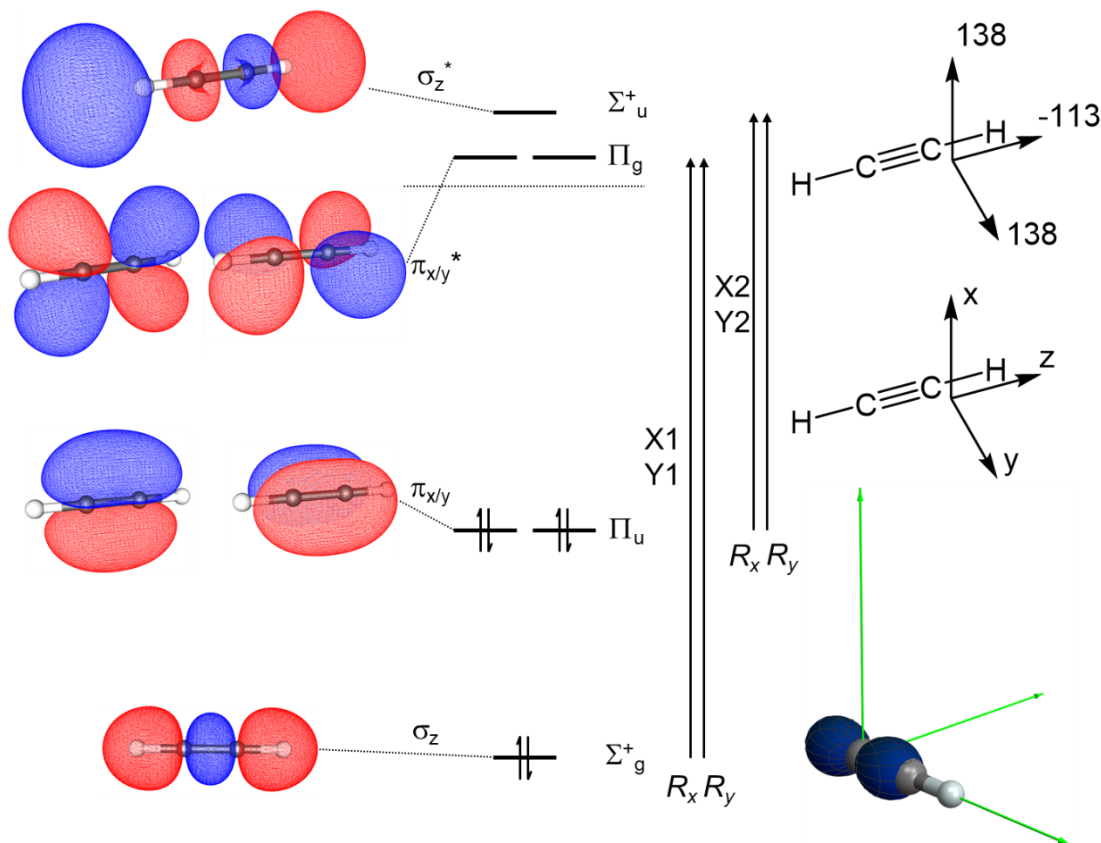


Figure 33. Selected FMOs of ethyne and key transitions identified using group theory, calculated in Orca at the PBE0/def2\_TZVPP level of theory with ZORA corrections and visualised in gOpenMol (left). Chemical shift tensors for ethyne calculated in Orca at the PBE0/def2\_TZVPP level of theory with ZORA corrections and visualised in Wolfram Mathematica with pictorial representations (right).

Key transitions responsible for deshielding in **[38]** are shown in Figure 33. Given that the  $\delta_x$  and the  $\delta_y$  tensors are equal, the orbitals involved must be degenerate. For  $\delta_x$  the transition must be between orbitals that are coupled by the rotational operator  $\hat{R}_x$ . The symmetry-allowed combinations must be  $\sigma_z \rightarrow \pi_y^*$ , X1, or  $\pi_y \rightarrow \sigma_z^*$ , X2. Figures 33 and 34 shows these two possible interactions. Due to the doubly degenerate nature of both the HOMO and LUMO, these are also the transitions responsible for  $\delta_y$ . Both transitions give rise to destructive interference between the two p orbitals and may contribute to  $\delta^{para}$  giving a deshielding tensor of  $\delta_{x/y} = 138$ . In this case, the lowest energy transition is HOMO  $\rightarrow$  LUMO+1 but there is a large proportion of orbital density on the protons on the LUMO+1. This reduces the effective overlap and

therefore its contribution. This, combined with the larger 14.53 eV HOMO-1→LUMO transition, leads to only moderate deshielding.

Table 10. Energies of MOs of **[38]** and transitions relevant to chemical shift, calculated in Orca at the PBE0/def2\_TZVPP level of theory with ZORA corrections.

Orbital	E / eV	Transition	$\Delta E$ / eV
HOMO-1	-13.82	HOMO-1→LUMO $L_{x/y}$	14.53
HOMO (*2)	-8.33	HOMO→LUMO $L_z$	9.04
LUMO (*2)	0.71	HOMO→LUMO+1 $L_{x/y}$	10.13
LUMO+1	1.80		

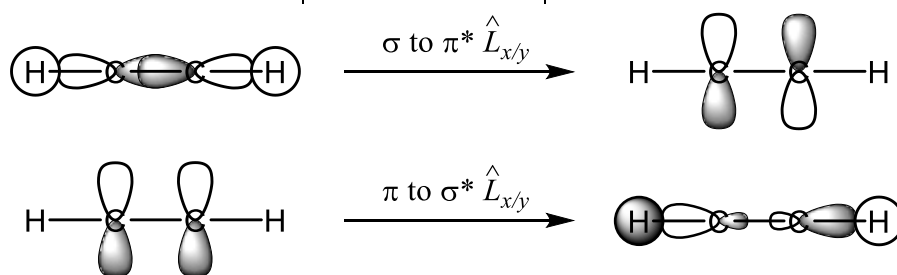


Figure 34. Orbital transitions responsible for deshielding along the x and y axes.

The  $\delta_z$  tensor can only arise from a transition between x and y orbitals, coupled by the rotational function  $\hat{R}_z$ . However, on transformation of the frontier molecular orbitals by  $\hat{R}_z$ , a  $90^\circ$  operator, gives rise to orbitals that possess the same symmetry as the initial orbital, Figure 35, due to the degenerate nature of the HOMO. The resultant symmetry of  $\Gamma_{\pi_x}$ ,  $\Gamma_{\hat{R}_z}$ , and  $\Gamma_{\pi_y}$  does not give rise to the totally symmetric representation for  $D_{\infty h}$ . Even though the HOMO and LUMO have a very narrow energy gap and are at  $90^\circ$  to each other, these orbitals cannot mix for the same reason as HOMO-HOMO mixing, any deshielding overlap generated by a  $90^\circ$  rotation is cancelled out by shielding of the same magnitude. The lack of symmetry allowed transitions dominates the chemical shift in this direction and leads to a very small deshielding contribution to  $\delta^{\text{para}}$ . Instead,  $\delta_{33}$  is dominated by  $\delta^{\text{dia}}$ .

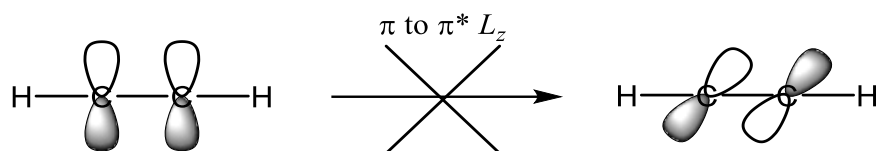


Figure 35. Orbital transitions responsible for deshielding along the z axis.

The presence of the symmetrical  $\pi$  system leads to a greater extent of deshielding in ethyne than ethane. However, the high symmetry means that the lowest energy transition has the poorest overlap and is highly shielding, although not as shielded as ethane. High symmetry forbids the lowest energy transitions leading to lower deshielding in ethyne than ethene.

### 2.7.3 Step by step orbital analysis and correlation to chemical shift tensors of ethane

As mentioned in 2.5.1, ethane shows a nearly totally symmetrical shielding around the carbon nuclei and a very low chemical shift anisotropy. Chemical shift is dominated by the large shielding values along each axis. The lack of deshielding can be attributed to the large energy gaps between orbitals and poor overlap. The lower energy orbitals have a high degree of carbon 2s character meaning that no mixing can occur due to the symmetrical nature of the orbitals. These two effects mean that there is a small constant contribution to deshielding in all directions.

## 2.8 Conclusions

In this chapter,  $^{13}\text{C}\{^1\text{H}\}$  SS NMR spectroscopy has been performed on the test complex **[35]** and a general methodology selected for the spectroscopy performed in this thesis. MAS has been employed resulting in the recording of sharp spectra of complexes **[2a]**BF<sub>4</sub>, **[10]**PF<sub>6</sub>, and **[35]**, as well as PPh<sub>3</sub>. The organometallic systems studied have spectra that are too complex and overlapped for static powder spectra to give meaningful values of  $\delta_{11}$ ,  $\delta_{22}$ , and  $\delta_{33}$ . As well as simplifying the spectra from resonance overlap, MAS has the added advantage that signals are averaged, leading to high intensity carbon spectra. The double resonance experiment CP MAS has been selected for the recording of  $^{13}\text{C}\{^1\text{H}\}$  spectra. CP decouples the  $^{13}\text{C}$  nuclei from  $^1\text{H}$  nuclei that are coupled *via* direct-dipole coupling interactions. As well as decoupling, when the Hartman-Hahn matching conditions are met, polarization transfer occurs between the  $^1\text{H}$  and  $^{13}\text{C}$  nuclei. This increases signal and means that relaxation processes are dictated by the spin-lattice relaxation of  $^1\text{H}$  nuclei rather than  $^{13}\text{C}$ , which are typically shorter in the solid-state.

As well as for detecting  $^{13}\text{C}$  nuclei, pulse programs have been selected for the recording of  $^{31}\text{P}$  and  $^{19}\text{F}$  spectra. With the CP experiment for  $^{31}\text{P}\{^1\text{H}\}$  and a  $90^\circ$  pulse for  $^{19}\text{F}$ . The methodology selected provides sharp and intense spectra with clear sidebands that can be analysed.

The magnitude of the spinning side bands has been modelled using the  $^{13}\text{C}\{^1\text{H}\}$  CP MAS SS NMR spectra of complex **[35]**. The iterative line fitting function SOLA has been using in TopSpin 3.6.1 pl7. MAS speeds,  $\nu^{\text{rot}}$ , have been selected where  $\nu^{\text{rot}} <$  chemical shift anisotropy, giving values of the principal components that represent chemical shift anisotropy well.

*Ab initio* computational calculations using DFT have been performed in Turbomole exploring the geometry optimisation of **[2a]**<sup>+</sup>. Geometries recovered using the GGA functionals BP86 and PBE0 are shown to have small variances in key bond lengths and angles around the ruthenium centre of **[2a]**<sup>+</sup>. Increasing the size of the basis set from double  $\zeta$ , def2\_SV(P), to triple  $\zeta$ , def2\_TZVPP, has been shown to have a small effect on optimised geometry when compared to the experimentally recovered XRD

crystal structure. The differences in geometry between def2\_SV(P) and def2\_TZVPP were not so large as to outweigh the large increase in computational run time. BP86/def2\_SV(P) were selected as the functional and basis set used to optimise geometry in this thesis. Electronic minima were identified by the absence of imaginary vibrational modes.

As well as geometry optimisation, the use of single point DFT calculations was explored in the calculation of chemical shift tensors using the programs Orca and Gaussian. It was found that neither program gave values of the principal components  $\delta_{11}$ ,  $\delta_{22}$ , and  $\delta_{33}$  that were comparable with the experimentally derived values. The inclusion of relativistic effects was achieved through the implementation of ZORA in Orca. Calculations using ZORA resulted in values of  $\delta_{11}$ ,  $\delta_{22}$ , and  $\delta_{33}$  that agreed with experimental values. PBE0/def2\_TZVPP ZORA was selected as a general methodology for the calculation of chemical shift tensors in this thesis.

With a general methodology for the recording and calculation of chemical shift tensors, the link between tensor reference frame and molecular reference frame could be explored. Conversion of the chemical shift tensor matrix to polar coordinates as described by Autschbach *et al.*<sup>73</sup> allows the chemical shift tensors reference frame to be correlated with the molecular frame.  $\delta_{11}$ ,  $\delta_{22}$ , and  $\delta_{33}$  can be assigned to the molecular axes x, y, and z.

Chemical shift is comprised of two major components,  $\delta^{\text{dia}}$  and  $\delta^{\text{para}}$ .  $\delta^{\text{dia}}$  is associated with the reduction of the effective magnetic field  $B_{\text{eff}}$  applied to the nucleus due to the interaction of  $B_0$  and the electrons in spherical orbitals around a nucleus. For larger nuclei such as  $^{13}\text{C}$ , this interaction is constant between different  $^{13}\text{C}$  environments and is shielding in nature. Shielding and deshielding in  $\delta^{\text{para}}$  is associated with transitions between molecular orbitals that are coupled by the magnetic rotational operator  $\hat{R}_n$ . Constructive, in-phase, overlap of the donor orbital (after the application of  $\hat{R}_n$ ) with the acceptor orbital leads to a shielding interaction along the molecular axis n. Destructive, out of phase, overlap between the orbitals leads to a deshielding interaction along the molecular axis n. The magnitude of the interaction is proportional to the overlap integral between the coupled orbitals and

inversely proportional to the energy gap between the orbitals. Analysis of the interactions responsible for the shielding and deshielding of ethene and ethyne are in line with literature understanding and have been shown to demonstrate how this analysis will be used for further work in this thesis.

Overall, this chapter has outlined the general methodologies that have been used for the collection and analysis of data in this work.

## Chapter 3. Investigation of fluorine effect on chemical shift in ruthenium vinylidene and alkynyl complexes

### 3.1 Introduction

In this chapter, the fluorine effect on M-C bonding has been investigated for a range of vinylidene and alkynyl complexes. The current understanding of the bonding in stable fluorinated vinylidene and alkynyl complexes is poor. This chapter has used SS NMR spectroscopy and quantum chemical calculations using DFT to further the understanding of these compounds. Exploring changes in bonding will help to add to the current understanding of the effect that fluorine has on fluorinated unsaturated organometallic and organic species.

Organo- and organometallo- fluorine containing species are common in many areas of chemistry. In this introduction, the unusual properties of the C-F bond will be discussed, including the gauche effect. Knowing that fluorine may cause changes to the physical properties of organic compounds, the coordination of organofluorine molecules to metals will also be discussed with a focus on fluorobenzenes. The use of fluorobenzene complexes as precatalysts will be briefly discussed. The directing effects of C-F bonds on the activation of fluorobenzenes will be discussed as examples of where the C-F bond influences the electronics of organic fragment. The electrophilic fluorination of ruthenium vinyl- and alkynyl- complexes to produce stable fluorine-containing vinylidene-, alkynyl, vinyl-, and carbene- complexes is discussed. The stability of the coordinated fluorovinylidene and fluoroalkynyl moiety will be compared to the uncoordinated examples. The understanding of fluorovinylidene and fluoroalkynyl species has been developed in this chapter with an aim to better predict reactivity.

### 3.1.1 Carbon-fluorine bonds

The fluorine atom is of great interest in synthetic chemistry, particularly in carbon-fluorine bonds, C-F. Fluorine is the most electronegative element, the high electronegativity of fluorine,  $\chi_{\text{F}} = 3.98$  (where  $\chi_{\text{H}} = 2.20$ ), is responsible for some of the unusual chemical properties of compounds containing C-F bonds. C-F bonds are very strong, with the bond enthalpies of the C-X bond in  $\text{CH}_3\text{X}$ , where X = F, H, Cl, Br, I, being  $D_{\text{H}298} = 481, 439, 350, 302, 241 \text{ kJ mol}^{-1}$ , respectively.<sup>78</sup> Although fluorine is largely absent from naturally occurring biomolecules, the introduction of fluorine into an organic molecule may improve lipophilicity, increase binding affinity to proteins, and increase metabolic stability.<sup>79</sup> Due to the aforementioned reasons, a large number of pharmaceuticals and agrochemicals are fluorine-containing. More recently, the metastable synthetic isotope of fluorine  $^{18}\text{F}$  has also been of interest for use in positron emission tomography (PET) for use in bioimaging.<sup>80</sup>

### 3.1.2 Effect of fluorine on structure and bonding – The gauche effect

The unusual properties of fluorine may influence the conformational isomerisation of an organomolecule, particularly when two fluorine atoms are bonded to adjacent carbons. A disubstituted ethane,  $\text{RH}_2\text{C-CRH}_2$ , may have free rotation about the C-C bond. The energy of rotation of the C-C bond is shown for butane in Figure 36.<sup>81</sup> Two conformational energy minima are observed, antiperiplanar (A) and gauche (G). Typically, the antiperiplanar conformation is the lowest energy conformation with the bulky substituents facing away from each other. However, if R = F, as in 1,2-difluoroethane, the gauche conformation becomes more stable than the antiperiplanar conformation.<sup>82</sup> This is known as the gauche effect.

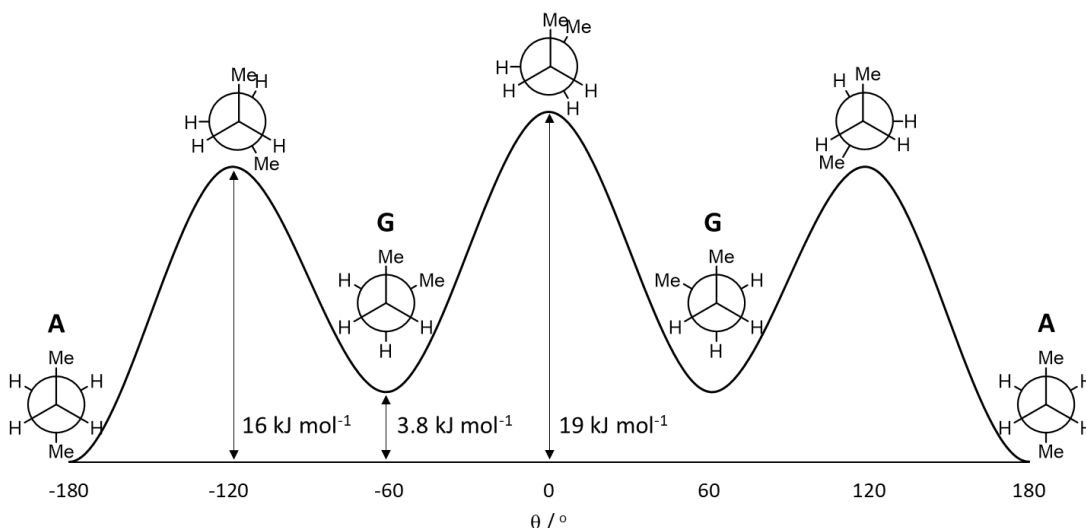


Figure 36. Energy profile for butane ( $R = \text{Me}$ ) on rotation of the C-C bond. Two local minima are observed, antiperiplanar (A) and gauche (G).<sup>81</sup>

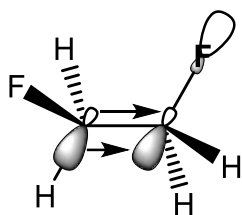


Figure 37. Hyperconjugation interaction between the C-H  $\sigma$  and the C-F  $\sigma^*$  orbitals in 1,2-difluoroethane.

In 1,2-difluoroethane, the C-H  $\sigma$ -bonding orbital may interact with the C-F  $\sigma^*$ -antibonding orbital of the adjacent carbon, donating electron density and providing stabilisation. The interaction is summarized in Figure 37. The presence of fluorine atoms simultaneously makes the C-H  $\sigma$ -bonding orbital a greater donor and the C-F  $\sigma^*$ -antibonding orbital a better acceptor leading to a strong stabilisation. This effect is known as hyperconjugation and in 1,2-difluoro compounds, this interaction may outweigh the repulsive interaction between the two fluorine atoms leading to a stable gauche isomer.<sup>83</sup>

### 3.1.3 Fluorobenzene complexes

As well as in the synthesis of fluorinated molecules, fluorine has a wide variety of uses in organometallic complexes which are in turn used for selective transformations. Metal complexes of fluorobenzenes are widely used as precatalysts with arene dissociation providing a fast route to coordinatively unsaturated metal centres.<sup>84</sup>

Fluorobenzene complexes have been used in the hydrogenation of alkynes by Rh<sup>I</sup> complexes, as shown in Figure 38.<sup>85</sup> The cationic complex **[39]**<sup>+</sup> acts as a source of coordinatively unsaturated Rh<sup>I</sup> which, in the presence of an alkyne, may hydrogenate. Controlling the stoichiometry of H<sub>2</sub> can lead to selective formation of the alkene over the alkane.

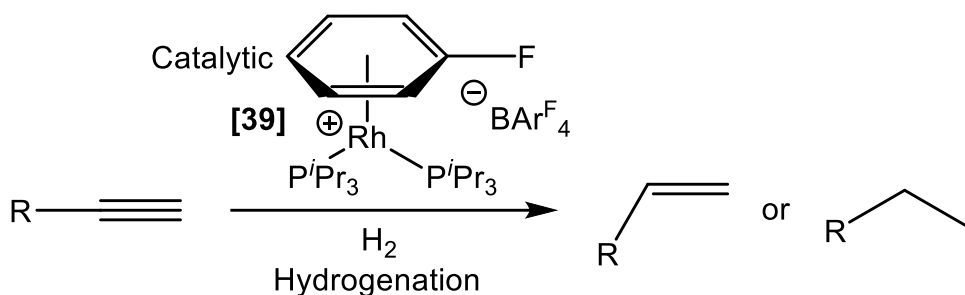


Figure 38. Hydrogenation of alkynes using a rhodium fluorobenzene complex.

Complex **[39]**BAr<sup>F</sup><sub>4</sub> is a rhodium complex of the general class [Rh<sup>I</sup>(C<sub>6</sub>H<sub>5</sub>F)(PR<sub>3</sub>)<sub>2</sub>]<sup>+</sup>BAr<sup>F</sup><sub>4</sub><sup>⊖</sup>. As well as in hydrogenation reactions, these complexes have also been shown to generate active catalysts used in amine-borane and phosphine-borane dehydrocoupling,<sup>86-89</sup> hydroacylation,<sup>90, 91</sup> and cross-coupling reactions.<sup>92</sup> (Figure 39).

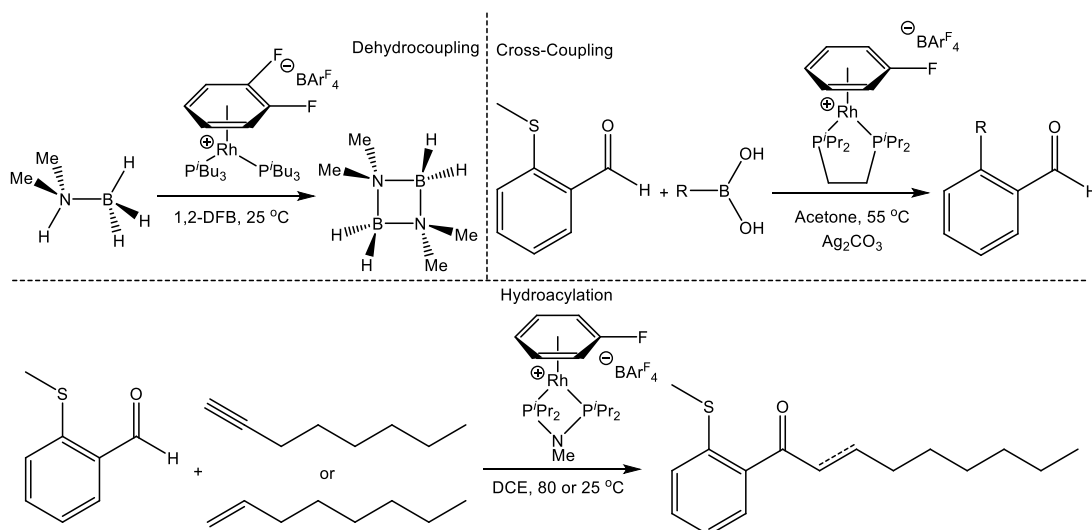


Figure 39. Examples of Rh<sup>I</sup> fluoroarene complex reactivity.

Naked group 13 cations such as Ga<sup>I</sup> or In<sup>I</sup> can be stabilised by coordination of fluorobenzene into a sandwich complex **[40]**<sup>+</sup>, **[41]**<sup>+</sup>, shown in Figure 40.<sup>93-95</sup> Ga<sup>I</sup> fluoroarene sandwich complexes have been used in the polymerisation of *iso*-butene with very low catalytic loadings of 0.007 %, also shown in Figure 40.

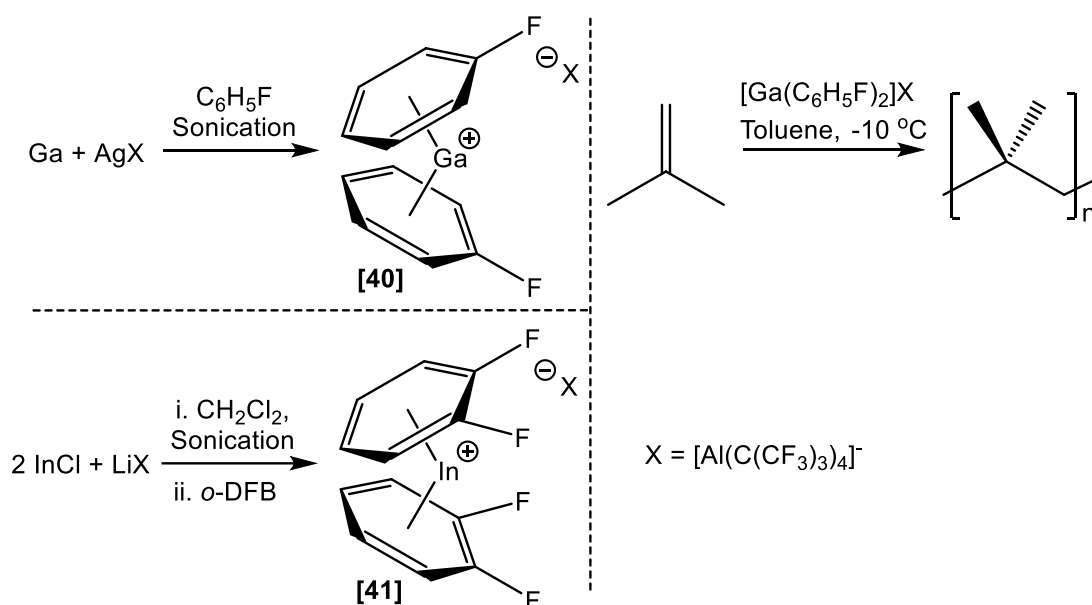


Figure 40. Fluoroarene sandwich complexes of Ga and In (left) and the polymerisation of *iso*-butene catalysed by Ga<sup>I</sup> (right).

### 3.1.4 C-H and C-F activation of fluoroarenes

Introduction of fluorine to an aromatic moiety can lead to large changes in the electronics of the ring. Arenes, such as fluorobenzene, are widely known to coordinate to metal centres as  $\eta^6$  face capping ligands.<sup>84</sup> However, C-H activation chemistry may occur as the arene slips to an  $\eta^2$ -coordination mode.<sup>96</sup>

The synthesis of the strongly chelated and coordinatively saturated Rh<sup>III</sup> complex **[42]**BARF<sub>4</sub> has allowed solid-state characterisation of a range of  $\eta^2$ -coordinated fluoroarene complexes, shown in Figure 41.<sup>97</sup> The tridentate bi-N-heterocyclic carbene pyridine (CNC) and biphenyl ligands prevent the benzene coordinating in the  $\eta^6$ -mode.

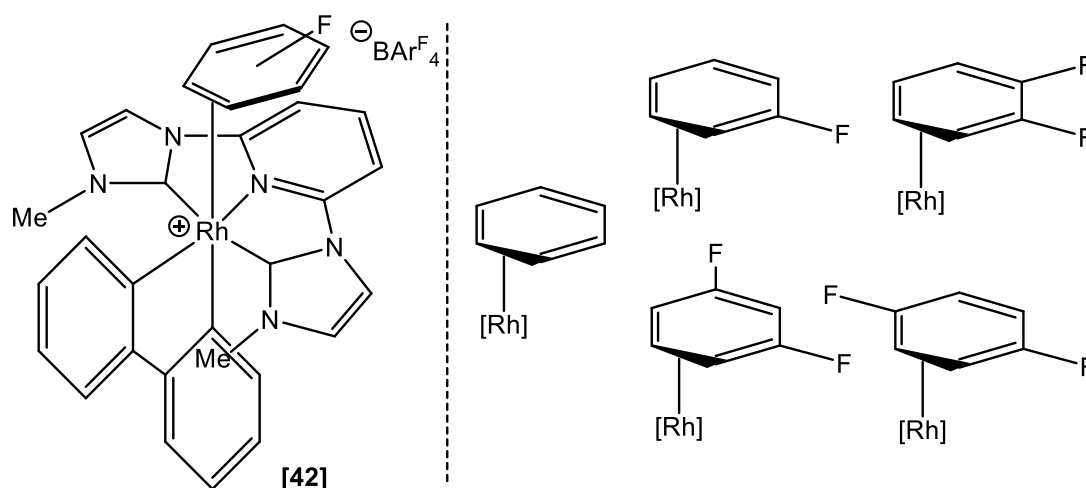


Figure 41. Forced  $\eta^2$ -coordinated fluoroarene complex coordination modes show clear preference for coordination *ortho*- to C-F bonds.

The arene shows a clear binding preference to the CH=CH moiety that is *ortho*- to fluorine in the solid state. DFT calculations suggest that the binding affinity of this position would be the highest. This may be relevant to the observed preferences in C-H activation of fluoroarenes by metal complexes.

Some early examples of preferential C-H activation of fluorobenzenes are by thermal and photochemical activation mediated by  $[\text{Rh}(\eta^5\text{-C}_5\text{Me}_5)\text{H}(\text{Ph})(\text{PMe}_3)]$  **[43]** and  $[\text{Rh}(\eta^5\text{-C}_5\text{H}_5)(\text{CH}_2\text{CH}_2)(\text{PMe}_3)]$  **[44]**.<sup>98</sup> The thermal activation using **[43]** is summarized in Figure 42.

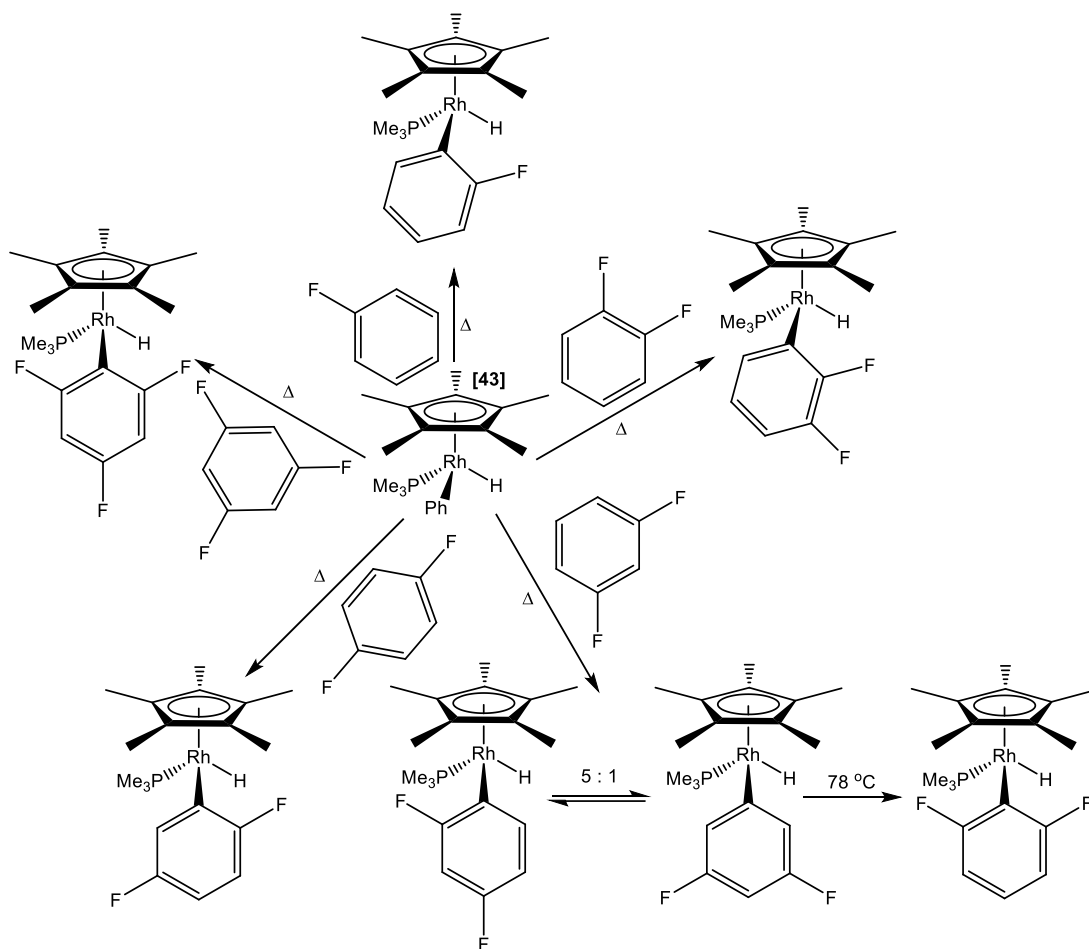


Figure 42. Thermal C-H activation of fluorobenzenes by a 16 electron Rh<sup>I</sup> complex.<sup>98</sup>

In all cases the thermodynamic end product is C-H activation *ortho*- to the C-F bond.<sup>98</sup> In the case of 1,3-difluorobenzene, the initial product is a mixture of kinetic products. Activation of the C-H that is *meta*- to both C-F bonds is least favourable with a larger ratio of activation of C-H that is *ortho*- to one C-F bond in the dynamic mixture. However, extended heating at a higher temperature causes isomerisation of both kinetic isomers to the end product of C-H activation at the bond *ortho*- to both C-F bonds.

Photochemically-initiated oxidative addition from [44] gives rise to similar results as the thermal activation of [43], also giving access to coordination of some higher fluorinated benzenes, shown in Figure 43.<sup>98</sup>

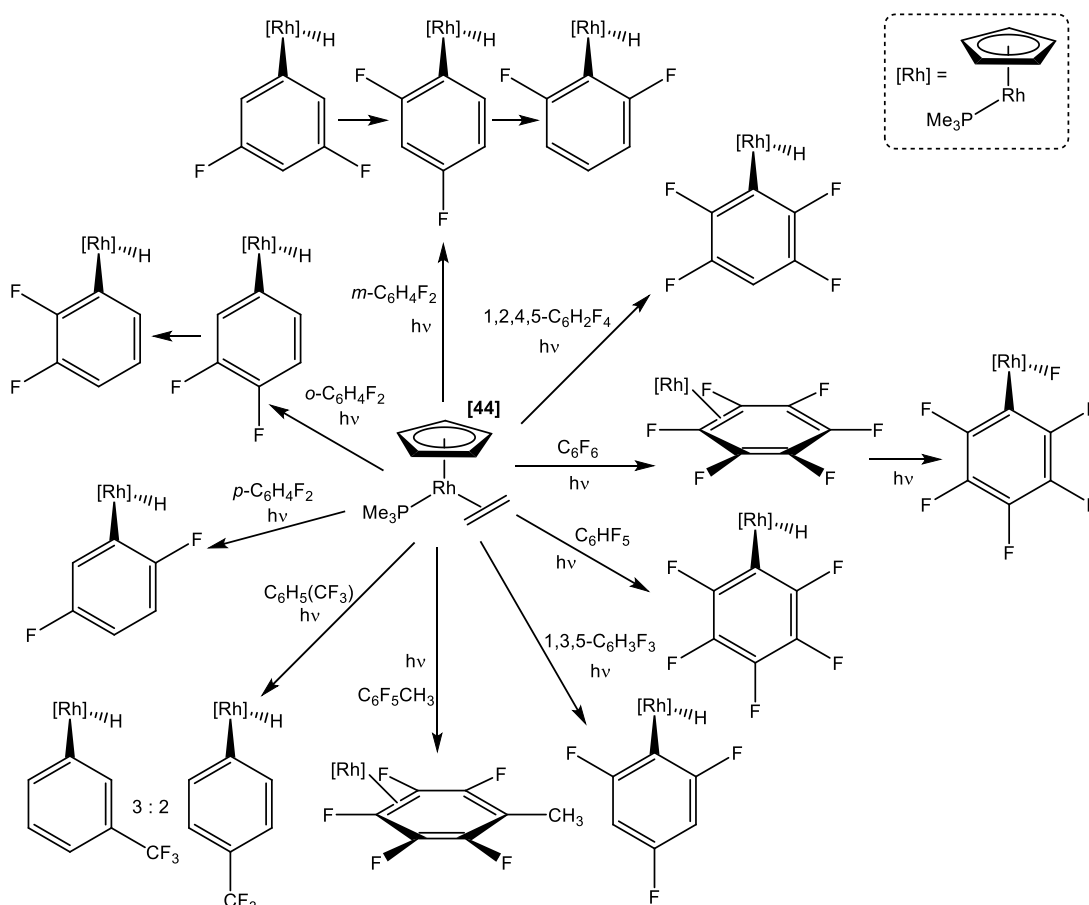


Figure 43. Photochemical C-H activation of fluorobenzenes by a 16 electron Rh complex and further C-F oxidative addition of hexafluorobenzene by  $\text{Rh}^{\text{I}}$ .<sup>98</sup>

Interestingly, the presence of the  $\text{CF}_3$  group of  $\alpha,\alpha,\alpha$ -trifluorotoluene does not induce the same *ortho*-directing effect.<sup>98</sup> Instead, activation is only observed *meta*- and *para*- to the  $\text{CF}_3$  group, with the major isomer being *meta*-. The fluorine atoms being removed from the  $\pi$ -system leads to a reverse in the selectivity that has been observed, with traditional steric and electronic effects dominating the activation.

Also shown in Figure 43, hexafluorobenzene initially coordinates  $\eta^2$ - to the Rh centre. Further irradiation of the complex causes oxidative addition of a highly stable C-F bond.<sup>99</sup> The C-H activation of fluorobenzenes by metal centres has been widely studied, with examples of C-H activation on several metals such as Rh, Ir, and Pt.

The C-H activation can be utilised for further reactivity such as with boronic acids in borylation reactions and cross-coupling.<sup>100, 101</sup> In both borylation and cross-coupling reactions, a strong *ortho*-directing effect is observed with fluorine compared to other

substituted benzenes. The *ortho*- effect is in competition with steric effects and kinetics of binding.

The *ortho*- effect can be clearly observed in the C-H activation of *ortho*-disubstituted benzenes by  $[\text{Ir}(\eta^5\text{-C}_5\text{Me}_5)(\text{Me})(\text{OTf})(\text{PMe}_3)]$  [45].<sup>102</sup> When *o*-dichlorobenzene and *o*-xylene undergo C-H activation the Ir-C bond is formed at the 4- position forming [46]. However, with *o*-difluorobenzene C-H activation occurs at both the 3- and 4-positions forming complexes [46] and [47]. This may be associated with the small size of the F atom providing less repulsion being in proximity of the metal, or the formation of a stronger M-C bond. This is summarized in Figure 44.

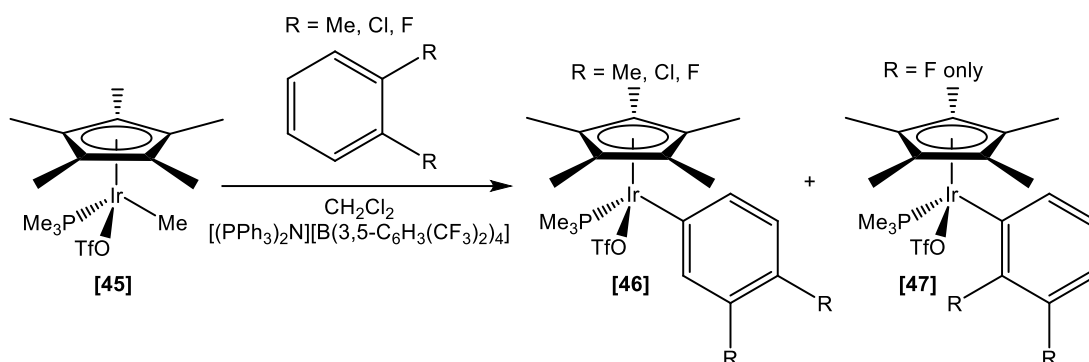


Figure 44. C-H activation of [45], forming [46] and [47]. [47] is only observed when *o*-difluorobenzene is used.<sup>102</sup>

A combination of DFT calculations and experimental work on the activation of C-H bonds of fluorobenzenes has shown that there is a correlation between the strength of the C-H bonds being broken and the C-M bonds being formed.<sup>103</sup> C-H bonds become stronger when *ortho*- to one or two C-F bonds. However, the strength of the M-C bond that is formed outweighs the increasing strength of C-H bonding. With the barrier to reductive elimination *ortho*- to 1 C-F bond being  $8 \text{ kJ mol}^{-1}$  stronger than not next to fluorine and activation *ortho*- to two C-F bonds being a further  $5 \text{ kJ mol}^{-1}$  stronger.<sup>104</sup> It was found that this effect is independent of the number of fluorine substituents.<sup>105</sup>

### 3.1.5 Stable fluoro-vinylidene and -alkynyl complexes

Metal complexes containing C-F bonds can be synthesised by the C-H or C-F activation of a fluorine containing organic molecule such as fluorobenzene. Another route to fluorine containing organometallic complexes is by reacting an organometallic with a fluorine source. Electrophilic sources of fluorine, "F<sup>+</sup>", are typically solid at room temperature, as well as being air and water stable.<sup>106</sup> The commercial availability of a range of electrophilic sources of fluorine has allowed for the synthesis of fluorinated molecules to move away from the use of fluorine gas (F<sub>2(g)</sub>), hydrogen fluoride (HF), and fluorine salts (F<sup>-</sup>) such as caesium fluoride (CsF). N-F "F<sup>+</sup>" sources can be synthesised from F<sub>2</sub> and the corresponding N compounds on a commercial scale without need for F<sub>2</sub> in the synthesis of fine chemicals.<sup>107</sup> Some examples of commonly available "F<sup>+</sup>" sources are shown in Figure 45, N-fluoro-2,4,6-trimethylpyridinium tetrafluoroborate (FTMP) **[48]**BF<sub>4</sub>,<sup>108</sup> N-fluorobenzenesulfonimide (NFSI) **[49]**,<sup>109</sup> and 1-Chloromethyl-4-fluoro-1,4-diazoniabicyclo[2.2.2]octane bis(tetrafluoroborate) (Selectfluor<sup>TM</sup>) **[50]**[BF<sub>4</sub>]<sub>2</sub>.<sup>110</sup>

Electrophilic fluorinating reagents have been used in the formation of fluorocarbene **[52]**X, fluorovinylidene **[3]**X, and fluoroalkynyl **[7]**' complexes of ruthenium from vinyl **[51]**, alkynyl **[1]** **[4]**' complexes by Slattery and Lynam.<sup>111-114</sup> This is also shown in Figure 45.

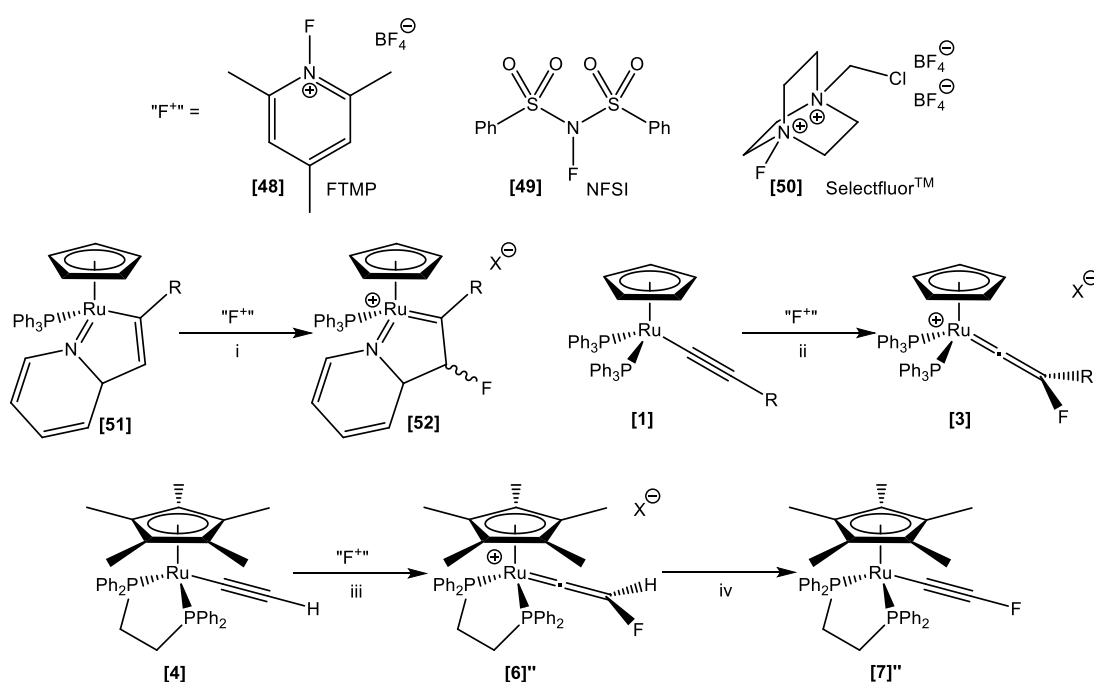


Figure 45. Outer-sphere electrophilic fluorination of ruthenium organometallics in the synthesis of fluorinated organometallic complexes. i.  $\text{CH}_2\text{Cl}_2$ , 20 °C, 16 h. ii.  $\text{CH}_2\text{Cl}_2$ , 20 °C, 1 h. iii. Toluene, -78 °C  $\rightarrow$  RT. iv. THF,  $\text{LiN}(\text{SiMe}_3)_2$ , -78 °C  $\rightarrow$  RT.<sup>111-114</sup>

The  $\text{C}_\beta$  of unsaturated ruthenium organometallic species is electron rich and reacts with electrophiles such as "F<sup>+</sup>". Fluorination at  $\text{C}_\beta$  has been shown to proceed without initial fluorination at ruthenium.<sup>112</sup> The fluorination takes place in the outer coordination sphere of the metal and is referred to as outer-sphere electrophilic fluorination (OSEF). The  $\text{C}_\alpha$  of fluorovinylidene and fluoroalkynyl complexes present unusual values of chemical shift compared to non-fluorinated equivalents.<sup>112-114</sup> The chemical shifts are displayed in Figure 46.

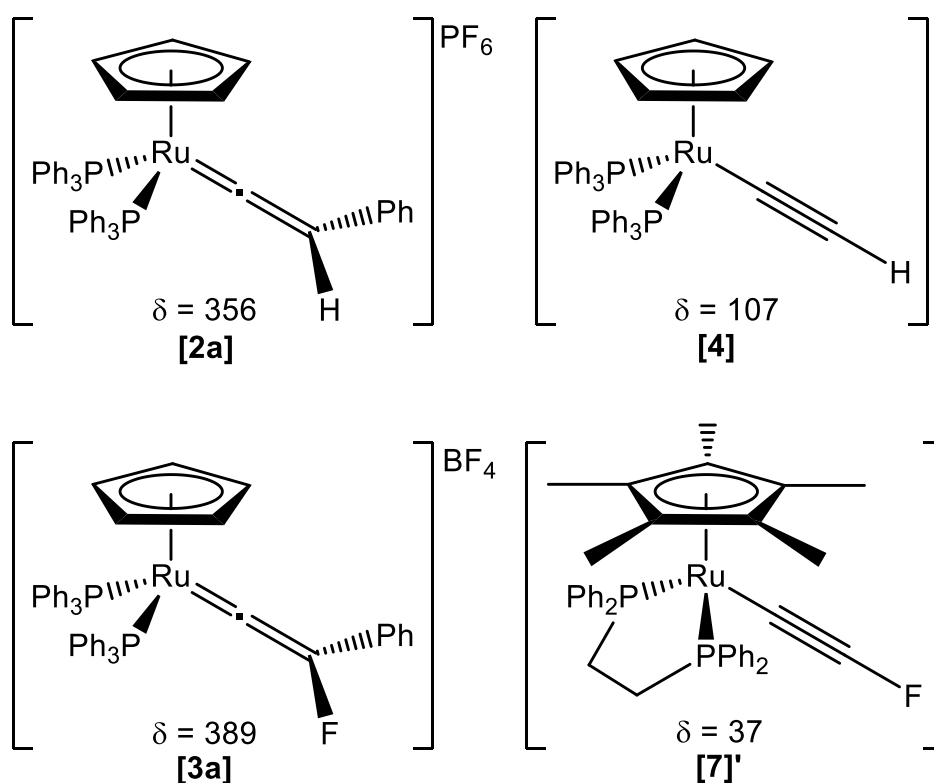


Figure 46. Fluorovinylidene (Bottom left) and fluoroalkynyl (Bottom right) complexes show significant changes to deshielding at  $\text{C}_\alpha$  compared to proteo-equivalents (Top).<sup>115</sup>

The chemical shift of  $\text{C}_\alpha$  for **[3a]** $\text{PF}_6$  is shifted significantly becoming more deshielded by > 30 ppm ( $\delta_{\text{C}} = 389$ ) compared to that of **[2a]** $\text{BF}_4$  ( $\delta_{\text{C}} = 356$ ).<sup>112</sup> Vinylidene  $\text{C}_\alpha$  are already highly deshielded environments,<sup>116</sup> but this increases when fluorine is

incorporated into the vinylidene moiety. The level of deshielding is very large considering the proximity of the fluorine from  $C_{\alpha}$ . As it is a  $^{13}\text{C}$  nuclei, the value of  $\delta^{\text{dia}}$  will not dictate the total deshielding. Changes to  $\delta^{\text{para}}$  will influence deshielding to a greater extent.

The chemical shift of  $C_{\alpha}$  of **[7]'** is  $\delta_{\text{C}} = 37$ , highly deshielded compared to **[4]** ( $\delta_{\text{C}} = 107$ ).<sup>115</sup> Changes to the chemical shift of  $^{13}\text{C}$  environments are not dictated by changes in electron density at the nucleus ( $\delta^{\text{dia}}$ ), but are dictated by changes to  $\delta^{\text{para}}$ . The unusual  $^{13}\text{C}$  chemical shift values of these metal complexes suggest that distinctive changes are occurring to the FMO structures of the complexes. The chemical shift is a representation of changes to bonding structure and energy, which must be attributed to the inclusion of fluorine.

Fluoroalkynyl and fluorovinylidene complexes could be synthetically relevant as building blocks in the synthesis of novel fluorinated organic molecules. A better understanding of the FMO structure could be used to predict and understand reactivity.

Complex **[7]'** is a bench stable molecule containing an sp C-F bond. Stable 1-fluoroalkynes are poorly represented in the literature. Fluoroethyne **[53]** and difluoroethyne **[54]** compounds are both formed by pyrolysis reactions. Compound **[53]** is formed from the pyrolysis of maleic anhydride **[55]**, **[54]** is formed from the pyrolysis of triazine **[56]**.<sup>117, 118</sup> This is shown in Figure 47. Compounds **[53]** and **[54]** are being susceptible to degradation at reduced temperatures. This degradation is by cyclotrimerization to form **[57]** in the case of **[53]**, or polymerisation in the case of **[54]**.

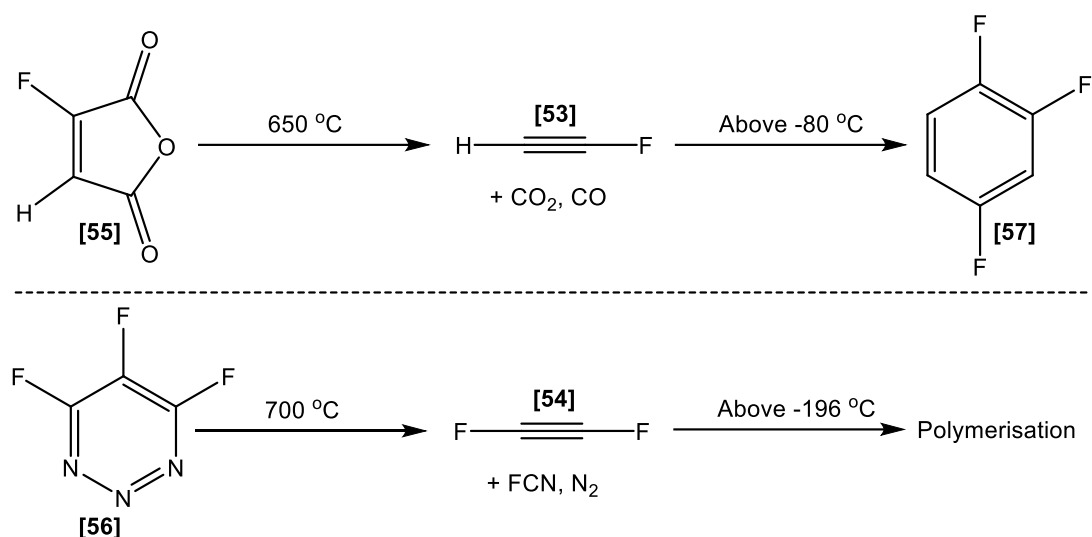


Figure 47. (Top) Synthesis of fluoroethyne, [53], and (Bottom) difluoroethyne, [54], by pyrolysis. Degradation of the fluoroalkyne occurs even at low temperatures.<sup>117, 118</sup>

Some other fluoroalkynes that have been synthesised are perfluoropropyne,<sup>119</sup> 1-fluoro-3,3-dimethylbut-1-yne,<sup>120, 121</sup> and 1-chloro-2-fluoroethyne.<sup>122</sup> Higher substitution of the alkyne leads to stabilisation of the molecule, but degradation and trimerization reactions still occur below room temperature. The fluoroalkynes show enhanced stability in the gas phase.

### 3.1.6 Aims

In this chapter, differences in chemical shift that arise after fluorination of organometallic species, specifically the effect on the vinylidene and alkynyl moieties, have been explored. SS NMR spectra have been recorded for a series of ruthenium alkynyl and vinylidene complexes. The chemical shift anisotropy is recovered from SS NMR spectra that have been recorded at low MAS speeds. The experimental chemical shift tensors have been compared to and used alongside quantum chemical calculation using DFT to explain differences in the frontier molecular orbital structure between fluorinated and non-fluorinated organometallic species, with particular focus on the effect on the metal bound C<sub>α</sub>. As well as focusing on the effect of fluorine on organometallic complexes, chemical shift anisotropy has been used to explore and

explain the role of the metal in these complexes compared to uncoordinated, metal-free species.

## 3.2 Synthesis and characterisation of complexes

Metal vinylidene complexes are well known in the literature. Ruthenium vinylidene complexes are typically synthesized following the preparation laid out by Bruce, which is shown in Figure 48.<sup>123</sup> Heating the ruthenium half-sandwich complex **[35]** in an alcohol solvent in the presence of a chloride-abstraction agent and a terminal alkyne leads to the formation of the desired vinylidene. Reactions were typically performed for 30 minutes as prolonged heating leads to the formation of alkoxycarbene complexes **[58]**PF<sub>6</sub>, which result from nucleophilic attack at the metal-bound carbon atom by the solvent.<sup>124</sup>

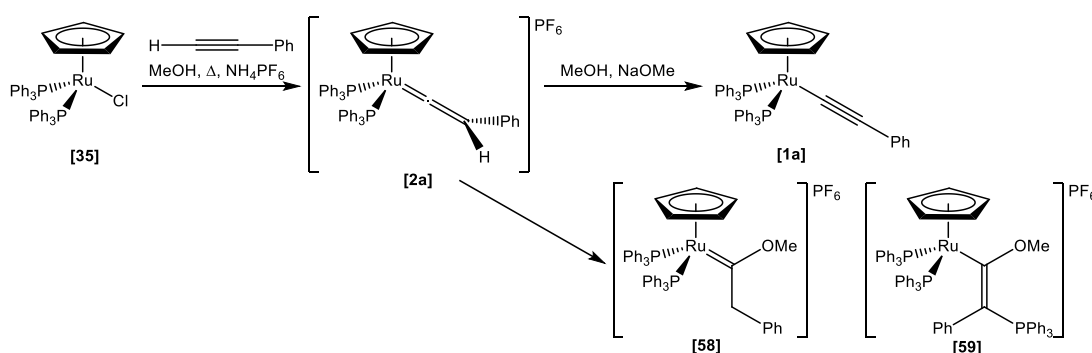


Figure 48. Formation of ruthenium alkynyl complex, overreaction of the intermediate vinylidene leads to carbene **[58]**<sup>+</sup> and phosphinovinyl **[59]**<sup>+</sup> species.<sup>125</sup>

Prolonged heating of complex **[2a]**PF<sub>6</sub> can cause additional side-reactions, which result from phosphine ligand dissociation. The dissociated phosphine can react with carbene **[58]**<sup>+</sup> to form phosphonium alkoxyvinyl complexes **[59]**PF<sub>6</sub>.<sup>125</sup> Because of the need in this project for high quality, solid, crystalline material, another method must be considered that avoids unnecessary contamination and any prolonged heating.

The preparation by Noppers and Low provides a modified route to the vinylidene with reduced contamination.<sup>126</sup> As shown in Figure 49, this method replaces elevated temperature by long reaction times at room temperature. At room temperature, the addition of the methanol solvent to the vinylidene to form **[58]**Cl is restricted. The formation of **[2a]**Cl was slow, but purity outweighs the need for speed in this case. Deprotonation by an organic base ensures that crystalline alkynyl complexes such as **[1a]** can be recovered with no contamination.

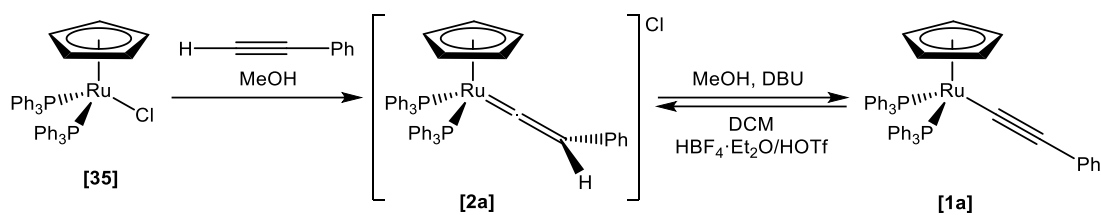


Figure 49. Formation of ruthenium alkynyl complex without heat or chloride abstraction agent using an organic base 1,8-diazobicyclo[5.4.0]undec-7-ene ( $\text{DBU}$ ). **[2a]** $\text{BF}_4$  can be formed by reacting **[1a]** with an acid in  $\text{DCM}$ .<sup>126</sup>

This preparation is typically performed on small scales (100 mg of **[35]**),<sup>126</sup> so it has been scaled up to half gram scale for the synthesis in this thesis. The limiting factor in production of the alkynyl complex was the formation of the vinylidene chloride salt **[2a]** $\text{Cl}$  in methanol. When smaller volumes of solvent were used, large masses of unreacted **[35]** was recovered after filtration of the reaction mixture before deprotonation. Increased solvent volumes pushed the reaction closer to completion and less starting material remained after filtration.

Large solvent volumes and an excess of terminal alkyne helped to drive the consumption of starting material and pure crystalline alkynyl complexes were observed in very high yields of over 90 %. The corresponding vinylidene complex was formed quickly and cleanly by dissolving the alkynyl complex in dichloromethane and adding tetrafluoroboric or trifluoromethanesulfonic acid dropwise with rapid stirring. An immediate change in colour from yellow to cherry red was observed consistent with the vinylidene complex **[2a]**<sup>+</sup> being formed in solution. The choice of acid used determined the nature of the counter-ion of the vinylidene complex. Typically, trifluoromethanesulfonic acid or tetrafluoroboric acid etherate were employed as the reaction has a high atom economy and the products were readily purified. As well as the change in colour, the isolated product showed the diagnostic appearance of the vinylidene proton in the  $^1\text{H}$  NMR spectra, as well as a shift in the  $\text{Cp } ^1\text{H}$  and  $\text{PPh}_3 \text{ } ^{31}\text{P}$  resonances consistent with a change in charge of the complex shown in Figure 50. The assignment of the resonances is described further in section 3.2.1. The product **[2a]** $\text{BF}_4$  was isolated as crystals by slow diffusion of either diethylether or pentane into a dichloromethane solution of the complex.

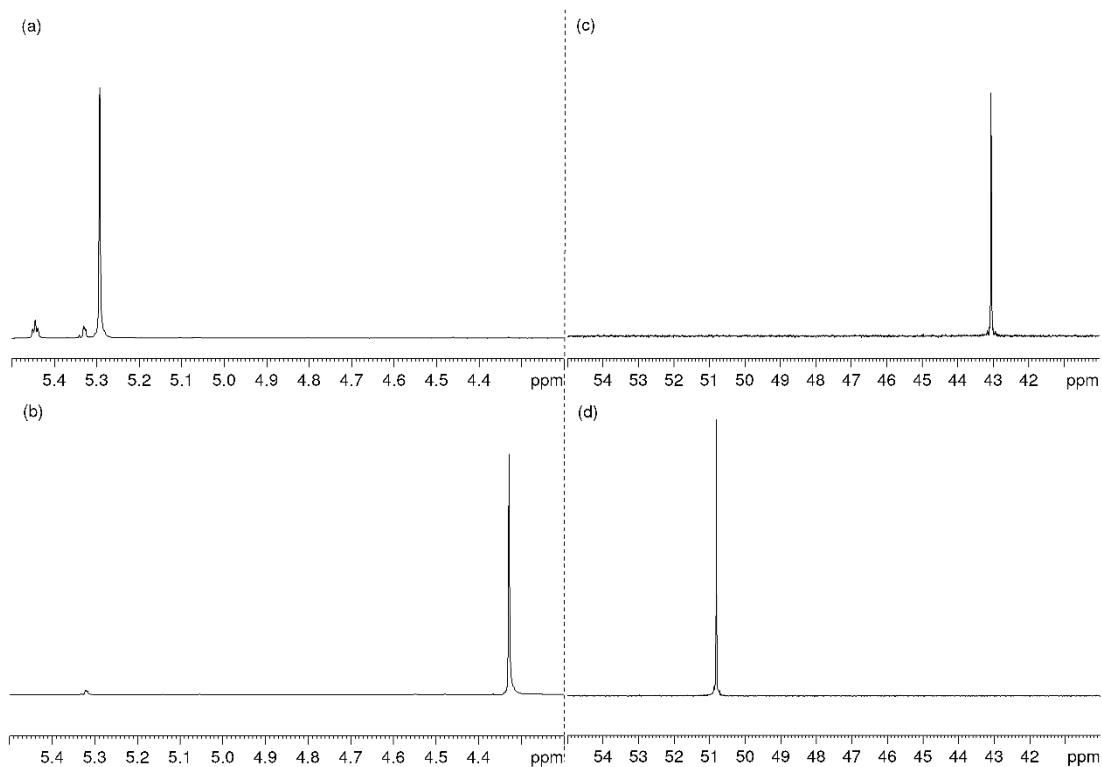
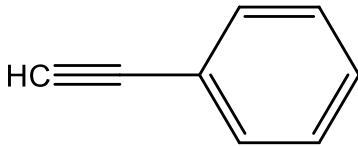
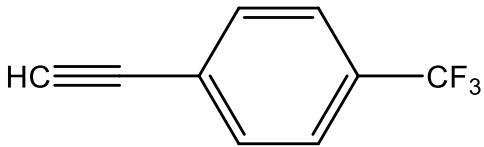
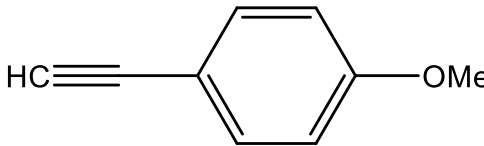
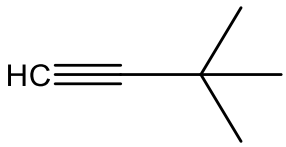


Figure 50.  $^1\text{H}$  NMR spectra recorded at 400 MHz of the vinylidene and Cp region of **[2a]**BF<sub>4</sub>, (a), recorded after addition of tetrafluoroboric acid etherate to **[1a]**, (b). The diagnostic vinylidene proton resonance is observed after protonation at  $\delta_{\text{H}} = 5.44$ .  $^{31}\text{P}\{^1\text{H}\}$  NMR spectra recorded at 162 MHz of **[2a]**BF<sub>4</sub>, (c), and **[1a]**, (d). All spectra recorded in *d*<sub>2</sub>-dichloromethane.

This modified preparation allowed the formation of both ruthenium alkynyl and vinylidene complexes in high yield, purity, and crystallinity, which are important factors in the subsequent study by SS NMR spectroscopy.

Table 11. Yields of alkynyl, vinylidene, and fluorovinylidene synthesis recovered as crystalline material.

Alkyne Used	% Yield Alkynyl Complex	% Yield Vinylidene Complex	% Yield Fluorovinylidene Complex
	80	71	70
	92	79	74
	90	79	72
	63	84	81

### 3.2.1 Characterisation of [1d], [2d]OTf, and [3d]PF<sub>6</sub>

Examples of the characterisation of an alkynyl ([1d]), vinylidene ([2d]OTf), and fluorovinylidene ([3d]PF<sub>6</sub>) complex using solution state NMR spectroscopy are described below

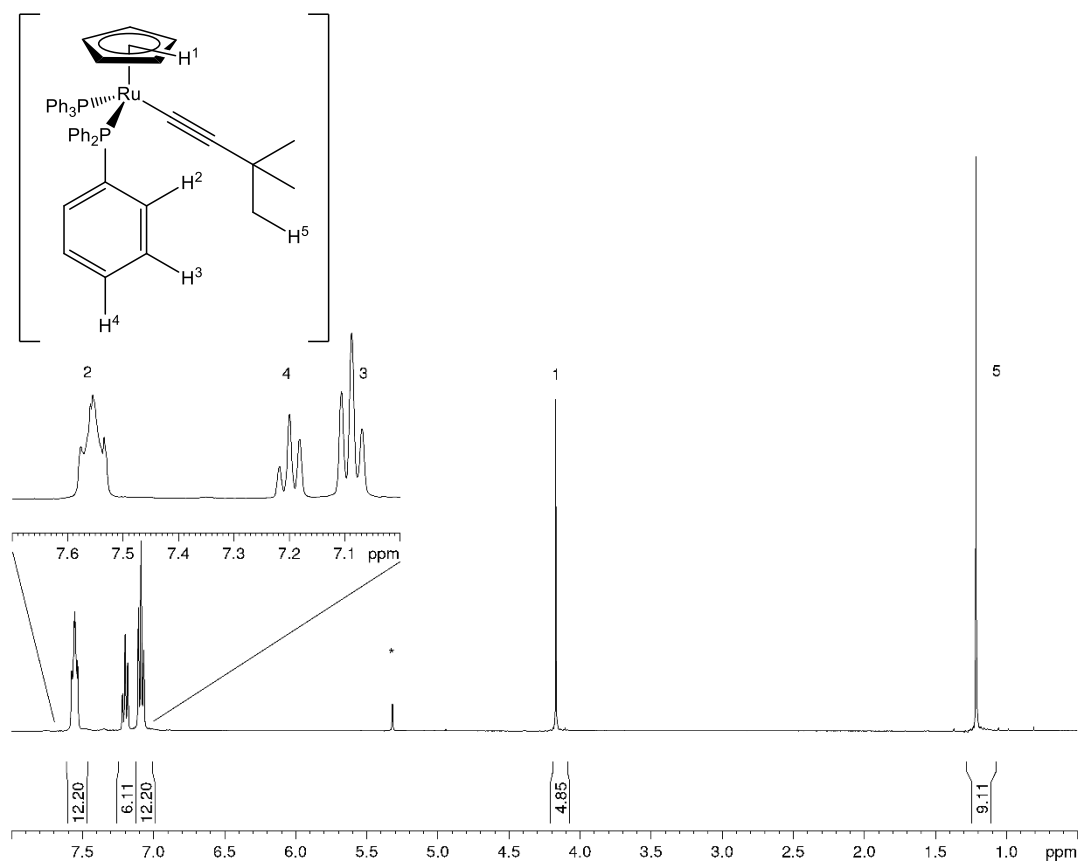


Figure 51.  $^1\text{H}$  NMR Spectrum of complex **[1d]** recorded at 400 MHz. The spectrum was recorded in  $d_2$ -dichloromethane, the residual  $d_1$ -dichloromethane was referenced to  $\delta_{\text{H}} = 5.32$  and is denoted by \*.

The  $^1\text{H}$  NMR spectrum of **[1d]** recorded in  $d_2$ -dichloromethane is shown in Figure 51. The Cp protons,  $\text{H}^1$ , are clearly observed as a sharp singlet resonance at  $\delta_{\text{H}} = 4.14$  with an integration of 5H. Rapid rotation of the Cp ring in solution leads to an isotropic resonance with no observed couplings to other environments. The *tert*-butyl protons,  $\text{H}^5$ , are also observed as a sharp singlet resonance with an integration of 9H at  $\delta_{\text{H}} = 1.19$ .

The aromatic resonances of the  $\text{PPh}_3$  ligands are observed as three resonances between  $\delta_{\text{H}} = 7.00 - 7.60$ . Rotation of the ligands leads to the three distinct  $^1\text{H}$  environments,  $\text{H}^2$ ,  $\text{H}^3$ , and  $\text{H}^4$ , corresponding to the *ortho*-, *meta*-, and *para*- positions of the phenyl rings. The *ortho*-proton,  $\text{H}^2$ , would exhibit coupling to  $\text{H}^3$  and to the nearby  $^{31}\text{P}$  nucleus.  $\text{H}_2$  was identified as the multiplet resonance at  $\delta_{\text{H}} = 7.56$  with an integration of 12H. The  $^3J_{\text{H-P}}$  interaction broadens the doublet into the multiplet

shape observed. H<sup>3</sup> was identified as the resonance at  $\delta_{\text{H}} = 7.09$ , also having an integration of 12H and exhibiting  $^3J_{\text{H-H}}$  coupling interactions to H<sup>2</sup> and H<sup>4</sup>, appearing as an apparent triplet. H<sup>4</sup> was identified as the final aromatic resonance at  $\delta_{\text{H}} = 7.20$ , having an integration of 6H and showing a true  $^3J_{\text{H-H}}$  triplet coupling to H<sup>3</sup>.

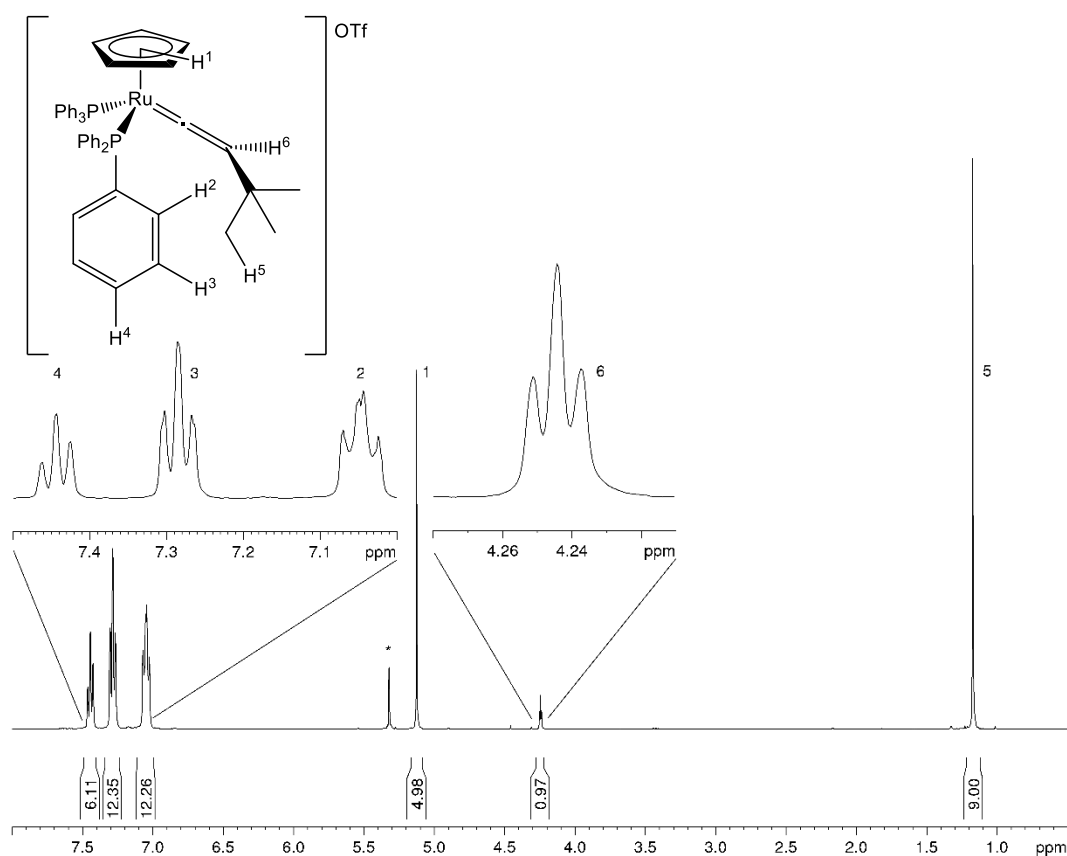


Figure 52. <sup>1</sup>H NMR Spectrum of complex **[2d]**OTf recorded at 400 MHz. The spectrum was recorded in *d*<sub>2</sub>-dichloromethane, the residual *d*<sub>1</sub>-dichloromethane was referenced to  $\delta_{\text{H}} = 5.32$  and is denoted by \*.

The <sup>1</sup>H NMR spectrum of a typical vinylidene complex, **[2d]**OTf, recorded in *d*<sub>2</sub>-dichloromethane solution is shown in Figure 52. As with **[1d]**, the Cp protons, H<sup>1</sup>, are clearly observed as a sharp singlet resonance with an integration of 5H. On protonation of **[1d]**, the H<sup>1</sup> environment becomes more deshielded, shifting from  $\delta_{\text{H}} = 4.14$  in **[1d]** to  $\delta_{\text{H}} = 5.12$  in **[2d]**OTf. This would be in line with the complex becoming cationic and more electron withdrawing from the ring environment.

The vinylidene proton H<sup>6</sup> is observed as a triplet resonance with an integration of 1H at  $\delta_{\text{H}} = 4.24$ . A small coupling to two other nuclei leads to the splitting of H<sup>6</sup> into a binomial triplet. This small coupling constant ( ${}^4J_{\text{H-P}} = 2.8$  Hz) is consistent with a long-range interaction between H<sup>6</sup> and the  $I = 1/2$  <sup>31</sup>P nuclei in the two PPh<sub>3</sub> ligands bound to the metal.

The *tert*-butyl protons H<sup>5</sup> of this complex are observed as a sharp, shielded singlet resonance at  $\delta_{\text{H}} = 1.17$ . The resonance could be easily identified as the only aliphatic resonance in the spectrum, possessing an integration of 9H. Free rotation of the *tert*-butyl group leads to a single isotropic resonance in solution.

The aromatic resonances of the phosphine ligands are observed between  $\delta_{\text{H}} = 7.00 - 7.50$ . Three distinct environments are observed, associated with the *ortho*-, *meta*-, and *para*-substituted positions of the ring. The *para*-proton H<sup>4</sup> was clearly identified as the only aromatic resonance with an integration of 6H at  $\delta_{\text{H}} = 7.45$ , exhibiting  ${}^3J_{\text{H-H}}$  triplet coupling to H<sup>3</sup>. The expected coupling to two H<sup>3</sup> protons is observed in the triplet. The *ortho*- (H<sup>2</sup>) and *meta*- (H<sup>3</sup>) positions would be expected as a doublet of doublet and doublet of triplet resonances respectively with integrations of 12H. As the resonance at  $\delta_{\text{H}} = 7.29$  is observed as a triplet with a small doublet coupling to <sup>31</sup>P, it was identified as H<sub>3</sub> leaving  $\delta_{\text{H}} = 7.05$  as H<sup>2</sup>.

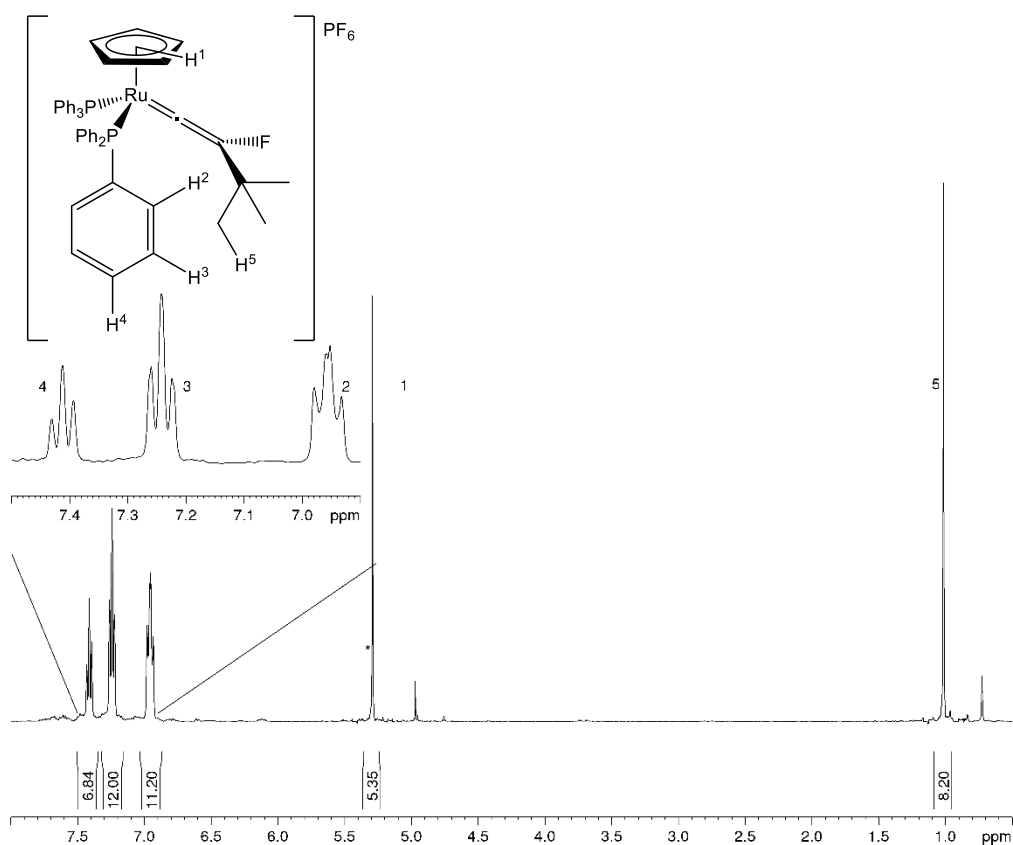


Figure 53.  $^1\text{H}$  NMR Spectrum of **[3d]**PF<sub>6</sub> recorded at 400 MHz. The spectrum was recorded in *d*<sub>2</sub>-dichloromethane. Residual *d*<sub>1</sub>-dichloromethane resonance obscured with the Cp resonance and is denoted by \*.

The assignment of the aromatic resonances in complexes **[2d]**OTf and **[3d]**PF<sub>6</sub> was performed based on multiplicity and integration. However, this assignment can be improved with  $^1\text{H}\{^{31}\text{P}\}$  experiments performed on a sample of **[3d]**PF<sub>6</sub>, shown in Figure 54. On decoupling from phosphorus, the most shielded aromatic multiplet resonance becomes a clear doublet resonance with  $^3J_{\text{H-H}} = 8$  Hz. This coupling constant matches both the other aromatic resonances. On decoupling from phosphorus, two resonances change multiplicity,  $\delta_{\text{H}} = 6.99$  and  $\delta_{\text{H}} = 7.27$  and the magnitude of the change is different. As the resonance at  $\delta_{\text{H}} = 6.99$  appears to be a triplet when coupled to phosphorus, the coupling constant must be around the same magnitude as the coupling to  $\delta_{\text{H}} = 7.27$ ,  $^3J_{\text{H-P}} \approx 8$  Hz. The much larger coupling to phosphorus would be observed for H<sub>2</sub> as the coupling constant decreases with

increasing number of bonds between the spins. This confirms the assignment of H<sup>2</sup> ( $\delta_{\text{H}} = 6.99$ ) and H<sup>3</sup> ( $\delta_{\text{H}} = 7.27$ ) in the vinylidene and fluorovinylidene proton spectra.

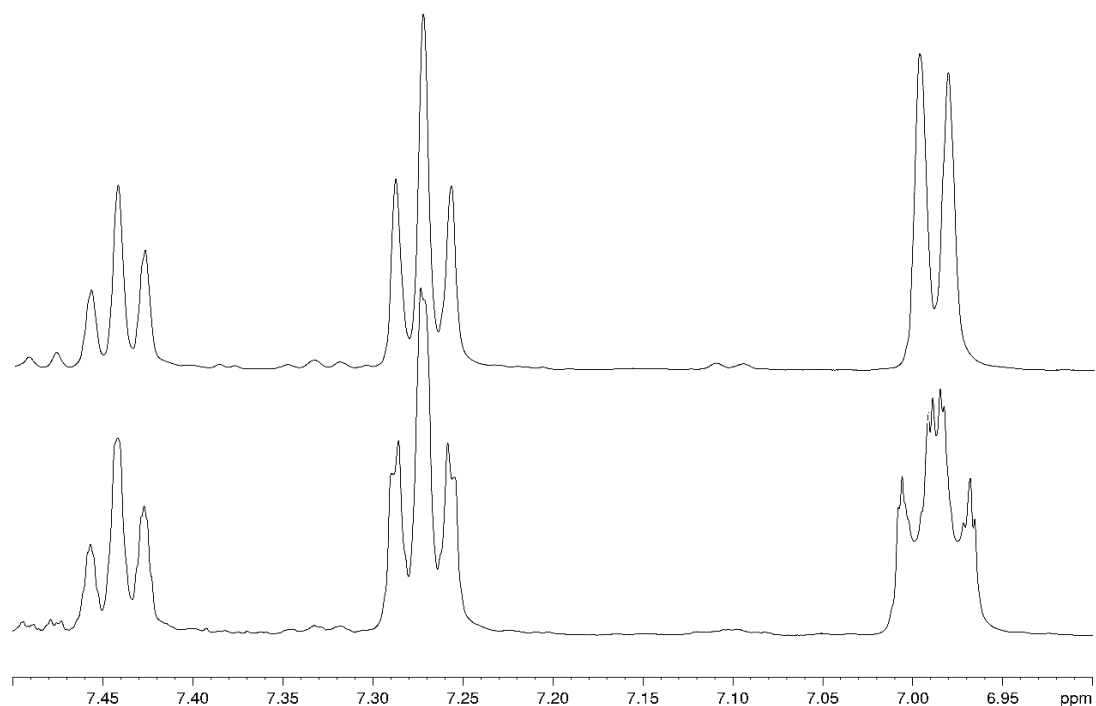


Figure 54.  $^1\text{H}\{^{31}\text{P}\}$  NMR spectrum of the aromatic resonances of complex **[3d]**PF<sub>6</sub> in *d*<sub>2</sub>-dichloromethane (Top) and  $^1\text{H}$  NMR spectrum of the aromatic resonances of **[3d]**PF<sub>6</sub> in *d*<sub>2</sub>-dichloromethane (Bottom) recorded at 500 MHz. Coupling to phosphorus is observed in the *ortho*- and *meta*-positions.

The related fluorovinylidene complex **[3d]**PF<sub>6</sub> shows NMR spectroscopic data that is comparable with **[2d]**OTf and is displayed in Figure 53. The  $^1\text{H}$  spectra of both compounds show the presence of analogous resonances that could be identified the same way as above. One major difference in the  $^1\text{H}$  spectrum in **[3d]**PF<sub>6</sub> is the lack of the vinylidene triplet resonance (H<sup>6</sup>). Small changes in chemical shift were observed for the *tert*-butyl and PPh<sub>3</sub> proton environments. The magnitude of this change is low as these environments are relatively electronically separated from the changing vinylidene. The resonance that has changed most notably is the Cp protons H<sup>1</sup>. The H<sup>1</sup> resonance has been deshielded to the point that it now overlaps with the residual *d*<sub>1</sub>-dichloromethane resonance.

A key piece of spectroscopic data was the identification of complex **[3d]**PF<sub>6</sub> by  $^{19}\text{F}$  NMR, (Figure 55). The hexafluorophosphate anion was observed as the expected

doublet resonance at  $\delta_F = -74$  with  $^1J_{P-F} = 711$  Hz.<sup>112</sup> This coupling matches the septet observed in the  $^{31}\text{P}\{^1\text{H}\}$  spectra. The other key resonance that appears after fluorination was the fluorovinylidene singlet at  $\delta_F = -216$ . This is in line with literature values for a fluorovinylidene resonance.<sup>112</sup>

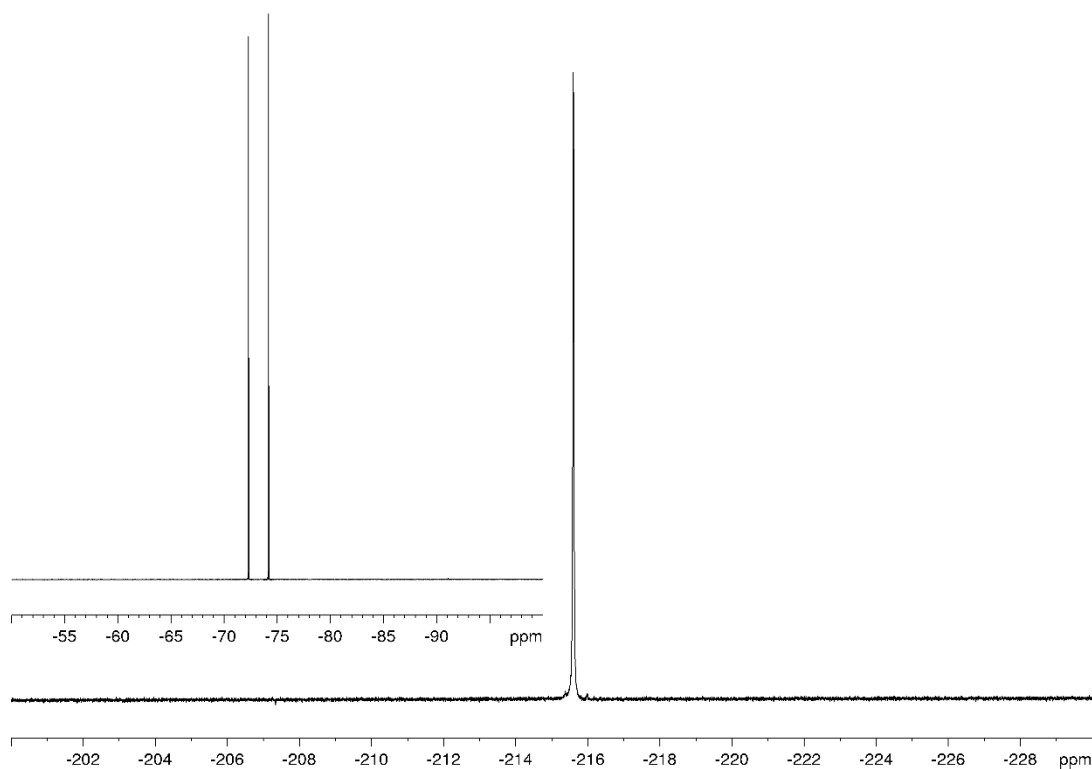


Figure 55.  $^{19}\text{F}$  spectra of **[3d]**PF<sub>6</sub> recorded in d<sub>2</sub>-dichloromethane at 376 MHz showing the fluorovinylidene resonance at  $\delta_F = -216$ .

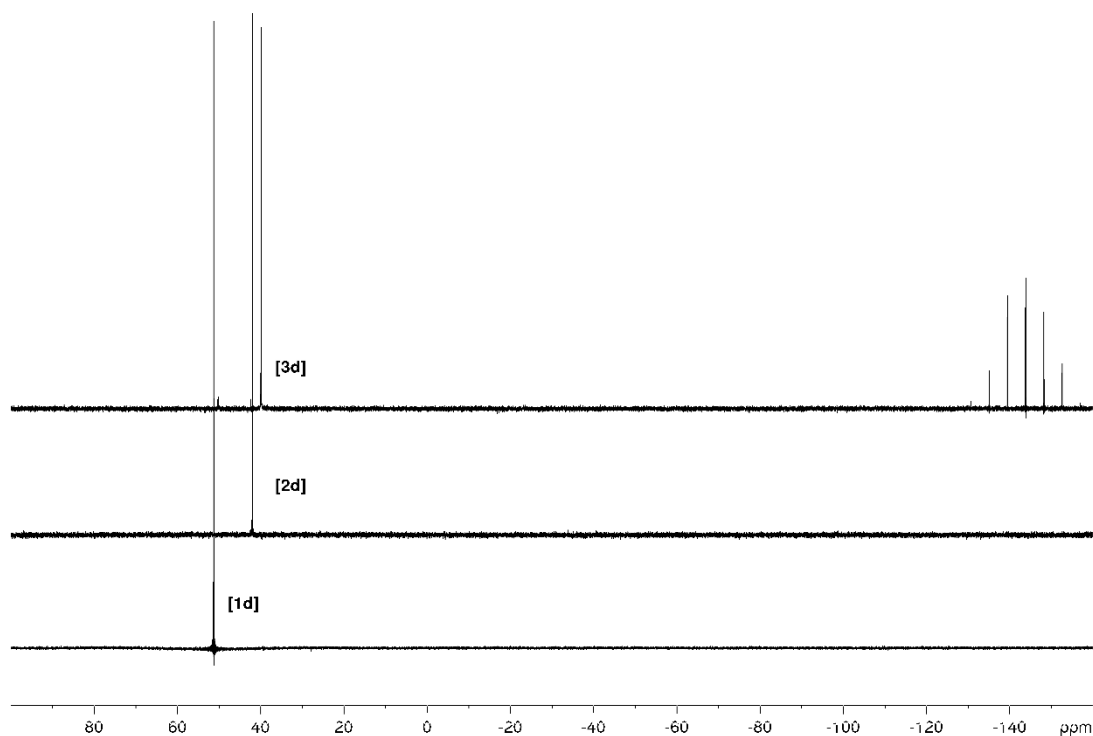


Figure 56.  $^{31}\text{P}\{^1\text{H}\}$  NMR spectra of **[1d]** (Bottom), **[2d]OTf** (Middle), and **[3d]PF<sub>6</sub>** (Top) recorded at 162 MHz in  $d_2$ -dichloromethane.

The  $^{31}\text{P}\{^1\text{H}\}$  experiments of **[1d]**, **[2d]OTf**, and **[3d]PF<sub>6</sub>** showed the presence of a single resonance for the coordinated  $\text{PPh}_3$  ligands at  $\delta_{\text{P}} = 51.2$  (**[1d]**),  $\delta_{\text{P}} = 42.0$  (**[2d]OTf**), and  $\delta_{\text{P}} = 39.9$  (**[3d]PF<sub>6</sub>**) shown in Figure 56. In the case of **[3d]PF<sub>6</sub>**, the hexafluorophosphate anion was observed as a binomial septet at  $\delta_{\text{P}} = -143.9$  with  $^1J_{\text{P-F}} = 711$  Hz. Complexes **[2d]OTf** and **[3d]PF<sub>6</sub>** exhibit asymmetry along the vinylidene bond, meaning each phosphorus should have a unique environment. This is not observed due to the rotation of the vinylidene bond at room temperature being faster than the NMR experiment timescale. The  $^{19}\text{F}$  NMR spectrum of **[3d]PF<sub>6</sub>** showed a diagnostic fluorovinylidene resonance at  $\delta_{\text{F}} = -215.6$ .

A different set of ruthenium(II) vinylidene and alkynyl complexes were identified for synthesis, based on the  $[\text{RuCl}(\text{dppe})_2]^+$  fragment. The *trans*-alkynyl and *trans*-vinylidene complexes **[1a]'**, **[2a]'**OTf, **[3a]'**PF<sub>6</sub>, **[4]'**, **[5]'**OTf, **[6]'**PF<sub>6</sub>, and **[7]'** were identified by  $^1\text{H}$ ,  $^{19}\text{F}$ , and  $^{31}\text{P}$  NMR spectroscopy. The complexes spectroscopic data matched the literature and their synthesis is described in Chapter 5.<sup>115</sup>

To aid in the characterisation of alkynyl and vinylidene complexes, electrospray ionisation (ESI) mass-spectrometry (MS) was also performed. Diagnostic  $m/z$  peaks for  $[2d]^+$  and  $[3d]^+$  were observed directly. In samples of  $[1d]$ , the  $m/z$  peak for  $[1d+H]^+$  was observed. This is the same as  $[2d]^+$  but the intensity of the signal is much lower for the alkynyl sample than the vinylidene due to the need for the ionisation of  $[1d]$ . This trend is matched in other vinylidene and alkynyl complexes.

### 3.3 Recording of Solid-state NMR spectra of complexes [1a] – [10]PF<sub>6</sub>

Solid-state NMR spectra were recorded for a range of ruthenium complexes shown in Figure 57. An example of the characterisation of the SS NMR spectra obtained is described in sections 3.3.1 – 3.3.3.

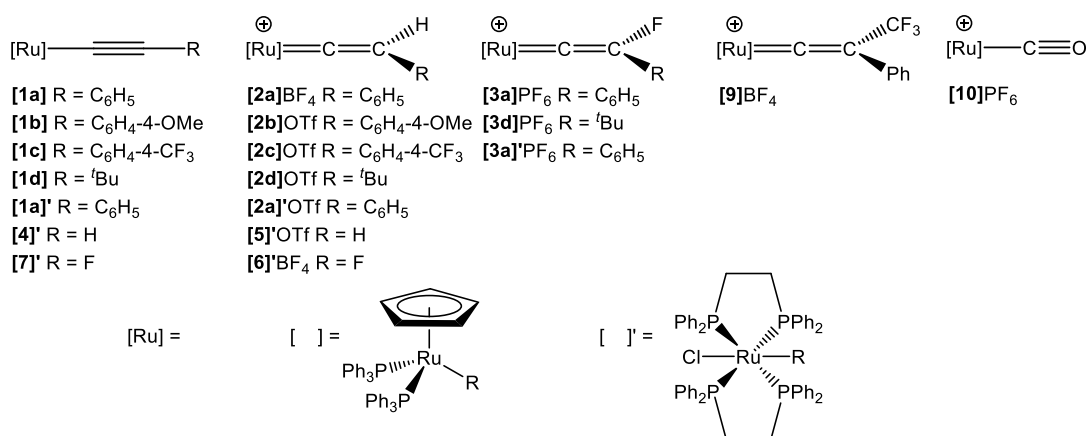


Figure 57. Ruthenium organometallic complexes studied by SS NMR spectroscopy

#### 3.3.1 Example of SS characterisation of <sup>13</sup>C{<sup>1</sup>H} CP MAS spectra, showing <sup>13</sup>C{<sup>1</sup>H} CP MAS spectra of [2a]BF<sub>4</sub>·Et<sub>2</sub>O

Although solution phase spectra of  $[1] - [10]$  are available in the literature, the values of the chemical shift tensors are not known. Before chemical shift tensors can be compared and interpreted, first, high resolution SS NMR spectra of each class of compound needed to be recorded. As there were no details in the literature for the SS NMR of any of the complexes that have been synthesized, new spectra had to

be recorded. This was achieved using the basic methodology that was developed in chapter 2. After grinding crystalline material of each sample, SS NMR could be recorded. The effect of crystallinity is discussed in section 3.3.4.

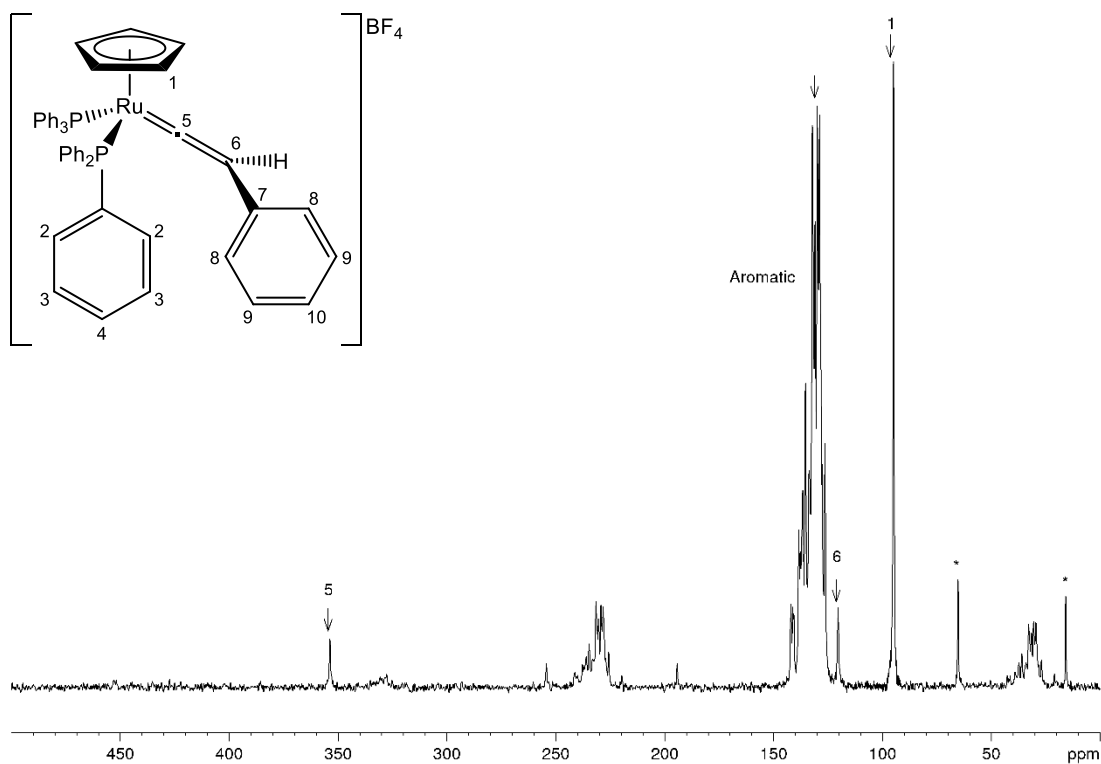


Figure 58.  $^{13}\text{C}\{^1\text{H}\}$  CP MAS SS NMR spectra of **[2a]** $\text{BF}_4 \cdot \text{Et}_2\text{O}$  recorded at 101 MHz at a spinning speed of 10 kHz. Isotropic resonances are denoted by an arrow. Resonance associated with the ether of crystallisation are denoted by asterisks (\*).

Table 12. Comparison of solid and solution phase  $^{13}\text{C}$  resonances of **[2a]X**. Solid-phase resonances recorded at 101 MHz at 10 kHz on a sample of **[2a]BF<sub>4</sub>**. Literature solution-phase resonances of **[2a]PF<sub>6</sub>** recorded at 123 MHz in *d*<sub>1</sub>-chloroform.<sup>123</sup>

$\text{C}_x$	$\delta_c$ (Solid) / ppm	$\delta_c$ (Solution) / ppm
$\text{C}_1$	95	95
$\text{C}_5$	354	356
$\text{C}_6$	120	120
$\text{C}_{\text{Aromatic}}$	125 – 143	127 – 135

A  $^{13}\text{C}\{^1\text{H}\}$  CP MAS spectrum of **[2a]BF<sub>4</sub>** is shown in Figure 58. The solid  $^{13}\text{C}\{^1\text{H}\}$  spectrum matches the literature solution-phase spectrum well, highlighted by the similarity of solution and solid values of  $\delta^{\text{iso}}$  in Table 12. The vinylidene  $\text{C}_\alpha$  ( $\text{C}_5$ ) is observed at  $\delta_c = 354$  in the solid state. This correlates well with the solution value of  $\delta_c = 356$  only shifting by 2 ppm. This could be associated with small changes in bond lengths of the vinylidene between the solution and solid-state structures. Both the  $\text{C}_\beta$  ( $\text{C}_1$ ) and  $\text{C}_\beta$  ( $\text{C}_6$ ) resonances remain unchanged between solid and solution. The span of the aromatic resonances increases in the solid phase. In the solution, rapid tumbling and rotation of bonds leads to the averaging of some of the carbon environments. In the solid state, each phenyl carbon will be in a different crystalline environment and therefore will give rise to unique resonances. The effect of this is that the aromatic resonances are observed over a slightly wider chemical shift range. As well as the resonances associated with the **[2a]BF<sub>4</sub>**, ether of crystallisation is also observed as two  $^{13}\text{C}$  signals at  $\delta_c = 65$  and 13.

SS NMR spectroscopy has been shown to correlate very closely with solution phase NMR spectroscopy for the recording of  $^{13}\text{C}$  spectra, with chemical shifts being observed within a small number of ppm of each other.

### 3.3.2 Example of SS characterisation of $^{31}\text{P}\{^1\text{H}\}$ CP MAS SS NMR spectra, showing $^{31}\text{C}\{^1\text{H}\}$ CP MAS spectra of $[\mathbf{2a}]\text{BF}_4\cdot\text{Et}_2\text{O}$

With  $^{13}\text{C}\{^1\text{H}\}$  spectra being recorded in the solid state being comparable to solution spectra.  $^{31}\text{P}\{^1\text{H}\}$  spectra were also recorded of  $[\mathbf{2a}]\text{BF}_4$ , which is shown in Figure 59 along with the solution phase spectra.

Figure 59 shows a clear difference between the solution and solid phase spectra of  $[\mathbf{2a}]\text{BF}_4$ . In solution, Figure 59 B, rotation and isomerisation of the vinylidene occurs leading to the single resonance being observed,  $\delta_{\text{P}} = 43$ . The apparent magnetic equivalence of the phosphine ligands is no longer present in the solid spectrum shown in Figure 59 A. As with the  $^{13}\text{C}$  spectra, the number of chemical environments is dependent on the number of crystallographic phosphorus sites of which there are two,  $\delta_{\text{P}} = 52, 35$ . This leads to two isotropic resonances being observed which are separated by 17 ppm. Although this is a large change from the solution, it does not impact values of the  $^{13}\text{C}$  chemical shift tensors.

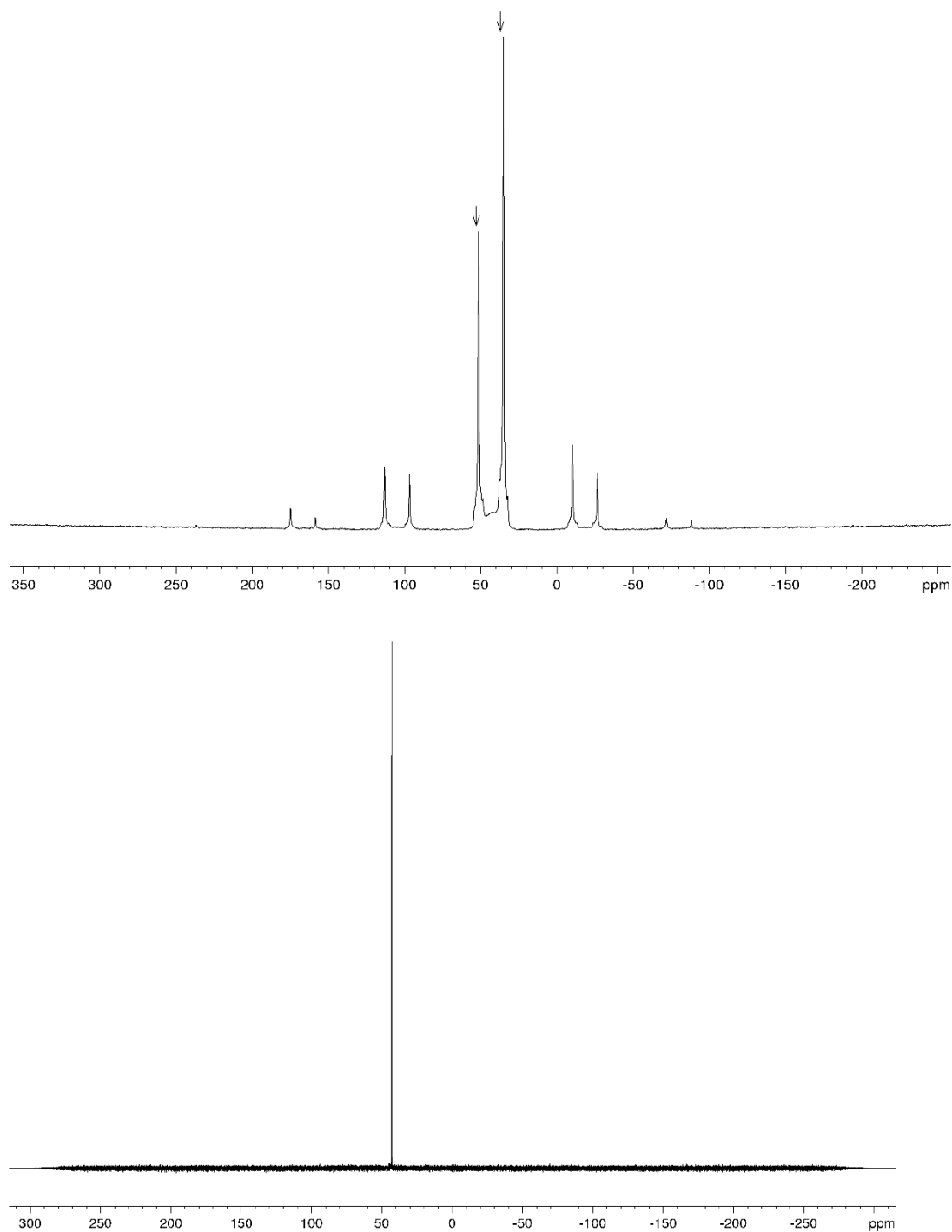


Figure 59. A (Top)  $^{31}\text{P}\{^1\text{H}\}$  CP MAS SS NMR spectra of  $[\mathbf{2a}]\text{BF}_4$  recorded at 162 MHz recorded at a spinning speed of 10 kHz. Isotropic resonances denoted by an arrow. B (Bottom)  $^{31}\text{P}\{^1\text{H}\}$  NMR spectra of  $[\mathbf{2a}]\text{BF}_4$  recorded at 162 MHz.

### 3.3.3 Example SS characterisation of $^{19}\text{F}$ MAS SS NMR spectra, showing $^{19}\text{F}$ MAS spectra of $[\mathbf{3a}]\text{PF}_6$

The  $^{19}\text{F}$  spectra of  $[\mathbf{3a}]\text{PF}_6$  has been shown in 2.2.4 as it was used for the initial optimisation of  $^{19}\text{F}$  SS NMR spectra in this thesis. The spectrum is shown again below, along with a solution-phase spectrum of the tetrafluoroborate salt in  $d_2$ -dichloromethane.

The data in Figure 60 shows that the chemical shift of the  $^{19}\text{F}$  resonance of  $[\mathbf{3a}]\text{X}$  does not change significantly between solid and solution samples, as  $\delta_{\text{F}} = -208$ , and  $-207$ , respectively. The fluorine resonance shows a large chemical shift anisotropy, with many side bands being observed even when spinning at 10 kHz. Because the magnitude of the anisotropy (in Hz) is much larger than  $\nu^{\text{rot}}$ , slower spinning speeds are not required for the recovery of the chemical shift tensors.

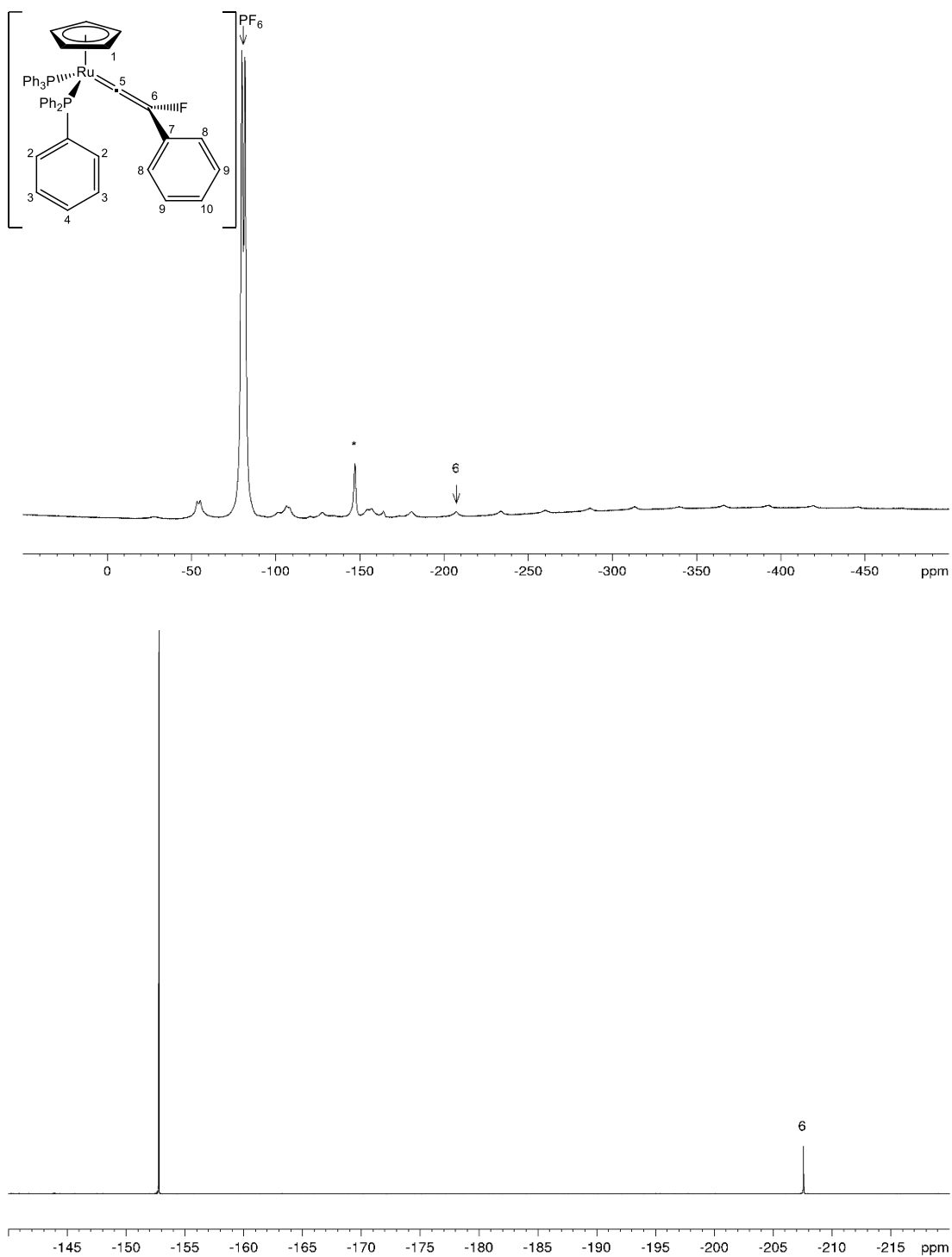


Figure 60. **A** (Top)  $^{19}\text{F}$  MAS SS NMR spectrum of complex **[3a]**PF<sub>6</sub> recorded at 376 MHz recorded at a spinning speed of 10 kHz. Isotropic resonances denoted by an arrow. **B** (Bottom)  $^{19}\text{F}$  NMR spectrum of complex **[3a]**BF<sub>4</sub> recorded in d<sub>2</sub>-dichloromethane at 376 MHz.

### 3.3.4 Effect of crystallinity on SS NMR Spectra

As SS NMR spectroscopy is a solid-state characterisation technique, the microscopic ordering of the sample can have a large effect on the quality of the recorded spectrum. This is shown in Figure 61.

Figure 61 A shows the  $^{13}\text{C}\{^1\text{H}\}$  spectra of **[3a]**BF<sub>4</sub> which was recovered as a green powder directly after fluorination. The aromatic and Cp resonances are very broad and the aromatic resonances of the phosphines show no fine detail. The expected resonances of the vinylidene C<sub>α</sub> and C<sub>β</sub> (C<sub>5</sub>, C<sub>6</sub>) are hard to distinguish from the baseline. The resolution of the spectra is very poor, even though the same sample gives data that cleanly matches literature solution-phase data ( $^1\text{H}$ ,  $^{19}\text{F}$ ,  $^{31}\text{P}$ ). The extreme broadening suggests that **[3a]**BF<sub>4</sub> recovered directly after synthesis is poorly defined in the solid state. This may be a combination of effects: polymorphism, and amorphism. There may be some polymorphism in the sample in Figure 61 A. With several unit cells present in the sample, there will be several distinct environments for each carbon. Each environment will have a unique chemical shift and chemical shift anisotropy meaning that the resonance is broadened. An amorphous powder would extend this effect even further with there being more environments, reducing sample intensity and increasing line broadening. The recovery of chemical shift tensors from broad spectra is highly challenging due to the large noise contributions to each side band. This causes the side bands to be lost into the baseline.

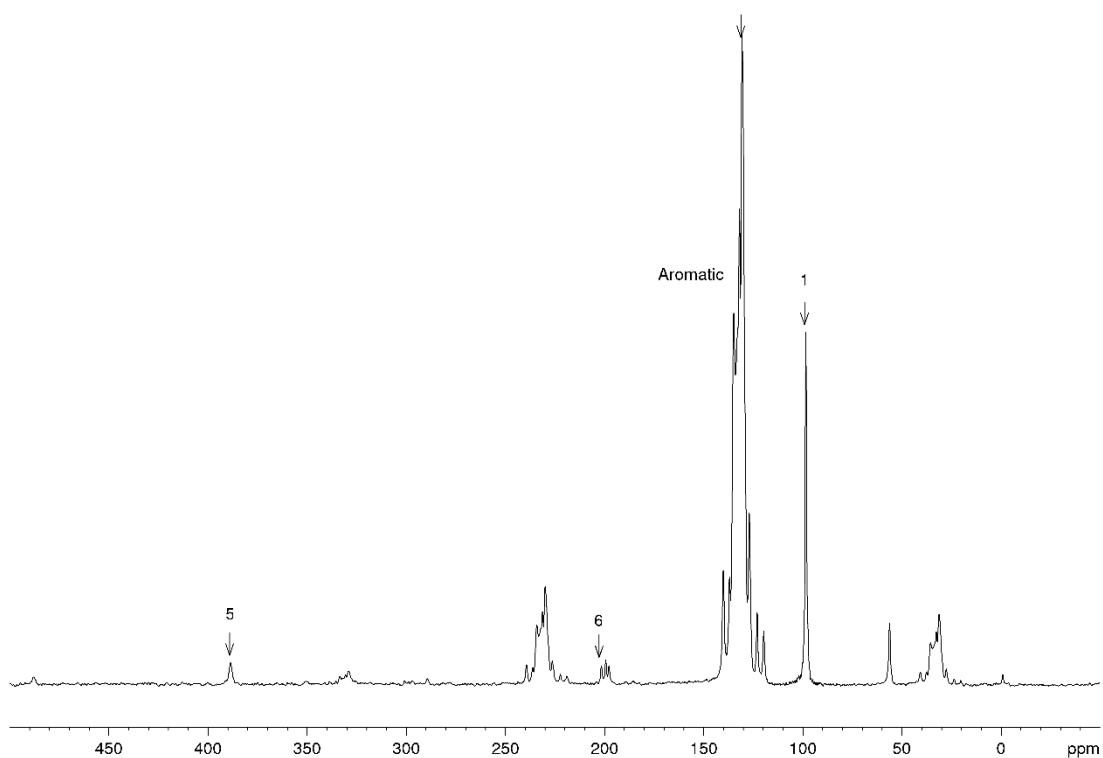
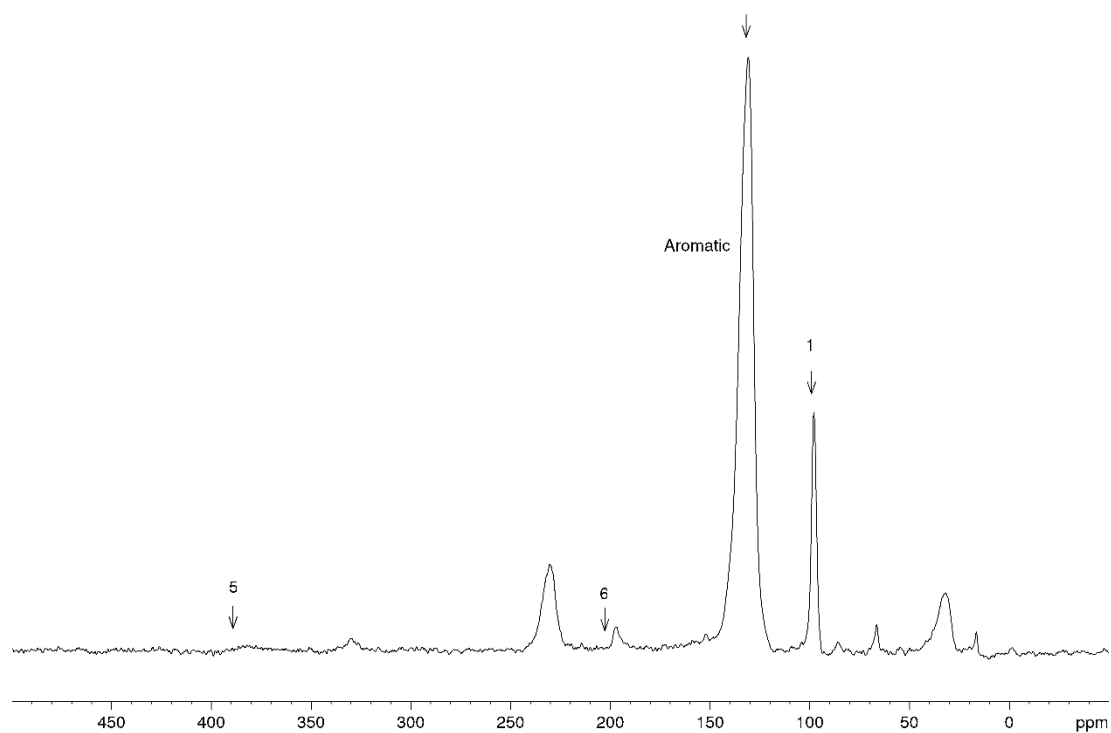


Figure 61.  $^{13}\text{C}\{^1\text{H}\}$  CP MAS SS NMR Spectra of complex **[3a]BF<sub>4</sub>** (A, Top) and **[3a]PF<sub>6</sub>** (orange polymorph) (B, Bottom) recorded at 101 MHz at a spinning speed of 10 kHz. Isotropic resonances are denoted by an arrow. B (Bottom) Isotropic resonances are denoted by an arrow.

Although **[3a]**BF<sub>4</sub> is not a well-defined solid, **[3a]**PF<sub>6</sub> is known to crystallise as two polymorphs.<sup>112</sup> As the recovery of the chemical shift tensors relies on well resolved resonances, **[3a]**PF<sub>6</sub> was prepared and crystallized as described in the literature. The orange form was obtained as the major polymorph, which could be separated from the green form by Pasteur separation. The spectrum is shown in Figure 61 *B* and shows clear differences from Figure 61 *A*. All resonances are much sharper when ground single crystals were used as the analyte, with the vinylidene resonances (C<sub>5</sub>, C<sub>6</sub>) being clearly observed above the baseline.

Single crystallinity ensures that the local microcrystalline environments are uniform within the sample. The presence of other microcrystalline environments leads to slight changes in chemical shift, reducing sample intensity and reducing sharpness. Small levels of contamination can complicate solid-state spectra. Although this is typically not as much of an issue in fast spinning samples but becomes more pronounced as spinning speed is reduced. The SS NMR of **[3a]**PF<sub>6</sub> has shown the necessity for analysing single crystalline material. As a result, spectra were only recorded on material that were single crystalline.

### 3.3.5 Summary of chemical shift tensors of ruthenium organometallics

SS NMR spectra were recorded for the series of ruthenium complexes described earlier in Figure 57. Chemical shift tensors were recovered following methodology from Chapter 2. The tensors were recovered for C<sub>α</sub> for the complexes by recording spectra with a reduced spinning speed of 4 kHz and by using a high number of scans (Ns = 4096) to improve the signal to noise ratio. The tensors for the complexes are summarized in Table 13.

Table 13. Chemical shift tensors recovered from  $^{13}\text{C}\{^1\text{H}\}$  CP MAS SS NMR spectra recorded at 101 MHz.

Compound	Isotropic Shift / ppm	$\delta_{11}$ / ppm	$\delta_{22}$ / ppm	$\delta_{33}$ / ppm
<b>[1a]</b>	119.2	235	145	-22
<b>[1b]</b>	116.7	232	162	-44
<b>[1c]</b>	125.9	N/A	N/A	N/A
<b>[1d]</b>	118.7	237	179	-61
<b>[2a]</b> BF <sub>4</sub>	353.7	558	289	214
<b>[2b]</b> OTf*	N/A	N/A	N/A	N/A
<b>[2c]</b> OTf	349.6	546	299	204
<b>[2d]</b> OTf	347.7	551	282	211
<b>[2a]'</b> OTf	356.4	584	290	195
<b>[3a]</b> PF <sub>6</sub>	388.5	493	444	228
<b>[3d]</b> PF <sub>6</sub>	385.0	504	438	212
<b>[3a]'</b> PF <sub>6</sub>	414.9	537	474	233
<b>[4]'</b>	120.1	267	158	-65
<b>[5]'</b> OTf	355.1	516	395	155
<b>[6]'</b> *PF <sub>6</sub>	382.4	N/A	N/A	N/A
<b>[7]'</b> *	44.7	N/A	N/A	N/A
<b>[9]</b> BF <sub>4</sub>	340.7	561	293	168
<b>[10]</b> PF <sub>6</sub>	202.7	383	300	-76

As seen from the data in Table 13, chemical shift tensors could not be recovered for some of the complexes. This was due to overlapping of sidebands with the resonance of interest, **[1c]**, or because the spectra, **[2b]**OTf, were very broad. This broadening led to the quality of the spectra being too low for recovery. Although tensors could not be recovered for **[6]**BF<sub>4</sub> and **[7]**, the isotropic chemical shifts were identifiable. It can be seen from the data in Table 13 that the magnitudes of the tensors largely correlate between different classes of complex. This is expected as the values of  $\delta^{\text{iso}}$  are similar between each class.

### 3.3.6 SS NMR spectroscopy of fluoroalkynyl complex, [7]

The synthesis of complex [7] is non-trivial and it posed a significant challenge to acquire enough pure material for SS NMR analysis. This issue with low yield of crystalline material was circumvented by the use of a part-packed rotor. An inert packing material was selected to co-pack the rotor. The packing material needed to be chemically inert and stable under MAS conditions. It was also preferable that the packing material did not contain any nuclei that would be interact with the SS NMR spectrum, such as  $^{13}\text{C}$ ,  $^{19}\text{F}$ , and  $^{31}\text{P}$ , to reduce competing signals and overlap in the subsequent spectra. The final requirement was that the material was aprotic, preferably with no protons at all. A common packing agent used is alumina, when complex [7] is passed down an alumina column, protonation is observed, resulting in [6]<sup>+</sup>. This drive to form the protonated product is so strong that even when loaded onto a basic alumina column and run with 10 % triethylamine, protonation is still observed. Boron nitride was selected as the packing agent of choice as it is inert and contains no nuclei of spectroscopic interest.

A proton-carbon CP experiment was run on a co-packed rotor of [7] and boron nitride. The spectrum is shown in Figure 62.

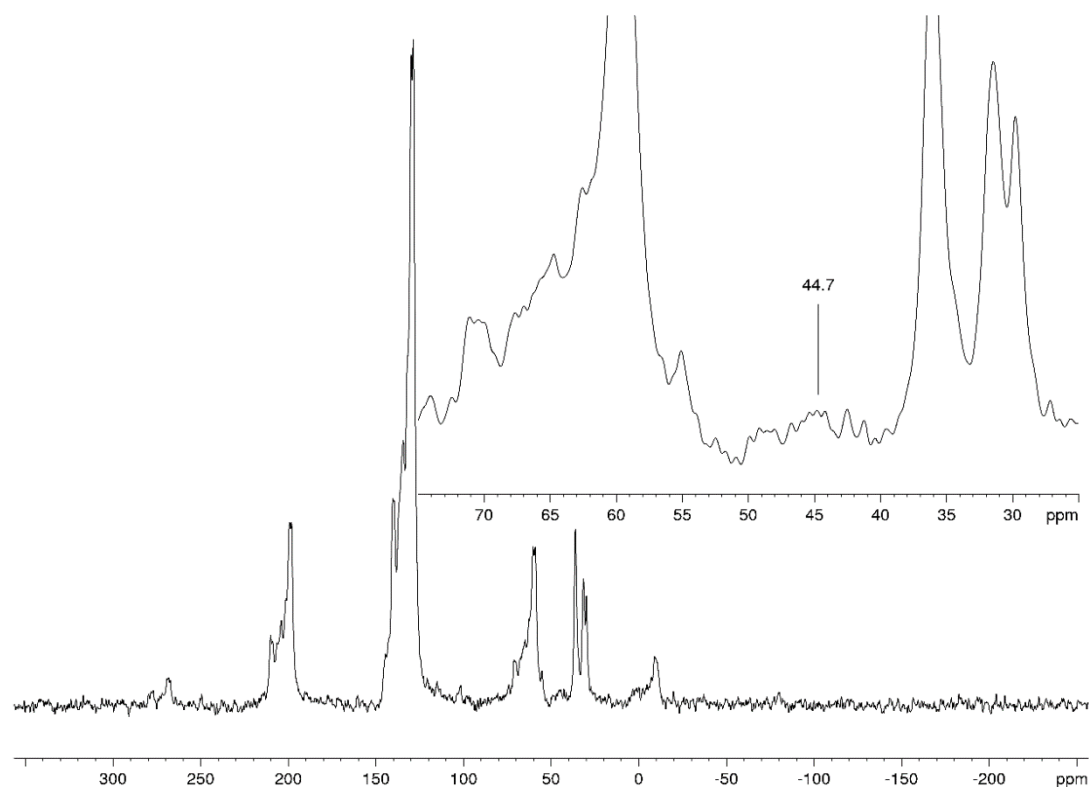


Figure 62. CP MAS SS NMR spectrum of complex **[7]** recorded at 101 MHz at a spinning speed of 10 kHz. The resonance for  $C_{\alpha}$  is observed at 44.7 ppm.

In general, a high intensity spectrum has been recorded even with the low mass of active material. By creating a plug using the boron nitride, the active sample has been centred in the region of the rotor that is probed during the NMR spectroscopic experiment. This has led to very little loss of sample intensity. Despite this, it can be seen in the spectra that the resonance for the alpha carbon is of very low intensity compared to all the others in the spectrum. The resonance is also close in chemical shift to those associated with the 1,2-*bis*-(diphenylphosphine)ethane (dppe) backbone carbons. This could potentially lead to obscuring of the desired sidebands by the higher intensity resonances.

CP techniques rely on large scalar coupling constants between a high  $\gamma$  nuclei and a less receptive nuclei. Proton-carbon is the most commonly employed cross polarisation technique as carbon hydrogen bonds are common and have a high scalar coupling constant. The  $C_{\alpha}$  of the fluoroalkynyl complex has no through bond couplings to protons. It only has a small  ${}^2J_{CF}$  coupling of 37 Hz. Because of this, it was

predicted that CP would only cause other nearby signals to become enriched, while not affecting the intensity of the  $C_{\alpha}$  resonance.

In an attempt to recover the chemical shift tensors for complex **[7]**, a different NMR experiment was collected. Rather than using a CP pulse program, a high-power decoupling (HPDEC) program was selected. The resulting spectrum is shown in Figure 63.

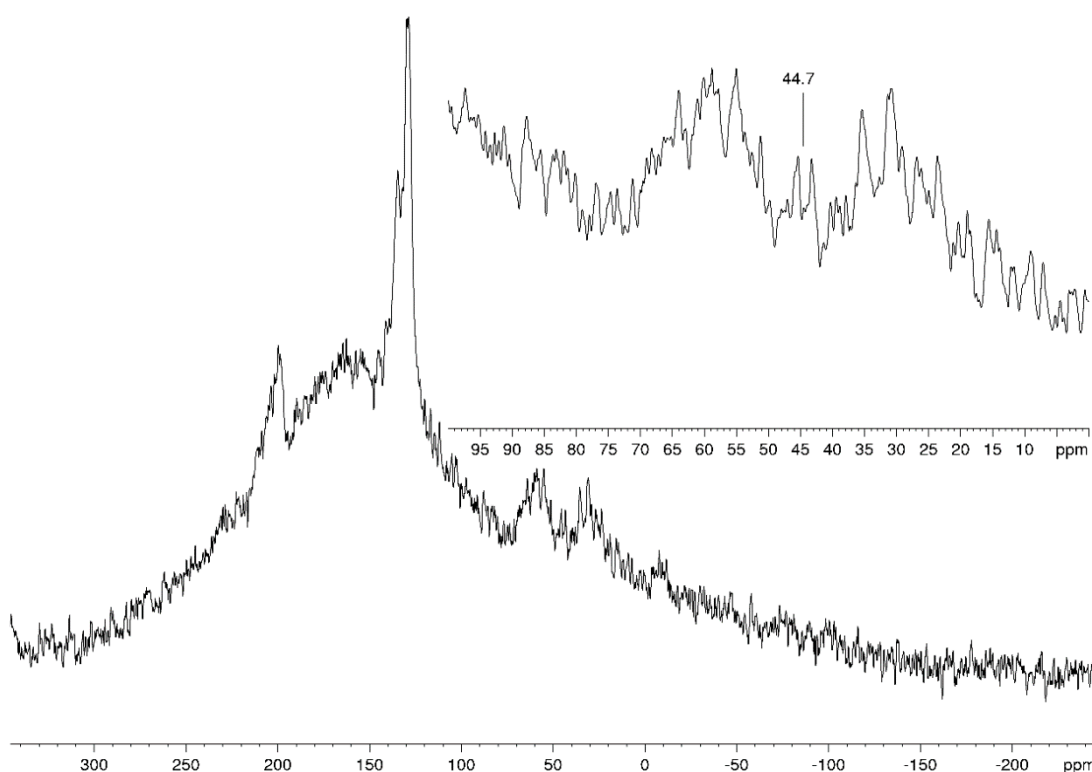


Figure 63. HPDEC MAS SS NMR spectrum of complex **[7]** recorded at recorded at 101 MHz at a spinning speed of 10 kHz. The intensity of the  $C_{\alpha}$  is still low, but the resonance is observed.

In Figure 63, the isotropic resonance for the  $C_{\alpha}$  is observed. As predicted, the signals for the other resonances are suppressed compared to the CP experiment. However, although the isotropic resonance is observable, the signal to noise ratio is still too poor to model. The chemical shift tensors could not be recovered this way.

As mentioned earlier, CP increases the signal to noise ratio when high  $\gamma$  nuclei transfer their polarisation to a less receptive nuclei.  $^{19}\text{F}$  has a high gyromagnetic ratio and can be used to transfer polarisation to carbon. However, CP from fluorine to

carbon has several disadvantages when compared to transfer from protons. The major disadvantage being that fluorine resonances have large chemical shift ranges compared to protons. Polarisation transfer can only occur at the Hartman Haan matching conditions: when the precession rate for both nuclei is matched.<sup>63</sup> As all proton transitions are in a narrow energy range, the matching frequency can induce transfer from all protons in the sample. For fluorine, the broad chemical shift dispersion means that transfer cannot be achieved from all nuclei. The only way that any meaningful transfer can be obtained is by spinning the sample at high spinning speeds, reducing the chemical shift anisotropy and therefore the range of transition energies. The other disadvantage of fluorine-carbon CP is that the sample is no longer being proton-decoupled, leading to large broadening of other resonances in the sample.

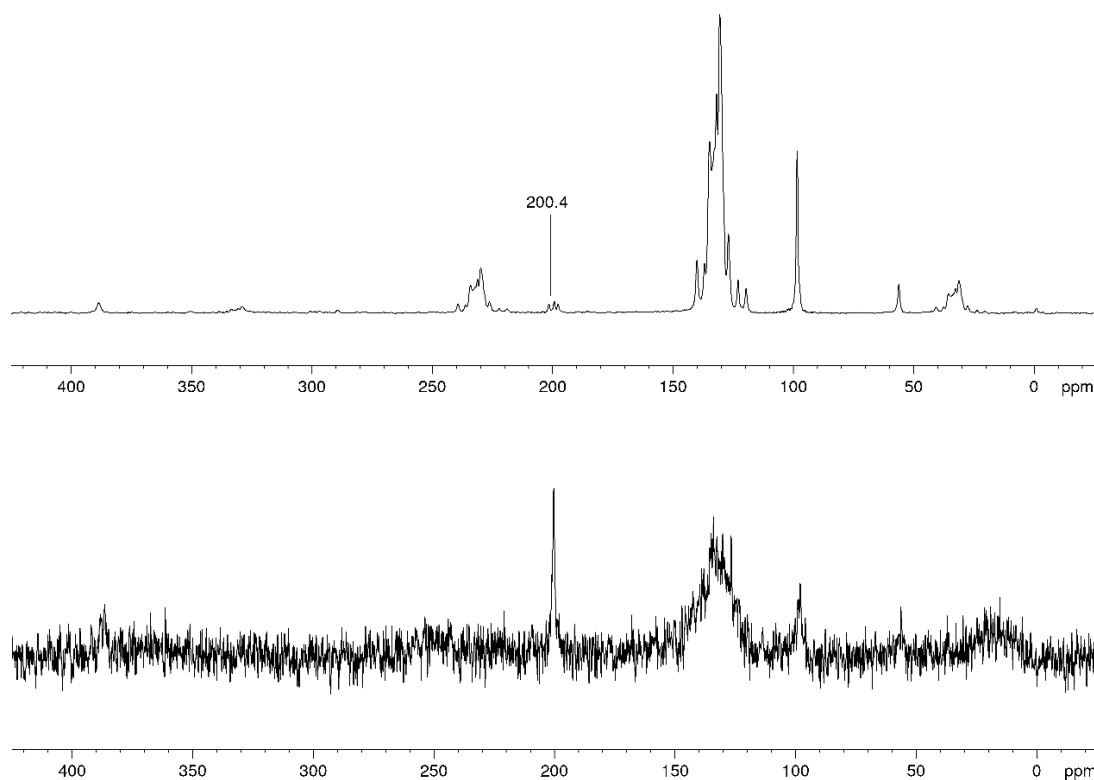


Figure 64. Proton-carbon (Top) and fluorine-carbon (Bottom) CP MAS SS NMR spectra of **[3a]**PF<sub>6</sub> recorded at recorded at 101 MHz at a spinning speed of 10 kHz.. The intensity of the beta carbon shows a large increase in relative intensity.

Fluorine-to-carbon CP experiments were optimised and conducted on samples of complex **[3a]**PF<sub>6</sub> Figure 64 and complex **[7]** Figure 61. As shown in Figure 64,

enrichment of the  $C_{\beta}$  resonance at 200 ppm is observed, this is due to the large one bond scalar coupling to the beta carbon. In general, the signal to noise is still poor, and there is little enrichment of the alpha carbon resonance at 389 ppm. Following from Figure 64, fluorine-carbon CP was conducted on **[7]**, also shown in Figure 65. As anticipated, the large one bond coupling to the  $C_{\beta}$  leads to enrichment of the resonance at 113 ppm. No enrichment is observed for the  $C_{\alpha}$ , most likely due to the relatively small  $^2J_{C-F} = 36$  Hz coupling between the fluorine and the carbon.

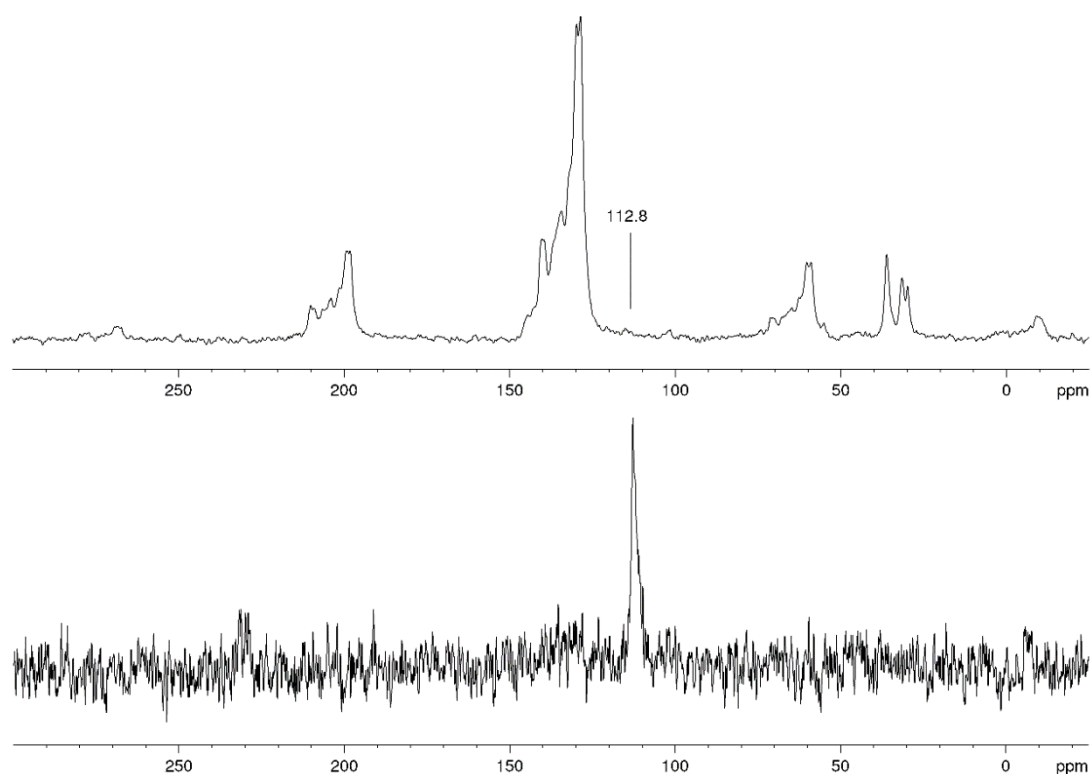


Figure 65. Proton-carbon (Top) and fluorine-carbon (Bottom) CP MAS SS NMR spectrum of **[7]** recorded at recorded at 101 MHz at a spinning speed of 10 kHz.. The intensity of  $C_{\beta}$  (112.8 ppm) shows a large increase in relative intensity.

The NMR spectroscopic experiments performed on complex **[7]** demonstrated that the chemical shift tensors could not be obtained due to the low intensity of the  $C_{\alpha}$  resonance. Another issue was potential overlap with the dppe backbone carbons and spinning side bands from the aromatic resonances. Although the chemical shift tensors could not be modelled, the isotropic resonance was still observed. It varies from the solution phase isotropic chemical shift, but this is likely due to changes in

geometry as the complex is dissolved and is no longer supported by the crystal matrix. All reasonable attempts to collect the chemical shift tensors for [7] were exhausted.

### 3.4 Calculation of chemical shift tensors for ruthenium vinylidene- and alkynyl- complexes

#### 3.4.1 Calculation of chemical shift tensors (coordinated)

With good experimental data in hand and good confidence in the method developed in chapter 2, the chemical shift tensors for a wider range of alkynyl- and vinylidene- complexes could be obtained by performing quantum chemical NMR calculations using DFT. This allows the scope of the analysis to expand, as well as to account for any compounds that were not observable due to technical limitations. The results are summarised in Table 14. The compounds are shown in Figure 66.

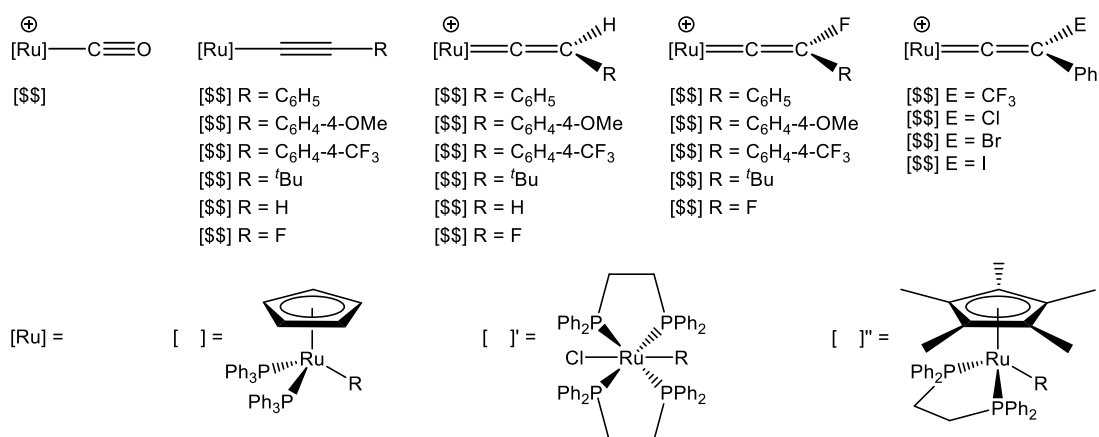


Figure 66. Ruthenium organometallic complexes studied by quantum chemical calculations using DFT.

Table 14. Chemical shift tensors of ruthenium alkynyl and vinylidene species. Optimized in Turbomole at the BP86/def2\_SV(P) level of theory, NMR calculations performed in Orca at the PBE0/def2\_TZVPP level of theory with ZORA corrections.

Complex	$\delta^{\text{iso}}$ / ppm	$\delta_{11}$ / ppm	$\delta_{22}$ / ppm	$\delta_{33}$ / ppm
<b>[10]<sup>+</sup></b>	203	360	340	-92
<b>[1a]</b>	134	221	205	-23
<b>[1b]</b>	127	211	202	-32
<b>[1c]</b>	145	239	210	-13
<b>[1d]</b>	105	198	186	-69
<b>[4]</b>	116	232	224	-107
<b>[7]</b>	30	104	96	-108
<b>[1a]'</b>	147	238	219	-14
<b>[4]'</b>	128	245	236	-97
<b>[7]'</b>	46	118	110	-90
<b>[1a]''</b>	139	231	208	-23
<b>[4]''</b>	121	238	232	-108
<b>[7]''</b>	34	110	100	-108
<b>[2a]<sup>+</sup></b>	357	552	295	225
<b>[2b]<sup>+</sup></b>	371	554	282	276
<b>[2c]<sup>+</sup></b>	359	550	308	218
<b>[2d]<sup>+</sup></b>	352	559	283	216
<b>[2a]'<sup>+</sup></b>	348	560	303	182
<b>[2a]''<sup>+</sup></b>	352	541	294	223
<b>[3a]<sup>+</sup></b>	418	531	471	251
<b>[3b]<sup>+</sup></b>	415	526	459	259
<b>[3c]<sup>+</sup></b>	423	554	483	231
<b>[3d]<sup>+</sup></b>	409	533	464	230
<b>[3a]'<sup>+</sup></b>	412	530	433	273
<b>[3a]''<sup>+</sup></b>	406	520	448	249
<b>[5]<sup>+</sup></b>	342	552	332	143
<b>[6]<sup>+</sup></b>	386	513	384	262

[8] <sup>+</sup>	421	626	465	172
[5] <sup>+</sup>	341	569	342	111
[6] <sup>+</sup>	381	529	346	269
[8] <sup>+</sup>	424	602	483	187
[5] <sup>''</sup>	338	543	336	136
[6] <sup>''</sup>	368	500	340	265
[8] <sup>''</sup>	395	557	455	172
[9] <sup>+</sup>	336	527	322	159
[11] <sup>+</sup>	366	528	292	277
[12] <sup>+</sup>	349	522	295	230
[13] <sup>+</sup>	330	510	299	180

Calculated tensors and experimental tensors can be correlated, as shown in Figure 67. In general, the fit between the values is good. This shows that there is only a small variance between that calculated values and their measured counterparts. Typically, the biggest deviations were for the complexes that possessed a *pseudo-∞* rotational symmetry about the M-C bond axis. The calculations predict that the  $\delta_{11}$  and  $\delta_{22}$  tensors are nearly identical, the experimental values deviate from this ideal. Some of the larger deviations are expressed in Table 15.

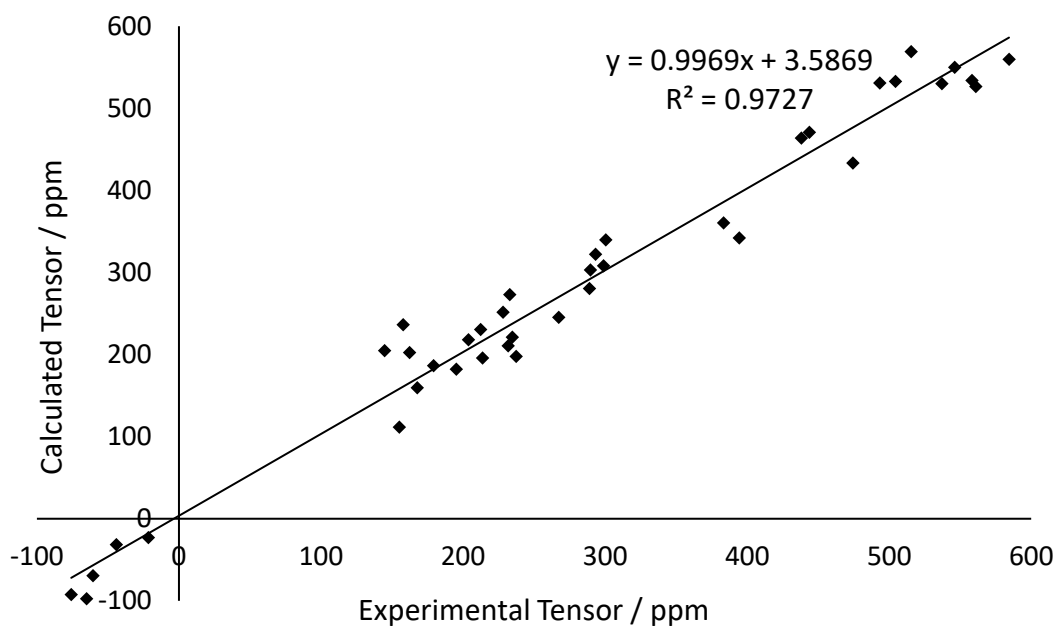


Figure 67. Fit between computationally- and experimentally- derived chemical shift tensors. The calculated values and trends match those observed experimentally.

Table 15. Chemical shift tensors of complexes possessing a *pseudo-∞* rotational axis. Calculated values are shown in brackets, calculated at the PBE0/def2\_TZVPP level of theory with the ZORA correction.

Complex	$\delta^{\text{iso}}$ / ppm	$\delta_{11}$ / ppm	$\delta_{22}$ / ppm	$\delta_{33}$ / ppm
<b>[1a]</b>	119 (134)	235 (221)	145 (205)	-22 (-23)
<b>[1b]</b>	117 (127)	232 (211)	162 (202)	-44 (-32)
<b>[1d]</b>	119 (105)	237 (198)	179 (186)	-61 (-69)
<b>[10]PF<sub>6</sub></b>	203 (203)	383 (360)	300 (340)	-76 (-92)
<b>[1a]'</b>	120 (116)	267 (232)	158 (224)	-65 (-107)

The discrepancies in the chemical shift tensors with *pseudo-∞* rotational axes can be rationalised as a combination of effects. The DFT calculations are based on isolated gas phase molecules and therefore the bond geometry is slightly different than the crystal structure. The crystal structure bonding may deviate from the gas phase minimum, changing the overlap and energy of the FMOs and therefore the chemical shift tensors. The other effect is the error introduced in the sideband simulation. As the spinning side bands possess their own contributions to noise, the experimental tensors will deviate from the real values. Spinning side echoes also contribute to small changes in experimental tensors.

Despite these challenges, the data in Figure 67 show that the trends observed in the chemical shift tensors are maintained. With good confidence in the methodology and good fit to all the experimentally observed tensors, the tensors could be correlated to molecular orbital transitions. The  $R^2$  value of the plot in Figure 67 is close to the ideal value of 1,  $R^2 = 0.9727$ , suggesting a relatively small average deviation from the line of best fit. The gradient is also very close to 1, being 0.9969x. The intercept of the graph is close to 0, all these factors suggest that there are no scaling effects occurring in the calculation of chemical shift.

### 3.4.2 Visualisation of chemical shift tensors

The chemical shift tensors that have been calculated in section 3.4.1 are good representations of the experimentally-derived chemical shift tensors. To correlate the chemical shift tensors to the molecular frame of reference, the tensors were visualised as described in section 2.6. Visualised chemical shift tensors of some key complexes are displayed in Figure 68.

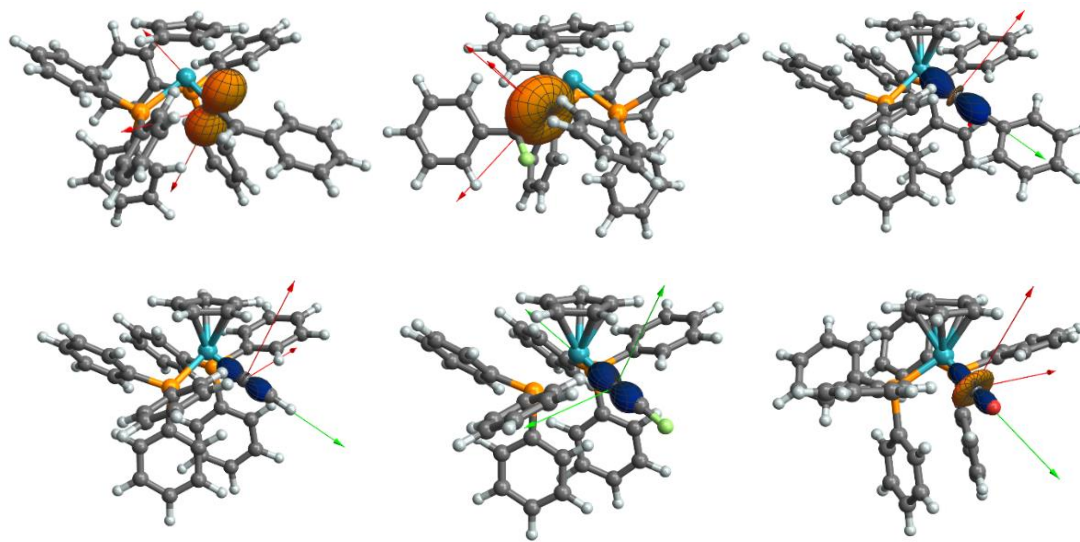


Figure 68. Visualised chemical shift tensors of key ruthenium organometallics. From top left going clockwise:  $[2a]^+$ ,  $[3a]^+$ ,  $[1a]$ ,  $[4]$ ,  $[7]$ ,  $[10]^+$ .

The visualised tensor plots can be used to map the individual tensors onto the molecular reference frame. Allowing the differences to be scrutinised.

## 3.5 Interpretation of vinylidene tensors

### 3.5.1 Identification of FMO transitions using simple uncoordinated vinylidene complex models

The NMR spectra of vinylidene complexes, such as  $[2a]OTf$ , show characteristic deshielding of  $C_\alpha$ , as shown in Table 16. However, the FMOs of these complexes are complicated due to the large number of electrons in the system. Identifying the molecular orbitals responsible for deshielding at  $C_\alpha$  poses a challenge

in large molecules. This is particularly the case in systems with many aromatic environments due to the low energy gaps of the FMOs of the aromatic systems.

Table 16. Characteristic deshielding patterns observed in ruthenium vinylidene complexes for  $C_{\alpha}$ .

Compound	$\delta_{iso}$	$\delta_{11}$	$\delta_{22}$	$\delta_{33}$
<b>[2a]</b> BF <sub>4</sub>	353.7	558	289	214
<b>[2c]</b> OTf	349.6	546	299	204
<b>[2a]'</b> OTf	356.4	584	290	195
<b>[9]</b> BF <sub>4</sub>	340.7	561	293	168

The FMOs of the vinylidene, **[60]**, and difluorovinylidene, **[61]**, moieties (Figure 69) can be used to simplify the analysis.

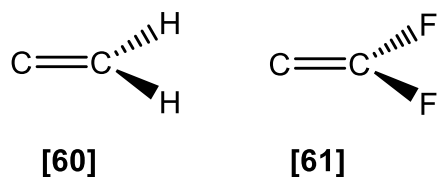


Figure 69. Structure of **[60]** and **[61]**, which are used as simple electronic models of vinylidene and fluorovinylidene complexes.

Given that the nature of the interactions between transition metal complexes and their ligands is often rationalised as the overlap of the FMOs of each fragment, insight into the electronic structure of uncoordinated vinylidenes provides a framework to discuss the subsequent metal complexes. Although **[60]** and **[61]** are not synthetically obtainable for SS NMR analysis, DFT calculations allow their NMR parameters to be calculated as described in Chapter 2. The chemical shift tensors were visualised as described in Chapter 2 and are also shown in Figure 70.

The key transitions that contribute to shielding for **[60]** were identified as outlined in section 2.7 and are shown in Figure 70. The orbitals lower in energy than  $\varphi_5$  were not considered to contribute to  $^{13}C$  paramagnetic deshielding as they are largely symmetric and antisymmetric combinations of carbon 1s and 2s orbitals. As  $\varphi_{1-4}$  are

dominated by s-orbital character, they cannot contribute to  $\sigma^{\text{para}}$  and instead contribute to  $\sigma^{\text{dia}}$ , which is consistent between carbon environments.

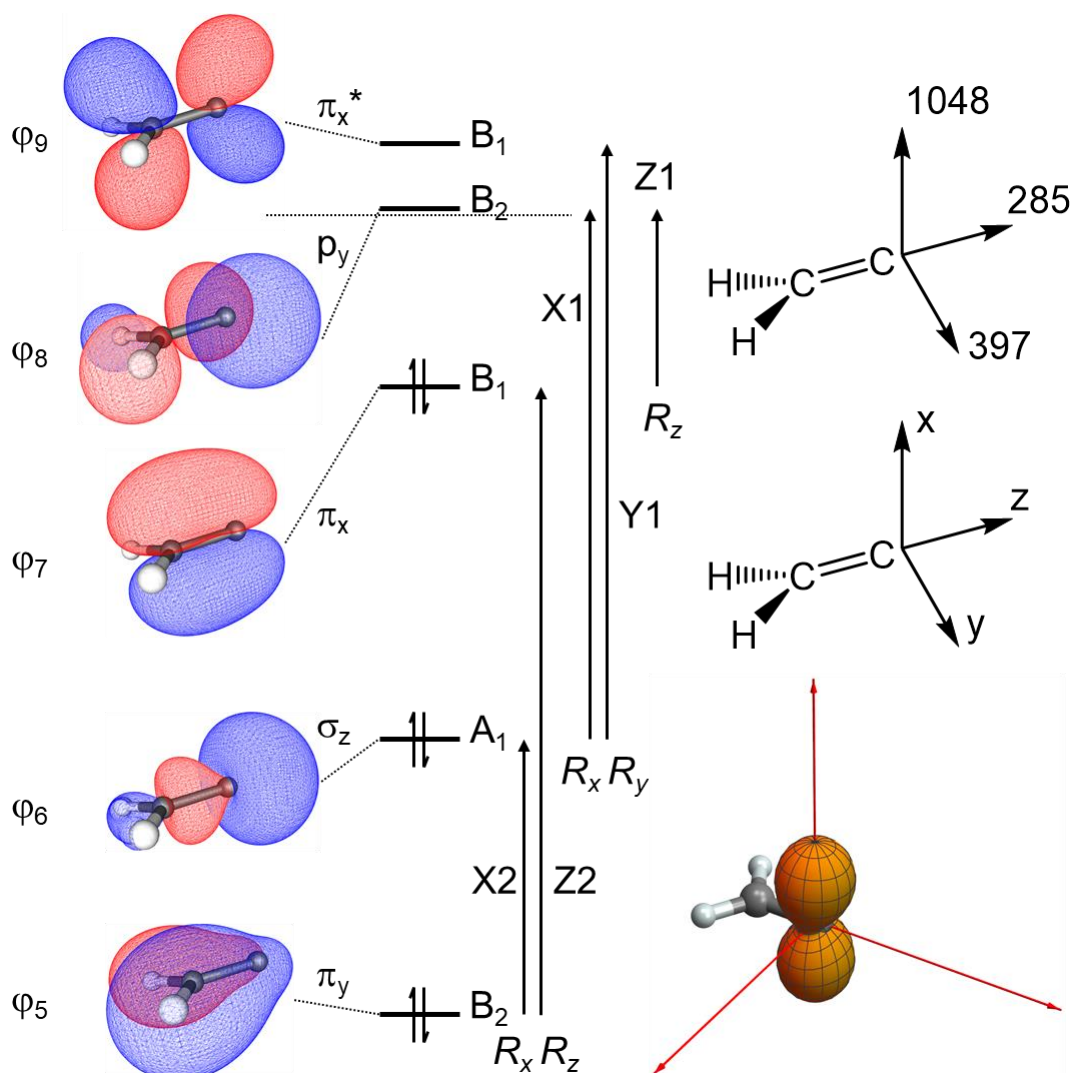


Figure 70. FMO diagram of **[60]** with selected orbitals visualised in gOpenMol (left). Key transitions identified using group theory. **[60]** optimised in Turbomole at the BP86/def2\_SV(P) level of theory, chemical shift tensors calculated in Orca at the PBE0/ def2\_TZVPP level of theory with ZORA corrections and visualised in Wolfram Mathematica with pictorial representations (right). The Barycentre is represented by the dotted line.

The deshielding in vinylidene **[60]** is largest along the x-axis, which is perpendicular to the plane containing the atoms of the vinylidene. Orbitals that are coupled by the rotational operator  $\hat{R}_x$  may give rise to deshielding. Vinylidene **[60]** possesses  $C_{2v}$  symmetry and therefore  $\hat{R}_x$  belongs to the  $B_2$  irreducible representation and transitions between orbitals with  $B_2$  and  $A_1$  symmetry are coupled. Two transitions were identified as symmetry allowed,  $\varphi_5 \xrightarrow{\hat{R}_x} \varphi_6$ , X2, and  $\varphi_6 \xrightarrow{\hat{R}_x} \varphi_8$ , X1. Transition X2 has a

small energy gap and is constructive in nature. However, overlap is poor due to the difference in carbon  $p_z$  localisation. Transition X1 also has a small energy gap, but the interference is destructive and therefore deshielding along the x-axis. Unlike X2, X1 possesses a strong overlap due to the large contribution from the  $C_\alpha$   $p_z$  orbital in  $\varphi_6$  mixing with the totally localised  $p_y$  orbital in  $\varphi_8$ . Transition X1 is responsible for the strong deshielding along the x-axis of  $\delta_{11} = 1048$ .  $\delta_{22}$  lies along the y axis and is strongly deshielded, with deshielding more than half the magnitude of  $\delta_{11}$ ,  $\delta_{22} = 397$ . Only one transition is symmetry allowed with coupling by  $\hat{R}_y$ .  $\Gamma_{\hat{R}_y}$  is  $B_1$ , therefore this transition must be between orbitals belonging to the  $A_1$  and  $B_1$  irreducible representations. The transition was identified as  $\varphi_6 \xrightarrow{\hat{R}_y} \varphi_9$ , Y1. Transition Y1 possesses a larger energy gap than X1 and is destructive in nature. The overlap is good, with p character on both carbons, but the difference in localisation reduces the effective overlap compared to transition X1. These effects combined lead to the reduced, but still large in magnitude, deshielding of  $\delta_{22} = 397$ .

$\delta_{33}$  is deshielding in nature and points along the z axis. It is associated with transitions facilitated by the rotational operator  $\hat{R}_z$ .  $\hat{R}_z$  is represented by the  $A_2$  irreducible representation, therefore any transition must be between orbitals with  $B_1$  and  $B_2$  symmetry. Two transitions were identified for **[60]**,  $\varphi_5 \xrightarrow{\hat{R}_z} \varphi_7$ , Z2, and  $\varphi_7 \xrightarrow{\hat{R}_z} \varphi_8$ , Z1. Z2 is constructive in nature and therefore contributes shielding to  $\delta_{33}$ . The energy gap is moderate and overlap good, meaning that strong shielding is observed from Z2. Conversely, Z1 is destructive in nature and therefore contributes deshielding to  $\delta_{33}$ . The overlap between  $\varphi_7$  and  $\varphi_8$  is only moderate, due to the lack of  $p_y$  character on the beta carbon in  $\varphi_8$ . Despite this, the narrow energy gap leads to a large deshielding interaction along the z axis. Because Z1 and Z2 are both contributing to the total deshielding along the z axis, a moderate deshielding of  $\delta_{33} = 285$  is observed.

To better understand the differences in deshielding between vinylidene and fluorovinylidene complexes, the chemical shift tensors were calculated for difluorovinylidene **[61]**. As with vinylidene **[60]**, the interactions between a metal-coordinated and an uncoordinated fluorovinylidene can be rationalised as overlap between the FMOs of the metal-containing and carbenoid fragments. The calculated

and visualized tensors for **[61]** are shown in Figure 71. The magnitudes of the chemical shift tensors are broadly similar along the x and y axes, but a large deshielding interaction is observed along the z axis. This is responsible for an increase in isotropic deshielding in fluorovinylidenes. The key transitions that have been identified to contribute to the deshielding are also shown in Figure 71.

Fluorovinylidene **[61]** belongs to the  $C_{2v}$  point group. Tensor  $\delta_{11}$  is deshielding and points along the z axis and is associated with transitions facilitated by the rotational operator  $\hat{R}_z$ .  $\Gamma_{\hat{R}_z}$  is  $A_2$ , therefore any transition must be between orbitals with  $B_1$  and  $B_2$  symmetry. Two transitions were identified for **[61]**,  $\varphi_9 \xrightarrow{\hat{R}_z} \varphi_{10}$ , Z2, and  $\varphi_{15} \xrightarrow{\hat{R}_z} \varphi_{16}$ , Z1. Z2 is constructive in nature and therefore should contribute shielding to  $\delta_{11}$  as in **[60]**. Unlike in **[60]**, the  $p_y$  character on the  $C_\alpha$  of **[61]** has very little character in  $\varphi_9$ , meaning that this transition does not contribute to shielding. Conversely, Z1 is destructive in nature and therefore contributes deshielding to  $\delta_{11}$ . The overlap between  $\varphi_{15}$  and  $\varphi_{16}$  is much greater in **[61]** than in **[60]** due to the increased localisation of the  $C_\beta$   $p_y$  orbital. Accompanying the increase in overlap, there is also a narrowing of the HOMO→LUMO energy gap further increasing the magnitude of deshielding.  $\delta_{11}$  is dominated by Z1 in **[61]**.

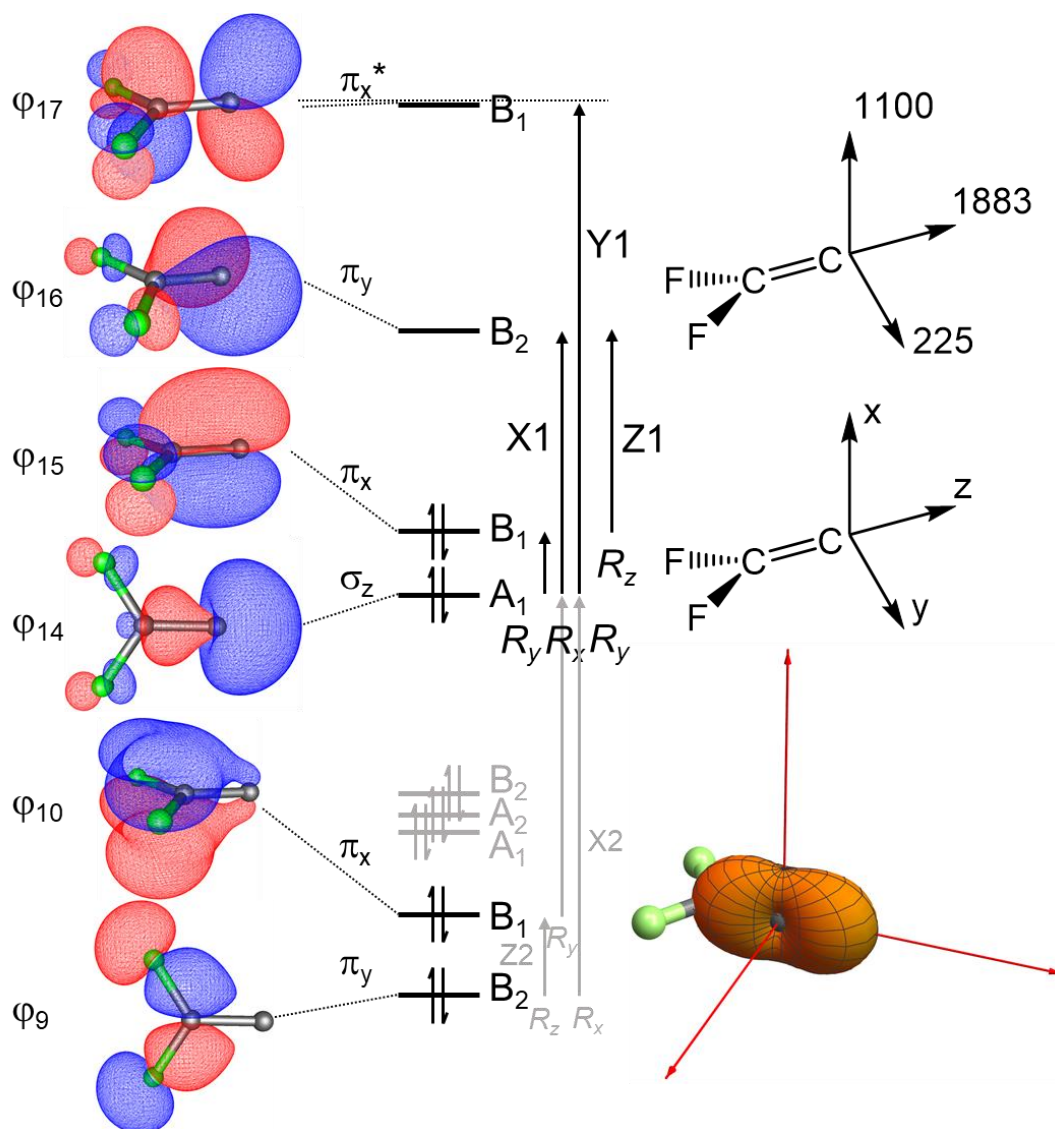


Figure 71. FMOs diagram of fluorovinylidene **[61]** with selected orbitals visualised in gOpenMol (left). Orbitals and transitions that do not contribute to deshielding are shown in grey. Key transitions identified using group theory. **[61]** optimised in Turbomole at the BP86/def2\_SV(P) level of theory, chemical shift tensors calculated in Orca at the PBE0/def2\_TZVPP level of theory with ZORA corrections and visualised in Wolfram Mathematica with pictorial representations (right). The Barycentre is represented by the dotted line.

Deshielding along  $\delta_{22}$  in **[60]** is similar in magnitude to the deshielding of  $\delta_{11}$  in **[61]**, with both laying along the x axis. The two transitions that are responsible for deshielding in **[60]** were also identified on **[61]** as  $\phi_9 \xrightarrow{\hat{R}_x} \phi_{14}$ , X2, and  $\phi_{14} \xrightarrow{\hat{R}_x} \phi_{16}$ , X1. X2 possesses a poor overlap due to the lack of  $C_\alpha$   $p_y$  in  $\phi_9$ , therefore X2 does not

contribute much to the deshielding.  $\delta_{22}$  is dominated by the strong X1 transition. This is destructive in nature and has a strong overlap on  $C_\alpha$ , leading to the large deshielding value of  $\delta_{22} = 1100$ .

It is clear from figures Figure 70 and Figure 71 that the changes on chemical shielding between vinylidene and difluorovinylidene are dominated by changes to the  $\delta_z$  tensor. The key orbitals are shown in Figure 72.

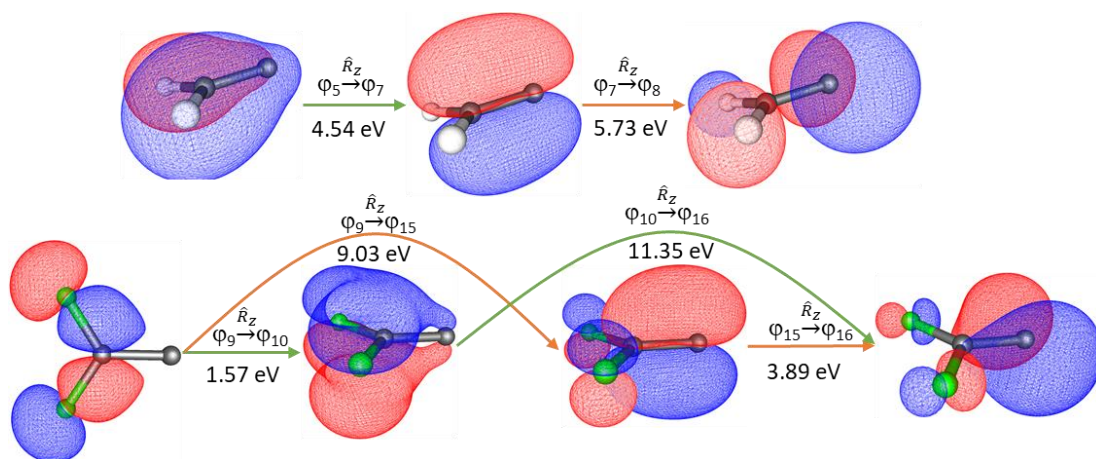


Figure 72. Key transitions responsible for deshielding along the z axes of **[60]** and **[61]** calculated in Orca at the PBE0/def2\_TZVPP level of theory with ZORA corrections. Constructive interactions are represented by green arrows and destructive interactions by red arrows.

One major difference on changing the R group in  $CCR_2$  from H to F is the presence of the p orbitals on F. The  $p_x$  orbitals may interact with the C-C  $\pi_x$  bonding orbital ( $\varphi_7$ ) in both bonding ( $\varphi_{10}$ ) and antibonding ( $\varphi_{15}$ ) arrangements. The separation of  $\varphi_7$  into  $\varphi_{10}$  and  $\varphi_{15}$  leads to constructive and destructive combinations of orbitals. Deshielding increases as the effective constructive overlap of  $\varphi_9 \rightarrow \varphi_{10}$  reduces. As well as this, destructive overlap of  $\varphi_{15} \rightarrow \varphi_{16}$  increases, accompanied by the compression of the energy gap from 5.73 eV to 3.89 eV.

### 3.5.2 Identification of FMO transitions using simple allene and vinyliminium compounds as vinylidene models

The chemical shift tensors of uncoordinated vinylidenes calculated in section 3.5.1 have similar weightings to coordinated vinylidene complexes, but with lower magnitudes. This may be due to the large differences that occur to the orbital energies and localisations on mixing of vinylidene and metal orbitals. To explore the effect of changing the FMO structure on chemical shift, it was hypothesized that the introduction of a terminal fragment to the vinylidene moiety could provide a better model to the deshielding in vinylidene complexes. As a metal vinylidene complex possesses bonding over 3 centres, extension of the  $\pi$ -system from an uncoordinated vinylidene may make the system better represent the electronics of a coordinated complex. Two classes of terminating fragment were selected for study,  $\text{CR}_2$  and the isoelectronic nitrogen equivalent  $\text{NR}_2^+$ . Adding  $\text{CR}_2$  to vinylidenes gives rise to allenes,  $\text{NR}_2^+$  gives vinyliminium cations. They are both shown in Figure 73.

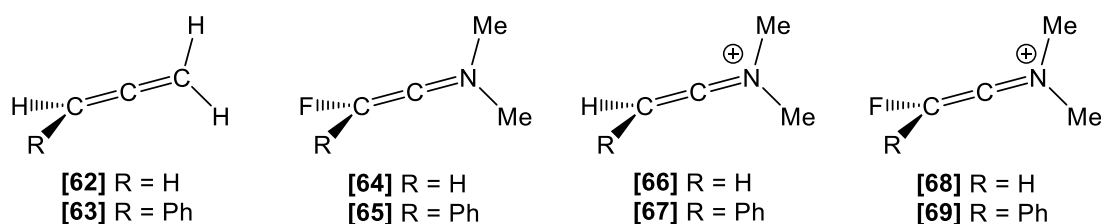


Figure 73. Allene and vinyliminium species **[62]** – **[67]**<sup>+</sup> identified as simple models for **[2a]**<sup>+</sup> and **[3a]**<sup>+</sup>.

Allenes and vinyliminium cations are, like vinylidenes, extended unsaturated systems. To better understand the deshielding in vinylidenes, the geometry of a series of allenes and vinyliminium cations were optimized and the chemical shift tensors calculated as described in Chapter 2. The visualised chemical shift tensors are displayed in Figure 74. The chemical shift tensors are summarized in Table 17.

Table 17. Chemical shift tensors of allene and vinyliminium compounds calculated in Orca at the PBE0/ def2\_TZVPP level of theory with ZORA corrections. Literature experimental shifts shown in brackets.

Compound	$\delta_{iso}$	$\delta_{11}$	$\delta_{22}$	$\delta_{33}$
CH <sub>2</sub> CCH <sub>2</sub> <b>[62]</b>	208 (208.5) <sup>127</sup>	229	229	166
CH <sub>2</sub> CCF <sub>2</sub> <b>[64]</b>	129 (179.9) <sup>128</sup>	190	107	89
CH <sub>2</sub> CCHPh <b>[63]</b>	206	227	204	187
CH <sub>2</sub> CCFPh <b>[65]</b>	200	232	209	158
<sup>+</sup> NMe <sub>2</sub> CCH <sub>2</sub> <b>[66]</b>	207	243	207	170
<sup>+</sup> NMe <sub>2</sub> CCF <sub>2</sub> <b>[68]</b>	264	478	202	111
<sup>+</sup> NMe <sub>2</sub> CCHPh <b>[67]</b>	232	290	242	165
<sup>+</sup> NMe <sub>2</sub> CCFPh <b>[69]</b>	279	479	221	136

From the data in Table 17, the magnitudes of the chemical shift tensors for allene and vinyliminium cations are much smaller than for uncoordinated vinylidenes such as **[60]** and **[61]** with the value of  $\delta_{11}$  reducing significantly, further investigation of the FMOs is required. The key FMOs of **[2a]<sup>+</sup>** will also include contributions from the ruthenium d orbitals as they are the correct symmetry to mix with the vinylidene moiety. Extension of the molecular orbitals over three centres has a large impact on the magnitude of the shielding, even if the shape of the deshielding is similar.

One key feature of the chemical shift calculations summarized in Table 17 is the fact that the trend in the isotropic chemical shift for the allene compounds is not the same as for coordinated complexes. On substitution of H for F, deshielding is not observed and the resulting complex is more shielded. However, the vinyliminium compounds do show a large deshielding shift in the fluorinated equivalents. The magnitude of the shift is comparable to the ruthenium equivalent, but the absolute values are more shielded.

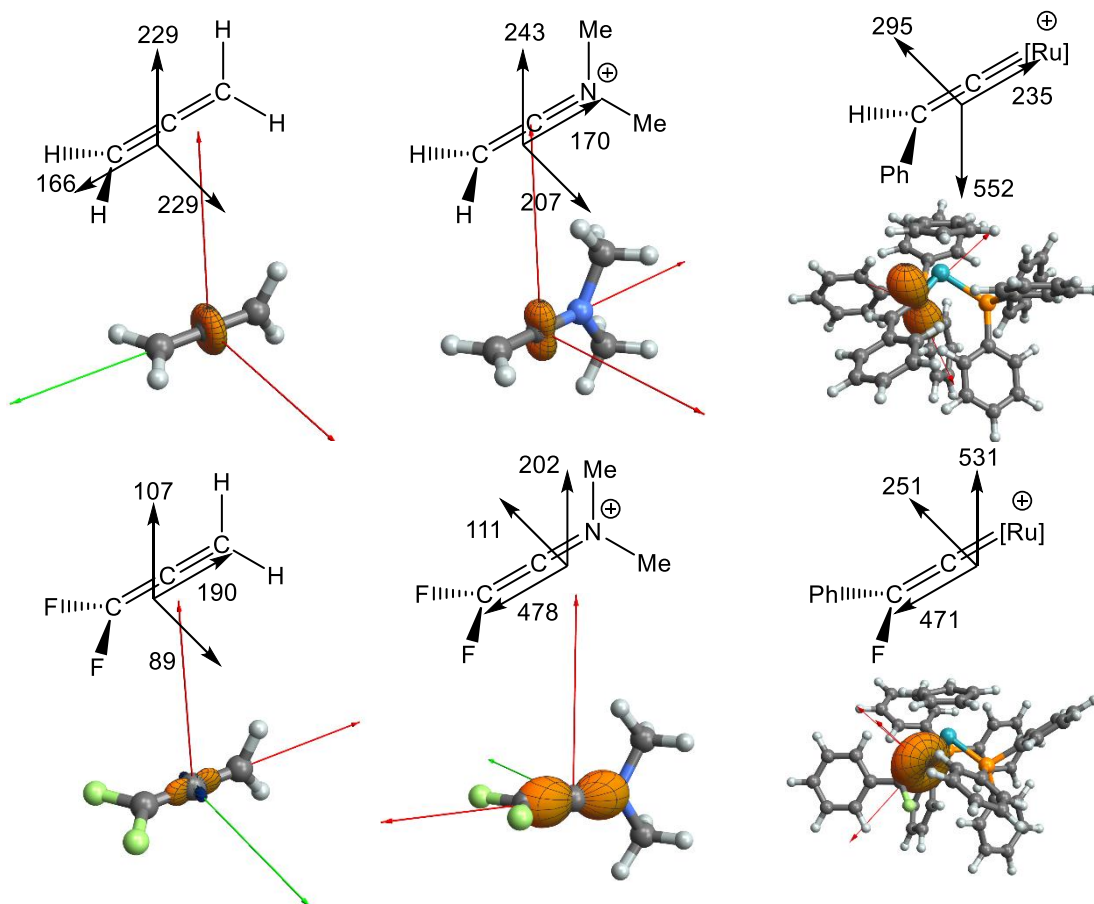


Figure 74. Effect of fluorination on the chemical shift tensors for allene, vinyliminium, and coordinated vinylidenes optimised in Turbomole at the BP86/def2\_SV(P) level of theory, chemical shift tensors calculated in Orca at the PBE0/def2\_TZVPP level of theory with ZORA corrections and visualised in Wolfram Mathematica with pictorial representations.

To further understand the differences in shielding in **[62]**, the key transitions were identified and are shown in Figure 75.

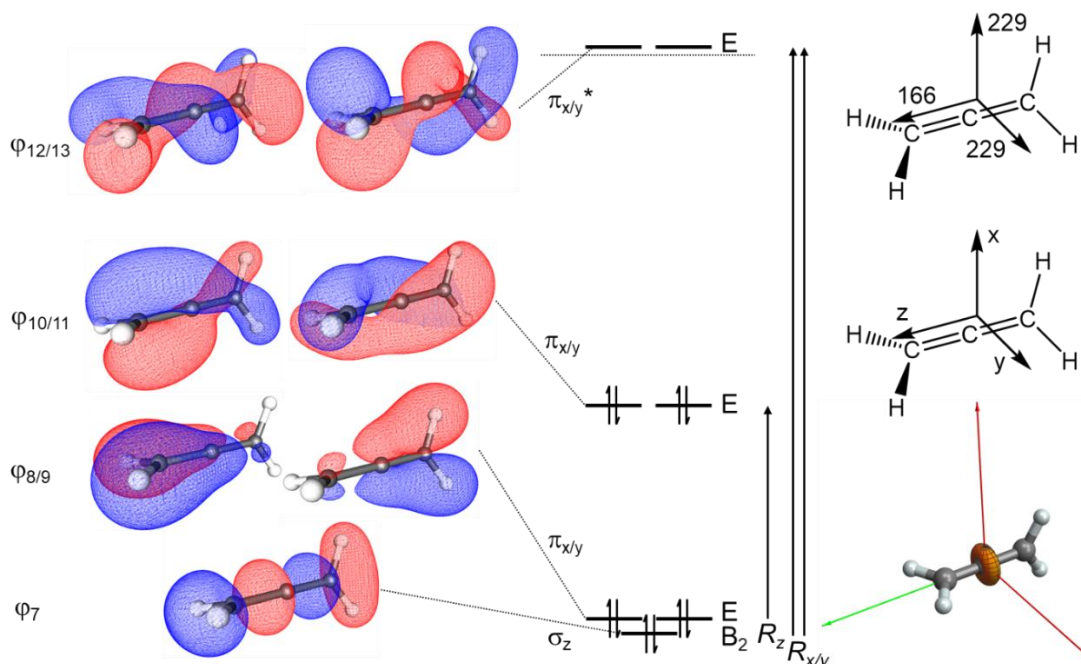


Figure 75. FMO diagram of **[62]** with selected orbitals visualised in gOpenMol (left). Key transitions identified using group theory. **[62]** optimised in Turbomole at the BP86/def2\_SV(P) level of theory, chemical shift tensors calculated in Orca at the PBE0/def2\_TZVPP level of theory with ZORA corrections and visualised in Wolfram Mathematica with pictorial representations (right). The barycentre is represented by the dotted line.

Compound **[62]** possesses  $D_{2d}$  symmetry. The FMO structure shown in Figure 75 differs slightly from that of **[60]**. One of the key MOs responsible for deshielding in **[60]** is the vacant vinylidene p orbital. In **[62]**, the high symmetry leads to the vacant p orbital on the central carbon being present as a set of degenerate helical orbitals.

The main deshielding interactions in **[62]** are  $\varphi_7 \xrightarrow{\hat{R}_x} \varphi_{12}$  and  $\varphi_7 \xrightarrow{\hat{R}_y} \varphi_{13}$ . These transitions are degenerate and have good destructive overlap but a large energy gap of 12.84 eV leading to  $\delta_{11/22} = 229$  ppm. This is much larger than the equivalent transition for **[60]**. High symmetry leads to smaller deshielding at the central carbon of allene.

Substitution of one  $\text{CH}_2$  end of the allene by  $\text{CMe}_2$  would reduce the symmetry from  $D_{2d}$  to  $C_{2v}$ , the same point group as **[60]**. The chemical shift tensors were calculated for 1,1-dimethylallene, but the tensors are unaffected by the change in symmetry. With minor changes to  $\delta^{\text{iso}}$  being observed ( $\delta_{\text{C}} = 207.7$  for allene,  $\delta_{\text{C}} = 202.6$  for 1,1-

dimethylallene). The changes were so small that the chemical shift tensors were not further analysed as this indicates that the orbital structure must remain unperturbed.

Although free allenes may exhibit some of the same reactivity as vinylidene complexes due to the LUMO possessing p orbital character at the central carbon, the chemical shift tensors show that allenes are not necessarily good models for deshielding in vinylidenes. The FMOs of allenes have been shown to be highly conjugated across the molecule with high levels of degeneracy. Breaking of the electronic symmetry, in uncoordinated or coordinated vinylidenes, leads to orbitals that are much more localised at  $C_{\alpha}$ . Highly localized orbitals are coupled much more effectively by rotational operators in the magnetic field, leading to the unique deshielding seen in vinylidenes. The result is that allenes are a poor model for the deshielding in coordinated vinylidene complexes. This also explains why the chemical shift tensors of **[64]** exhibit shielding compared to **[62]** unlike their vinylidene equivalents.

As  $CH_2$  was a poor model for  $[Ru(\eta^5-C_5H_5)(PPh_3)_2]^+$ ,  $^+NMe_2$  was also examined as an electronic model for  $[Ru(\eta^5-C_5H_5)(PPh_3)_2]^+$ . Even though both  $CH_2$  and  $^+NMe_2$  are isolobal with  $[Ru(\eta^5-C_5H_5)(PPh_3)_2]^+$ ,  $^+NMe_2$  carries the same charge and leads to vinylidene type compounds that possess  $C_{2v}$  symmetry. The FMOs responsible for deshielding in **[66]**<sup>+</sup> are shown in Figure 76.

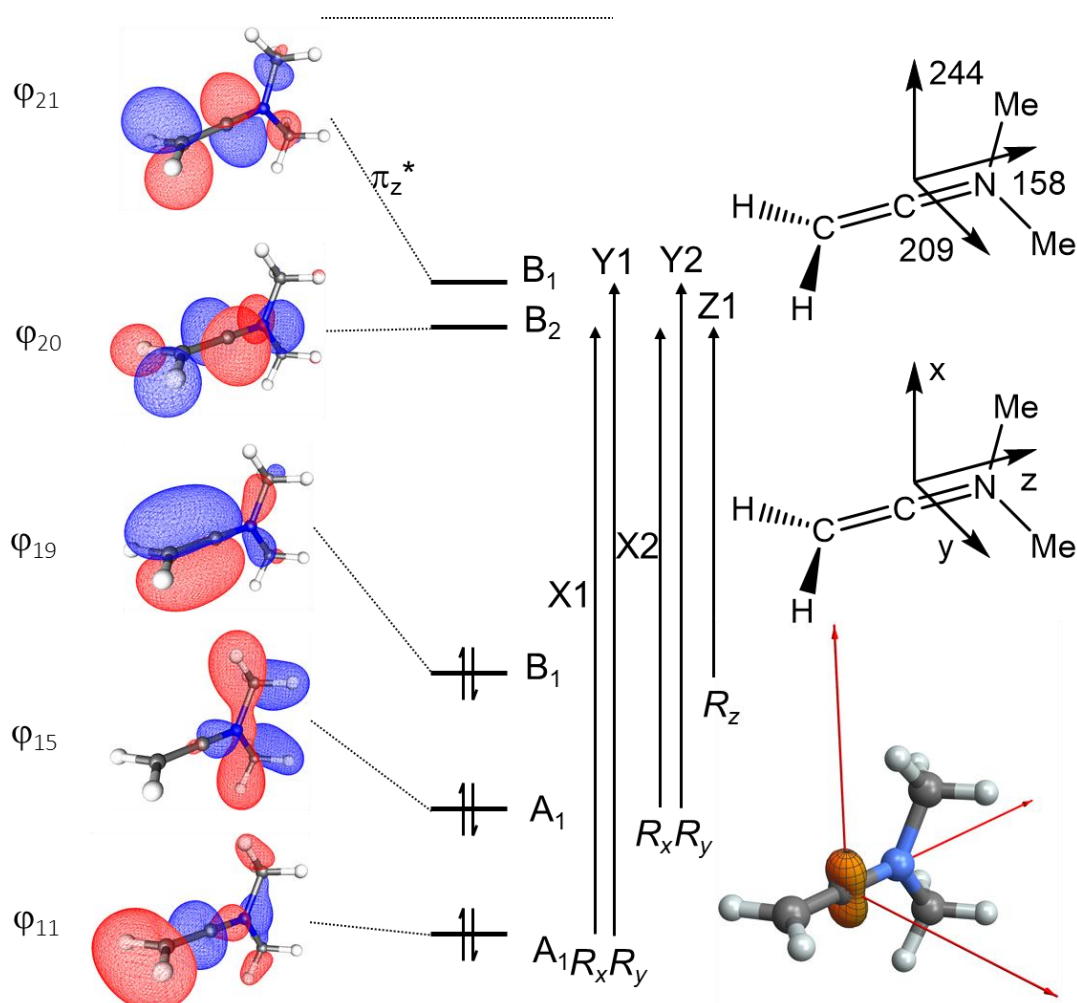


Figure 76. FMO diagram of  $[66]^+$  with selected orbitals visualised in gOpenMol (left). Key transitions identified using group theory.  $[66]^+$  optimised in Turbomole at the BP86/def2\_SV(P) level of theory, chemical shift tensors calculated in Orca at the PBE0/def2\_TZVPP level of theory with ZORA corrections and visualised in Wolfram Mathematica with pictorial representations (right). The barycentre is represented by the dotted line.

$^+NMe_2$  appears to give similar changes to the chemical shift tensors as  $[CpRu(PPh_3)_2]^+$ . Although  $CMe_2$  and  $^+NMe_2$  are isoelectronic,  $^+NMe_2$  mirrors the charge of the ruthenium fragment.

Two transitions were observed that were responsible for the large deshielding along  $\delta_{11}$ , which lies along the x axis,  $\phi_{11} \xrightarrow{\hat{R}_x} \phi_{20}$  (X1) and  $\phi_{15} \xrightarrow{\hat{R}_x} \phi_{20}$  (X2). Although X2 has a narrower energy gap than X1, X1 dominates the deshielding interaction due to the very low  $C_\alpha$  p orbital character in  $\phi_{15}$ . This large deshielding interaction is very similar

to that in the free vinylidene, but with a larger energy gap of 13.69 eV vs 5.77 eV. This explains the large reduction in deshielding in  $\delta_{11}$  compared to **[60]** with  $\delta_{11} = 244$  ppm vs  $\delta_{11} = 1048$  ppm.

### 3.5.3 Explanation of the changes in deshielding of coordinated vinylidene complexes

Now with a good understanding of the transitions responsible for deshielding in free vinylidene, **[60]**, and the extended allene and vinyliminium, **[62]** **[66]**<sup>+</sup>, the deshielding of **[2a]**<sup>+</sup> can be explored.

The chemical shift tensors of **[2a]**<sup>+</sup> are similar to those of the uncoordinated equivalent **[60]**. The main difference between the two species is the magnitude of the  $\delta_{11}$  tensor. In **[60]** this is associated with the  $\sigma_{z \rightarrow p_y}^{\hat{R}_x}$  transition. On coordination to the metal centre the overlap and energy of this transition reduces, leading to the large chemical shift tensors observed. The relative orbital energy gap between fluorinated and non-fluorinated vinylidenes remains constant.

The chemical shift tensors of fluorovinylidene complex **[3a]**PF<sub>6</sub> differ from those of **[2a]**BF<sub>4</sub> by the magnitude of the  $\delta_z$  tensor,  $\delta_{22}$  in **[3a]**PF<sub>6</sub> and  $\delta_{33}$  in **[2a]**BF<sub>4</sub>. The deshielding along z in **[60]** and **[61]** is dominated by the  $\pi_{x \rightarrow p}^{\hat{R}_z}/\pi_y$  transition, the same transition is responsible for the deshielding along z in **[2a]**BF<sub>4</sub> and **[3a]**PF<sub>6</sub> and is destructive in both complexes. This is the HOMO→LUMO transition. The HOMO and LUMO of **[2a]**<sup>+</sup> and **[3a]**<sup>+</sup> are shown in Figure 77. Increasing  $\pi$  bonding character between the C <sub>$\alpha$</sub>  and C <sub>$\beta$</sub>  in the fluorovinylidene leads to a larger overlap between the two orbitals. This is accompanied by contraction of the HOMO→LUMO energy gap, 3.89 eV in **[2a]**<sup>+</sup> vs 3.32 eV in **[3a]**<sup>+</sup>. Both effects combined result in the large change in deshielding along the z axis and the large 35 ppm change in  $\delta^{\text{iso}}$  observed between the two species:  $\delta^{\text{iso}} = 353.7$  ppm vs  $\delta^{\text{iso}} = 388.6$  ppm.

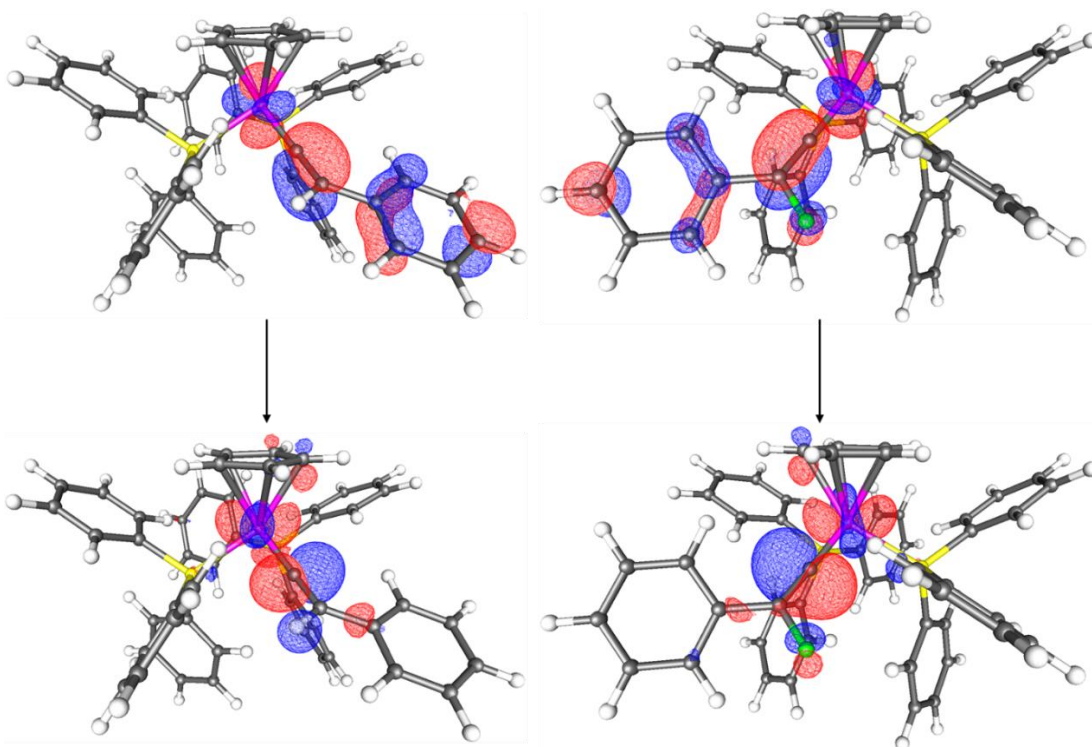


Figure 77. HOMO (top) and LUMO (bottom) of **[2a]<sup>+</sup>** (left) and **[3a]<sup>+</sup>** (right) showing the change in bonding character on fluorination. This transition dominates the changes to  $\delta^{\text{para}}$  along the z axis.

### 3.5.4 Discussion of vinylidene tensors

The FMOs of **[66]<sup>+</sup>**, shown in Figure 76, are very similar to those of **[60]**, Figure 70, with the key transitions being conserved. The magnitude of the chemical shift tensors in **[66]<sup>+</sup>** have similar weightings to both free and ruthenium coordinated vinylidenes. But the absolute magnitude decreases: **[60]** >> **[2a]<sup>+</sup>** > **[66]<sup>+</sup>**. The symmetry of all the NMR relevant FMOs is the same in all compounds. The deshielding in **[66]<sup>+</sup>** differs from **[2a]<sup>+</sup>** mostly along the x axis, which is dominated by a  $\sigma_z \xrightarrow{\hat{R}_x} p_y$  transition. The energy gap between these orbitals must be larger in **[66]<sup>+</sup>** suggesting depression of the  $\sigma_z$ -orbital in energy.

The bonding orbital being contributed by the <sup>+</sup>NMe<sub>2</sub> fragment will have a large degree of N 2p<sub>z</sub> character, with a small N 2s contribution, which may mix with the vinylidene  $\sigma_z$  orbital. The orbital contributed by a ruthenium fragment will be nearly entirely

$4d_{z^2}$  in character. The mixing between the N-based orbital and the vinylidene will be much more similar electronically to the mixing with Ru compared to the free vinylidene due to the molecular orbital energies being similar. This allows stabilisation of the vinylidene orbitals. Increased mixing will depress the energy of the in-phase combinations and increase the energy of the antiphase combinations. This is the origin of the reduced deshielding in **[66]**<sup>+</sup> and **[2a]**<sup>+</sup> compared to **[60]**. Deshielding increases vastly in the uncoordinated vinylidenes **[60]** and **[61]**. Small energy gaps between the FMOs, combined with extremely well-localised orbitals, leads to large increases in deshielding along all axes. The similar deshielding values observed in **[66]**<sup>+</sup> and **[2a]**<sup>+</sup> suggest similar electronic localisations and energies. The tensors being more deshielded in **[2a]**<sup>+</sup> suggest that the bonding orbitals are slightly higher in energy than the equivalent orbitals in **[66]**<sup>+</sup>. The chemical shift tensors suggest that vinyliminium compounds may exhibit some of the same reactivity as fluorovinylidene complexes, allowing the synthesis of novel fluorinated compounds without the need for the metal.

Substitution of a proton for a fluorine in vinylidene complexes leads to a substantial change to isotropic deshielding,  $\delta^{iso}$ , shown in Figure 46 in section 3.1.5 and Figure 78. SS NMR spectroscopy reveals that the changes to deshielding are accompanied by a change in chemical shift anisotropy shown in Figure 78.

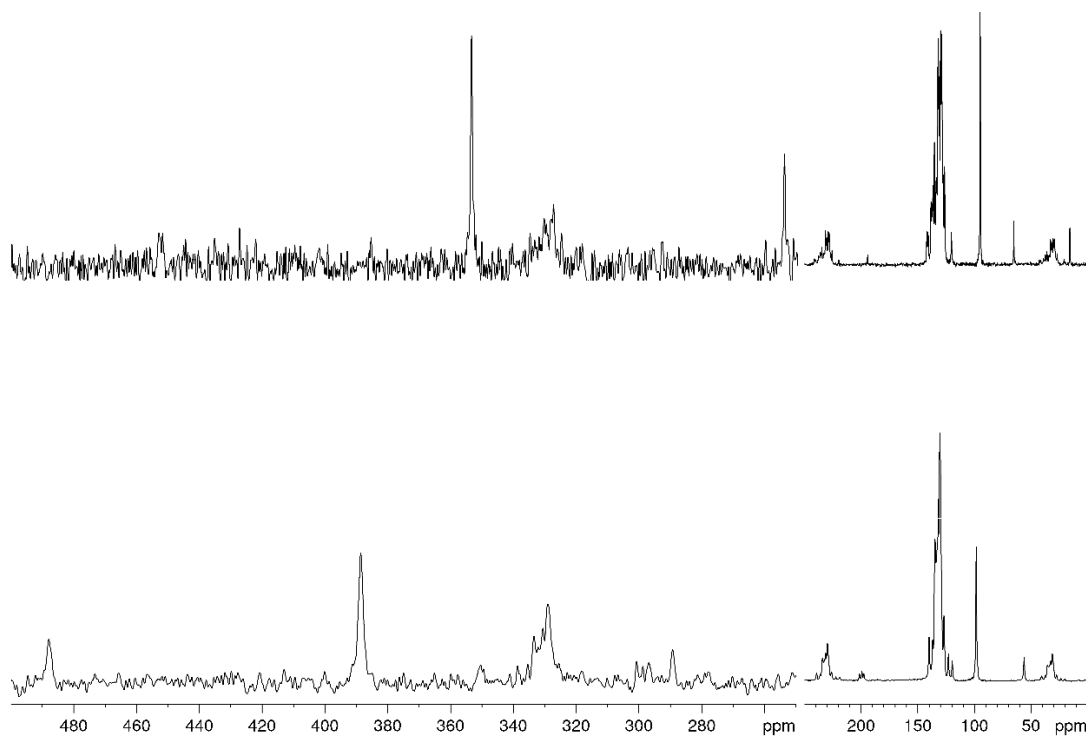


Figure 78.  $^{13}\text{C}\{^1\text{H}\}$  CP MAS SS NMR Spectra of **[2a]**BF<sub>4</sub> (Top) and **[3a]**PF<sub>6</sub> (Bottom) recorded at 101 MHz at a spinning speed of 10 kHz showing changes to  $\delta^{\text{iso}}$ . The intensity of the vinylidene resonances has been increased to aid identification.

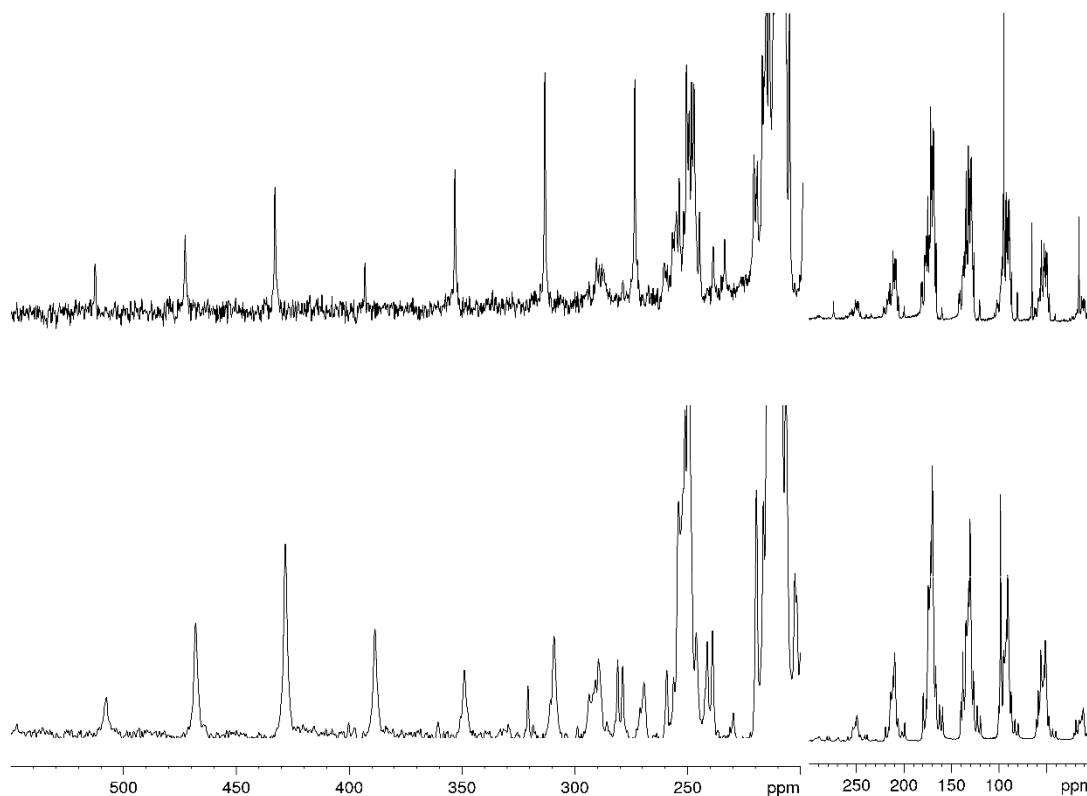


Figure 79.  $^{13}\text{C}\{^1\text{H}\}$  CP MAS SS NMR Spectra of **[2a]**BF<sub>4</sub> (Top) and **[3a]**PF<sub>6</sub> (Bottom) recorded at a spinning speed of 4 kHz showing changes to CSA. The intensity of the vinylidene resonances has been increased to aid identification.

The changes in anisotropy were revealed to be associated with changes to a single tensor,  $\delta_z$ . Changes in  $\delta_z$  are mirrored in uncoordinated vinylidene species, **[60]** and **[61]**, although the magnitudes of changes are much greater in uncoordinated vs coordinated vinylidenes as described earlier. The major orbitals responsible for deshielding along  $\delta_z$  are the same in both vinylidenes, with the HOMO→LUMO transition being dominant. The key FMO energies are shown in Figure 80.

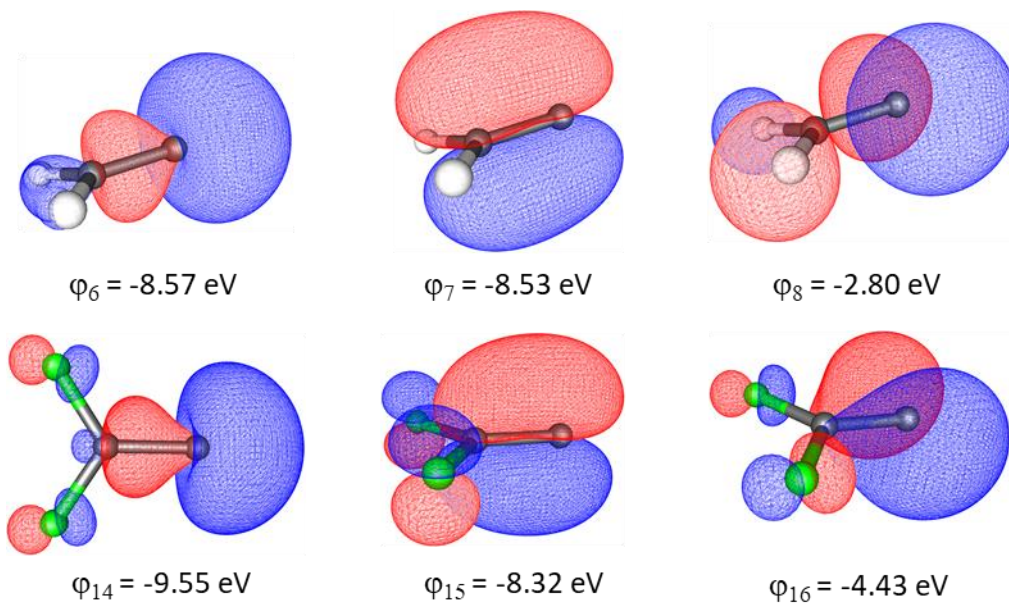


Figure 80. Key orbitals of **[60]** and **[61]** responsible for deshielding with orbital energies, calculated in Orca at the PBE0/def2\_TZVPP level of theory with ZORA corrections.

Changes to deshielding along the x axes are not observed between vinylidene and difluorovinylidene. As shown in Figure 80 above, the LUMO of **[61]** is lower in energy than in **[60]** by 1.63 eV. However, as well as lowering of the energy of the LUMO, the  $\sigma_z$  bonding orbital of **[61]** also is lower in energy than the proteo- equivalent by 0.98 eV. This means that the energy gap changes from 5.77 eV (**[60]**) to 5.17 eV (**[61]**). This small compression in energy is accompanied by small changes to overlap. Introduction of fluorine to the vinylidene moiety causes both bonding and antibonding orbitals to lower in energy but keeps the relative energy similar leading to constant deshielding along  $\delta_x$ .

Unlike the deshielding along  $\delta_x$ , the relative energies of the HOMO and LUMO change on introduction of fluorine, changing the magnitude of  $\delta_z$ . Although the LUMO decreases in energy, the energy of the HOMO remains constant: -8.53 eV vs -8.32 eV. The result of the constant energy of the HOMO is that the energy gap narrows and deshielding is observed.

Coordination of ruthenium to vinylidene and fluorovinylidene fragments mirrors this trend with the energy of the HOMO only changing from -8.02 eV (**[2a]<sup>+</sup>**) to -7.97 eV

([3a]<sup>+</sup>). All changes observed in the deshielding must arise from the compression of the LUMO from -4.13 eV ([2a]<sup>+</sup>) to -4.58 eV ([3a]<sup>+</sup>) and the increased destructive overlap of this transition. The change in energy of the LUMO in the ruthenium coordinated fluorovinylidene complexes is much smaller than in the free fluorovinylidene, therefore the deshielding is significantly reduced on coordination.

Metal bound vinylidenes have been reported in the literature with a range of halogen atoms, and values of  $C_{\alpha} \delta^{iso}$  recorded; the structures are shown in Figure 81. Chemical shift tensors are shown in Table 18.<sup>112</sup> Of the halogenovinylidenes synthesized, the isotropic chemical shift of the vinylidene  $C_{\alpha}$  is only strongly deshielded with respect to  $R = H$  by  $R = F$ . The presence of other halogens does not lead to the large deshielding interaction observed with fluorine and experimentally the deshielding at  $C_{\alpha}$  decreases as the halogen increases in size. The chemical shift tensors of the vinylidenes in Figure 81 were calculated, the same trends were observed. The visualised tensors are shown in Figure 82.

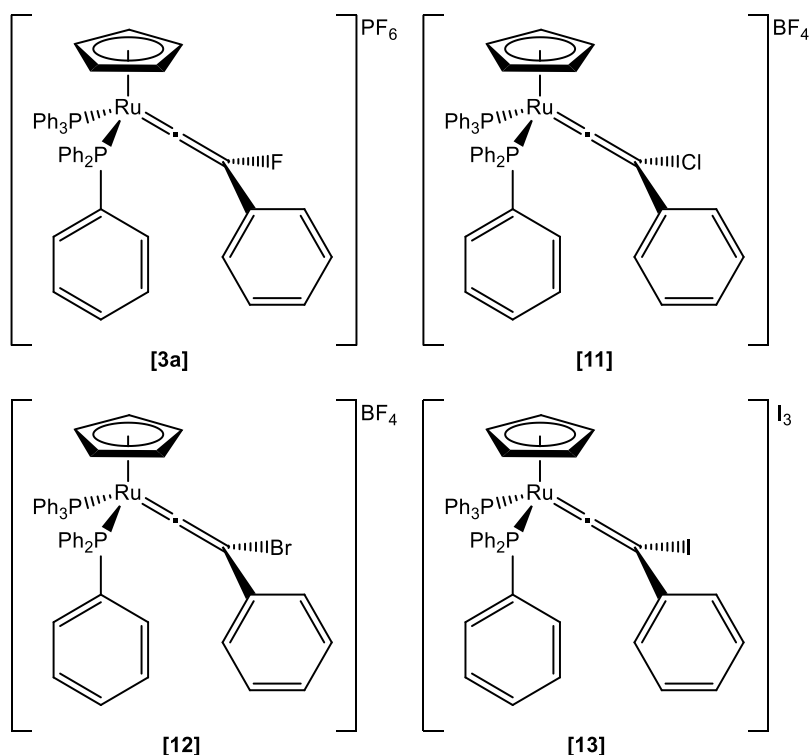


Figure 81. Structure of halogenovinylidene complexes synthesized by Lynam and Slattery.

The isotropic chemical shift,  $\delta^{\text{iso}}$ , becomes more shielded as halogen size increases  $\text{F} \gg \text{Cl} > \text{Br} > \text{I}$ . The changing deshielding is represented in Table 18 below. The chemical shift tensors were also calculated for  $\text{C}_\beta$  and the results are shown in Table 19.

Table 18. Chemical shift tensors of halogen vinylidene complexes  $\text{C}_\alpha$  calculated in Orca at the PBE0/def2\_TZVPP level of theory with ZORA corrections. Numbers in parentheses are experimental results reported by Slattery and Lynam.<sup>112</sup>

Complex	$\delta^{\text{iso}}$ / ppm	$\delta_{11}$ / ppm	$\delta_{22}$ / ppm	$\delta_{33}$ / ppm
<b>[3a]</b> <sup>+</sup>	418 (389.0)	531	471	251
<b>[11]</b> <sup>+</sup>	366 (353.5)	528	292	278
<b>[12]</b> <sup>+</sup>	349 (340.3)	522	295	230
<b>[13]</b> <sup>+</sup>	330 (323.6)	510	299	180

Table 19. Chemical shift tensors of halogen vinylidene complexes  $\text{C}_\beta$  calculated in Orca at the PBE0/def2\_TZVPP level of theory with ZORA corrections.

Complex	$\delta^{\text{iso}}$ / ppm	$\delta_{11}$ / ppm	$\delta_{22}$ / ppm	$\delta_{33}$ / ppm
<b>[3a]</b> <sup>+</sup>	185	240	205	109
<b>[11]</b> <sup>+</sup>	133	163	157	78
<b>[12]</b> <sup>+</sup>	124	172	118	83
<b>[13]</b> <sup>+</sup>	114	172	111	57

As well as the general shielding trend that is observed for  $\text{C}_\alpha$  ( $\text{F} \gg \text{Cl} > \text{Br} > \text{I}$ ), the same trend is observed for  $\text{C}_\beta$  with shielding increasing with halogen size. The magnitude of the change between F and Cl is much larger for both carbon environments than from Cl to Br or Br to I.

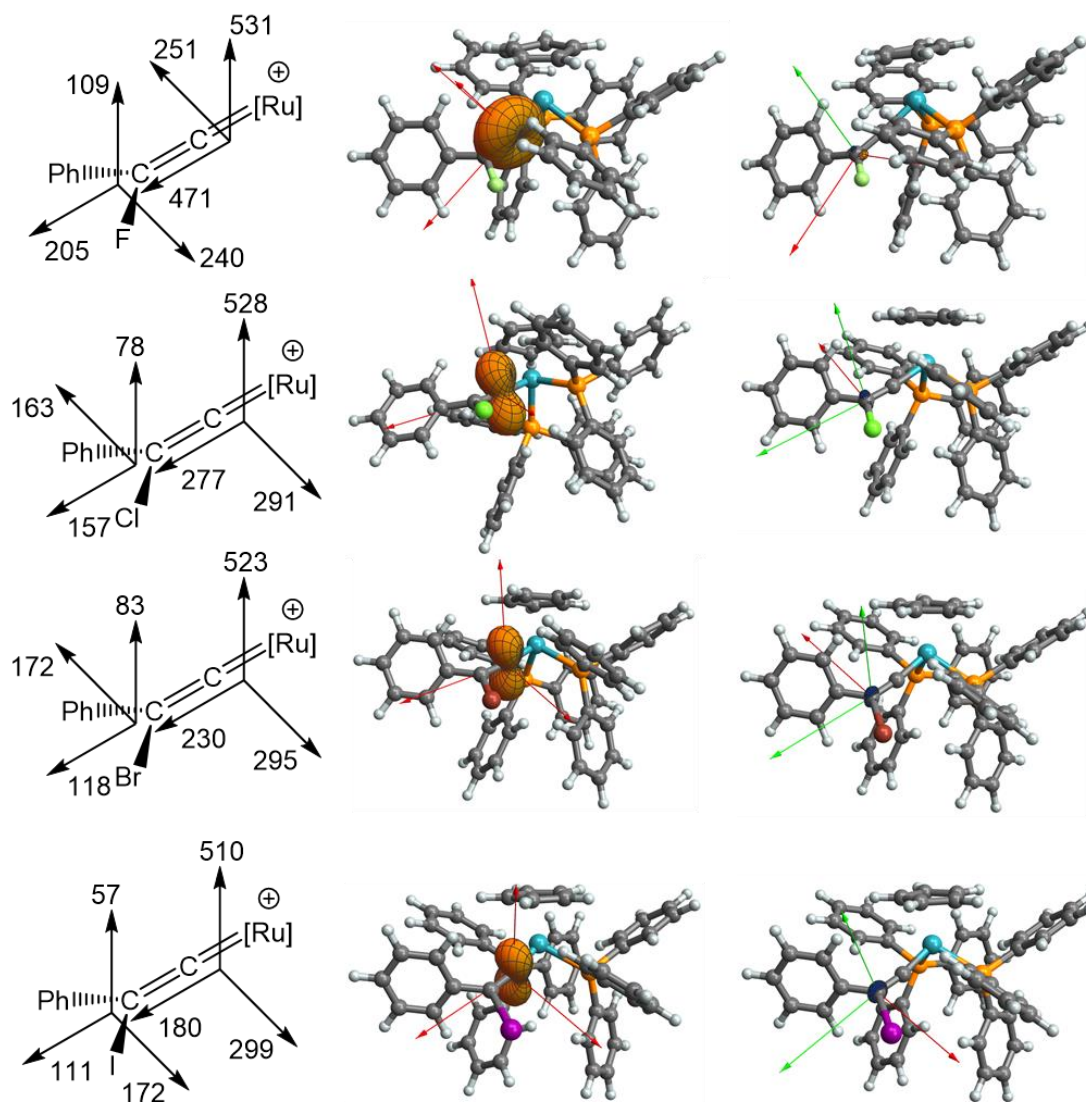


Figure 82. Pictorial (left) and visualised chemical shift tensors ( $C_{\alpha}$ , middle) ( $C_{\beta}$ , right) of halogenovinylidene complexes.

The magnitude of  $\delta_{11}$  remains largely constant between all complexes (between 530.7 for R = F, and 510.1 for R = I). However, the magnitude of  $\delta_{22}$  remains relatively unchanged between R = Cl, Br, and I, but the value for R = F is some 200 ppm greater. The shape of the tensors for these complexes are more similar to **[2a]<sup>+</sup>**.

Fluorine is unique in that the 2p orbital interacts strongly the vinylidene LUMO, depressing it in energy. The decreasing energy gap and increasing orbital overlap of the HOMO→LUMO transition on substitution of H for F lead to the observed changes in deshielding. Other halogen atoms do not interact as strongly with the HOMO, with

the magnitude of change in chemical shift tensors along  $\delta_z$  being reduced, showing chemical shift tensor weightings that are much more similar to **[2a]**<sup>+</sup>.

## 3.6 Interpretation of alkynyl tensors

### 3.6.1 Identification of FMO transitions using simple alkyne models

The chemical shielding of ethyne **[38]** has been described in section 2.7.2. The high symmetry of ethyne leads to axially symmetric deshielding. The key transitions for deshielding are  $\sigma_z \xrightarrow{\hat{R}_{y/x}} \pi_{x/y}^*$  and  $\pi_{x/y} \xrightarrow{\hat{R}_{y/x}} \sigma_z^*$ . The chemical shift tensors for the free alkyne **[38]** and the coordinated alkynyl complex **[4]** are similar, as shown in Figure 83, with deshielding observed symmetrically around the x and y axes and shielding along the z axis. This suggests that, although the formal symmetry of **[4]** is  $C_s$ , a local symmetry exists at  $C_\alpha$  resulting in the chemical shift tensors possessing similar weightings.

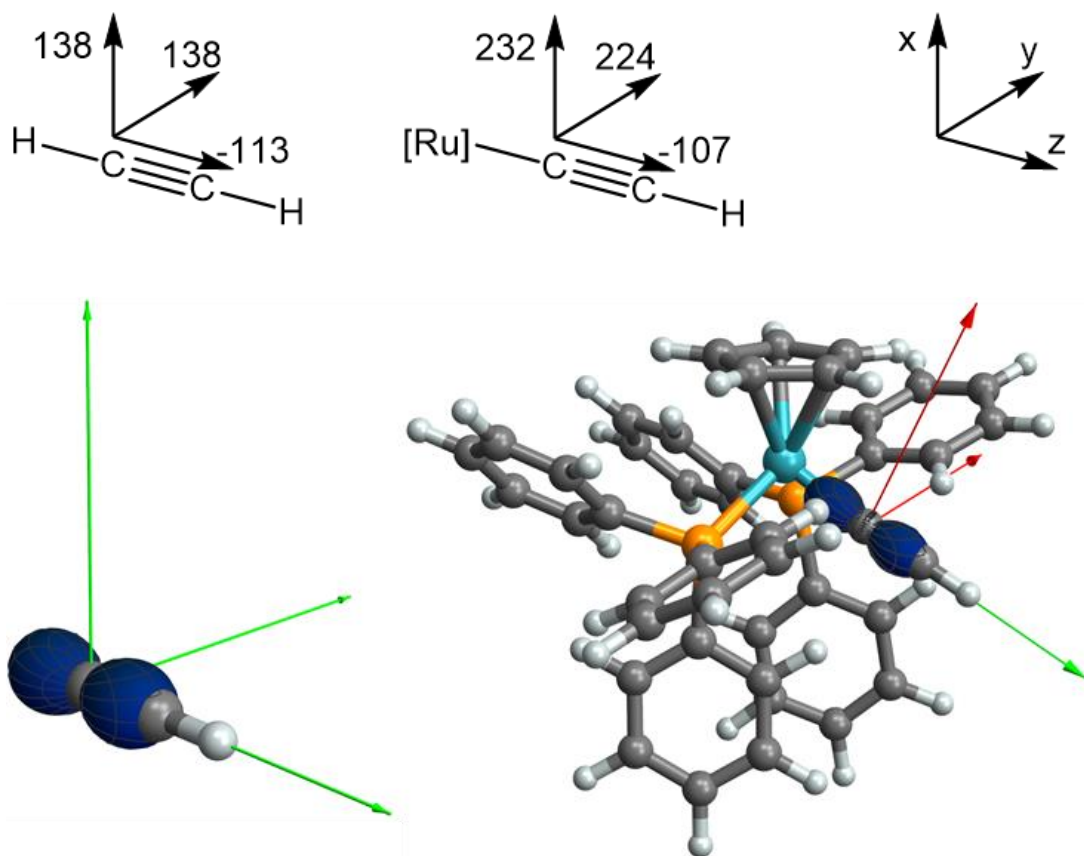


Figure 83. Pictorial (Top) and visualised (bottom) chemical shift tensors of **[38]** and **[4]**.

The  $\delta_{33}$  tensors of **[38]** and **[4]** are similar with the main difference being in the deshielding of  $\delta_{11}$  and  $\delta_{22}$  (**[38]**;  $\delta_{11} = 138$ ,  $\delta_{22} = 138$ ,  $\delta_{33} = -113$ , **[4]**;  $\delta_{11} = 232$ ,  $\delta_{22} = 224$ ,  $\delta_{33} = -107$ ). In **[38]**, no orbitals possess the correct symmetry to overlap and contribute to deshielding along the z axis. This results in the similarity of the  $\delta_{33}$  tensors. The orbitals that possess strong character along the x and y axes at  $C_\alpha$  are shown in Figure 33 in section 2.7.2. These orbitals do not possess the correct symmetry for any overlap when coupled by  $\hat{R}_z$ .

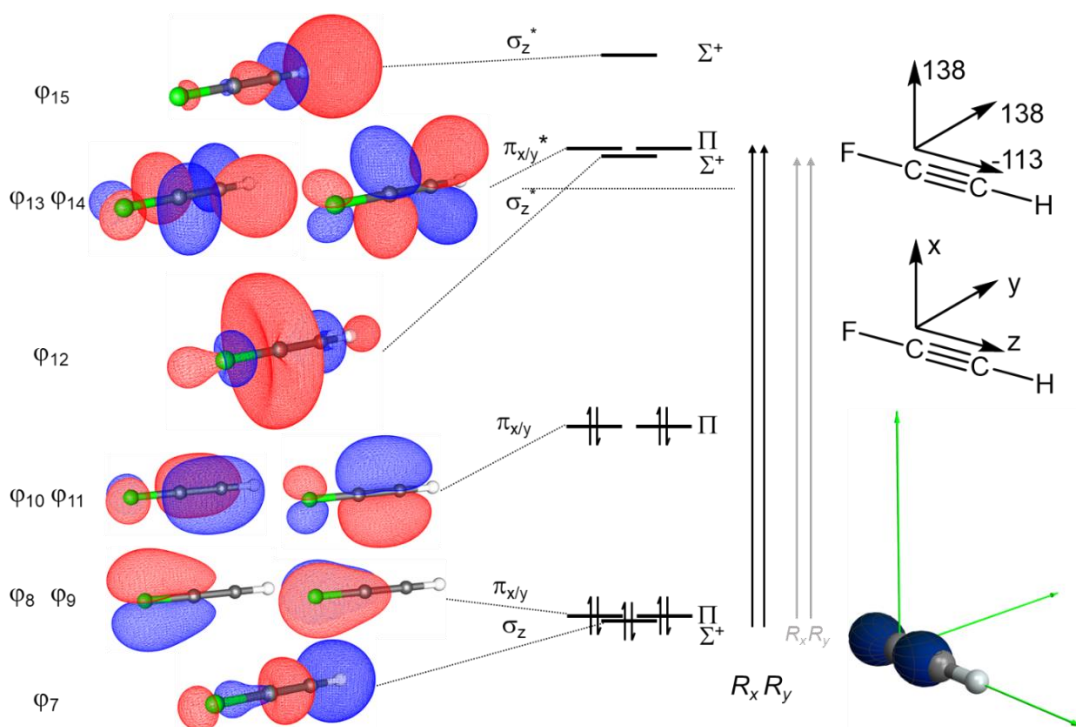


Figure 84. FMO diagram of fluoroethyne **[53]** with selected orbitals visualised in gOpenMol (left). Key transitions identified using group theory. **[53]** optimised in Turbomole at the BP86/def2\_SV(P) level of theory, chemical shift tensors calculated in Orca at the PBE0/def2\_TZVPP level of theory with ZORA corrections and visualised in Wolfram Mathematica with pictorial representations (right). The barycentre is represented by the dotted line.

No orbital transitions contribute strongly to deshielding along the z,  $\delta_{33}$ , axis. Large changes to  $\delta_{iso}$  are observed between **[38]** and **[53]**, with  $C_\alpha$  of **[53]** being shielded by  $\sim 70$  ppm. This large shift is identified as reduction of deshielding along the x and y axes. To understand the chemical shift tensors of **[53]**, chemical shift tensors were calculated for fluoroethyne, **[53]**. The key transitions are shown in Figure 84.

Introduction of the fluorine  $2p_{x/y}$  orbitals to the alkyne  $\pi$  system has little effect on the energy of the LUMO. However, the  $2p_z$  orbital of fluorine can interact with the alkyne  $\sigma$  bonding interaction, stabilising this orbital making it more bonding and lower in energy. Increasing the energy gap from 14.53 eV (**[38]**) to 16.17 eV (**[53]**) halves the magnitude of the deshielding along the x and y axes.

The Kohn-Sham FMO diagram results in orbitals that show good similarity to Brueckner orbitals calculated in the literature.<sup>113, 114</sup> In the work by Lynam and Slattery, Brueckner orbitals were generated for: HCCH, HCCF, FCCF, [Ru]CCH, and [Ru]CCF. The energies of the Brueckner orbitals agree more closely with the photoelectron spectroscopy of HCCH, HCCF, and FCCF than the Kohn-Sham orbitals. The order of the  $\sigma$  bonding and  $\pi$  bonding orbitals  $\varphi_7$  and  $\varphi_{8/9}$  are reversed. The  $\sigma_z$  orbital becomes progressively more stabilised on introduction of fluorine to the alkyne. As this orbital depresses in energy, the energy gap between this and the LUMO increases, decreasing the deshielding interaction.

### 3.6.2 Coordinated alkynyl complexes

Unlike **[60]** and **[2a]<sup>+</sup>**, the differences in chemical shift tensors between **[38]** and **[4]** are small suggesting that the changes to the electronics in vinylidenes on coordination to a metal are much larger compared to the exchange of the alkyne terminal proton for a metal. The key transitions in **[4]** are the same transitions responsible for deshielding in **[38]**. As the chemical shift tensors are so similar, it can be inferred that the FMO energies and localisations are much closer in alkynes than in vinylidenes. Interaction of the ruthenium d orbitals with both the  $\sigma$  and  $\pi$  systems of the alkyne lead to FMOs with similar relative energies as the free alkynes. Not only does the orbital localisation structure of the alkyne remain relatively unperturbed, but the relative energies of the orbitals also remain constant. The same trends are observed on substitution of a proton for a fluorine with the deshielding along the x and y axes reducing significantly.

### 3.6.3 Discussion of alkynyl tensors

The chemical shift tensors for alkynes and alkynyl complexes are similar. The trends observed at  $C_\alpha$  on changing the terminal group from H to Ph to F are conserved. This suggests that, although the metal has orbitals that may mix with the  $\pi$  system, the fundamental FMO structure is conserved. Nevertheless, the  $\delta_{11}$  and  $\delta_{22}$

tensors show greater deshielding in the metal bound equivalents. The origin of this effect is the destabilisation of the  $\sigma$  bonding orbital. Increasing the energy of this orbital reduces the energy gap between the  $\sigma$  bonding orbital and the degenerate LUMOs. Because of energy change being associated with the  $\sigma$  bonding orbital, there is no correlation between the UV-*vis* transitions and the magnitude of deshielding, unlike **[2a]**<sup>+</sup> and **[3a]**<sup>+</sup>.

The reduction in deshielding along the  $\delta_{11}$  and  $\delta_{22}$  between **[4]** and **[7]** is also observed in the free alkynes **[38]** and **[53]**. All the changes in  $\delta^{\text{iso}}$  are associated with these tensors and the trends are observed independent of coordination to a metal centre. This suggests that the metal has a relatively small effect on the FMOs of alkynes when coordinated in an  $\eta^1$  fashion.

### 3.7 Correlation of chemical shift tensors and first excitation energy

As the deshielding in vinylidene complexes along  $\delta_z$  is correlated to transitions involving the HOMO and LUMO, it was theorised that the deshielding could be correlated to the lowest energy excitation. To explore this, time dependent (TD) DFT calculations were performed in Orca at the PBE0/def2\_TZVPP level of theory with ZORA approximations. The first 10 excitations were calculated for a range of vinylidene and alkynyl complexes as shown in Figure 85 and the energy of the first excitation tabulated in Table 20. The energy of the first excitation was plotted against the chemical shift tensors. Trends were only observed when the excitation energies were plotted against the tensor that lies along the M-C bond axis as is shown in Figure 86.

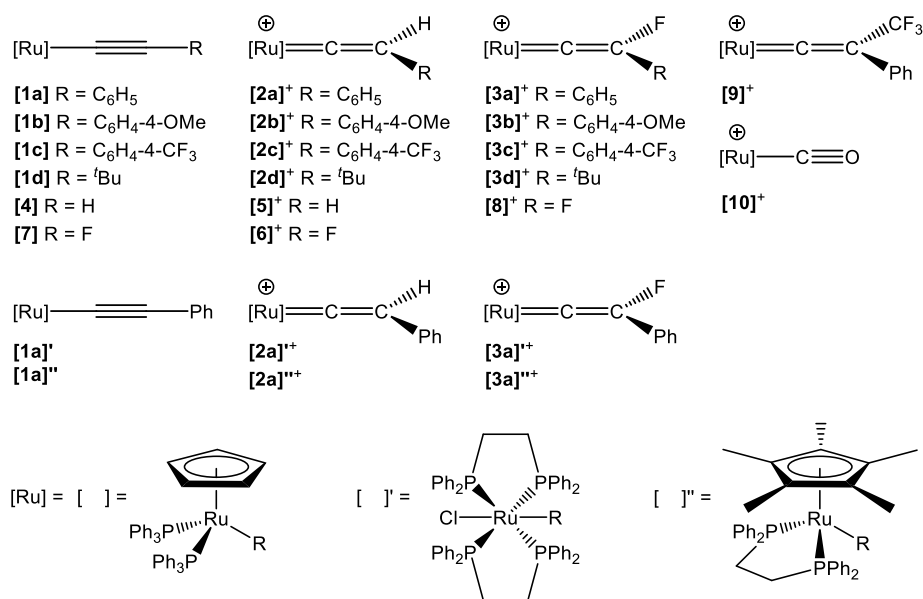


Figure 85. Ruthenium organometallic complexes studied by quantum chemical calculations using DFT and TD TDF.

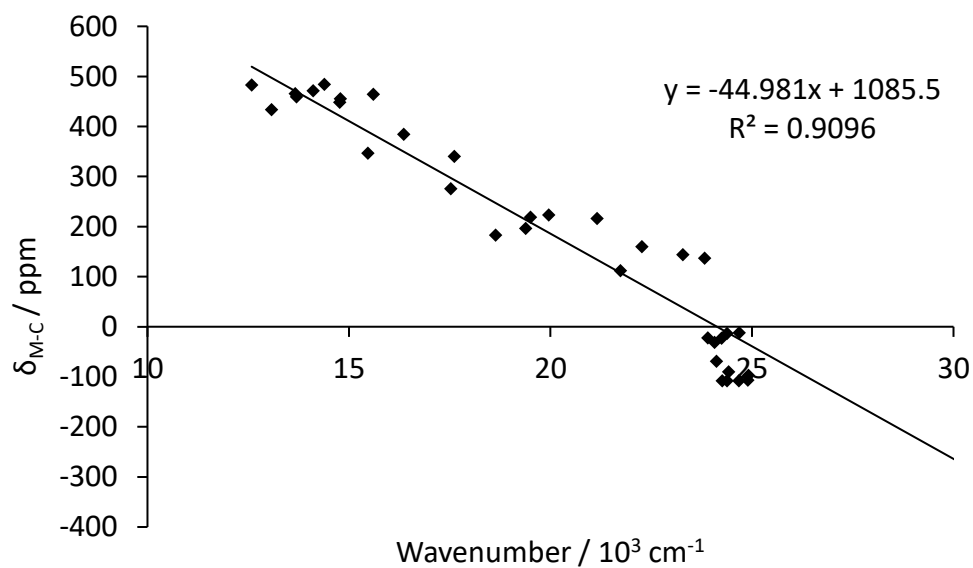


Figure 86. Correlation of the first excitation energy calculated using TD DFT and chemical shift tensors pointing along the M-C bond axis. Both calculated in Orca at the PBE0/def2\_TZVPP level of theory with ZORA corrections.

Table 20. Calculated chemical shift tensors along the M-C bond axis ( $\delta_{M-C}$ ) and calculated wavelength and wavenumber of the first excitation of ruthenium organometallics. Both calculated at the PBE0/def2\_TZVPP level of theory with ZORA corrections.

Complex	$\delta_{M-C}$ / ppm	Calculated First Excitation	
		Wavelength / nm	Wavenumber / $10^3$ $cm^{-1}$
<b>[1a]</b>	-23	413	24
<b>[1a]'</b>	-14	410	24
<b>[1a]''</b>	-23	418	24
<b>[1b]</b>	-32	416	24
<b>[1c]</b>	-13	405	25
<b>[1d]</b>	-69	415	24
<b>[2a]<sup>+</sup></b>	196	516	19
<b>[2a]<sup>++</sup></b>	182	537	19
<b>[2a]<sup>+++</sup></b>	223	501	20
<b>[2b]<sup>+</sup></b>	276	571	18
<b>[2c]<sup>+</sup></b>	218	513	20
<b>[2d]<sup>+</sup></b>	216	473	21
<b>[3a]<sup>+</sup></b>	471	709	14
<b>[3a]<sup>++</sup></b>	433	765	13
<b>[3a]<sup>+++</sup></b>	448	677	15
<b>[3b]<sup>+</sup></b>	459	730	14
<b>[3c]<sup>+</sup></b>	483	695	14
<b>[3d]<sup>+</sup></b>	464	641	16
<b>[4]</b>	-107	402	25
<b>[4]'</b>	-97	401	25
<b>[4]''</b>	-108	410	24
<b>[5]<sup>+</sup></b>	143	429	23
<b>[5]<sup>++</sup></b>	111	460	22
<b>[5]<sup>+++</sup></b>	136	420	24

[6] <sup>+</sup>	384	611	16
[6] <sup>'+</sup>	346	647	15
[6] <sup>''+</sup>	340	568	18
[7]	-108	405	25
[7] <sup>'</sup>	-90	410	24
[7] <sup>''</sup>	-108	412	24
[8] <sup>+</sup>	465	732	14
[8] <sup>'+</sup>	483	795	13
[8] <sup>''+</sup>	455	676	15
[9] <sup>+</sup>	159	449	22
[10] <sup>+</sup>	-92	331	30

Unlike vinylidene complexes, the deshielding along the z axis in alkynyl complexes is not represented by a transition involving the HOMO and LUMO as the overlap is poor. In general, as deshielding increases along  $\delta_z$ , the energy of the first excitation decreases. This suggests that the chemical shift tensors are correlated to the HOMO→LUMO transition. Given that the HOMO→LUMO transition is not always responsible for deshielding, the correlation is not necessarily absolute.

It may be possible to identify a target system where the HOMO→LUMO transition is also responsible for deshielding. In this system, the changes to deshielding would be able to be correlated with visible absorption frequencies. This would require further study beyond this thesis and has not been explored further.

### 3.8 Discussion of differences in tensors between metal fragments

To investigate the effect of the metal fragment in alkynyl and vinylidene complexes, NMR calculations were performed on [1a], [2a]<sup>+</sup>, and [3a]<sup>+</sup>. To contrast these complexes the chemical shift tensors of [1a]<sup>'</sup>, [2a]<sup>'+</sup>, [3a]<sup>'+</sup>, [1a]<sup>''</sup>, [2a]<sup>''+</sup>, and [3a]<sup>''+</sup> were calculated, shown in Figure 87. The difference between these complexes is the metal fragment. In general, the chemical shift tensors that were recovered are relatively constant. This invariance is relatively independent from the type of

complex, even though  $[\text{Cp}^*\text{Ru}(\text{dppe})]^+$  is often seen as a more electron rich than  $[\text{CpRu}(\text{PPh}_3)_2]^+$ .

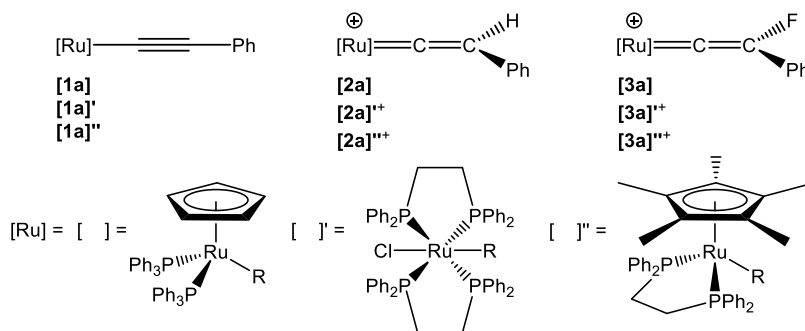


Figure 87. Structure of different ruthenium fragments used to study the effect of metal fragment on alkynyl- and vinylidene  $C_\alpha$  chemical shift. The chemical shift of  $C_\alpha$  was largely invariant on changing metal fragment.

As the chemical shift tensors are influenced by the molecular orbitals, it can be inferred that the molecular orbitals of each class of complex share similar localisations and orbital energy gaps. The reactivity of the complexes is not the same. One major difference that may not be accounted for in their reactivity is the steric effect and this is likely what causes the difference in reactivity between metal fragments. The magnitudes of the tensors of  $C_\alpha$  suggest that the molecular orbitals of the organic fragments involved in deshielding do not change localisation or relative energy with changing metal fragment. The other possible explanation is that the relative energies of the MOs do not change between fragments, but the total energies of the orbitals do change.

### 3.9 Discussion of differences in $C_\alpha$ chemical shift tensors in metal vinylidene- and alkynyl- complexes on changing remote conjugated substituents (R groups)

Unlike the steric effects described earlier, changing the remote conjugated R group for a particular class of complex does influence the magnitudes of the chemical shift tensors. The R group being the terminal group on the alkyne,  $[\text{Ru}]-\text{C}\equiv\text{C}-\text{R}$ , and the vinylidene  $[\text{Ru}]=\text{C}=\text{CRR}'$ . The general shape of the chemical shift tensors remains

the same due to the presence of shared orbitals transitions, but the fine electronic effects change the energy gaps and localisations of the orbitals. The changes in chemical shift tensors are enough to see small changes in the isotropic chemical shifts that would be observed in solution.

One notable exception from the small changes to chemical shift is the changes of tensor on exchange of a proton (H) and a fluorine (F) in both vinylidene- and alkynyl-complexes described Sections 3.5 and 3.6, leading to large observed changes in chemical shift. Complexes **[1a]** – **[1d]** represent substitution of the R group of the alkyne where: a = -C<sub>6</sub>H<sub>5</sub>, b = -C<sub>6</sub>H<sub>4</sub>-*p*-OMe, c = -C<sub>6</sub>H<sub>4</sub>-*p*-CF<sub>3</sub>, d = -C<sub>4</sub>H<sub>9</sub>. The largest changes are observed from **[1a]** to **[1d]**, representing a change of R from a phenyl ring for a *tert*-butyl group (<sup>t</sup>Bu). This change of R has the largest effect on  $\delta_{33}$  in alkynes between **[1a]** and **[1d]**. Further substitution of the phenyl ring has a much smaller effect, the fine electronic effects on the chemical shift tensors have not been studied in this work.

The chemical shift tensors observed for the F and H terminated alkynyl complex differ significantly, so much so that the isotropic chemical shift is shielded by approximately 70 ppm in the fluoroalkynyl complex. The fluorovinylidene shows the opposite trend and the isotropic shift is deshielded by approximately 35 ppm. To understand the change on fluorination to the chemical shift, the chemical shift tensors needed orienting on the molecular frame. This has allowed the orbitals responsible for deshielding to be interpreted.

### 3.10 Conclusions

As shown in section 3.6, the chemical shift tensors for alkynes are similar to the tensors for alkynyl complexes such as **[1a]**. Unlike the vinylidenes described in section 3.5, both the isotropic chemical shift and the weighting of the tensors in alkynes remains constant.

Because of the large differences observed between **[60]** and **[2a]<sup>+</sup>**, the effect of the metal on the frontier molecular orbitals is clear. Overlap with the ruthenium d orbitals changes both the energy gaps and the localisations of orbitals that are key to deshielding. **[66]<sup>+</sup>** is a good electronic model for a coordinated vinylidene given that the magnitude of the chemical shift tensors is similar to **[2a]<sup>+</sup>**. However, the magnitudes of the chemical shift tensors suggest that the  $\sigma$ -bonding FMOs of coordinated vinylidenes are higher in energy than the vinyliminium equivalents. Despite this, vinyliminium species may exhibit the same interesting reactivity as vinylidenes and could be used in the formation of novel fluorinated compounds under mild outer sphere electrophilic fluorination conditions.

Alkynes **[38]** and **[4]** show comparable <sup>13</sup>C chemical shift values by NMR spectroscopy, but the reactivity differs significantly. Although the chemical shift tensors give an insight into the frontier molecular orbital structures, the NMR spectroscopic analysis of organometallics can be complex. A direct link to reactivity may not be observed, as the orbital energy gaps and localisations are probed but not the absolute energies. As well as the absolute energies, some orbitals are NMR silent without effective overlap to other orbitals. If the reactivity of the system is dictated by an NMR silent orbital, the chemical shift cannot be used as a probe of reactivity.

Two contrasting fluorine effects on chemical shift have been observed on the generation of fluorovinylidene/alkynyl complexes versus their non fluorinated equivalents. Both effects can be explained by changes to the frontier molecular orbital energies and overlaps of the non-fluorinated vinylidene- and alkynyl-complexes **[2a]<sup>+</sup>** and **[4]'** and their fluorinated equivalents complexes **[3a]<sup>+</sup>** and **[7]'**. In vinylidene complexes, the changes in orbital character and contraction of HOMO→LUMO energy gap lead to the large change in  $\delta^{iso}$  observed. In **[2a]<sup>+</sup>** and

**[3a]<sup>+</sup>**, where  $\delta^{\text{iso}}$  is 353.7 and 388.6 ppm, respectively, this energy gap contracts from 4.06 to 3.32 eV and is accompanied by a 236 ppm increase in deshielding along the M-C bond axis. Alkynyl complexes **[4]** and **[7]** show an alternative trend in  $\delta^{\text{iso}}$ . A shielding of  $\delta^{\text{iso}}$  from 116 ppm to 30 ppm is observed, associated with depression of the  $\sigma$ -bonding orbital depressing in energy and increasing the energy gap to the LUMO. This effect results in the  $\delta_x$  and  $\delta_y$  tensors reducing from ~230 to ~100 ppm. Both the fluorine effect on the chemical shift of  $C_\alpha$  and the nature of Ru-C bonding have been explored in vinylidene and alkynyl species.

## Chapter 4. Exploration of metal chemical shift tensors

### 4.1 Introduction

This chapter is focused on extending the methodology used in chapters 2 and 3 towards a new system of study. There are many examples of metal-ligand bonding characterisation that are focused on spectroscopy of the ligand. Methods for analysing the metal directly are less widely utilized. The focus of this chapter is on the recording of SS NMR spectra to recover the chemical shift tensors and quantum chemical calculations with DFT in the analysis of metal FMOs.  $^{103}\text{Rh}$  SS NMR is explored with the aim to use chemical shift tensors to probe the bonding in rhodium complexes that are relevant to the hydroformylation reaction.  $^{195}\text{Pt}$  SS NMR spectra were recorded and chemical shift tensors recovered to help with the analysis and interpretation of  $^{103}\text{Rh}$  tensors.

This introduction describes the general reaction of hydroformylation. Early cobalt-catalysed hydroformylation will be described, including the mechanism of the reaction of alkenes with  $\text{CO}/\text{H}_2$  in the presence of  $\text{HCo}(\text{CO})_4$  and the origin of the linear and branched problem. The identification of simple rhodium systems that catalyse the hydroformylation reaction are explained as well as the key issues with hydroformylation; catalyst degradation, side reactions, and unselectivity. The effect of phosphine bite angle on simple rhodium hydroformylation catalysis will be described. More recent developments to heterogeneous hydroformylation will be briefly discussed, but are beyond the scope of this review.

Improved understanding of the effect of bite angle and ligand nature on the chemical shift tensors may help future development of catalysts with improved selectivity. The general methodology may be applied to other metal systems in the future.

#### 4.1.1 The hydroformylation reaction (oxo process)

Hydroformylation is the chemical process in which H<sub>2</sub> and CO are added over an alkene C=C bond to produce an aldehyde.<sup>129</sup> H<sub>2</sub> and CO are added over the double bond to give a formyl group, -CHO, and a hydro group, -H, on adjacent carbon atoms of the alkene, hence the name hydroformylation. The reaction is summarized in Figure 88 below. A range of side reactions may occur, the key side products are summarized in Figure 89 below.

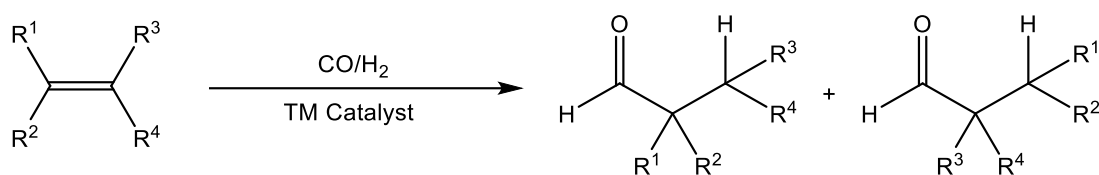


Figure 88. General scheme for the hydroformylation of an alkene to produce aldehydes. The transition metal catalyst used is typically a group 9 hydridecarbonyl complex of Co or Rh.

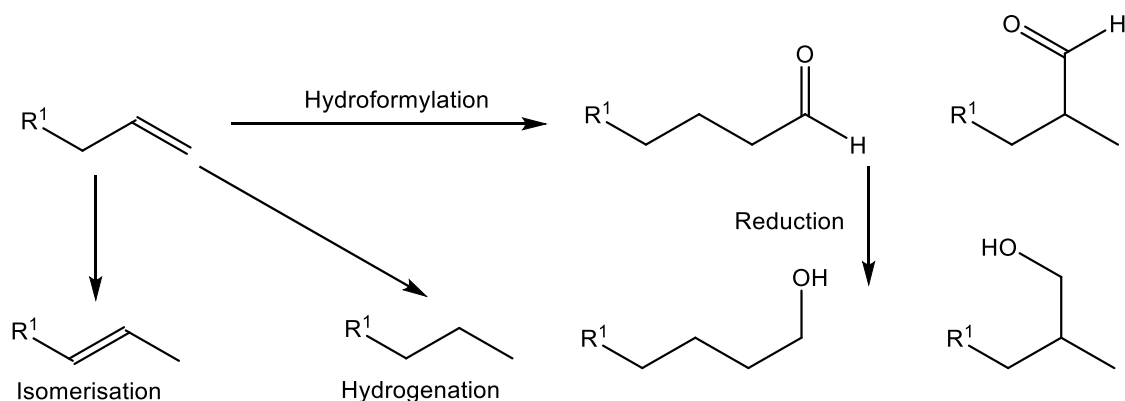


Figure 89. Key side products in hydroformylation of terminal alkenes. Aldol condensation products not shown.

In hydroformylation reactions, the H<sub>2</sub> and CO are typically supplied as a mixture known as syngas and reactions are performed under high temperatures and pressures of syngas, 40 – 170 °C, 10 – 300 Bar.<sup>130, 131</sup> Hydroformylation is industrially relevant in the production of bulk chemicals and the reaction is highly atom efficient.<sup>129, 131</sup> The reactivity of alkenes with H<sub>2</sub>/CO is catalysed by the addition of a transition metal catalyst.

Hydroformylation, first reported in a patent as the oxo process, was developed by Roelen in 1938 and utilized a  $\text{HCo}(\text{CO})_4$  pre-catalyst. Although, the mechanism for the reaction was not elucidated until 1961.<sup>132</sup> This mechanism is described in Figure 90.

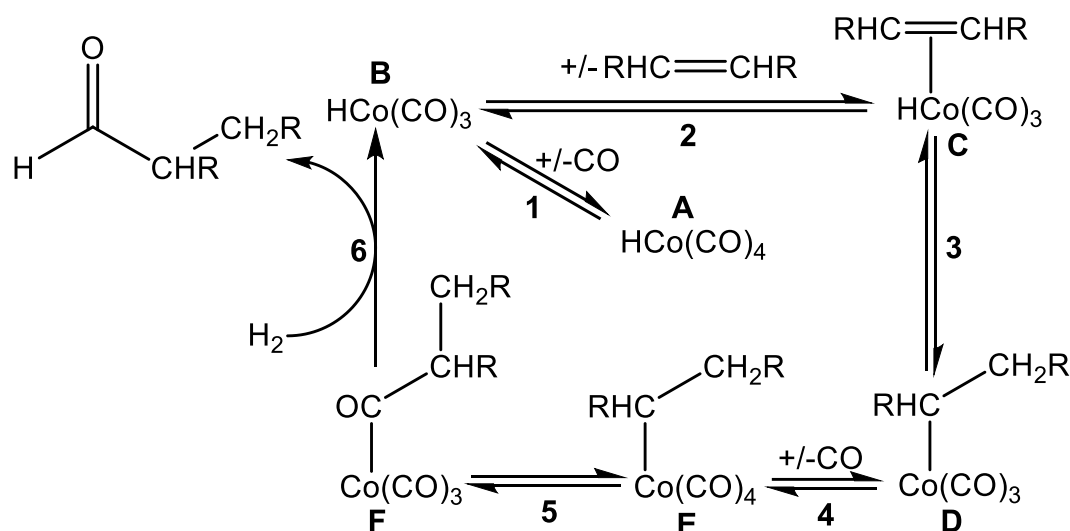


Figure 90. Mechanism of cobalt-catalysed hydroformylation as described by Heck and Breslow.<sup>132</sup>

The elucidated mechanism shows that the active catalytic species is a tricarbonyl species **B** rather than the tetracarbonyl **A**. This is supported by the fact that the reaction of alkene and **A** is inhibited by CO at low temperatures. At 0 °C, no aldehyde production is observed.<sup>132</sup> At higher temperatures, 25 °C, aldehyde formation occurs due to the increased lability of the ligands and allowing for CO dissociation and coordination of the alkene to form of alkene complex **C**. Step **3** is the rearrangement of the alkene hydride complex through olefin insertion to form an alkyl complex **D**. Reoordination of CO under the CO atmosphere must occur before insertion of CO from **E** to form **F**. The subsequent reduction may occur by utilising **A**, but under hydroformylation conditions,  $\text{H}_2$  may act as the reductant reforming **B** and releasing the aldehyde.

#### 4.1.2 Hydroformylation using rhodium catalysts

As well as hydroformylation with cobalt, alkenes were shown to undergo hydroformylation in the presence of rhodium catalysts.<sup>133, 134</sup> Rhodium catalysts were shown to have higher selectivity and turnover numbers compared to cobalt catalysts when low boiling point alkenes were used. Rhodium catalysts are generally more tolerant of functionality and active at lower temperatures, making isomerisation reactions less prevalent.

Complexes of the type *trans*-[RhX(CO)L<sub>2</sub>] were shown to undergo hydroformylation by Wilkinson *et al.* where X is a halogen ligand and L a neutral 2e<sup>-</sup> donor such as a phosphine.<sup>135</sup> One key example is in the use of *trans*-[Rh(Cl)(CO)(PPh<sub>3</sub>)<sub>2</sub>], *trans*-[**15**], which has also been shown to be active in hydrogenation.<sup>135, 136</sup> The catalytic species was shown to be the hydride carbonyl complex of rhodium after protodehalogenation.<sup>135</sup>

#### 4.1.3 Effect of diphosphine bite angle on linear:branched (l:b) ratio

There is a large industrial demand for the production of linear aldehydes as they provide good substrates for further reactivity or functionalisation. For example in 2002, the production of 1-butanal alone from propene was 8.0 × 10<sup>6</sup> tonnes per annum.<sup>137</sup> Figure 90 shows the cobalt-mediated hydroformylation for a symmetrical alkene. The mechanism is shown in Figure 91 for an asymmetrical alkene showing the deviation point of the linear and branched pathways between [C] and [D]. Phosphine ligands have been widely used as coordinating ligands in the hydroformylation of alkenes. This is partly owing to the wealth of literature on phosphine parameterisation and the favourable NMR spectroscopic qualities of the <sup>31</sup>P nucleus.

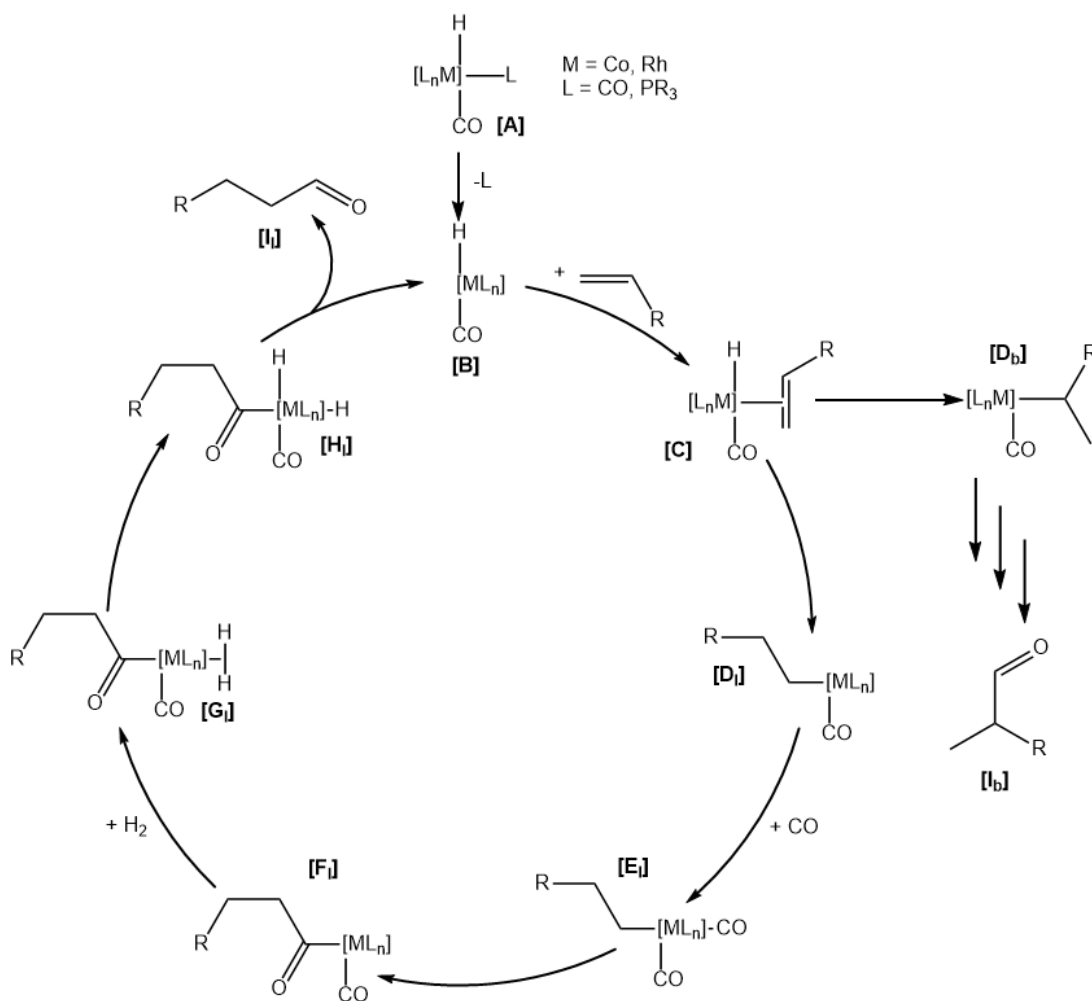


Figure 91. Hydroformylation of a terminal alkene. The subscript l and b denote the proto-linear and proto-branched pathways.<sup>138</sup>

Van der Veen *et al.* explored the effect of phosphine basicity on the linear:branched ratio of hydroformylation, aiming to explore the electronic effect of the bidentate diphospheneligands.<sup>139</sup> The results of their work showed that although the basicity affected the solution structure of the catalyst, changes in l:b ratio did not correlate. Instead, the l:b ratio correlated better with the natural bite angle of diphosphines.

The ratio of l:b aldehyde can be increased towards formation of linear product with the addition of a bidentate diphosphine ligand. The effect of diphosphine bite angle on hydroformylation selectivity has been extensively studied by van Leeuwen particularly using rigid Xantphos-type ligands, large natural bite angles generally improve the proportion of linear aldehyde recovered.<sup>140-142</sup> It is thought that the bite angle of the ligand influences the structure of the catalyst. For example, **[A]** is a five

coordinate species and the geometry around the rhodium core will likely be trigonal bipyramidal as the major isomer. With a diphosphine ligand, two states are observed with the phosphine coordinating in both equatorial positions (EE) or one equatorial and one axial position (EA), as shown in Figure 92.

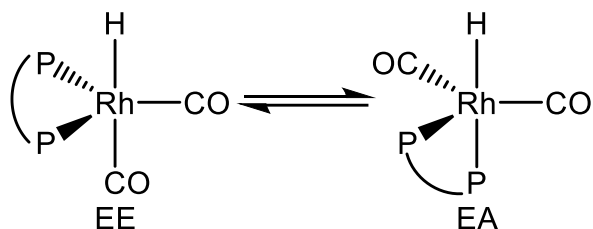


Figure 92. Equilibrium between EE and EA for **[A]**.

Bidentate diphosphine ligands with larger bite angles show a preference for coordinating in the EE mode as the natural bite angle of the ligand is closer to the optimal angle of  $120^\circ$  rather than the  $90^\circ$  angle of the EA mode. However, the coordination mode of the diphosphine in the precatalyst is not the sole contributor to the l:b ratio.<sup>139</sup> However, it is clear that the presence of bidentate diphosphine ligands with large bite angles ( $>100^\circ$ ) do improve the proportion of linear aldehyde, as in the industrial hydroformylation of but-1-ene giving 94 % *n*-pentanal.<sup>139</sup>

#### 4.1.4 Heterogeneous Rh-catalysed hydroformylation

Rhodium has been shown to be a highly active catalytic metal with rhodium catalysts being employed in hydroformylation under a range of conditions, but one of the key issues experienced in the reaction is deactivation and degradation of the catalyst.<sup>134</sup> Homogeneous catalysts are more prone to degradation reactions in solution. The other advantage of heterogeneous catalysts over homogeneous catalysts is that catalyst recovery is easier as the solid phase can be filtered from the reaction medium.

Rhodium catalysts have been immobilized on silica to produce heterogeneous catalysts for hydroformylation, which has been summarized recently by Schunk *et al.*, Figure 93.<sup>143</sup>

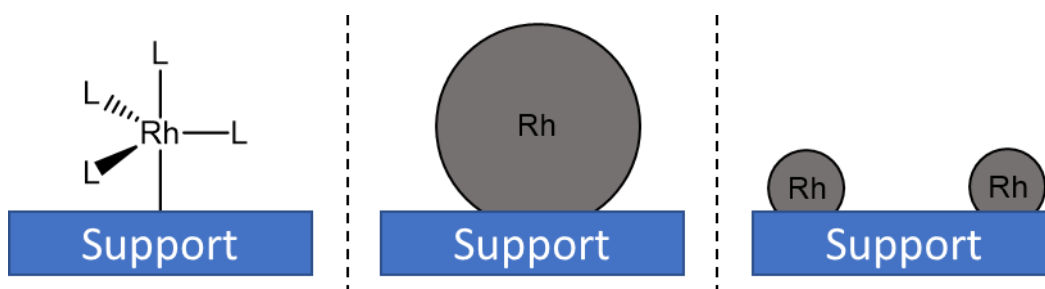


Figure 93. Schematic examples of heterogeneous rhodium hydroformylation catalysts as summarized by Schunk; supported Rh complexes where L = phosphine or CO (left), supported metallic Rh nanoparticles (middle), and supported single atom Rh catalysts (right).<sup>143</sup>

The prevalence of heterogeneous rhodium catalysts makes them a prime subject for study by SS NMR spectroscopy. The rhodium may be combined with the solid phase by coordination of the ligand and/or metal,<sup>144</sup> adhering of nanoparticles or single atom catalysts,<sup>143</sup> or interaction through surface decoration such as a polymer or an ionic liquid.<sup>145, 146</sup> Heterogeneous catalysis has not been described in detail in this introduction, but improved understanding of hydroformylation *via* chemical shift tensor analysis may be applicable to the area in future.

#### 4.1.5 Aims

Both NMR spectroscopy and SS NMR spectroscopy have been used to analyse and interpret the bonding in organometallic compounds. In this chapter, we have used SS NMR spectroscopy to record high resolution spectra of metal nuclei and recover chemical shift tensors of the target metal complexes. This, combined with quantum chemical calculations using DFT, will allow the FMOs of a series of platinum-containing metal complexes to be studied as a test case for the understanding of the chemical shift of metals. This understanding has been used to analyse a series of rhodium-containing complexes that are relevant to hydroformylation, focusing on changing the coordinating pnictogen atom of the ligand in *trans*-[RhCl(CO)L<sub>2</sub>] complexes and the L-Rh-L angle in a range of *cis*-[RhCl(CO)L<sub>2</sub>] complexes. By not using

reporter ligands, the MOs may be directly interpreted to gain a greater understanding into structure, bonding, and reactivity.

## 4.2 Synthesis and characterisation of rhodium carbonyl chloride complexes

### 4.2.1 Identification and synthesis of target Rh complexes

Rhodium has only one naturally occurring isotope,  $^{103}\text{Rh}$ . As well as being 100% abundant,  $^{103}\text{Rh}$  also possesses a spin  $I = \frac{1}{2}$ . Not being quadrupolar, the expected NMR resonances should be sharp and the dominant interaction of the magnetic field with the nucleus is the Zeeman interaction. Because of this, a series of simple rhodium complexes were identified for synthesis and study by SS NMR spectroscopy. The complexes are shown in Figure 94.

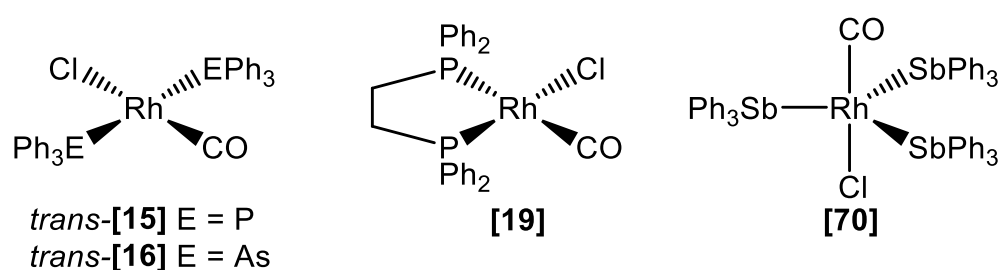


Figure 94. Target Vaska-type complexes identified for SS NMR analysis.

The complexes shown in Figure 94 allow the investigation of the effect of the increasing size of the group 15 pnictogen element. As well as this, complexes *trans*-[15] and [19] can be used to probe the effect of *cis*- and *trans*- geometries at rhodium on the chemical shift anisotropy.

The *trans*-complexes could all be synthesized following literature preparations from rhodium(III) chloride.<sup>136, 147</sup> Addition of triphenylstibine (SbPh<sub>3</sub>) led to the formation of trigonal bipyramidal [70] over square planar *trans*-[17]. The *cis*- complex [19] was synthesized from Rh<sub>2</sub>(CO)<sub>4</sub>Cl<sub>2</sub>.<sup>148</sup>

## 4.3 Recording of $^{103}\text{Rh}$ and $^{195}\text{Pt}$ metal SS NMR spectra

The collection of metal SS NMR spectra poses significant challenge compared to more common nuclei such as  $^{19}\text{F}$ ,  $^{13}\text{C}$ ,  $^{31}\text{P}$ . Typically, the spectra of  $I = \frac{1}{2}$  nuclei are much simpler than quadrupolar,  $I > \frac{1}{2}$ , nuclei as the Zeeman interaction between the

nuclear spin and the magnetic field is the largest interaction in the sample. In quadrupolar nuclei, the Zeeman splitting can be a similar magnitude to the electric quadrupolar interaction. As well as increased relaxation times reducing signal intensity, the quadrupolar interaction can convolute spectra. Many common metal nuclei are quadrupolar or NMR silent and therefore characterisation is both technically demanding and rare. Some notable exceptions to this are  $^{103}\text{Rh}$  and  $^{195}\text{Pt}$  as both nuclei are NMR active with  $I = \frac{1}{2}$ . Although solution phase characterisation is common, solid-state characterisation of species containing these nuclei is rarer.

Both  $^{103}\text{Rh}$  and  $^{195}\text{Pt}$  have broad chemical shift ranges, excitation over the entire frequency range would require very short, very high-power pulses. As the spectral width has a large frequency range in  $\text{s}^{-1}$ , the acquisition time must be short in seconds to give large ranges of  $\text{s}^{-1}$  on Fourier transform. This can be circumvented experimentally by recording spectra over a series of chemical shift ranges rather than a single excitation. As well as possessing a broad dispersion, metal nuclei possess large chemical shift anisotropies of several thousand ppm. The range is so large that the MAS rotation speed,  $\nu^{\text{rot}}$ , will typically be significantly lower than the chemical shift anisotropy. As described earlier in section 1.2.2, if  $\nu^{\text{rot}} >$  chemical shift anisotropy, the anisotropy will be averaged out and the isotropic resonance will dominate. If  $\nu^{\text{rot}} <$  chemical shift anisotropy, then chemical shift anisotropy will dominate the resonance resulting in a procession of spinning side bands. When calculating chemical shift tensors from an experimental spectrum, many side bands improve the approximation of  $\delta_{11}$ ,  $\delta_{22}$ , and  $\delta_{33}$ . As the number of side bands increases, the proportion of signal dilution increases. This signal dilution is one of the main limitations of direct SS NMR spectroscopy.

Although the focus of this chapter is on the use of chemical shift tensors for the analysis of hydroformylation-relevant complexes,  $^{103}\text{Rh}$  is a more technically demanding nuclei to record NMR spectra of. Initial test spectra have been recorded on  $^{195}\text{Pt}$ .

#### 4.3.1 SS NMR spectrum of $K_2PtCl_6$

SS NMR spectra of metal nuclei are technically demanding to run. The chemical shift ranges of metals are typically over several thousand ppm. This is much wider than for other commonly studied nuclei such as  $^1H$ ,  $^{13}C$ ,  $^{19}F$ , and  $^{31}P$ , which have typical chemical shift ranges of tens ( $^1H$ ) or hundreds of ppm. As well as large chemical shift ranges, large chemical shift anisotropies are also observed.

$K_2PtCl_6$ ,  $K_2[71]$ , is used as the  $^{195}Pt$  reference compound for solution phase NMR spectroscopy. It is typically used as the  $D_2O$  solution.  $K_2PtCl_6$  is also a convenient compound to study by SS NMR spectroscopy. As well as being commercially available and a well-defined salt, the single platinum environment possesses octahedral  $O_h$  symmetry. If the  $^{195}Pt$  nuclei are in the  $O_h$  environment, all three chemical shift tensors will point along one of the Pt-Cl axes. The chemical shift interaction of the magnetic field with the  $^{195}Pt$  nucleus will be the same for each tensor and therefore the chemical shift anisotropy must be equal to zero. If chemical shift anisotropy is zero, then only the isotropic resonance will be observed with no spinning side bands. Some spinning side echoes will be observed but most of the signal will contribute to the isotropic resonance.

The solution phase  $^{195}Pt$  spectrum in  $D_2O$  shows that the  $[71]^{2-}$  anion is dynamic due to water loss and coordination of  $D_2O$  or  $OH^-$ . The extent of substitution depends on the pH of the solution. The solid-state spectrum cannot be dynamic as the ligands cannot undergo intermolecular rearrangement being locked in the crystal structure. This makes the solid-state spectrum simpler to interpret. A SS NMR spectrum was recorded of a ground crystalline sample of  $K_2[71]$  to test receptivity. This is shown in Figure 95.

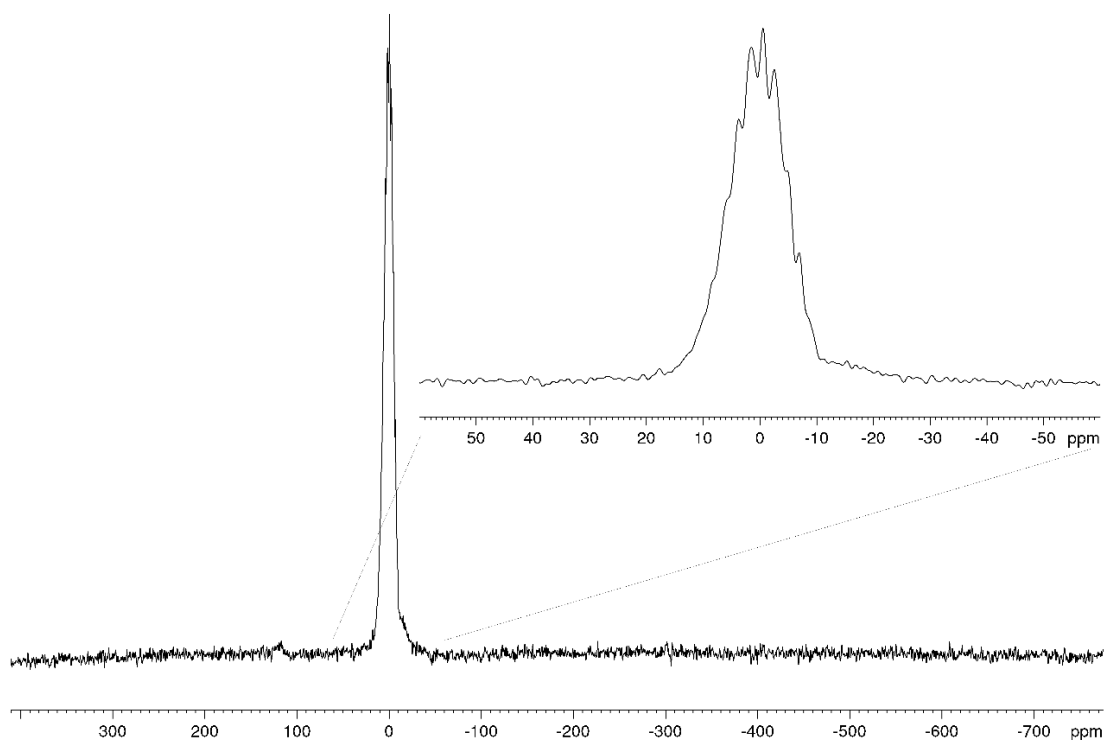


Figure 95. SS  $^{195}\text{Pt}$  NMR spectrum of  $\text{K}_2\text{PtCl}_6$  recorded at 86 MHz at a spinning speed of 10 kHz.

As shown in Figure 95, a single broad resonance is observed with a low chemical shift anisotropy. On closer inspection of the single resonance, it can be seen that the one Pt environment is actually several resonances with slightly different chemical shifts. The line shape is a result of several isotopologues being present in the sample,  $\text{Pt}^{35}\text{Cl}_n^{37}\text{Cl}_{6-n}$ . Each isotopologue results in a slightly different chemical shift leading to distinctive fingerprint overlap based on the statistical population distribution of chloride isotopes. At a spinning speed of 10 kHz, the chemical shift anisotropy is much lower than  $\nu^{\text{rot}}$  leading to the presence of small spinning side echoes, as predicted for the octahedral moiety.

#### 4.3.2 SS NMR spectrum of $\text{K}_2\text{PtCl}_4$

The tetrachloroplatinate anion of  $\text{K}_2\text{PtCl}_4$ ,  $\text{K}_2[\mathbf{72}]$ , adopts a square planar geometry, unlike the hexachloroplatinate anion  $[\mathbf{71}]^{2-}$ . This means that the chemical shift anisotropy will no longer be 0 ppm as the platinum nuclei are no longer in a fully symmetric environment. Two axes will possess identical shielding, with the other axis

possessing a different shielding value. SS NMR spectra were recorded on a ground crystalline sample of  $K_2PtCl_4$ . An initial spectrum was recorded centred at  $\delta_{Pt} = -1700$ , near the solution phase isotropic chemical shift of  $\delta_{Pt} = -1618$ . The spectrum is shown in Figure 96.

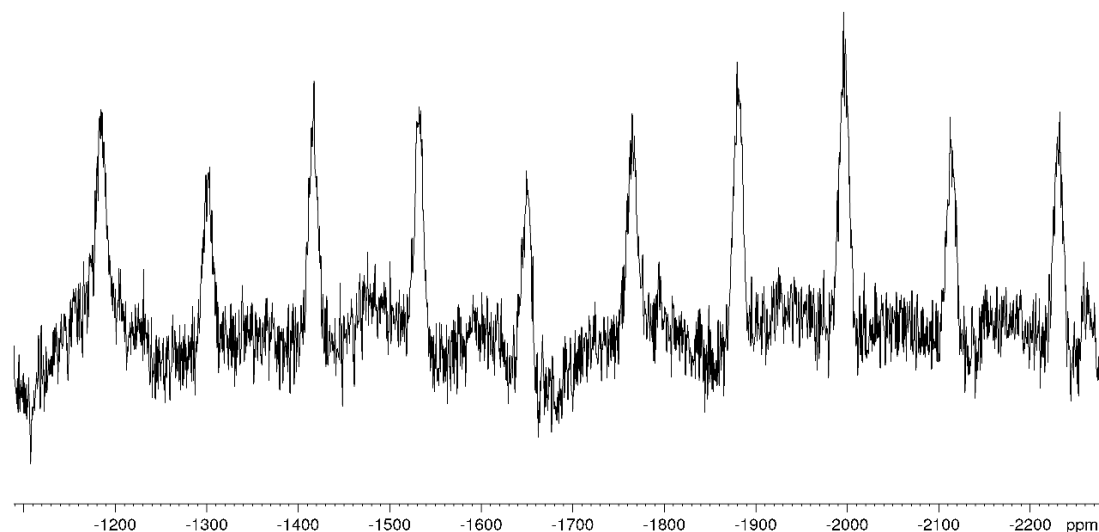


Figure 96. SS NMR MAS  $^{195}Pt$  spectra recorded at 86 MHz between -1000 and -2300 ppm at a spinning speed of 10 kHz.  $N_s = 4096$ .

As seen in Figure 96, only a single Pt resonance was observed as a series of spinning side bands between the region of  $\delta_{Pt} = -1100 - -2300$ . Recording of a spectrum at a spinning speed of 9 kHz indicated that the isotropic chemical shift in the solid-state was  $\delta_{iso}^{SS} = -1647$ . The span of the chemical shift anisotropy is much greater than  $\nu^{rot}$  leading to no decrease in the intensity of the spinning sidebands. The spectral width was maintained at 1200 ppm and the full spectrum was recorded in overlapping spectra with multiple excitation frequency intervals as a single pulse could not excite the whole spectral region of  $\delta_{Pt} = 6000 - -6000$ . The full spectral range is shown in Figure 97.

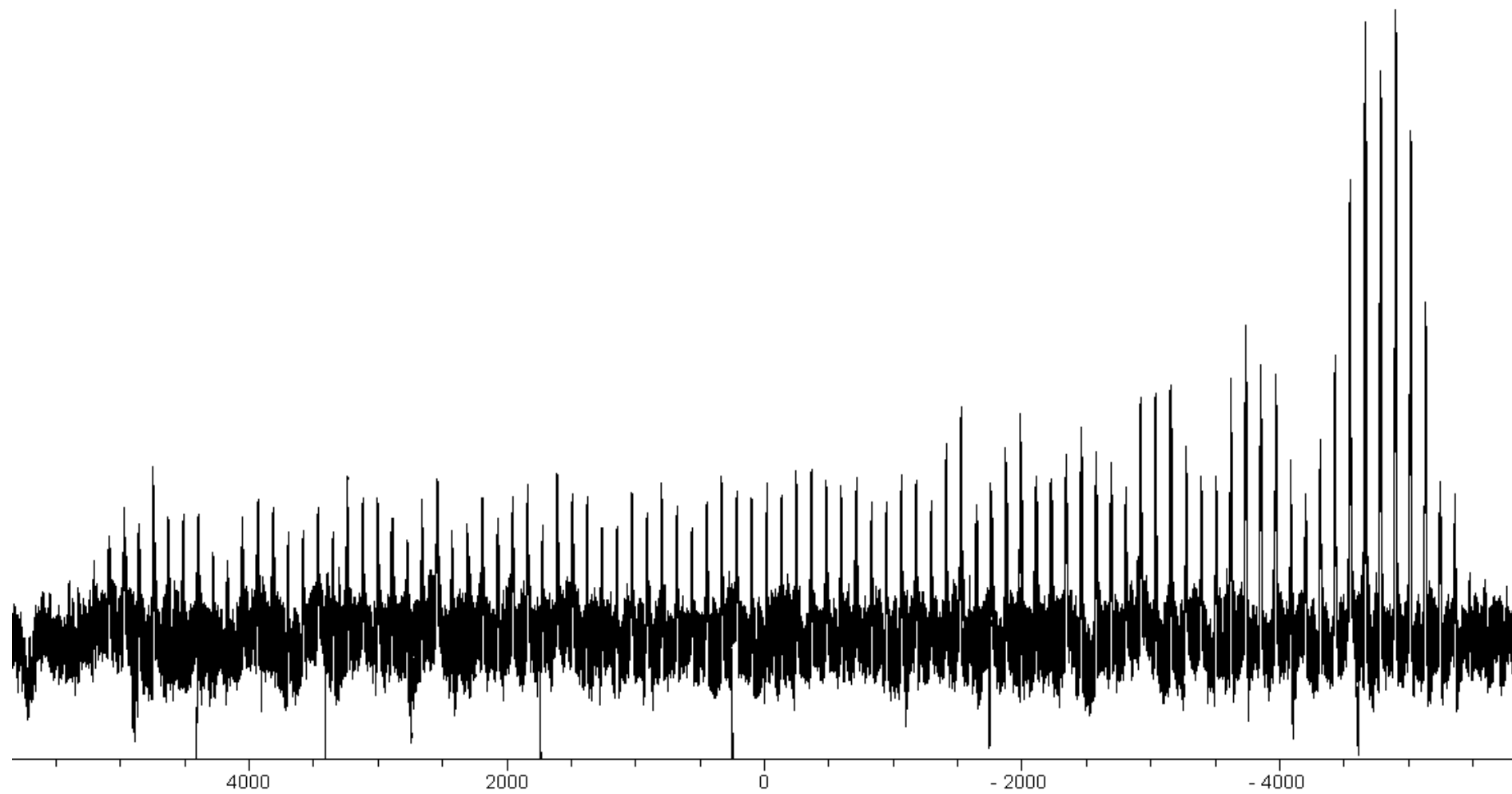


Figure 97. SS NMR MAS  $^{195}\text{Pt}$  spectra of  $\text{K}_2$ [72] recorded at 86 MHz between 6000 and -6000 ppm at a spinning speed of 10 kHz.

As shown in Figure 97, the solid state  $^{195}\text{Pt}$  spectrum of  $\text{K}_2$ [**72**] is much more complex than  $\text{K}_2$ [**71**]. It is also much more complex than the solution phase spectra of  $\text{K}_2$ [**72**] in which the large anisotropy is rotationally averaged. The individual spectra can be combined as they have good overlap. Some negative artifacts are observed due to baseline fitting functions poorly representing the edges of the individual spectra. The chemical shift tensors can be recovered for  $\text{K}_2$ [**72**]. The spectrum in Figure 97 represents a large amount of spectrometer time being recorded in segments over two weeks. The large spectrometer time demands of  $^{195}\text{Pt}$  NMR spectra have restricted the number of complexes that could be recorded in this thesis.

#### 4.3.3 Attempted recording of $^{195}\text{Pt}$ SS NMR spectra of $[\text{Pt}(\text{ppyH})(\text{ppy})\text{Cl}]$ and $[\text{Pt}(\text{ppy})_2\text{Cl}_2]$

To compare to the platinate salts  $\text{K}_2$ [**71**] and  $\text{K}_2$ [**72**], two other platinum complexes were identified for analysis:  $[\text{Pt}(\text{ppyH})(\text{ppy})\text{Cl}]$  (**[73]**), and  $[\text{Pt}(\text{ppy})_2\text{Cl}_2]$  (**[74]**), Figure 98. The complexes are further examples of Pt in octahedral and square planar geometries but are more chemically relevant as they both possess Pt-C bonds and are organometallic rather than inorganic salts. Both complexes were synthesized following literature procedures.<sup>149, 150</sup>

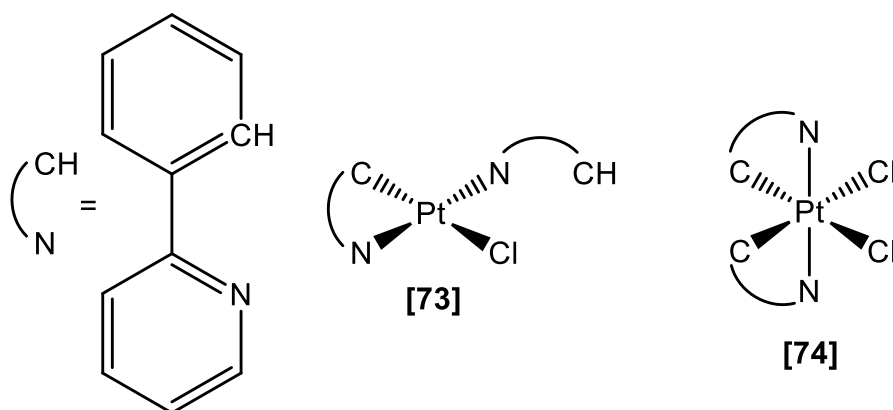


Figure 98. Structure of  $[\text{Pt}(\text{ppyH})(\text{ppy})\text{Cl}]$  (**[73]**), and  $[\text{Pt}(\text{ppy})_2\text{Cl}_2]$  (**[74]**). ppyH = 2-phenylpyridine.

The  $^{195}\text{Pt}$  SS NMR spectra were collected of **[73]** and **[74]**. However, the intensity of the two Pt resonances were much lower than for the platinate salts described earlier.

The signal-to-noise ratio meant that the solid-state  $^{195}\text{Pt}$  NMR spectra could not be recovered/interpreted. The resonances were not clearly distinguished from the baseline even after a large number of scans,  $N_s = 4096$ . The recording of the SS NMR for **[73]** and **[74]** was too technically demanding using parameters that give high resolution spectra of simple salts.

#### 4.3.4 Attempts to record $^{103}\text{Rh}$ SS NMR spectra

The  $^{195}\text{Pt}$  nucleus has a Larmor frequency of 86.015 MHz at 9.310 T ( $^1\text{H} = 400$  MHz) and a natural abundance of 33.3 %.  $^{103}\text{Rh}$  is another metal nucleus with  $I = \frac{1}{2}$  and is therefore another metal nucleus that could be used to directly probe metal-ligand bonding. Unlike  $^{195}\text{Pt}$ ,  $^{103}\text{Rh}$  is 100 % abundant. However, the Larmor frequency of  $^{103}\text{Rh}$  is low. At 9.310 T, the magnet used for all SS NMR spectra in this project,  $^{103}\text{Rh}$  has a Larmor frequency of 12.750 Hz. This value is below the range of a typical heteronuclear probe and in the absence of a designated probe, no solid-state  $^{103}\text{Rh}$  spectra could be recorded in-house. The low value of the Larmor frequency also directly correlates to the magnitude of the Zeeman interaction and therefore the sensitivity of the nucleus.

The need for a magnet with a larger field was identified. The UK high-field SS NMR facility located in Warwick houses a 19.967 T magnet. The Larmor frequency of  $^1\text{H}$  at this field strength is 850.130 MHz. The Larmor frequency of  $^{103}\text{Rh}$  increases from 12.750 MHz at 9.310 T to 27.089 MHz at 19.967 T. The 850.130 MHz spectrometer has both 4- and 7-mm probes that can tune to  $^{103}\text{Rh}$ . Samples were recorded using a 4 mm probe as  $^1\text{H}$  decoupling was needed to remove the large dipole-dipole coupling interactions. A 7 mm probe was available and would allow for more material to be in the NMR active region of the rotor. However, the 7 mm probe only had a single channel and could only be tuned to  $^{103}\text{Rh}$  with no decoupling available. With the relative receptivity of  $^{103}\text{Rh}$  already being low,  $R_{\text{H}}(\text{Rh}) = 3.17 \times 10^{-5}$ , decoupling from  $^1\text{H}$  is essential to prevent the signal being lost into the baseline. The 4 mm probe has multiple channels and can therefore be used more effectively as decoupling from  $^1\text{H}$

is available, for this reason the 4 mm probe was selected for the recording of  $^{103}\text{Rh}$  SS NMR spectra.

Spectra were initially going to be collected on a sample of *trans*-[15] but it was realised that *trans*-[15] contains two  $^{31}\text{P}$  nuclei that are close to the  $^{103}\text{Rh}$  centre. This will incur a large dipole-dipole coupling meaning that the recording of a sharp resonance would be challenging. The interaction of the two  $^{31}\text{P}$  nuclei with the  $^{103}\text{Rh}$  centre is observed in the solution phase  $^{31}\text{P}\{^1\text{H}\}$  NMR spectra of *trans*-[15] shown in Figure 99. The  $^{31}\text{P}$  resonance from the two equivalent phosphine environments is observed as a doublet with  $^1J_{\text{Rh-P}} = 127 \text{ Hz}$ .

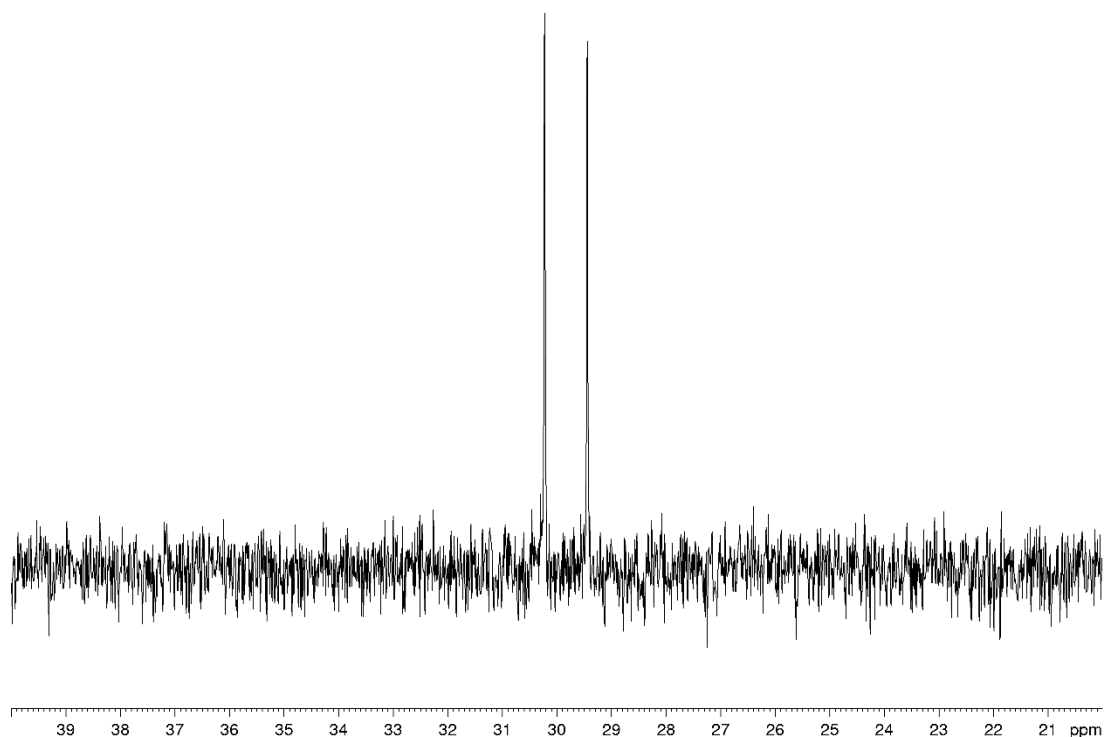


Figure 99. Solution phase  $^{31}\text{P}\{^1\text{H}\}$  NMR spectra of *trans*-[15] recorded at 162 MHz in  $d_2$ -dichloromethane.

Instead, a rotor was packed with the arsine equivalent of *trans*-[15], *trans*-[16]. *trans*-[16] contains  $^{75}\text{As}$  in place of  $^{31}\text{P}$ ,  $^{75}\text{As}$  is  $l = 3/2$  and is therefore quadrupolar. The large dipole-dipole coupling will not be present making the sample more receptive.

The chemical shift range of  $^{103}\text{Rh}$  was scanned. However, even with large numbers of scans ( $N_s = 4096$ ) no resonances were observed above the baseline. Pulse sequences were tried using both CP and decoupling but the SS resonance was unobservable. To

test the receptivity of the sample and to ensure that the correct spectral window was being observed, the rotor was unpacked and a solution of *trans*-[16] in  $d_1$ -chloroform was prepared and loaded into the spectrometer. The resulting spectrum is shown in Figure 100

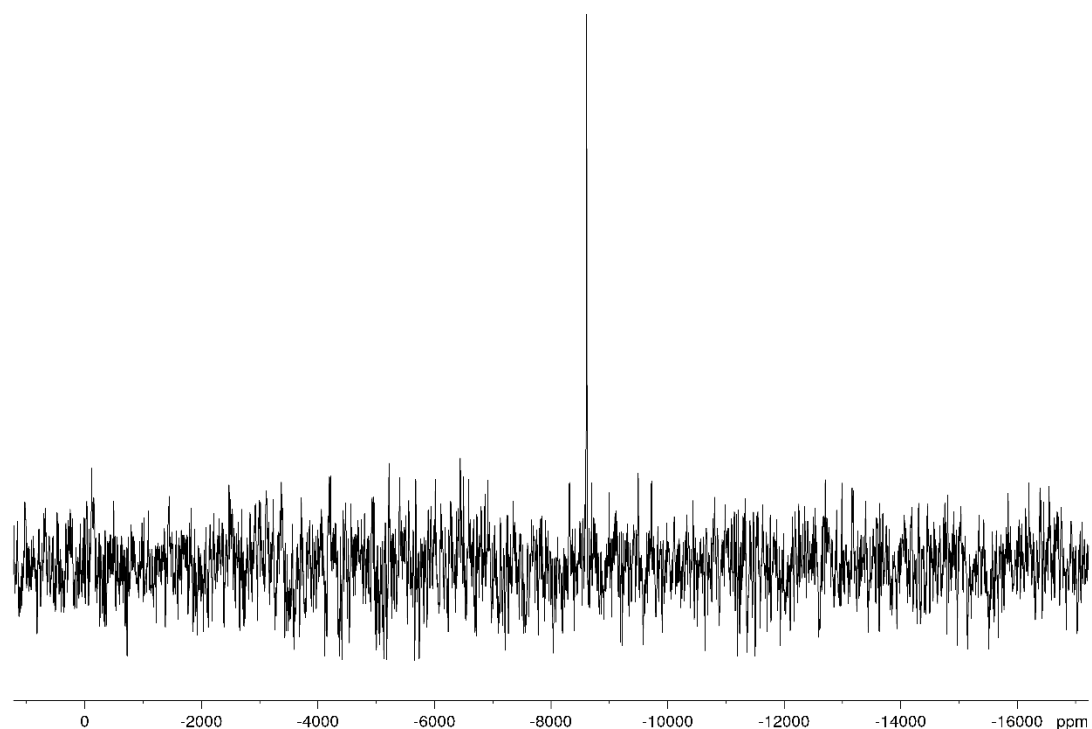


Figure 100.  $^{103}\text{Rh}\{^1\text{H}\}$  NMR spectra of *trans*-[16] recorded in  $d_1$ -chloroform at 27 MHz.

As seen in Figure 100, a  $^{103}\text{Rh}$  resonance is clearly observed as a singlet with no coupling to other nuclei and only a single environment. Further sweeping of the spectral window showed no further resonances. Although a rhodium resonance could be observed, due to spectrometer time constraints the solution phase  $^{103}\text{Rh}\{^1\text{H}\}$  spectrum could only be obtained for *trans*-[16].  $^{103}\text{Rh}$  NMR spectroscopy proved to be too technically demanding a nucleus for study by direct SS NMR spectroscopy in the course of this thesis due to restricted spectrometer time. With more time and a better target rhodium complex, high resolution SS NMR spectra may be recorded and used to for benchmarking of chemical shift tensors calculations as done with  $^{13}\text{C}$  in chapter 3.

## 4.4 Computational methodology for the calculation of geometries and NMR properties of metal nuclei

### 4.4.1 Geometry optimisation of simple Pt species [72]<sup>2-</sup>

The computational methodology developed in chapter 2 and used in this thesis provides good estimation of molecular geometry for organic and organometallic systems. However, the chemical shift of metal nuclei is dependent on the diamagnetic ( $\delta^{\text{dia}}$ ), paramagnetic ( $\delta^{\text{para}}$ ), and spin-orbit ( $\delta^{\text{S.O}}$ ) components of chemical shift. Unlike carbon nuclei, the magnitude of  $\delta^{\text{S.O}}$  can be a significant contributor to the total observed chemical shift and chemical shift anisotropy, particularly in simple systems that contain several metal-chloride bonds.<sup>151</sup> A series of geometry optimisation calculations were performed to benchmark the differences in metal geometry and bond lengths to ensure that the chemical shift calculations would provide meaningful values of chemical shift tensors. Geometry optimisation quantum chemical calculations were performed in Turbomole and Orca on [72]<sup>2-</sup> to test the optimisation methodology. The results are shown in Table 21

Table 21. Tabulated Pt-Cl bond lengths from geometry optimisation calculations for  $[\mathbf{72}]^{2-}$  calculated in Turbomole and Orca. Mean values are denoted by an asterisk (\*). Experimental value obtained from literature crystal structure.<sup>152</sup>

Program	Functional	Basis Set	Pt-Cl / Å
Experiment	N/A	N/A	2.309
Turbomole	BP86	def2_SV(P)	2.408
Turbomole	PBE0	def2_SV(P)	2.383
Turbomole	BP86	def2_TZVPP	2.366
Turbomole	PBE0	def2_TZVPP	2.341
Turbomole	BP86	def2_QZVPP	2.360
Turbomole	PBE0	def2_QZVPP	2.336
Orca	BP86	def2_SV(P)	2.409*
Orca	PBE0	def2_SV(P)	2.383*
Orca	BP86	def2_TZVPP	2.367*
Orca	PBE0	def2_TZVPP	2.347*
Orca	BP86	def2_TZVPP_ZORA	2.247*
Orca	PBE0	def2_TZVPP_ZORA	2.228*

As seen from the data in Table 21, the Pt-Cl bond contracts with increasing number of basis functions. Bond lengths are slightly shorter using PBE0 as the functional over BP86. The experimentally measured bond length from the crystal structure of  $\text{K}_2\text{PtCl}_4$  is 2.309 Å. The quantum chemical calculations overestimate this value, except for when ZORA is implemented in Orca. The extension of the Pt-Cl bond length could be expected, as  $\text{PtCl}_4^{2-}$  is dianionic but calculated here in the gas phase. The crystal contacts and dielectric continuum in the condensed phase allow this high negative charge to be diffused. Optimisations in Turbomole result in tetrachloroplatinate(II) anions that are  $D_{4h}$  in symmetry, deviations from square planar are observed from the Orca calculations. Using this methodology, the best approximation of geometry comes from calculations performed in Turbomole at the PBE0/def2\_QZVPP level of theory. For the simple  $\text{PtCl}_4^{2-}$  ion, it is possible to use such a high level of theory, however, it is not time efficient for larger systems.

#### 4.4.2 Inclusion of solvent corrections in geometry optimisation of [72]<sup>2-</sup>

As described in section 4.4.1, Pt-Cl bond lengths in [72]<sup>2-</sup> are overestimated when calculated in the gas phase compared to those from the experimental condensed phase structure. Both Turbomole and Orca have a way of modelling solvation effects. In Turbomole, solvation is described using the Conductor-like Screening Model (COSMO). In Orca, solvation is described using the Polarizable Continuum Model (PCM). The PCM can be polarizable or conductor like, DPCM and CPCM respectively. The CPCM is similar to COSMO so was selected over DPCM. Calculations were performed in Turbomole and Orca with COSMO and CPCM enabled. The results are summarized in Table 22.

The general trend from the data in Table 22 is that the Pt-Cl bond length contracts as the size of the basis set increases, def2\_SV(P)>def2\_TZVPP>def2\_QZVPP. Optimisations performed with the PBE0 functional also result in smaller Pt-Cl bond lengths, as with the calculations performed in section 4.4.1 earlier. Inclusion of a water COSMO in Turbomole led to an average bond contraction of 0.027 Å whereas a chloroform COSMO led to an average bond contraction of 0.020 Å. A similar effect was observed using a CPCM in Orca. Optimisations in Orca led to deviations from *D*<sub>4h</sub> square planar geometry. Turbomole was found to be more effective for geometry optimisation calculations.

Table 22. Tabulated Pt-Cl bond lengths from geometry optimisation calculations for **[72]**<sup>2-</sup> calculated in Turbomole and Orca with COSMO and CPCM implemented.

Program	Functional	Basis Set	Solvent	Pt-Cl / Å
Experiment	N/A	N/A	N/A	2.309 <sup>152</sup>
Turbomole	BP86	def2_SV(P)	Water	2.379
Turbomole	BP86	def2_SV(P)	Acetone	2.381
Turbomole	BP86	def2_SV(P)	Chloroform	2.387
Turbomole	PBE0	def2_SV(P)	Water	2.356
Turbomole	PBE0	def2_SV(P)	Chloroform	2.363
Turbomole	BP86	def2_TZVPP	Water	2.338
Turbomole	BP86	def2_TZVPP	Chloroform	2.345
Turbomole	PBE0	def2_TZVPP	Water	2.315
Turbomole	PBE0	def2_TZVPP	Chloroform	2.322
Turbomole	BP86	def2_QZVPP	Water	2.334
Turbomole	BP86	def2_QZVPP	Chloroform	2.341
Turbomole	PBE0	def2_QZVPP	Water	2.312
Turbomole	PBE0	def2_QZVPP	Chloroform	2.318
Orca	BP86	def2_SV(P)	Water	2.382
Orca	BP86	def2_SV(P)	Chloroform	2.387
Orca	PBE0	def2_SV(P)	Water	2.357
Orca	PBE0	def2_SV(P)	Chloroform	2.362
Orca	BP86	def2_TZVPP	Water	2.341
Orca	BP86	def2_TZVPP	Chloroform	2.345
Orca	PBE0	def2_TZVPP	Water	2.322
Orca	PBE0	def2_TZVPP	Chloroform	2.327

Inclusion of solvent corrections is important in the geometry optimisation of platinum complexes, particularly complexes bearing a negative charge. Good approximations for the geometry of **[72]**<sup>2-</sup> were obtained after optimisation in Turbomole at the PBE0/def2\_TZVPP and PBE0/def2\_QZVPP levels of theory with a water COSMO. Due

to the time scaling moving to a quadruple  $\zeta$  basis set, PBE0/def2\_TZVPP with a water COSMO was selected for the geometry optimisation methodology of simple platinum complexes.

#### 4.4.3 Dependence of chemical shielding of $[72]^{2-}$ on geometry

Quantum chemical calculations were performed using DFT to calculate the chemical shift tensors of  $[72]^{2-}$  with varying values of Pt-Cl bond length. The geometries of the first and second entries are from calculations performed on optimised geometries from quantum chemical calculations, the third entry is from a calculation performed directly on the crystal geometry.<sup>152</sup> Entry 1 = BP86/def2\_SV(P) (from Table 21), entry 2 = PBE0/def2\_TZVPP with COSMO (H<sub>2</sub>O) implemented (from Table 22), entry 3 = XRD crystal structure coordinates. The results are summarized in Table 23.

Table 23. Chemical shift tensors of  $[72]^{2-}$  against Pt-Cl bond length. Tensors calculated in Orca at the PBE0/def2\_TZVPP level of theory with ZORA corrections. The Basis functions of Pt were represented by the SARC\_TZVPP basis set.

No.	Pt-Cl / Å	$\delta^{iso}$ / ppm	$\delta_{11}$ / ppm	$\delta_{22}$ / ppm	$\delta_{33}$ / ppm
1	2.408	3000	14306	-2652	-2652
2	2.315	-533	7411	-4506	-4506
3	2.309	-690	7088	-4580	-4580

As seen from the data in Table 23, the values of the chemical shift tensors and the isotropic chemical shift are sensitive to bond lengths in  $[72]^{2-}$ . As the Pt-Cl bond length contracts, the deshielding of  $\delta_{11}$  halves from 14306 ppm to 7088 ppm. At the same time, the shielding of  $\delta_{22}$  and  $\delta_{33}$  both reduce from -2652 ppm to -4580 ppm. The general methodology selected for the optimisation of simple metal complexes was that in entry 2, which gives values of chemical shift that are much closer to when the experimental geometry is used in entry 3. This highlights how important good

approximations for geometry are in the calculation of metal tensors and why a new optimisation methodology needed to be used than that described in chapter 3.

#### 4.5 Calculation of metal chemical shift tensors

Using the modified methodology developed in section 4.4, the chemical shift tensors for a series of metal complexes of platinum and rhodium, shown in Figure 101, were calculated. The results are summarized in Table 24.

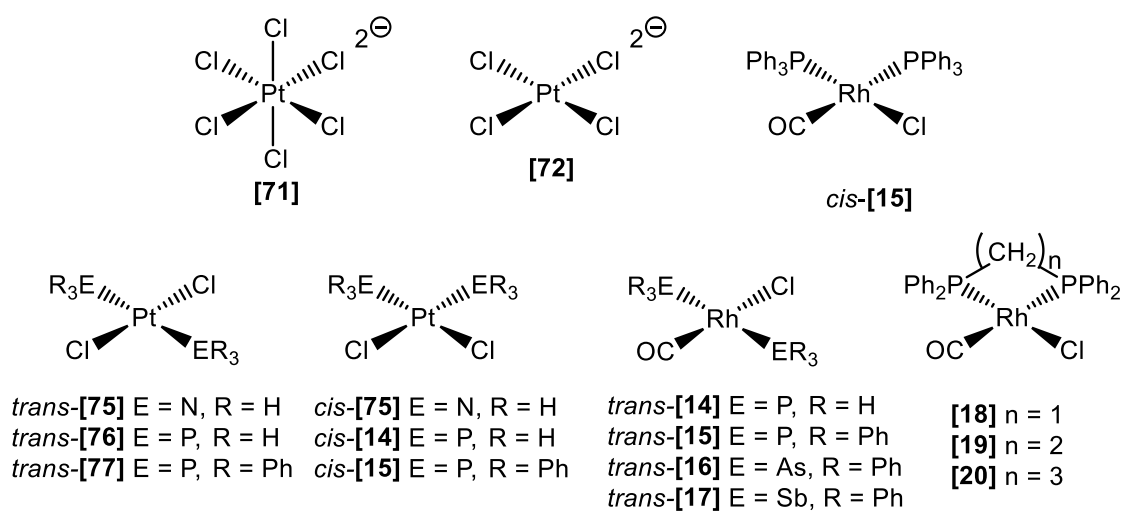


Figure 101. Platinum and rhodium complexes studied in this chapter.

Table 24. Platinum and rhodium chemical shift tensor calculate in Orca at the PBE0/def2\_TZVPP level of theory with ZORA corrections. The Basis functions of Pt were represented by the SARC\_TZVPP basis set.

Complex	$\delta^{iso}$ / ppm	$\delta_{11}$ / ppm	$\delta_{22}$ / ppm	$\delta_{33}$ / ppm
<b>[71]<sup>2-</sup></b>	3434	3434	3434	3434
<b>[72]<sup>2-</sup></b>	-533	7411	-4505	-4506
<i>cis</i> - <b>[75]</b>	-2126	3208	-4704	-4883
<i>cis</i> - <b>[76]</b>	-5143	-2954	-6054	-6421
<i>trans</i> - <b>[76]</b>	-4130	-1223	-4263	-6903
<i>Cis</i> - <b>[77]</b>	-4727	-1851	-5966	-6363
<i>trans</i> - <b>[77]</b>	-4061	-722	-4399	-7063
<i>cis</i> - <b>[14]</b>	978	2007	763	165
<i>trans</i> - <b>[14]</b>	882	1865	1517	-735
<i>trans</i> - <b>[15]</b>	1162	2429	1804	-747
<i>trans</i> - <b>[16]</b>	1273	2965	1881	-1027
<i>trans</i> - <b>[17]</b>	1156	2998	1932	-1464
<i>cis</i> - <b>[15]</b>	971	2843	116	-46
<b>[18]</b>	1756	3603	1012	654
<b>[19]</b>	1201	2360	1093	149
<b>[20]</b>	1170	2585	908	17

As SS <sup>103</sup>Rh NMR spectra could not be acquired, the reference value used to convert chemical shielding to chemical shift was set to 0 ( $\sigma_{iso}^{ref} = 0$ ). A series of simple platinum complexes were calculated and referenced to complex *cis*-[PtCl<sub>2</sub>(SMe<sub>2</sub>)<sub>2</sub>].<sup>153</sup> The high symmetry of the complexes can be used to make analysis of the FMOs simpler. These simple systems have been used to solidify understanding of the orbital transitions that can extended to the more complex, lower symmetry, rhodium system.

## 4.6 Analysis of metal complex FMOs

### 4.6.1 Analysis of $K_2[PtCl_6]^{2-}$ chemical shift tensors and FMOs

The hexachloroplatinate(IV) anion of  $K_2[71]$  is highly symmetrical and the chemical shift tensors have been explored.<sup>154</sup> The Pt environment is perfectly octahedral and the anion belongs to the  $O_h$  point group. All rotational operators belong to the triply degenerate  $T_{1g}$  irreducible representation. As all operators belong to the same irreducible representation, the orbital transitions responsible for deshielding must be the same for  $\delta_x$ ,  $\delta_y$ , and  $\delta_z$ . Group theory dictates that the shielding is isotropic, showing no difference in the magnitude of deshielding along all axes. Both the calculations and the experimental data agree with this, with a single environment being observed in the SS NMR of  $K_2[71]$  shown in Figure 95 earlier. The metal-based frontier orbitals in the  $O_h$  point group belong to two irreducible representations:  $E_g$  for the empty  $d_{x^2-y^2}$  and  $d_{z^2}$ , and  $T_{2g}$  for the filled  $d_{xy}$ ,  $d_{xz}$ , and  $d_{yz}$  orbitals. The FMOs of  $[71]^{2-}$  responsible for deshielding are shown in Figure 102.

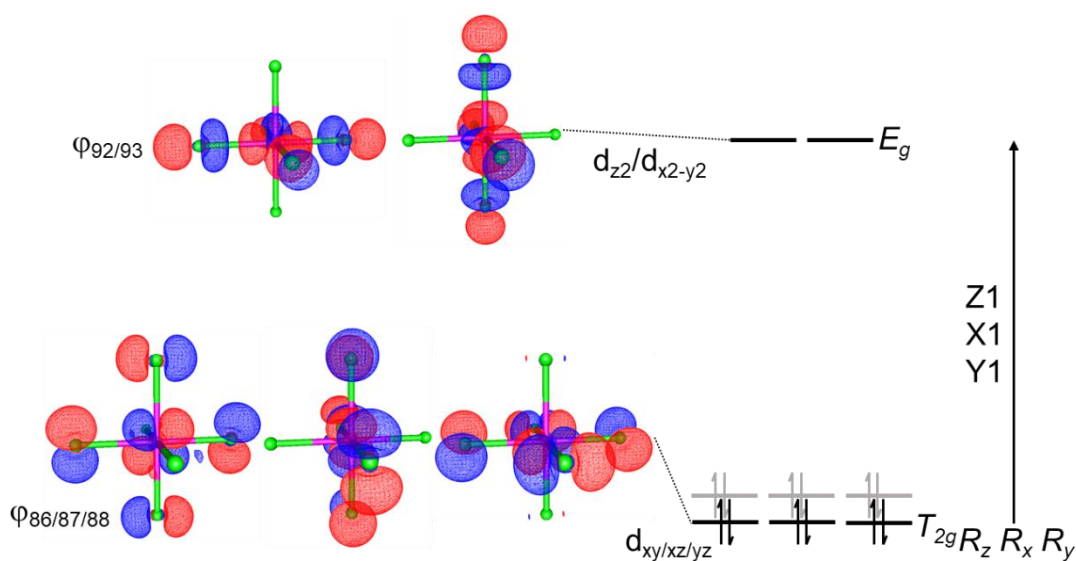


Figure 102. Visualised FMOs of  $[71]^{2-}$  with d character. Transitions are allowed between  $T_{2g}$  and  $E_g$  orbitals.  $[71]^{2-}$  optimised in Turbomole at the PBE0/def2\_TZVPP level of theory with a water COSMO implemented. Chemical shift tensors calculated in Orca at the PBE0/def2\_TZVPP level of theory with ZORA corrections. The platinum was represented with the SARC\_TZVPP basis set. Ligand-based orbitals are shown in grey.

Due to the degeneracy of  $\hat{R}_x$ ,  $\hat{R}_y$ , and  $\hat{R}_z$ , only a single transition would be possible for the d orbital subset between the occupied  $T_{2g}$  orbitals and the unoccupied  $E_g$  orbitals. Multiplication of the irreducible representations is shown below.

$$E_g \times \begin{bmatrix} \Gamma_{\hat{R}_z} \\ \Gamma_{\hat{R}_y} \\ \Gamma_{\hat{R}_x} \end{bmatrix} \times T_{2g} = E_g \times T_{1g} \times T_{2g} = A_{1g} + E_g + T_{1g} + T_{2g}$$

As the product does contain the totally symmetric representation for  $O_h$ ,  $A_{1g}$ , the transitions between d orbitals are symmetry allowed. However, as the rotational operators belong to the same irreducible representation, an isotropic deshielding is observed.

#### 4.6.2 Analysis of $K_2[PtCl_4]^{2-}$ chemical shift tensors and FMOs

The chemical shift tensors of the tetrachloroplatinate(II) anion have been recorded and predicted in the literature.<sup>153, 154</sup> The tensors of  $K_2[PtCl_4]$  have been rerecorded and recalculated as a reference for further metal calculations, as shown in section 4.5. The MO transitions responsible for deshielding in  $[72]^{2-}$  are shown in Figure 103.

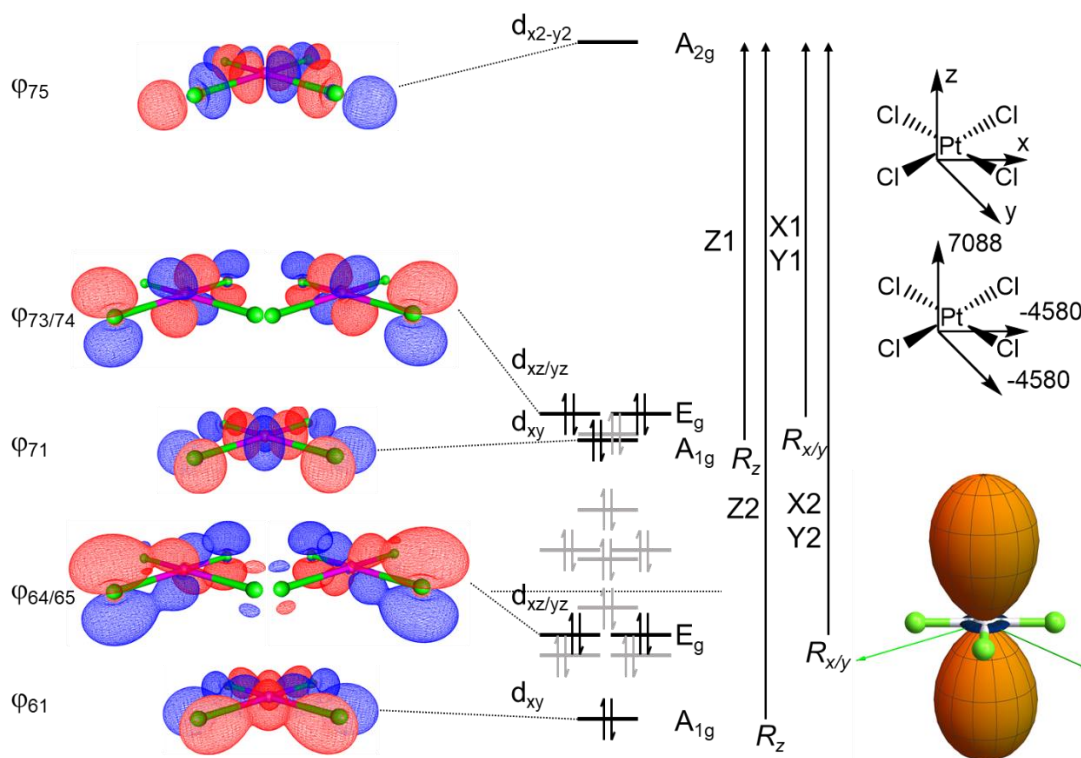


Figure 103. FMO diagram of  $[72]^{2-}$  with selected orbitals visualised in gOpenMol (left). Key transitions identified using group theory.  $[72]^{2-}$  optimised in Turbomole at the PBE0/def2\_TZVPP level of theory with a water COSMO implemented. Chemical shift tensors calculated in Orca at the PBE0/def2\_TZVPP level of theory with ZORA corrections. The platinum was represented with the SARC\_TZVPP basis set. Chemical shift tensors visualised in Wolfram Mathematica with pictorial representations (right). The barycentre is represented by the dotted line. Ligand-based orbitals are shown in grey.

The tetrachloroplatinate(II) anion belongs to the  $D_{4d}$  point group. The z axis is perpendicular to the molecular plane. The x and y axes lie parallel to the square planer geometry, with both sitting between two Pt-Cl bonds. This is shown in Figure 103. The  $\delta_{11}$  tensor points along the z axis and shows a very large deshielding

interaction of 7088 ppm. As  $\text{PtCl}_4^{2-}$  belongs to  $D_{4d}$ ,  $\Gamma_{\hat{R}_z}$  belongs to the  $A_{2g}$  irreducible representation and transitions between orbitals with  $A_{1g}$  and  $A_{2g}$  symmetry are allowed. Two symmetry allowed transitions that are coupled by  $\hat{R}_z$  are responsible for the deshielding along  $\delta_z$ ,  $\varphi_{71} \xrightarrow{\hat{R}_z} \varphi_{75}$ , Z1, and  $\varphi_{61} \xrightarrow{\hat{R}_z} \varphi_{75}$ , Z2, shown in Figure 103. Z1 contributes the largest deshielding to  $\delta_z$ , having a small energy gap of 7.1409 eV for the transition and very good overlap of the Pt d orbitals. Z2 is also a contributor to deshielding along the z axis but has a larger energy gap of 10.8359 eV and therefore contributes less.

Both the x and y axes exhibit very small deshielding interactions.  $\Gamma_{\hat{R}_{x/y}}$  belong to the  $E_g$  irreducible representation and transitions between orbitals with  $E_g$  and  $A_{2g}$  symmetry are allowed. Two symmetry-allowed transitions that are coupled by  $\hat{R}_{x/y}$  are responsible for the deshielding along  $\delta_x$  and  $\delta_y$ ,  $\varphi_{64/65} \xrightarrow{\hat{R}_{x/y}} \varphi_{75}$ , X1 and Y1, and  $\varphi_{73/74} \xrightarrow{\hat{R}_{x/y}} \varphi_{75}$ , X2 and Y2, shown in Figure 103. X1 and Y1 contribute shielding to  $\delta_x$  and  $\delta_y$ , while X2 and Y2 contribute deshielding to  $\delta_x$  and  $\delta_y$ . X1 and Y1 contribute more due to the smaller energy gap, but overlap of the Pt d orbitals are much poorer for the X and Y transitions compared to the Z transition. Hence, the chemical shift tensors are dominated largely by Z1. This assessment is in agreement with the analysis shown by Gilbert and Ziegler.<sup>153</sup>

#### 4.6.3 Analysis of *cis*-[PtCl<sub>2</sub>(NH<sub>3</sub>)<sub>2</sub>] chemical shift tensors and FMOs

As with K<sub>2</sub>[72], the chemical shift tensors of *cis*-platin *cis*-[75] have been predicted in the literature.<sup>153</sup> The MO transitions responsible for deshielding in *cis*-[75] are shown in Figure 104.

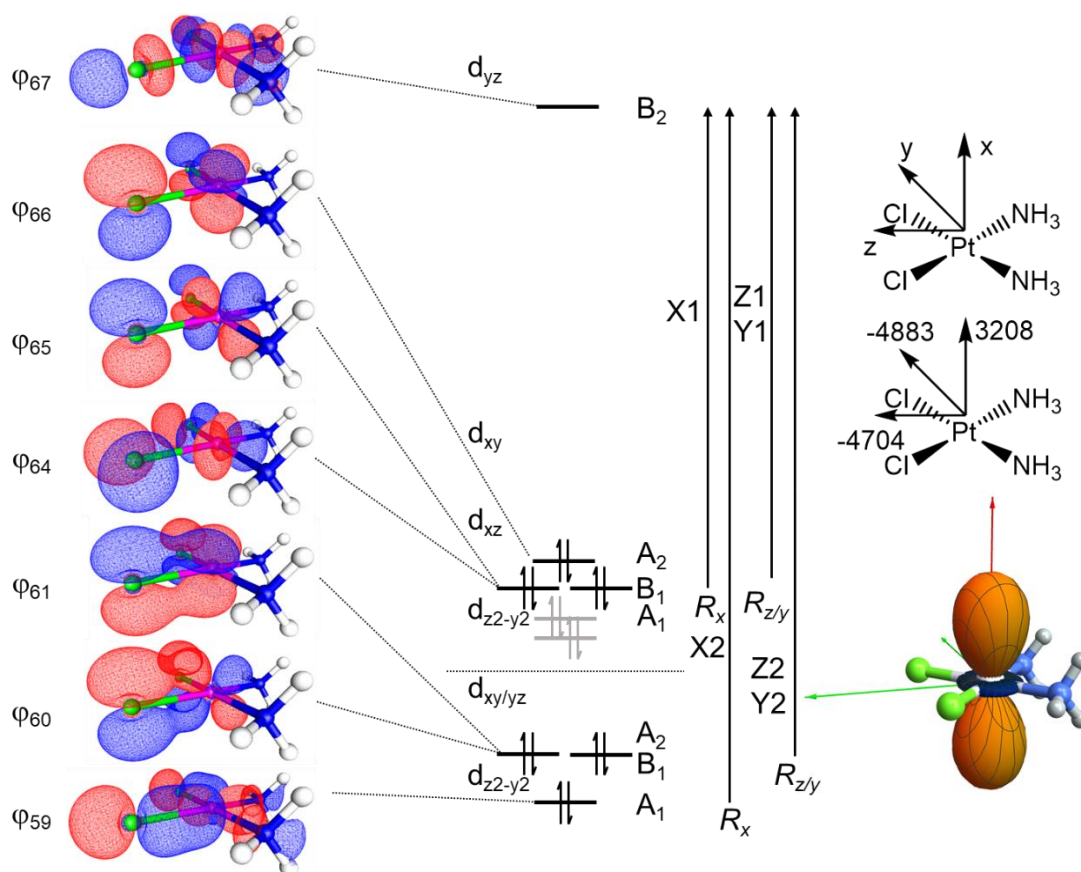


Figure 104. FMO diagram of *cis*-[75] with selected orbitals visualised in gOpenMol (left). Key transitions identified using group theory. *cis*-[75] optimised in Turbomole at the PBE0/def2\_TZVPP level of theory with a water COSMO implemented. Chemical shift tensors calculated in Orca at the PBE0/def2\_TZVPP level of theory with ZORA corrections. The platinum was represented with the SARC\_TZVPP basis set. Chemical shift tensors visualised in Wolfram Mathematica with pictorial representations (right). The barycentre is represented by the dotted line. Ligand-based orbitals are shown in grey.

Complex *cis*-[75] belongs to the  $C_{2v}$  point group. The  $z$  axis is parallel to the plane of the molecule and runs between the two Pt-Cl bonds. The  $x$  axis is perpendicular to the plane of the molecule and the  $y$  axis lies parallel to the square planar geometry

pointing in between the Pt-Cl and Pt-N bonds. This is shown in Figure 104. Because of the symmetry, the platinum d orbitals have non-canonical representations compared to **[72]**<sup>2-</sup>. The change in the principal rotation axis from being perpendicular to the molecular plane to being between the Pt-Cl bonds in the molecular plane results in d orbitals that have been given non-canonical labels.

Although the symmetry of *cis*-**[75]** is lower than for **[72]**<sup>2-</sup>, the shape and magnitudes of the chemical shift tensors are similar. The  $\delta_{11}$  tensor points along the x axis and shows a large deshielding interaction. As *cis*-**[75]** belongs to the  $C_{2v}$  point group,  $\Gamma_{\hat{R}_x}$  belongs to the  $B_2$  irreducible representation and transitions between orbitals with  $A_1$  and  $B_2$  symmetry are allowed. Two symmetry allowed transitions that are coupled by  $\hat{R}_x$  are responsible for the deshielding along  $\delta_x$ ,  $\phi_{64} \xrightarrow{\hat{R}_x} \phi_{67}$ , X1, and  $\phi_{59} \xrightarrow{\hat{R}_x} \phi_{67}$ , X2, shown in Figure 104. X1 contributes the largest deshielding to  $\delta_x$ , having a small energy gap for the transition and very good overlap of the Pt d orbitals. X2 is also a contributor to deshielding along the x axis.

Both the z and y axes exhibit small deshielding interactions.  $\Gamma_{\hat{R}_z}$  belongs to the  $A_2$  irreducible representation and transitions between orbitals with  $B_2$  and  $B_1$  symmetry are allowed. Two symmetry allowed transitions that are coupled by  $\hat{R}_z$  are responsible for the deshielding along  $\delta_z$ ,  $\phi_{60} \xrightarrow{\hat{R}_z} \phi_{67}$ , Z1, and  $\phi_{65} \xrightarrow{\hat{R}_z} \phi_{67}$ , Z2, shown in Figure 104.

$\Gamma_{\hat{R}_y}$  belongs to the  $B_1$  irreducible representation and transitions between orbitals with  $B_2$  and  $A_2$  symmetry are allowed. Two symmetry-allowed transitions that are coupled by  $\hat{R}_y$  are responsible for the deshielding along  $\delta_y$ ,  $\phi_{61} \xrightarrow{\hat{R}_y} \phi_{67}$ , Y1, and  $\phi_{66} \xrightarrow{\hat{R}_y} \phi_{67}$ , Y2, shown in Figure 104.

Z1 and Y1 contribute shielding to  $\delta_z$  and  $\delta_y$ , while Z2 and Y2 contribute deshielding to  $\delta_z$  and  $\delta_y$ . Z1 and Y1 are larger than Z2 and Y2 due to the smaller energy gap, but overlap of the Pt d orbitals is still poor for Z and Y transitions compared to the X transition. Overall deshielding is dominated largely by X1.

The shielding interaction along  $\delta_y$  is slightly larger than that of  $\delta_z$ , as the energy gap of transition Y1 is slightly compressed. This leads to the observed differences in the  $\delta_{22}$  and  $\delta_{33}$  tensors observed in *cis*-[**75**] compared to [**72**]<sup>2-</sup>.

#### 4.6.4 Analysis of *cis*-[PtCl<sub>2</sub>(PH<sub>3</sub>)<sub>2</sub>] chemical shift tensors and FMOs

The phosphorus equivalent of *cis*-[PtCl<sub>2</sub>(NH<sub>3</sub>)<sub>2</sub>] (*cis*-[**75**]), *cis*-[PtCl<sub>2</sub>(PH<sub>3</sub>)<sub>2</sub>] *cis*-[**76**], exhibits values of chemical shift tensors that vary from the nitrogen containing equivalent. The transitions responsible for deshielding are shown in Figure 105. As with *cis*-[**75**], the d orbitals are represented by non-canonical descriptors as a consequence of the point group.

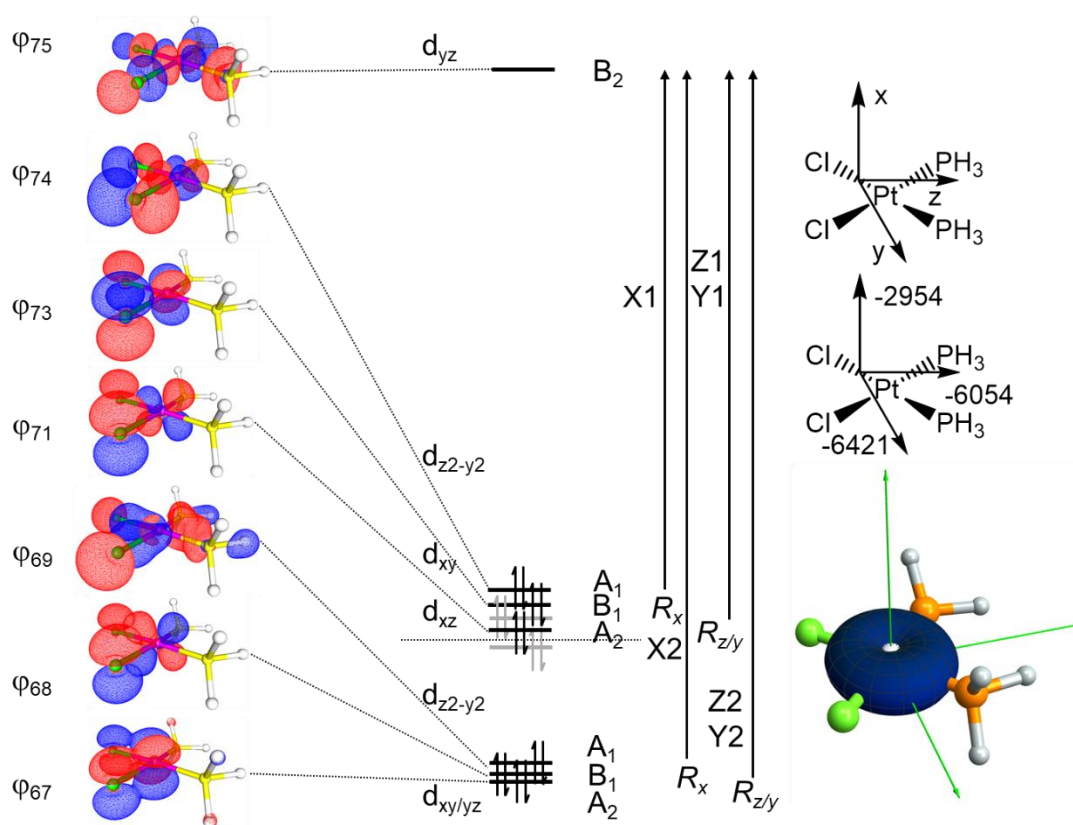


Figure 105. FMO diagram of *cis*-[**76**] with selected orbitals visualised in gOpenMol (left). Key transitions identified using group theory. *cis*-[**76**] optimised in Turbomole at the PBE0/def2\_TZVPP level of theory with a water COSMO implemented. Chemical shift tensors calculated in Orca at the PBE0/def2\_TZVPP level of theory with ZORA corrections. The platinum was represented with the SARC\_TZVPP basis set. Chemical

shift tensors visualised in Wolfram Mathematica with pictorial representations (right). The barycentre is represented by the dotted line. Ligand-based orbitals are shown in grey.

The  $\delta_{11}$  tensor points along the x axis and shows a slight deshielding interaction. As *cis*-[**76**] also belongs to the  $C_{2v}$  point group,  $\Gamma_{\hat{R}_x}$  belongs to the  $B_2$  irreducible representation and transitions between orbitals with  $A_1$  and  $B_2$  symmetry are allowed. Two symmetry allowed transitions that are coupled by  $\hat{R}_x$  are responsible for the deshielding along  $\delta_x$ ,  $\varphi_{74} \xrightarrow{\hat{R}_x} \varphi_{75}$ , X1, and  $\varphi_{64} \xrightarrow{\hat{R}_x} \varphi_{75}$ , X2, shown in Figure 105.

A large change is observed along the  $\delta_x$  tensor, with the large deshielding being further reduced along the series [**72**]<sup>2-</sup> > *cis*-[**75**] > *cis*-[**76**]. The magnetic coupling of MOs containing heavy element atomic orbital contributions becomes increasingly important in the contribution to deshielding. Orbital  $\varphi_{73}$  contains nearly no phosphorus character, as phosphorus is much larger than nitrogen, it has a large effect on the magnitude of the magnetic coupling of  $\varphi_{73}$  and  $\varphi_{75}$ . The effect is that X1 becomes a poor contributor to deshielding and deshielding along  $\delta_x$  becomes dominated by the smaller X2 transition. The reduction of the contribution of X1 leads to the small deshielding interaction observed.

As with *cis*-[**75**], deshielding is observed along  $\delta_z$  and  $\delta_y$  with the same Z1/2 and Y1/2 transitions being responsible and not being large contributors to deshielding. Lack of phosphorus orbital character in the MO reduces the magnetic coupling of these orbitals in *cis*-[**76**] further reducing deshielding.

#### 4.6.5 Analysis of *cis*-[Rh(Cl)(CO)(PH<sub>3</sub>)<sub>2</sub>] chemical shift tensors and FMOs

Complex *cis*-[Rh(Cl)(CO)(PH<sub>3</sub>)<sub>2</sub>], *cis*-[**14**], is a truncated version of *cis*-[Rh(Cl)(CO)(PPh<sub>3</sub>)<sub>2</sub>] *cis*-[**15**] with the PPh<sub>3</sub> ligands substituted for phosphine ligands. The chemical shift tensors are fully asymmetric due to the molecule possessing low symmetry and displaying deshielding along all axes. The key MOs and transitions have been visualised and are displayed in Figure 106.

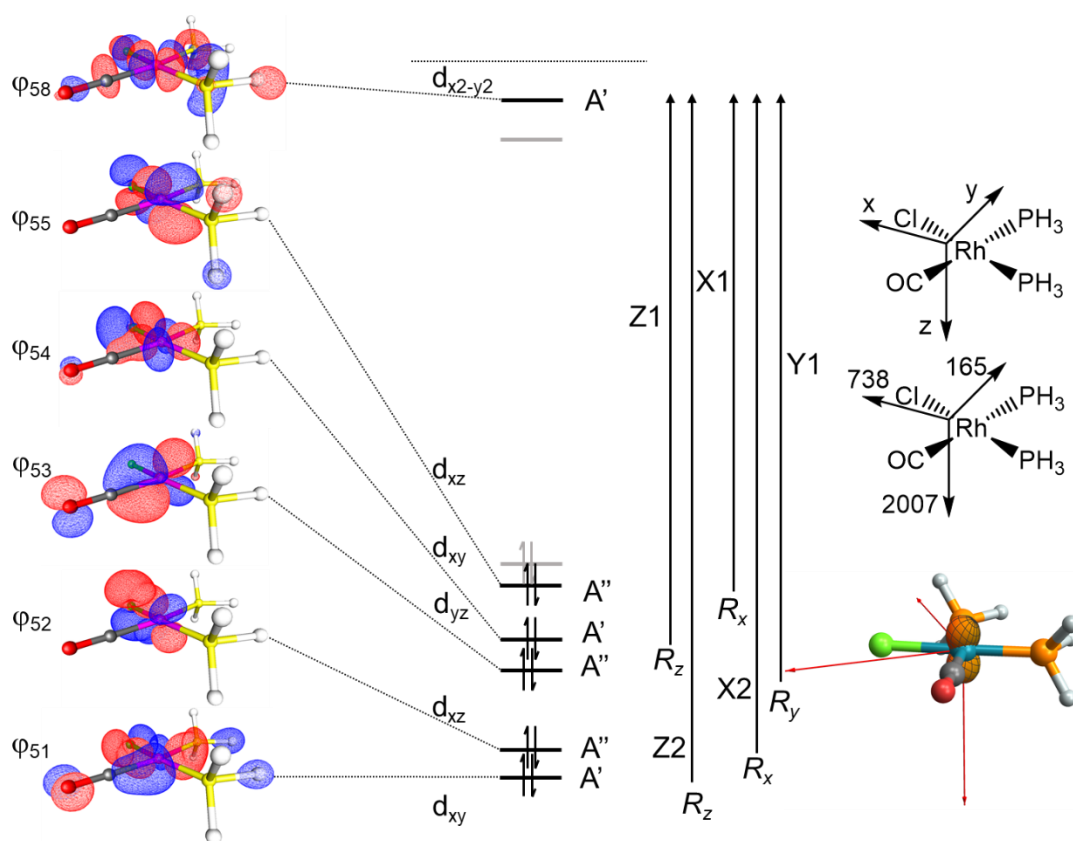


Figure 106. FMO diagram of *cis*-[**14**] with selected orbitals visualised in gOpenMol (left). Key transitions identified using group theory. *cis*-[**14**] optimised in Turbomole at the PBE0/def2\_TZVPP level of theory with a water COSMO implemented. Chemical shift tensors calculated in Orca at the PBE0/def2\_TZVPP level of theory with ZORA corrections. Chemical shift tensors visualised in Wolfram Mathematica with pictorial representations (right).

Complex *cis*-[**14**] has lower symmetry than *cis*-[**75**] due to the presence of the inequivalent chloride and carbonyl ligands. This means that *cis*-[**14**] belongs to the  $C_s$  point group. The largest deshielding interaction,  $\delta_{11}$ , is along the  $z$  axis and is associated with the transition  $\varphi_{54} \xrightarrow{\hat{R}_z} \varphi_{58}$ , Z1. Another transition is coupled by  $\hat{R}_z$ ,  $\varphi_{51} \xrightarrow{\hat{R}_z} \varphi_{58}$ , Z2, although the energy of the transition is larger and the magnetic coupling lower leading to Z1 being the larger contributor to the interaction. The smallest deshielding tensor,  $\delta_{33}$ , is associated with transitions coupled by  $\hat{R}_y$ . The only transitions that is symmetry allowed is  $\varphi_{53} \xrightarrow{\hat{R}_y} \varphi_{58}$ , Y1. The magnetic coupling of this interaction is poor meaning that very little deshielding is observed along the  $y$  axis.

$\delta_{22}$  is similar to  $\delta_{33}$  in that the magnetic coupling of  $\varphi_{55} \xrightarrow{\hat{R}_x} \varphi_{58}$ , X1, is poor. However, the narrowing energy gap increases the deshielding contribution to  $\delta_{22} = 738$ . The chemical shift tensors of *cis*-[15], [18], [19], and [20] are associated with the same transitions and possess the same pseudo-symmetry.

#### 4.6.6 Analysis of *trans*-[Rh(Cl)(CO)(PH<sub>3</sub>)<sub>2</sub>] chemical shift tensors and FMOs

Complex *trans*-[Rh(Cl)(CO)(PH<sub>3</sub>)<sub>2</sub>], *trans*-[14], is a truncated version of *trans*-[Rh(Cl)(CO)(PPh<sub>3</sub>)<sub>2</sub>], *trans*-[15], with the PPh<sub>3</sub> ligands substituted for phosphine. The complex *trans*-[14] belongs to the *C*<sub>2v</sub> point group. The key MOs and transitions have been visualised and are displayed in Figure 107.

The FMOs of *trans*-[14] differ from the *cis*- equivalent. Due to the symmetry of the molecule, the d orbitals have been labelled non-canonically. The chemical shift tensors also differ significantly between *cis*- and *trans*- geometries. One conserved feature is that the largest deshielding tensor lies perpendicular to the square plane of the molecule. Although the symmetry of *trans*-[14] is different from *cis*-[14], the interactions that give rise to the largest deshielding tensor,  $\delta_{11}$ , are the same. Transitions facilitated by  $\hat{R}_x$  in the *C*<sub>2v</sub> point group must be between orbitals with *A*<sub>1</sub> and *B*<sub>2</sub> symmetry. Two transitions were identified:  $\varphi_{53} \xrightarrow{\hat{R}_x} \varphi_{58}$ , X1, and  $\varphi_{51} \xrightarrow{\hat{R}_x} \varphi_{58}$ , X2. Both X1 and X2 contribute to deshielding along the x axis with X1 being the stronger contributor with the lower energy gap. A large amount of phosphorus character in the LUMO+1 slightly reduces the coupling of X1. The total deshielding of X1 and X2 is similar to the combined deshielding of Z1 and Z2 in *cis*-[14].

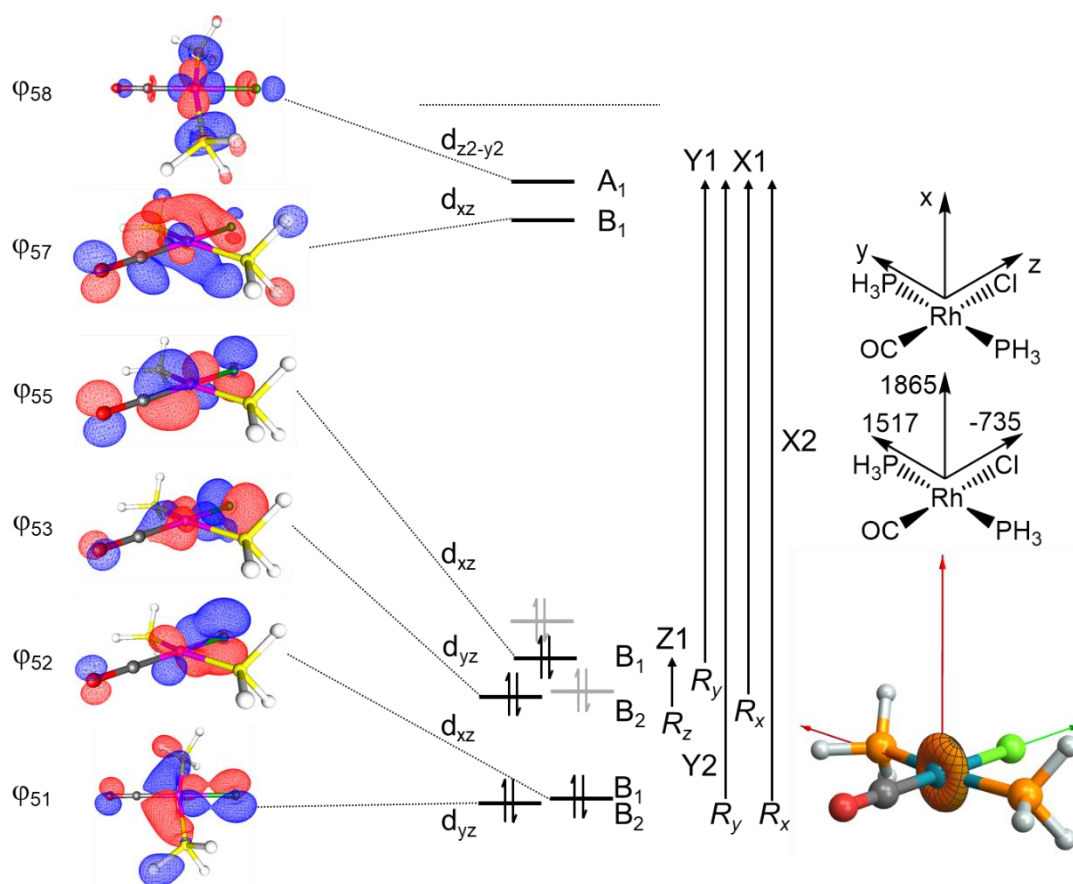


Figure 107. FMO diagram of *trans*-[14] with selected orbitals visualised in gOpenMol (left). Key transitions identified using group theory. *trans*-[14] optimised in Turbomole at the PBE0/def2\_TZVPP level of theory with a water COSMO implemented. Chemical shift tensors calculated in Orca at the PBE0/def2\_TZVPP level of theory with ZORA corrections. Chemical shift tensors visualised in Wolfram Mathematica with pictorial representations (right).

The  $\delta_{33}$  tensor is along the z axis which points along the Rh-Cl bond. Transitions facilitated by  $\hat{R}_z$  in the  $C_{2v}$  point group must be between orbitals with  $B_1$  and  $B_2$  symmetry. The main interaction is coupling between two filled orbitals  $\phi_{53} \xrightarrow{\hat{R}_z} \phi_{55}$ ,  $Y_1$ . This interaction has a low energy gap and is shielding in nature, but the magnitude of the shielding is relatively small as the transition is occupied to occupied.

The  $\delta_{22}$  tensor is along the y axis which points along the Rh-P bond. Transitions facilitated by  $\hat{R}_y$  in the  $C_{2v}$  point group must be between orbitals with  $A_1$  and  $B_1$  symmetry. Two transitions were identified as the major contributors to deshielding

along the y axis:  $\phi_{55}^{\hat{R}_y} \rightarrow \phi_{58}$ , Y1, and  $\phi_{52}^{\hat{R}_y} \rightarrow \phi_{58}$ , Y2. Both interactions contribute deshielding and have energy gaps comparable to X1 and X2. The total deshielding along the y axis is smaller than along the x axis. Coupling between the  $d_{xz}$  and  $d_{z^2-y^2}$  orbitals is less effective than coupling between  $d_{yz}$  and  $d_{z^2-y^2}$  orbitals, reducing the deshielding to  $\delta_y = 1517$  vs  $\delta_x = 1865$ .

## 4.7 Discussion

### 4.7.1 Effect of pnictogen on $^{103}\text{Rh}$ chemical shift tensors in *trans*-rhodium Vaska-type complexes

The transitions responsible for deshielding in *trans*-rhodium Vaska complexes have been identified in section 4.6.6 earlier. As previously shown in Figure 101, chemical shift tensors for a range of rhodium Vaska-type complexes with *trans*-geometry were calculated. The results of the calculations are summarised again in Table 25 and the visualized tensors displayed in Figure 108.

Table 25. Chemical shift tensors of rhodium Vaska-type complexes calculated at the PBE0/def2\_TZVPP.

Complex	$\delta^{\text{iso}}$ / ppm	$\delta_{11}$ / ppm	$\delta_{22}$ / ppm	$\delta_{33}$ / ppm
<i>trans</i> -[14]	882	1865	1517	-735
<i>trans</i> -[15]	1162	2429	1804	-747
<i>trans</i> -[16]	1273	2965	1881	-1027
<i>trans</i> -[17]	1156	2998	1932	-1464

As with the *cis*-Vaska-type complexes, the changes to  $\delta_{22}$  are small in the *trans*-complexes. Moving between phosphine, arsine, and stibine ligands,  $\delta_{33}$  becomes more deshielding. At the same time, the deshielding of  $\delta_{11}$  also changes. The pictorial and visualised tensors of the *trans*-Vaska-type complexes are displayed in Figure 108.

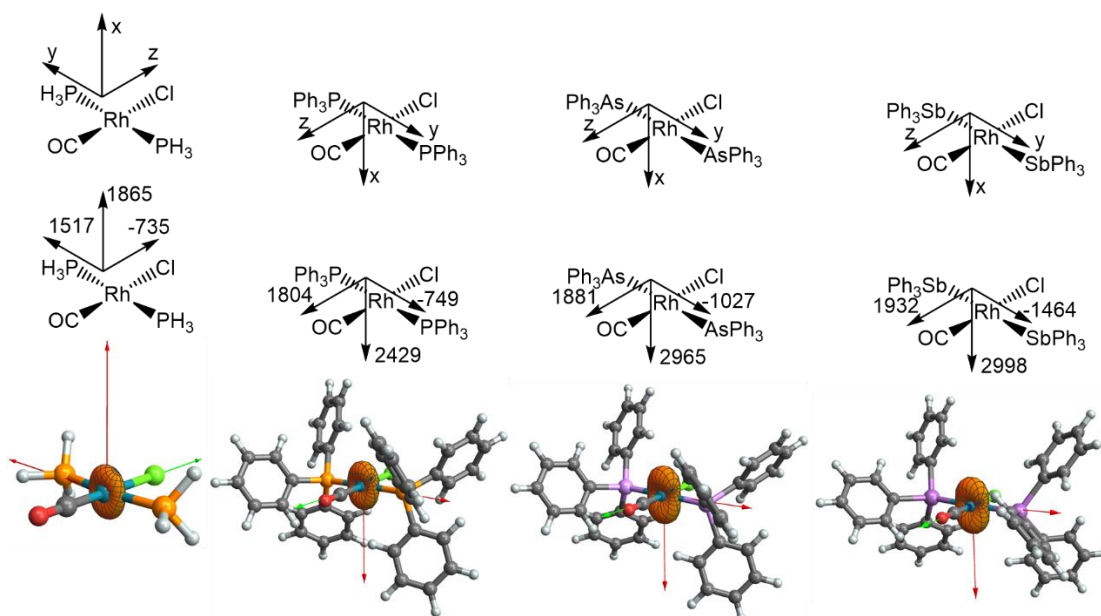


Figure 108.  $^{103}\text{Rh}$  chemical shift tensors of rhodium Vaska-type complexes in pictorial (Top) and visualized (Bottom) forms. Chemical shift tensors visualised in Wolfram Mathematica.

The magnitude of  $\delta_{33}$  becomes more deshielding on exchanging P for As by 280 ppm. It becomes a further 437 ppm more deshielded exchanging between As and Sb. This must be associated with a contraction of energy of the Z1 transition and therefore a larger shielding interaction. The magnitude of this change is relatively small in comparison to the magnitude of the total anisotropy. However, combined with the changes to  $\delta_{11}$ , it is enough to keep the isotropic chemical shift relatively constant.

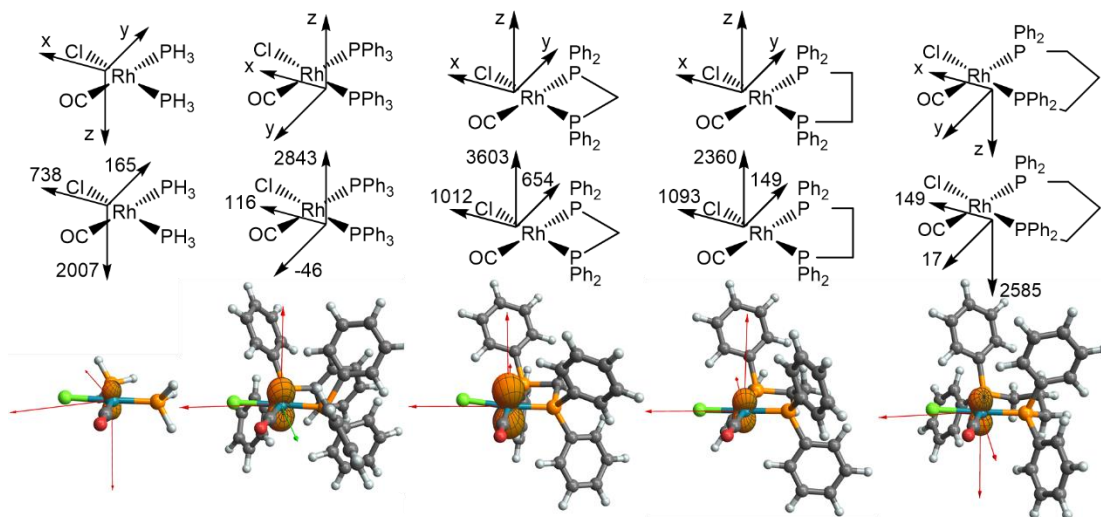
The increasing deshielding of  $\delta_{11}$  is large on exchanging P for As, 536 ppm, but the change between As and Sb is much smaller, 33 ppm. This suggests that a contraction of energy is observed in the X1 or X2 transitions. It is likely that the bonding orbital of X2 rises in energy between P and As causing the increased deshielding. The small change observed between As and Sb may be associated with the similar size of the As and Sb orbitals due to the lanthanide contraction. The lack of ligand orbital character in the Z1 transition may explain why the contraction is not observed directly.

#### 4.7.2 Effect of L-Rh-L bite angle on $^{103}\text{Rh}$ chemical shift tensors in *cis*-rhodium Vaska-type complexes

The transitions responsible for deshielding in *cis*-rhodium Vaska-type complexes have been identified in section 4.6.5 earlier. As previously shown in Figure 101, chemical shift tensors for a range of rhodium Vaska-type complexes with *cis*-geometry were calculated. The results of the calculations are summarised again in Table 26 and the visualized tensors displayed in Figure 109.

Table 26. Chemical shift tensors and P-Rh-P angles of rhodium Vaska-type complexes calculated at the PBE0/def2\_TZVPP.

Complex	$\delta^{\text{iso}}$ / ppm	$\delta_{11}$ / ppm	$\delta_{22}$ / ppm	$\delta_{33}$ / ppm	P-Rh-P / °
<i>cis</i> -[14]	978	2007	763	165	96.91
<i>cis</i> -[15]	971	2843	116	-46	98.91
[18]	1756	3603	1012	654	73.32
[19]	1201	2360	1093	149	85.47
[20]	1170	2585	908	17	93.50



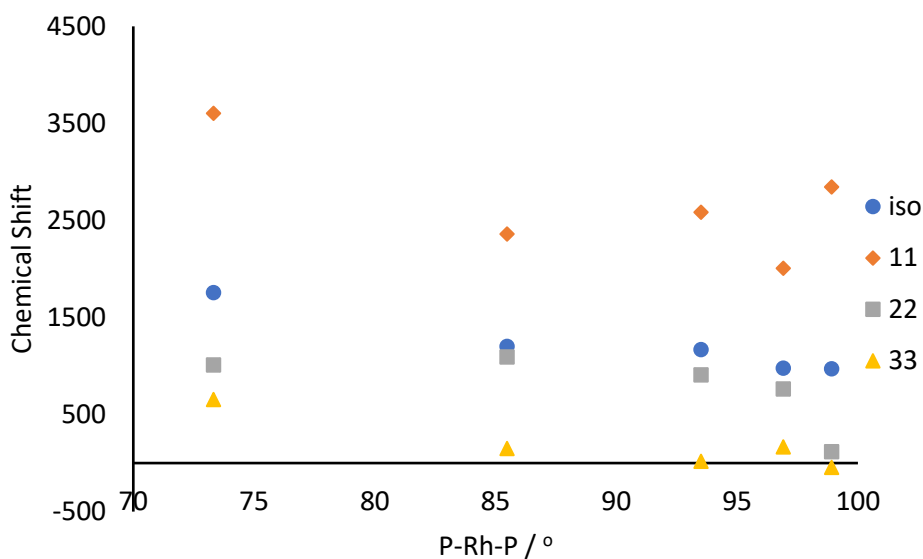


Figure 109.  $^{103}\text{Rh}$  chemical shift tensors of rhodium Vaska-type complexes in pictorial (Top) and visualized (Middle) forms. Chemical shift tensors visualised in Wolfram Mathematica. Angular dependence of NMR parameters based on P-Rh-P angle (Bottom).

As shown in Figure 109, the weightings of the chemical shift tensors for the Vaska type complexes are the same, with  $\delta_{11}$  being along the z axis perpendicular to the plane of the molecule and  $\delta_{33}$  along the y axis offset from the P-Rh-C bond. Focusing particularly on moving from dppm to dppe to dppp, the isotropic chemical shift decreases as the P-Rh-P angle increases. The contribution of  $\delta_{33}$  to total deshielding decreases with a large change between dppm and dppe (505 ppm) and a smaller change between dppe and dppp (132 ppm). The more acute angle means better coupling between the  $d_{yz}$  and  $d_{x^2-y^2}$  orbitals.<sup>155-157</sup> This effect is very small suggesting little change to orbital energy between the three ligands.

$\delta_{33}$  follows the trend dppm > dppe  $\approx$  dppp.  $\delta_{11}$  shows similarity with the magnitude following the trend dppm > dppp  $\approx$  dppe with the difference between dppm and dppp being 1018 ppm and the difference between dppp and dppe being 225 ppm. The particularly large deshielding effect along the z axis is associated with coupling between  $d_{xy}$  and  $d_{x^2-y^2}$  orbitals. When dppm is used as the ligand, the very small bite angle means that the antibonding overlap of phosphorus orbitals with the  $d_{x^2-y^2}$

orbitals is poorer, meaning a smaller energy gap and larger deshielding in the Z1 type interaction.

The difference between dppe and dppp likely arises from the same interaction in the bonding overlap of phosphorus orbitals with the  $d_{xy}$  orbital. The smaller bite angle of dppe lowers the energy of this interaction leading to a larger energy gap and smaller deshielding in the Z2 type interaction. The total deshielding along the z axis is dominated by large changes to the Z1 interaction when the bite angle is small, but as bite angle increases, the decreasing Z2 interaction becomes important.

Understanding whether subtle ligand effects can be used to explain differences in catalytic activity and I:b ratios would require more study on catalytic intermediates. However, changes to the chemical shift tensors have been used to explore changes to orbital energies and overlaps on increasing bite angle of *cis*-Vaska type complexes.

## 4.8 Conclusions and future work

The angular dependence of the calculated chemical shift of a series of rhodium complexes that are relevant to rhodium-catalysed hydrogenation and hydroformylation has been explored in this chapter. Increasing phosphine bite angle decreases the  $^{103}\text{Rh}$   $\delta^{\text{iso}}$ . Large deshielding along the z axis, which is perpendicular to the plane of the complex, decreases significantly when the bite angle is increased from 73 °, with dpdm, to 85 ° and 94 °, with dppe and dppp respectively.

Increased interaction of the phosphine with the  $d_{x^2-y^2}$  orbital of rhodium increases the energy gap and reduces deshielding. This effect is less pronounced between dppe and dpdm as the decreasing interaction between phosphine and  $d_{xy}$  orbitals reduces the energy gap and therefore increasing deshielding. This secondary effect is smaller when bite angle is very small.

The effect of bite angle could be further explored by screening a larger span of ligands with well characterized bite angles. For example, a larger sweep of phosphine ligands may provide more insight into the correlation between ligand to metal overlap and chemical shift. However, careful consideration must be used in the selection of ligands for study due to potentially large changes to FMO energy and character by, for instance, changing donor atoms from phosphorus.

Phosphine bite angle is known to affect the ratio of linear to branched hydroformylated product. To further explore this, the rhodium and carbon chemical shift tensors could be calculated for each state along the hydroformylation catalytic cycle with different bite angle phosphine ligands giving particular focus on the key isomer determining step. Inclusion of phosphine ligands with a range of natural bite angles will strain the rhodium centre as overlap with the rhodium orbitals changes. The chemical shift tensors of the rhodium centre and metal bound carbons will show dependence to bite angle and could provide insight into the energies of the molecular orbitals at rhodium, providing an explanation to the linear/branched preference of rhodium catalysed hydroformylation. With this, ligands may be designed with preference to forming either linear or branched aldehyde.

## Chapter 5. Conclusions and future work

This thesis has been focused on using the three-dimensional chemical shift interaction, or chemical shift tensors, to probe the FMO interactions between metals and their coordinating ligands. We have developed a robust methodology for the calculation of chemical shift tensors, particularly of carbon nuclei that are bound to metals, using the GIAO framework in Orca with ZORA. The predictive power of the quantum chemical calculations has been shown to be robust for organometallic and organic compounds. Although the prediction of the chemical shift tensors for purely organic compounds is less accurate than for organometallic compounds, this is likely a referencing artifact given this body of work's focus on organometallic compounds. Future work in this area can focus on the recording SS NMR spectra of more organometallic and organic compounds so that another reference can be selected that will give improved predictive power in more shielded compounds such as simple alkanes. The methodology used here has been compared to chemical shift tensor analysis that has been performed in the literature of ethene and ethyne to demonstrate the robustness of the computational methodology.

SS NMR spectra have been recorded for the first time for a series of ruthenium organometallic vinylidene and alkynyl complexes and their chemical shift tensors recovered. Distinctive deshielding patterns were observed in both vinylidene and alkynyl complexes. Fluorinated equivalents of vinylidene and alkynyl complexes show large changes to the shielding of the metal bound carbon,  $C_{\alpha}$ . The changes to  $\delta_{iso}$  in complexes **[4]** and **[7]** have been shown to be associated with depression of the  $\sigma$ -bonding orbital, depressing in energy and increasing the energy gap to the LUMO. This effect results in the  $\delta_x$  and  $\delta_y$  tensors reducing from  $\sim 230$  to  $\sim 100$  ppm. SS NMR spectroscopy has been used to provide complimentary data to UV-vis spectroscopy in alkynyl complexes. The changes to  $\delta_{iso}$  in complexes **[2a]<sup>+</sup>** and **[3a]<sup>+</sup>** have been shown to be associated with lowering of the LUMO in energy, narrowing the HOMO $\rightarrow$ LUMO energy gap. In **[2a]<sup>+</sup>** and **[3a]<sup>+</sup>**, where  $\delta^{iso}$  is 353.7 and 388.6 ppm, respectively, this energy gap contracts from 4.06 to 3.32 eV and is accompanied by a

236 ppm increase in deshielding along the M-C bond axis and correlating to an observed colour change.

The chemical shift tensors of vinylidene complexes have been calculated to be similar to vinyliminium compounds. Chemical shift tensors could have introduced us to a new series of organic compounds in which electrophilic fluorination could be performed on. Future work in this area can use the insight gained from the chemical shift tensors to synthesize organic compounds bearing the “yneamine” moiety and treating them with a source of “F<sup>+</sup>”, providing a route to novel fluorinated compounds.

As well as probing the metal bound carbon C<sub>α</sub>, this project has started the exploration of rhodium and platinum chemical shift tensors. Attempts to record high resolution SS NMR spectra of <sup>103</sup>Rh and <sup>195</sup>Pt nuclei have yielded mixed results with high resolution spectra being obtained for the potassium salts of the tetrachloro- and hexachloro- platinate di-anions. With more time, further work in this area will expand the number of high-resolution <sup>195</sup>Pt SS NMR spectra recorded. With a larger repository of <sup>195</sup>Pt SS NMR spectra, more trends in the chemical shift interaction for metal nuclei can be explored through the inclusion of different coordinating ligands with different geometries. <sup>103</sup>Rh tensors have been explored in complexes relevant to the hydroformylation of alkenes focusing specifically on the effect of pnictogen atom and bidentate phosphine bite angle on the chemical shift tensors. Increased matching of the bidentate phosphine bite angle with the d<sub>x<sup>2</sup>-y<sup>2</sup></sub> orbital lobes of rhodium increases the energy gap and reduces deshielding.

Overall, the work in this thesis has focused on developing an analytical method in interpreting the FMOs *via* the chemical shift interaction. Future work using this methodology will allow this analytical method to be applied to a range of systems that are currently poorly described by other spectroscopic methods. This method has been developed using organometallic complexes but may be applied more generally to understanding the reactivity and bonding in organic chemical systems.

## Chapter 6. Experimental

### 6.1 General considerations

All experimental procedures in this report were performed under a nitrogen atmosphere using Schlenk line apparatus and glove-box techniques. Dichloromethane, hexane, toluene, tetrahydrofuran, and diethyl ether were dried with the aid of an Innovative Technologies anhydrous solvent engineering system. Methanol was dried over magnesium and iodine under argon and distilled before use. Pentane was dried over sodium under argon and distilled before use. Deuterated dichloromethane and acetonitrile were dried over  $\text{CaH}_2$  and degassed with three freeze-pump-thaw cycles before trap-to-trap transfer to ampoules fitted with a PTFE Young's tap. The solvent was then stored under a nitrogen atmosphere in a glove-box.  $\text{RuCl}_3 \cdot x\text{H}_2\text{O}$  and  $\text{RhCl}_3 \cdot 3\text{H}_2\text{O}$  was purchased from Precious Metals Online. Dicyclopentadiene, *tert*-butylacetylene, triphenylarsine, and triphenylstibine were purchased from Sigma Aldrich. Phenylacetylene was purchased from Alfa Aeser. 4-ethynyl- $\alpha,\alpha,\alpha$ -trifluorotoluene was purchased from Apollo Chemicals. Trimethylsilylacetylene, 4-ethynylanisole, and triphenylphosphine were purchased from Fluorochem. 1,2-*bis*-(diphenylphosphino)ethane was purchased from Activate Scientific. Due to the spectroscopic nature of this work, analytical purity of synthesized compounds was not tested by CHN microanalysis. However, the synthesized compounds were purified so that their NMR spectra were clear of contamination for SS NMR analysis, further purification was deemed unnecessary.

Solution phase NMR spectra were performed in NMR sample tubes fitted with PTFE Young's taps. The NMR spectra were acquired on a JEOL ECX-400 (operating frequencies: 399.78 MHz for  $^1\text{H}$ , 161.83 MHz for  $^{31}\text{P}$ , and 376.17 MHz for  $^{19}\text{F}$ ).  $^{31}\text{P}$  NMR spectra were recorded with proton decoupling. Solid state experiments were acquired on a Bruker AVHDIII 400 solids spectrometer (operating frequencies: 400.13 MHz for  $^1\text{H}$ , 100.61 MHz for  $^{13}\text{C}$ , 376.50 MHz for  $^{19}\text{F}$ , and 161.98 MHz for  $^{31}\text{P}$ ).  $^{13}\text{C}$  and  $^{31}\text{P}$  NMR spectra were recorded with proton decoupling. The solid-state NMR samples were finely ground and packed into 4 mm  $\text{ZrO}_2$  rotors fitted with Kel-F caps. Spectra were processed using TopSpin 3.5.

Single-crystal X-ray diffraction data were collected on a single source from the two available sources (Cu-K $\alpha$  radiation, 1.54184 Å, or Mo-K $\alpha$  radiation, 0.71073 Å) Oxford Diffraction SuperNova X-ray diffractometer. Crystals were cooled to 110 K with an Oxford Instruments CryoJet. The Diffractometer control, unit cell determination and refinement, data collection, and frame integration were performed with CrysAlisPro. OLEX2 was used for structure solution and refinement. Non-hydrogen atoms were refined anisotropically, hydrogen atoms were placed using a “riding model” and included in the refinement at calculated positions. The data were collected and refined by Adrian Whitwood, Rachel Parker, and Theo Tanner.

Recording of ESI mass spectrometry measurements were performed on a Bruker microTOF MS. Data were collected by Karl Heaton.

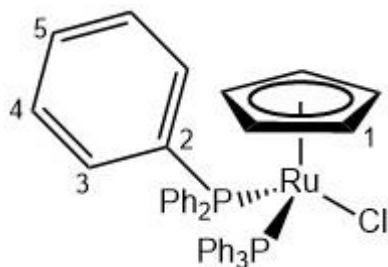
Initial geometry optimisations were performed at the (RI-)BP86/def2\_SV(P) level, followed by frequency calculations at the same level. Local minima were identified by the absence of imaginary frequency vibrations. In the (RI-)BP86/def2\_SV(P) calculations, a 60 electron quasi-relativistic ECP replaced the core electrons of Ru. No symmetry constraints were applied during optimisations. All optimisation calculations were performed using the TURBOMOLE V6.40 package using the resolution of identity (RI) approximation.

NMR single point calculations were performed within the GIAO framework using Orca 4.0.2.1 package. Single-point calculations on the (RI-)BP86/SV(P) optimised geometries were performed using the hybrid PBE0 functional and the flexible def2-TZVPP-ZORA basis set. The single point NMR calculations were performed using within the GIAO framework using the ORCA 4.0.2.1 package. Relativistic effects were treated by the 2 component zeroth order regular approximation (ZORA). The tensors were represented in 3D as polar plots of the chemical shielding tensor matrix with scaling factors of 0.5.

Orbital plots were obtained from the single point calculations using the orca\_plot interactive menu. The number of grid intervals was set to 120. The .plt files were visualised in gOpenMol, setting the isosurface values to 0.05 and -0.05.

Structures and tensors were visualised and modified using Gaussview, gOpenMol, and Wolfram Mathematica.

## 6.2 Synthesis of $[\text{Ru}(\text{Cl})(\eta^5\text{-C}_5\text{H}_5)(\text{PPh}_3)_2]$ , [35]



Synthesised from the literature procedure.<sup>66</sup>

A distillation set up fitted with a Vigreux column was used to crack dicyclopentadiene (45 mL). The round bottom flask containing the dimer was stirred whilst being slowly heated to 180 °C, the temperature at the top of the Vigreux column was maintained at 35 °C.

In a 2 L round bottom flask, triphenylphosphine (21 g, 0.08 mol) and anti-bumping granules were placed under nitrogen before the addition of degassed ethanol (1 L). The mixture was heated at reflux.

$\text{RuCl}_3 \cdot x\text{H}_2\text{O}$  (4.98 g, 0.02 mol) was dissolved in degassed ethanol (80 mL) and transferred to the round bottom flask (2 L) *via* a cannula transfer. The freshly distilled cyclopentadiene (10 mL) was added to degassed ethanol (10 mL) and transferred to the round bottom flask (2 L) dropwise. The reaction mixture was heated at reflux for 1 h. The black solution changed to red before orange powder began to precipitate. This continued as the solution became orange and then yellow. The solution was cooled to room temperature and stored at 20 °C overnight to afford [35] as an orange microcrystalline powder. The product was air stable and was washed with ethanol (4 x 25 mL) and diethyl ether (4 x 25 mL). (Yield: 10.9718 g, 76 %).

$^1\text{H NMR}$  ( $\text{CD}_2\text{Cl}_2$ , 400 MHz, 295 K): 4.09 (s, 5H,  $\text{H}_1$ ), 7.08 – 7.18 (m, 12H,  $\text{H}_{3/4}$ ), 7.19 – 7.28 (m, 6H,  $\text{H}_5$ ), 7.32 – 7.42 (m, 12H,  $\text{H}_{3/4}$ )

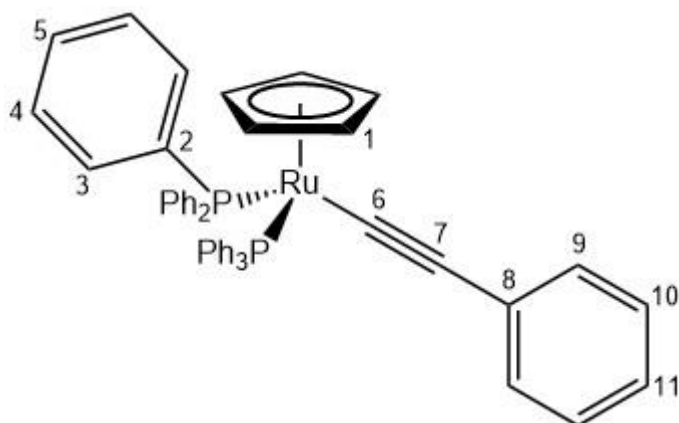
$^{13}\text{C}\{^1\text{H}\}$  NMR (Solid, 101 MHz, 295 K): 80.4 (s,  $\text{C}_1$ ), 122.8 – 145.8 (m,  $\text{C}_{\text{arom}}$ )

$^{31}\text{P}\{^1\text{H}\}$  NMR ( $\text{CD}_2\text{Cl}_2$ , 162 MHz, 295 K): 39.4 (s,  $\text{PPh}_3$ )

$^{31}\text{P}\{^1\text{H}\}$  NMR (Solid, 162 MHz, 295 K): 35.9 (s,  $\text{PPh}_3$ ), 42.2 (s,  $\text{PPh}_3$ )

**ESI-MS** ( $m/z$ ): Expected for  $C_{41}H_{35}P_2Ru$   $[M-Cl]^+ = 691.1252$ ; Observed = 691.1273  $[M-Cl]^+$  (Error =  $-0.9$  mDa).

### 6.3 Synthesis of $[\text{Ru}(\eta^5\text{-C}_5\text{H}_5)(\text{-C}\equiv\text{C-Ph})(\text{PPh}_3)_2]$ , [1a]



Synthesised from a modified literature procedure.<sup>126</sup>

An oven dried Schlenk tube was charged with  $[\text{Ru}(\text{Cl})(\eta^5\text{-C}_5\text{H}_5)(\text{PPh}_3)_2]$  (500 mg, 0.69 mmol) in methanol (50 mL). Phenylacetylene (151  $\mu\text{L}$ , 1.38 mmol) was added. The solution was stirred for 3 h and a colour change from orange to red was observed. The solution was filtered *via* a cannula to remove unreacted starting material and 1,8-diazabicyclo[5.4.0]undec-7-ene (DBU) (15 drops) was added down the side of the Schlenk tube. Yellow crystals of  $[\text{CpRu}(\text{PPh}_3)_2(\text{-C}\equiv\text{C-Ph})]$  precipitated out from the solution. The yellow crystals were isolated by filtration and washed with methanol (25 mL) to afford [1a] (Yield: 435 mg, 80 %).

$^1\text{H NMR}$  ( $\text{CD}_2\text{Cl}_2$ , 400 MHz, 295 K): 4.34 (s, 5H,  $\text{H}_1$ ), 7.07 – 7.19 (m, 17H,  $\text{H}_{\text{arom}}$ ), 7.20 – 7.28 (m, 6H,  $\text{H}_5$ ), 7.45 – 7.54 (m, 12H,  $\text{H}_{\text{arom}}$ )

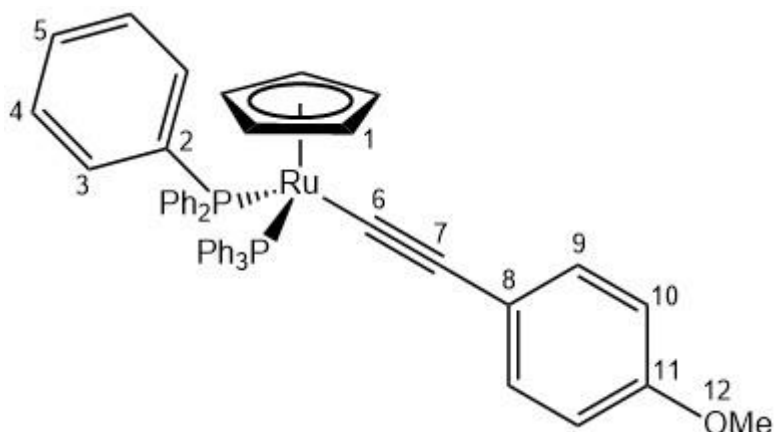
$^{13}\text{C}\{^1\text{H}\}$  NMR (Solid, 101 MHz, 295 K): 85.4 (s,  $\text{C}_1$ ), 116.7 (s,  $\text{C}_7$ ), 119.2 (s,  $\text{C}_6$ ), 121.6 – 148.2 (m,  $\text{C}_{\text{arom}}$ )

$^{31}\text{P}\{^1\text{H}\}$  NMR ( $\text{CD}_2\text{Cl}_2$ , 162 MHz, 295 K): 50.8 (s,  $\text{PPh}_3$ )

$^{31}\text{P}\{^1\text{H}\}$  NMR (Solid, 162 MHz, 295 K): 49.0 (s,  $\text{PPh}_3$ ), 58.0 (s,  $\text{PPh}_3$ )

ESI-MS ( $m/z$ ): Expected for  $\text{C}_{49}\text{H}_{41}\text{P}_2\text{Ru}$   $[\text{M}+\text{H}]^+ = 793.1722$ ; Observed = 793.1755  $[\text{M}+\text{H}]^+$  (Error = – 2.0 mDa).

## 6.4 Synthesis of $[\text{Ru}(\eta^5\text{-C}_5\text{H}_5)(\text{-C}\equiv\text{C-(C}_6\text{H}_4\text{-}i>p\text{-OMe))}(\text{PPh}_3)_2]$ , **[1b]**



Synthesised from a modified literature procedure.<sup>126</sup>

An oven dried Schlenk tube was charged with  $[\text{Ru}(\text{Cl})(\eta^5\text{-C}_5\text{H}_5)(\text{PPh}_3)_2]$  (500 mg, 0.69 mmol) in methanol (50 mL). 4-Ethynylanisole (134 mg, 1.01 mmol) was added. The solution was stirred for 3 h and a colour change from orange to dark red was observed. The solution was filtered *via* a cannula to remove unreacted starting material and 1,8-diazabicyclo[5.4.0]undec-7-ene (DBU) (15 drops) was added down the side of the Schlenk tube. Yellow crystals of **[1b]** precipitated out from the solution. The yellow crystals were isolated by filtration and washed with cold methanol (20 mL) to afford **[1b]** (Yield: 510 mg, 90 %).

$^1\text{H NMR}$  ( $\text{CD}_2\text{Cl}_2$ , 400 MHz, 295 K): 3.77 (s, 3H,  $\text{H}_{12}$ ), 4.32 (s, 5H,  $\text{H}_1$ ), 6.73 (d,  $^3J_{\text{HH}} = 8.8$  Hz, 2H,  $\text{H}_{9/10}$ ), 7.05 (d,  $^3J_{\text{HH}} = 8.8$  Hz, 2H,  $\text{H}_{9/10}$ ), 7.08 – 7.16 (m, 12H,  $\text{H}_{3/4}$ ), 7.19 – 7.27 (m, 6H,  $\text{H}_5$ ), 7.45 – 7.54 (m, 12H,  $\text{H}_{3/4}$ )

$^{13}\text{C}\{^1\text{H}\}$  NMR (Solid, 101 MHz, 295 K): 53.8\* (s,  $\text{C}_{12}$ ), 85.5 (s,  $\text{C}_1$ ), 113.8\* (s,  $\text{C}_6$ ), 115.5\* (s,  $\text{C}_7$ ), 122.1 – 159.6 (m,  $\text{C}_{\text{arom}}$ )

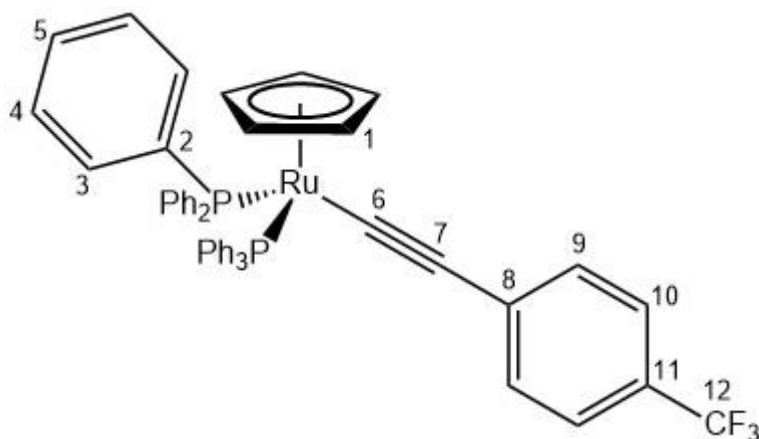
$^{31}\text{P}\{^1\text{H}\}$  NMR ( $\text{CD}_2\text{Cl}_2$ , 162 MHz, 295 K): 50.7 (s,  $\text{PPh}_3$ )

$^{31}\text{P}\{^1\text{H}\}$  NMR (Solid, 162 MHz, 295 K): 46.6\* (s,  $\text{PPh}_3$ ), 54.0\* (s,  $\text{PPh}_3$ )

\*Multiple resonances were observed for this environment in the SS NMR spectrum due to inequivalence in the solid state. The more up field resonance has been reported in this case.

**ESI-MS** ( $m/z$ ): Expected for  $C_{50}H_{43}OP_2Ru$   $[M+H]^+$  = 823.1827; Observed = 823.1848  
 $[M+H]^+$  (Error =  $-0.7$  mDa).

## 6.5 Synthesis of $[\text{Ru}(\eta^5\text{-C}_5\text{H}_5)(\text{-C}\equiv\text{C-(C}_6\text{H}_4\text{-}i{p}\text{-CF}_3\text{))}(\text{PPh}_3)_2]$ , **[1c]**



Synthesised from a modified literature procedure.<sup>126</sup>

An oven dried Schlenk tube was charged with  $[\text{Ru}(\text{Cl})(\eta^5\text{-C}_5\text{H}_5)(\text{PPh}_3)_2]$  (500 mg, 0.69 mmol) in methanol (50 mL). 4-Ethynyl- $\alpha,\alpha,\alpha$ -trifluorotoluene (225  $\mu\text{L}$ , 1.38 mmol) was added. The solution was stirred for 24 h. The orange solution was filtered *via* a cannula to remove unreacted starting material and 1,8-diazabicyclo[5.4.0]undec-7-ene (DBU) (15 drops) was added down the side of the Schlenk tube. Yellow crystals of **[1c]** precipitated out from the solution. The yellow crystals were isolated by filtration and washed with methanol (20 mL) to afford **[1c]** (Yield: 546 mg, 92 %).

**<sup>1</sup>H NMR** ( $\text{CD}_2\text{Cl}_2$ , 400 MHz, 295 K): 4.36 (s, 5H, H<sub>1</sub>), 7.09 – 7.15 (m, 12H, H<sub>3/4</sub>), 7.16 (d, <sup>3</sup>J<sub>HH</sub> = 8 Hz, 2H, H<sub>9/10</sub>), 7.21 – 7.27 (m, 6H, H<sub>5</sub>), 7.39 (d, <sup>3</sup>J<sub>HH</sub> = 8 Hz, 2H, H<sub>9/10</sub>), 7.42 – 7.49 (m, 12H, H<sub>3/4</sub>)

**<sup>13</sup>C{<sup>1</sup>H} NMR** (Solid, 101 MHz, 295 K): 86.1 (s, C<sub>1</sub>), 115.5 (s, C<sub>7</sub>), 120.4 – 147.6 (m, C<sub>6/12/arom</sub>)

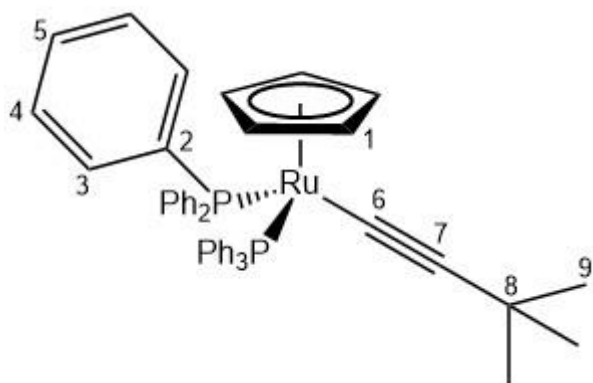
**<sup>19</sup>F NMR** ( $\text{CD}_2\text{Cl}_2$ , 376 MHz, 295 K): 70.0 (s, F<sub>12</sub>)

**<sup>31</sup>P{<sup>1</sup>H} NMR** ( $\text{CD}_2\text{Cl}_2$ , 162 MHz, 295 K): 50.8 (s, PPh<sub>3</sub>)

**<sup>31</sup>P{<sup>1</sup>H} NMR** (Solid, 162 MHz, 295 K): 48.7 (s, PPh<sub>3</sub>), 57.1 (s, PPh<sub>3</sub>)

**ESI-MS** ( $m/z$ ): Expected for  $\text{C}_{50}\text{H}_{40}\text{F}_3\text{P}_2\text{Ru}$   $[\text{M}+\text{H}]^+$  = 861.1595; Observed = 861.1613  $[\text{M}+\text{H}]^+$  (Error = – 0.4 mDa).

## 6.6 Synthesis of $[\text{Ru}(\eta^5\text{-C}_5\text{H}_5)(\text{-C}\equiv\text{C-}^t\text{Bu})(\text{PPh}_3)_2]$ , **[1d]**



Synthesised from a modified literature procedure.<sup>126</sup>

An oven dried Schlenk tube was charged with  $[\text{Ru}(\text{Cl})(\eta^5\text{-C}_5\text{H}_5)(\text{PPh}_3)_2]$  (500 mg, 0.69 mmol) in methanol (50 mL). 3,3-Dimethyl-1-butyne (170  $\mu\text{L}$ , 1.38 mmol) was added. The solution was stirred for 24 h and an orange vinylidene was observed. The solution was filtered *via* a cannula to remove unreacted starting material and 1,8-diazabicyclo[5.4.0]undec-7-ene (DBU) (15 drops) was added down the side of the Schlenk tube. Yellow crystals of **[1d]** precipitated out from the solution. The yellow crystals were isolated by filtration and washed with methanol (20 mL) to afford **[1d]** (Yield: 335 mg, 63 %).

$^1\text{H NMR}$  ( $\text{CD}_2\text{Cl}_2$ , 400 MHz, 295 K): 1.19 (s, 9H,  $\text{H}_9$ ), 4.14 (s, 5H,  $\text{H}_1$ ), 7.02 – 7.10 (m, 12H,  $\text{H}_{3/4}$ ), 7.14 – 7.20 (m, 6H,  $\text{H}_5$ ), 7.49 – 7.57 (m, 12H,  $\text{H}_{3/4}$ )

$^{13}\text{C}\{^1\text{H}\}$  NMR (Solid, 101 MHz, 295 K): 31.1 (s,  $\text{C}_8$ ), 35.5 (s,  $\text{C}_9$ ), 85.1 (s,  $\text{C}_1$ ), 89.7 (s,  $\text{C}_7$ ), 118.7 (s,  $\text{C}_6$ ), 123.4 – 147.7 (m,  $\text{C}_{\text{arom}}$ )

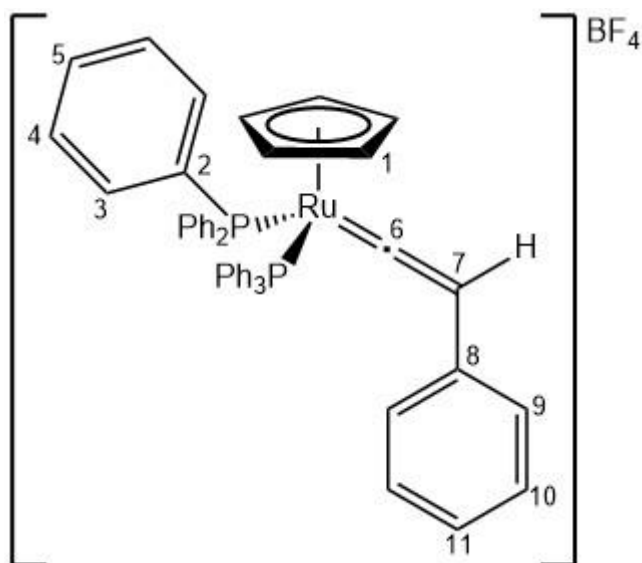
$^{31}\text{P}\{^1\text{H}\}$  NMR ( $\text{CD}_2\text{Cl}_2$ , 162 MHz, 295 K): 51.2 (s,  $\text{PPh}_3$ )

$^{31}\text{P}\{^1\text{H}\}$  NMR (Solid, 162 MHz, 295 K): 46.4\* (s,  $\text{PPh}_3$ ), 53.1\* (s,  $\text{PPh}_3$ )

\*Multiple resonances were observed for this environment in the SS NMR spectrum due to inequivalence in the solid state. The more up field resonance has been reported in this case.

**ESI-MS** ( $m/z$ ): Expected for  $\text{C}_{47}\text{H}_{45}\text{P}_2\text{Ru}$   $[\text{M}+\text{H}]^+ = 773.2035$ ; Observed = 773.2055  $[\text{M}+\text{H}]^+$  (Error =  $-0.7$  mDa).

## 6.7 Synthesis of $[\text{Ru}(\eta^5\text{-C}_5\text{H}_5)(\text{PPh}_3)_2(=\text{CHPh})]\text{BF}_4$ [**2a**] $\text{BF}_4$



An oven dried Schlenk tube was charged with  $[\text{Ru}(\eta^5\text{-C}_5\text{H}_5)(\text{-C}\equiv\text{C-Ph})(\text{PPh}_3)_2]$  (400 mg, 0.50 mmol) in diethyl ether (50 mL). To this,  $\text{HBF}_4\cdot\text{Et}_2\text{O}$  (97  $\mu\text{L}$ , 0.71 mmol) was added. The yellow suspension was stirred for 1 h to yield a pink suspension. The solvent was removed *via* a cannula filtration and the solid washed with diethyl ether (2  $\times$  20 mL). The pink solid was dried under vacuum to yield **[2a]** $\text{BF}_4\cdot\frac{1}{2}\text{Et}_2\text{O}$  (Yield: 327 mg, 71 %). Crystals were grown of **[2a]** $\text{BF}_4$  by slow diffusion of pentane into a DCM solution of the complex.

$^1\text{H NMR}$  ( $\text{CD}_2\text{Cl}_2$ , 400 MHz, 295 K): 1.12 (t,  $^3J_{\text{HH}} = 7$  Hz, 3H,  $\text{O}(\text{CH}_2\text{CH}_3)_2$ ), 3.44 (q,  $^3J_{\text{HH}} = 7$  Hz, 2H,  $\text{O}(\text{CH}_2\text{CH}_3)_2$ ), 5.29 (s, 5H,  $\text{H}_1$ ), 5.44 (t,  $^4J_{\text{HP}} = 2.4$  Hz, 1H,  $\text{H}_7$ ), 7.01 – 7.13 (m, 14H,  $\text{H}_{3/4}$ ,  $\text{H}_{9/10}$ ), 7.14 – 7.20 (m, 1H,  $\text{H}_{11}$ ), 7.21 – 7.32 (m, 14H,  $\text{H}_{3/4}$ ,  $\text{H}_{9/10}$ ), 7.39 – 7.47 (m, 6H,  $\text{H}_5$ )

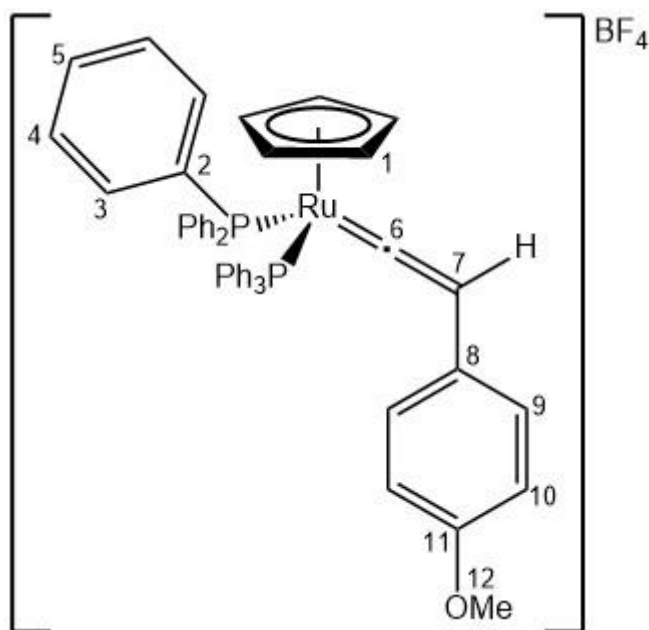
$^{13}\text{C}\{^1\text{H}\}$  NMR (Solid, 101 MHz, 295 K): 15.8 (s,  $\text{O}(\text{CH}_2\text{CH}_3)_2$ ), 65.2 (s,  $\text{O}(\text{CH}_2\text{CH}_3)_2$ ), 94.9 (s,  $\text{C}_1$ ), 120.3 (s,  $\text{C}_7$ ) 123.2 – 144.7 (m,  $\text{C}_{\text{arom}}$ ), 353.7 (s,  $\text{C}_6$ )

$^{31}\text{P}\{^1\text{H}\}$  NMR ( $\text{CD}_2\text{Cl}_2$ , 162 MHz, 295 K): 43.1 (s,  $\text{PPh}_3$ )

$^{31}\text{P}\{^1\text{H}\}$  NMR (Solid, 162 MHz, 295 K): 35.1 (s,  $\text{PPh}_3$ ), 51.5 (s,  $\text{PPh}_3$ )

ESI-MS ( $m/z$ ): Expected for  $\text{C}_{49}\text{H}_{41}\text{P}_2\text{Ru}$   $[\text{M}]^+ = 793.1722$ ; Observed = 793.1750  $[\text{M}]^+$  (Error = – 1.6 mDa).

## 6.8 Synthesis of $[\text{Ru}(\eta^5\text{-C}_5\text{H}_5)(\text{PPh}_3)_2(=\text{CH}(\text{C}_6\text{H}_4\text{-}p\text{-OMe}))]\text{OTf}$ [**2b**] $\text{OTf}$



An oven dried Schlenk tube was charged with  $[\text{Ru}(\eta^5\text{-C}_5\text{H}_5)(\text{C}\equiv\text{C}(\text{C}_6\text{H}_4\text{-}p\text{-OMe}))(\text{PPh}_3)_2]$  (250 mg, 0.30 mmol) in diethyl ether (50 mL). To this, trifluoromethane sulfonic acid (39  $\mu\text{L}$ , 0.44 mmol) was added. The yellow suspension was stirred for 1 h to yield a pink suspension. The solvent was removed *via* a cannula filtration and the solid washed with diethyl ether (2  $\times$  20 mL). The pink solid was dried under vacuum to yield [**2b**] $\text{OTf}$  (Yield: 235 mg, 79 %).

$^1\text{H NMR}$  ( $\text{CD}_2\text{Cl}_2$ , 400 MHz, 295 K): 3.77 (s, 3H,  $\text{H}_{12}$ ), 5.27 (s, 5H,  $\text{H}_1$ ), 5.43 (t,  $^4J_{\text{HP}} = 2.4$  Hz, 1H,  $\text{H}_7$ ), 6.84 (d,  $^3J_{\text{HH}} = 8$  Hz, 2H,  $\text{H}_{9/10}$ ), 7.00 – 7.10 (m, 14H,  $\text{H}_{9/10, 3/4}$ ), 7.20 – 7.30 (m, 12H,  $\text{H}_{3/4}$ ), 7.39 – 7.47 (m, 6H,  $\text{H}_5$ )

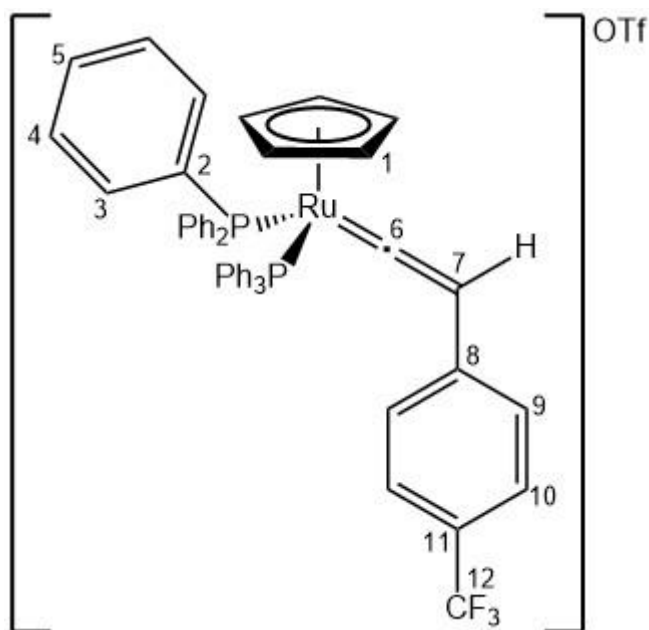
$^{13}\text{C}\{^1\text{H}\}$  NMR (Solid, 101 MHz, 295 K): 55.8 (br. s,  $\text{C}_{12}$ ), 96.2 (br. s,  $\text{C}_1$ ), 119.6 (br. s,  $\text{C}_7$ ) 124.4 – 148.3 (m,  $\text{C}_{\text{arom}}$ ), 354.5 (br. s,  $\text{C}_6$ )

$^{31}\text{P}\{^1\text{H}\}$  NMR ( $\text{CD}_2\text{Cl}_2$ , 162 MHz, 295 K): 43.4 (s,  $\text{PPh}_3$ )

$^{31}\text{P}\{^1\text{H}\}$  NMR (Solid, 162 MHz, 295 K): 43.9 (br. s,  $\text{PPh}_3$ )

ESI-MS ( $m/z$ ): Expected for  $\text{C}_{50}\text{H}_{43}\text{OP}_2\text{Ru}$   $[\text{M}]^+ = 823.1827$ ; Observed = 823.1855  $[\text{M}+\text{H}]^+$  (Error = – 1.4 mDa).

## 6.9 Synthesis of $[\text{Ru}(\eta^5\text{-C}_5\text{H}_5)(\text{PPh}_3)_2(=\text{CH}(\text{C}_6\text{H}_4\text{-}p\text{-CF}_3))]\text{OTf}$ [**2c**] $\text{OTf}$



An oven dried Schlenk tube was charged with  $[\text{Ru}(\eta^5\text{-C}_5\text{H}_5)(\text{-C}\equiv\text{C}(\text{C}_6\text{H}_4\text{-}p\text{-CF}_3))(\text{PPh}_3)_2]$  (250 mg, 0.29 mmol) in diethyl ether (50 mL). To this, trifluoromethane sulfonic acid (39  $\mu\text{L}$ , 0.44 mmol) was added. The yellow suspension was stirred for 1 h to yield a pink suspension. The solvent was removed *via* a cannula filtration and the solid washed with diethyl ether (2  $\times$  20 mL). The pink solid was dried under vacuum to yield [**2c**] $\text{OTf}$ .

Crystals were grown of  $[\text{CpRu}(\text{PPh}_3)_2(=\text{CH}(\text{C}_6\text{H}_4\text{-}p\text{-CF}_3))]\text{OTf}$  by slow diffusion of diethyl ether into a DCM solution of the complex (Yield: 233 mg, 79 %).

$^1\text{H NMR}$  ( $\text{CD}_2\text{Cl}_2$ , 400 MHz, 295 K): 5.34 (s, 5H,  $\text{H}_1$ ), 5.49 (t,  $^4J_{\text{HP}} = 2.4$  Hz, 1H,  $\text{H}_7$ ), 7.00 – 7.10 (m, 12H,  $\text{H}_{3/4}$ ), 7.13 (d,  $^3J_{\text{HH}} = 7$  Hz, 2H,  $\text{H}_{9/10}$ ), 7.20 – 7.30 (m, 12H,  $\text{H}_{3/4}$ ), 7.40 – 7.49 (m, 8H,  $\text{H}_{9/10, 5}$ )

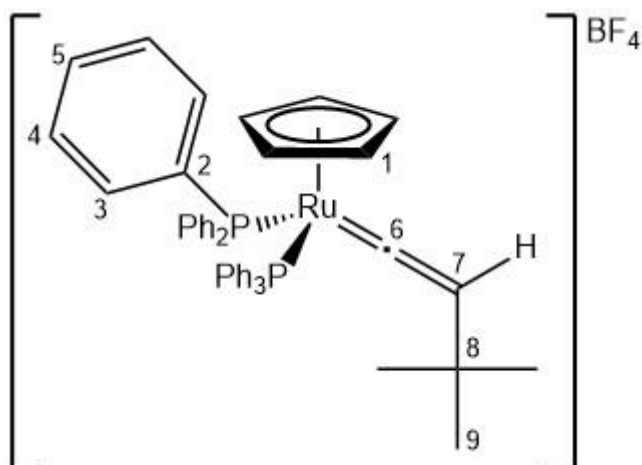
$^{13}\text{C}\{^1\text{H}\}$  NMR (Solid, 101 MHz, 295 K): 85.9 (s,  $\text{C}_{12}$ ), 96.6 (s,  $\text{C}_1$ ), 119.8 (s,  $\text{C}_7$ ), 122.5 – 144.6 (m,  $\text{C}_{\text{arom}}$ ), 349.7 (s,  $\text{C}_6$ )

$^{19}\text{F NMR}$  ( $\text{CD}_2\text{Cl}_2$ , 376 MHz, 295 K): -62.6 (s, 3F,  $\text{F}_{12}$ ), -78.7 (s, 3F,  $(\text{CF}_3)\text{SO}_3^-$ )

$^{31}\text{P}\{^1\text{H}\}$  NMR ( $\text{CD}_2\text{Cl}_2$ , 162 MHz, 295 K): 42.2 (s,  $\text{PPh}_3$ )

$^{31}\text{P}\{^1\text{H}\}$  NMR (Solid, 162 MHz, 295 K): 46.7 (s,  $\text{PPh}_3$ ), 47.3 (s,  $\text{PPh}_3$ )

## 6.10 Synthesis of $[\text{Ru}(\eta^5\text{-C}_5\text{H}_5)(\text{PPh}_3)_2(=\text{CH}^t\text{Bu})]\text{BF}_4$ [**2d**] $\text{BF}_4$



An oven dried Schlenk tube was charged with  $[\text{Ru}(\eta^5\text{-C}_5\text{H}_5)(\text{-C}\equiv\text{C}^t\text{Bu})(\text{PPh}_3)_2]$  (250 mg, 0.32 mmol) in dichloromethane (15 mL). To this, trifluoromethane sulfonic acid (43  $\mu\text{L}$ , 0.48 mmol) was added. The solution was stirred for 1 h, an immediate colour change was observed from yellow to orange. The volume of the solvent was reduced approximately 1 mL *in vacuo* and the solution layered with diethyl ether (50 mL). Slow diffusion afforded orange crystals of [**2d**] $\text{OTf}$  (Yield: 244 mg, 84 %).

$^1\text{H NMR}$  ( $\text{CD}_2\text{Cl}_2$ , 400 MHz, 295 K): 1.17 (s, 9H,  $\text{H}_9$ ), 4.24 (t,  $^4J_{\text{HP}} = 2.8$  Hz, 1H,  $\text{H}_7$ ), 5.12 (s, 5H,  $\text{H}_1$ ), 7.00 – 7.09 (m, 12H,  $\text{H}_3$ ), 7.24 – 7.33 (m, 12H,  $\text{H}_4$ ), 7.41 – 7.48 (m, 8H,  $\text{H}_5$ )

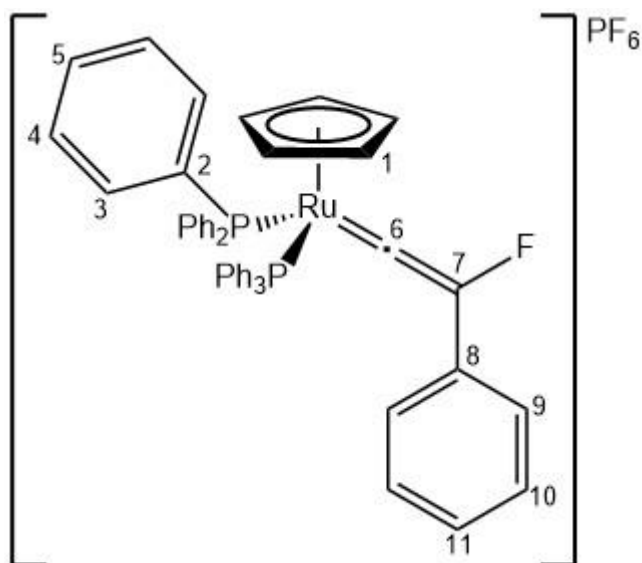
$^{13}\text{C}\{^1\text{H}\}$  NMR (Solid, 101 MHz, 295 K): 33.9 (s,  $\text{C}_9$ ) 96.2 (s,  $\text{C}_1$ ), 120.0 – 146.1 (m,  $\text{C}_{\text{arom}} + \text{C}_7$ ), 347.7 (s,  $\text{C}_6$ )

$^{19}\text{F NMR}$  ( $\text{CD}_2\text{Cl}_2$ , 376 MHz, 295 K): -78.8 (s, 3F,  $(\text{CF}_3)\text{SO}_3^-$ )

$^{31}\text{P}\{^1\text{H}\}$  NMR ( $\text{CD}_2\text{Cl}_2$ , 162 MHz, 295 K): 42.0 (s,  $\text{PPh}_3$ )

$^{31}\text{P}\{^1\text{H}\}$  NMR (Solid, 162 MHz, 295 K): 41.3 (s,  $\text{PPh}_3$ ), 44.9 (s,  $\text{PPh}_3$ )

## 6.11 Synthesis of $[\text{Ru}(\eta^5\text{-C}_5\text{H}_5)(\text{PPh}_3)_2(=\text{CPh})]\text{PF}_6$ [**3a**] $\text{PF}_6$



Prepared as described in the literature.<sup>112</sup>

An oven-dried Schlenk tube was charged with  $[\text{Ru}(\eta^5\text{-C}_5\text{H}_5)(\text{-C}\equiv\text{C-Ph})(\text{PPh}_3)_2]$  (350 mg, 0.44 mmol) in dichloromethane (15 ml). 1-fluoro-2,4,6-trimethylpyridinium tetrafluoroborate (91 mg, 0.40 mmol) was added, and the solution sonicated. An immediate colour change was observed from yellow to green. The volume of solvent was reduced under vacuum to approximately 0.5 mL, and a green solid precipitated on the addition of excess diethyl ether. The suspension was stirred vigorously for 30 minutes. The solid was recovered by filtration and washed with diethyl ether (20 mL) and dried under vacuum.

The dark green solid was re-dissolved in dichloromethane (10 mL) and sodium hexafluorophosphate (1.34 g, 8 mmol) was added. The solution was stirred for 1 h. The solution was filtered *via* a cannula to remove excess sodium hexafluorophosphate. Orange crystals were grown by slow diffusion of pentane into a dichloromethane solution. The orange crystals were recovered by filtration and washed with diethyl ether (20 mL) and dried under vacuum to yield [**3a**] $\text{PF}_6$  (Yield: 296 mg, 70 %).

$^1\text{H NMR}$  ( $\text{CD}_2\text{Cl}_2$ , 400 MHz, 295 K): 5.44 (s, 5H,  $\text{H}_1$ ), 6.97 – 7.05 (m, 14H,  $\text{H}_{3/4}$ ,  $\text{H}_{9/10}$ ), 7.22 – 7.29 (m, 13H,  $\text{H}_{3/4}$ ,  $\text{H}_{11}$ ), 7.30 – 7.37 (m, 2H,  $\text{H}_{9/10}$ ), 7.40 – 7.47 (m, 6H,  $\text{H}_5$ )

**$^{13}\text{C}\{^1\text{H}\}$  NMR** (Solid, 101 MHz, 295 K): 98.4 (s,  $\text{C}_1$ ), 117.8 – 142.7 (m,  $\text{C}_{\text{arom}}$ ), 199.5 (m,  $\text{C}_7$ ), 388.6 (s,  $\text{C}_6$ )

**$^{19}\text{F}$  NMR** ( $\text{CD}_2\text{Cl}_2$ , 376 MHz, 295 K): -207.3 (s, 1F,  $\text{F}_7$ ), -73.1 (d,  $^1J_{\text{FP}} = 715$  Hz, 6F,  $\text{PF}_6^-$ )

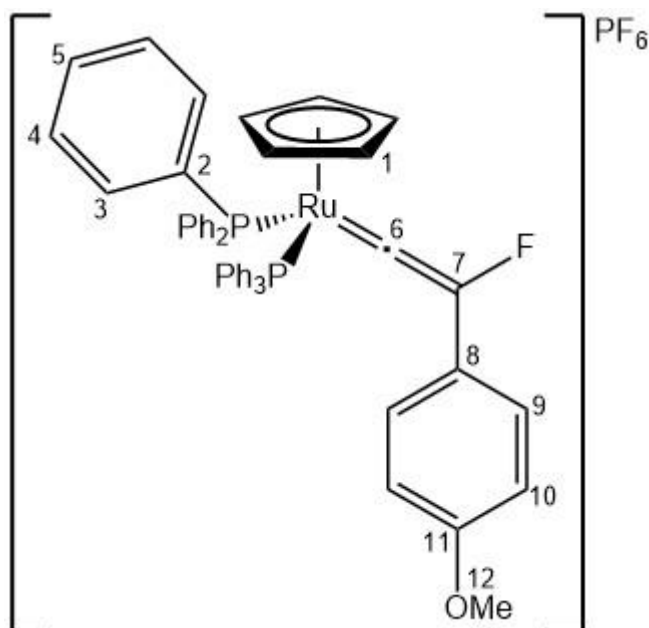
**$^{19}\text{F}$  NMR** (Solid, 376 MHz, 295 K): -207.6 (s, 1F,  $\text{F}_7$ ), -80.8 (d,  $^1J_{\text{FP}} = 715$  Hz, 6F,  $\text{PF}_6^-$ )

**$^{31}\text{P}\{^1\text{H}\}$  NMR** ( $\text{CD}_2\text{Cl}_2$ , 162 MHz, 295 K): -143.0 (septet,  $^1J_{\text{FP}} = 715$  Hz,  $\text{PF}_6^-$ ), 42.1 (s,  $\text{PPh}_3$ )

**$^{31}\text{P}\{^1\text{H}\}$  NMR** (Solid, 162 MHz, 295 K): -143.3 (septet,  $^1J_{\text{FP}} = 715$  Hz,  $\text{PF}_6^-$ ), 34.8 (s,  $\text{PPh}_3$ ), 52.6 (s,  $\text{PPh}_3$ )

**ESI-MS** ( $m/z$ ): Expected for  $\text{C}_{49}\text{H}_{40}\text{FP}_2\text{Ru}$   $[\text{M}]^+ = 811.1627$ ; Observed = 811.1654  $[\text{M}]^+$   
(Error = - 1.4 mDa).

## 6.12 Synthesis of $[\text{Ru}(\eta^5\text{-C}_5\text{H}_5)(\text{PPh}_3)_2(=\text{CF}(\text{C}_6\text{H}_4\text{-}p\text{-OMe}))]\text{BF}_4$ [**3b**] $\text{BF}_4$



Prepared as described in the literature.<sup>112</sup>

An oven-dried Schlenk tube was charged with  $[\text{Ru}(\eta^5\text{-C}_5\text{H}_5)(\text{-C}\equiv\text{C}(\text{C}_6\text{H}_4\text{-}p\text{-OMe}))(\text{PPh}_3)_2]$  (350 mg, 0.43 mmol) in dichloromethane (15 ml). 1-fluoro-2,4,6-trimethylpyridinium tetrafluoroborate (87 mg, 0.39 mmol) was added and the solution sonicated. An immediate colour change was observed from yellow to green. The volume of solvent was reduced under vacuum to approximately 0.5 mL and a green solid precipitated on the addition of excess pentane. The suspension was stirred vigorously for 30 minutes. The solid was recovered by filtration and washed with pentane (20 mL) and dried *in vacuo*. The green solid [**3b**] $\text{BF}_4$  was recovered (Yield: 284 mg, 72 %).

**$^1\text{H}$  NMR** ( $\text{CD}_2\text{Cl}_2$ , 400 MHz, 295 K): 3.83 (s, 3H,  $\text{H}_{12}$ ), 5.39 (s, 5H,  $\text{H}_1$ ), 6.88 – 6.94 (d,  $^3J_{\text{HH}} = 9$  Hz, 2H,  $\text{H}_{9/10}$ ), 6.96 – 7.06 (m, 14H,  $\text{H}_{3/4}$ ,  $\text{H}_{9/10}$ ), 7.20 – 7.29 (m, 2H,  $\text{H}_{9/10}$ ), 7.39 – 7.46 (m, 6H,  $\text{H}_5$ )

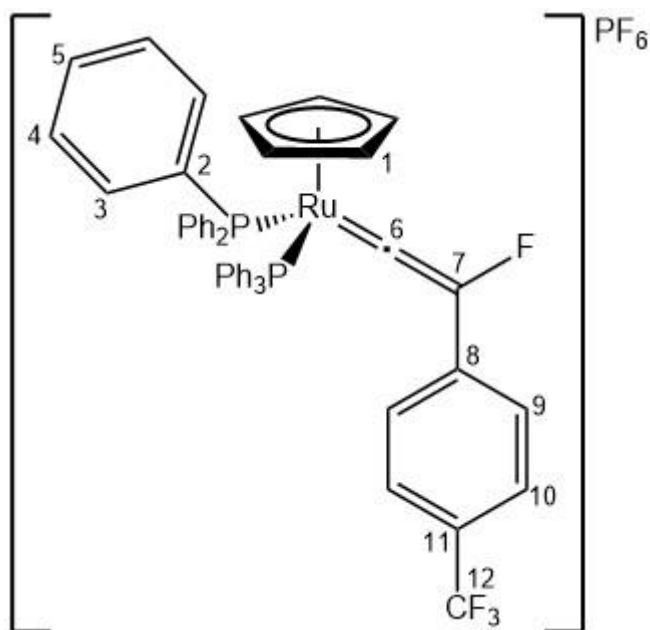
**$^{19}\text{F}$  NMR** ( $\text{CD}_2\text{Cl}_2$ , 376 MHz, 295 K): -199.7 (s, 1F,  $\text{F}_7$ ), -152.9 (s, 4F,  $\text{BF}_4^-$ )

**$^{31}\text{P}\{^1\text{H}\}$  NMR** ( $\text{CD}_2\text{Cl}_2$ , 162 MHz, 295 K): 42.0 (s,  $\text{PPh}_3$ )

**ESI-MS** ( $m/z$ ): Expected for  $\text{C}_{50}\text{H}_{43}\text{FOP}_2\text{Ru}$   $[\text{M}]^+ = 841.1733$ ; Observed = 841.1767  $[\text{M}]^+$  (Error = - 2.0 mDa).



### 6.13 Synthesis of $[\text{Ru}(\eta^5\text{-C}_5\text{H}_5)(\text{PPh}_3)_2(=\text{CF}(\text{C}_6\text{H}_4\text{-}p\text{-}\text{CF}_3))]\text{PF}_6$ [**3c**] $\text{PF}_6$



Prepared as described in the literature.<sup>112</sup>

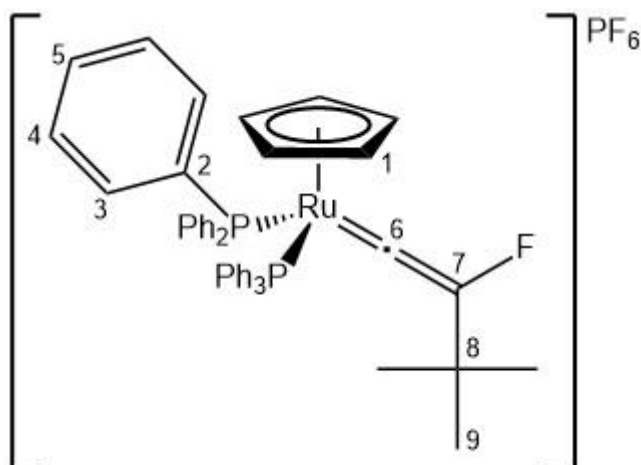
An oven-dried Schlenk tube was charged with  $[\text{Ru}(\eta^5\text{-C}_5\text{H}_5)(\text{-C}\equiv\text{C}(\text{C}_6\text{H}_4\text{-}p\text{-}\text{CF}_3))(\text{PPh}_3)_2]$  (350 mg, 0.43 mmol) in dichloromethane (15 ml). 1-fluoro-2,4,6-trimethylpyridinium tetrafluoroborate (87 mg, 0.39 mmol) was added and the solution sonicated. An immediate colour change was observed from yellow to green. The volume of solvent was reduced under vacuum to approximately 0.5 mL and a green solid precipitated on the addition of excess pentane. The suspension was stirred vigorously for 30 minutes. The solid was recovered by filtration and washed with pentane (20 mL) and dried *in vacuo*. The green solid [**3c**] $\text{BF}_4$  was recovered (Yield: 301 mg, 72 %).

**<sup>1</sup>H NMR** ( $\text{CD}_2\text{Cl}_2$ , 400 MHz, 295 K): 5.48 (s, 5H, H<sub>1</sub>), 6.92 – 7.02 (m, 12H, H<sub>3/4</sub>), 7.01 (d, <sup>3</sup>J<sub>HH</sub> = 9 Hz, 2H, H<sub>9/10</sub>), 7.20 – 7.27 (m, 12H, H<sub>3/4</sub>), 7.38 – 7.43 (m, 6H, H<sub>5</sub>) 7.43 – 7.43 (m, 2H, H<sub>9/10</sub>)

**<sup>19</sup>F NMR** ( $\text{CD}_2\text{Cl}_2$ , 376 MHz, 295 K): -210.9 (s, 1F, F<sub>7</sub>), -152.4 (s, 4F, BF<sub>4</sub><sup>-</sup>), -62.8 (s, 3F, F<sub>12</sub>)

**<sup>31</sup>P{<sup>1</sup>H} NMR** ( $\text{CD}_2\text{Cl}_2$ , 162 MHz, 295 K): 40.2 (s, PPh<sub>3</sub>)

## 6.14 Synthesis of $[\text{Ru}(\eta^5\text{-C}_5\text{H}_5)(\text{PPh}_3)_2(\text{=CF}^t\text{Bu})]\text{PF}_6$ [**3d**] $\text{PF}_6$



Prepared as described in the literature.<sup>112</sup>

An oven dried Schlenk tube was charged with  $[\text{Ru}(\eta^5\text{-C}_5\text{H}_5)(\text{-C}\equiv\text{C}^t\text{Bu})(\text{PPh}_3)_2]$  (300 mg, 0.39 mmol) dissolved in toluene (*ca.* 25 mL) and cooled to 0°C. Separately a solution of NFSI (148 mg, 0.46 mmol) in toluene was cooled to 0°C and added to the cold ruthenium solution. The solution was stirred for 15 minutes at 0°C before warming to room temperature over 1 hour. The toluene was removed in vacuo and the green residue washed with toluene (1 x 5 mL) and pentane (2 x 5 mL). The green solid was dried in vacuo to yield a green solid ( $[\mathbf{3d}]\text{N}(\text{SO}_2(\text{C}_6\text{H}_5))_2$ ).  $[\mathbf{3d}]\text{N}(\text{SO}_2(\text{C}_6\text{H}_5))_2$  was dissolved in a minimum of dichloromethane and 20 equivalents of  $\text{NaPF}_6$  added. The solution was stirred for one hour before being filtered *via* a cannula. Green crystals of  $[\mathbf{3d}]\text{PF}_6$  were grown by slow diffusion of pentane into a dichloromethane solution of the complex. Yield = 295 mg (81 %)

$^1\text{H NMR}$  ( $\text{CD}_2\text{Cl}_2$ , 400 MHz, 295 K): 1.01 (s, 9H,  $\text{H}_9$ ), 5.29 (s, 5H,  $\text{H}_1$ ), 6.92 – 7.00 (m, 12H,  $\text{H}_{3/4}$ ), 7.21 – 7.28 (m, 12H,  $\text{H}_{3/4}$ ), 7.38 – 7.44 (m, 6H,  $\text{H}_5$ )

$^{13}\text{C}\{^1\text{H}\}$  NMR (Solid, 101 MHz, 295 K): 28.8 (s,  $\text{C}_8$ ), 33.9 (s,  $\text{C}_9$ ), 98.3 (s,  $\text{C}_1$ ), 122.8 – 153.3 (m,  $\text{C}_{\text{arom}}$ ), 204.6 (d,  $1\text{JCF} = 230$  Hz,  $\text{C}_7$ ), 385.4 (s,  $\text{C}_6$ )

$^{19}\text{F NMR}$  ( $\text{CD}_2\text{Cl}_2$ , 376 MHz, 295 K): -73.2 (d,  $^1\text{J}_{\text{FP}} = 720$  Hz,  $\text{PF}_6^-$ ), -215.6 (s,  $\text{F}_7$ )

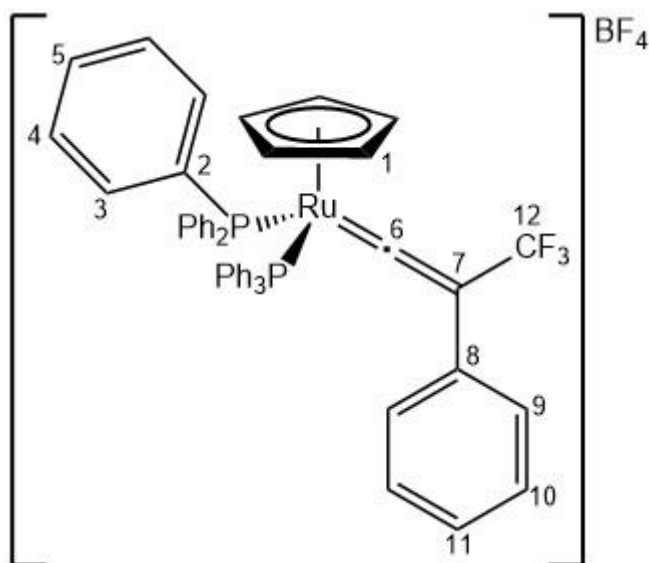
$^{19}\text{F NMR}$  (Solid, 376 MHz, 295 K): -78.8 (d,  $^1\text{J}_{\text{FP}} = 711$  Hz,  $\text{PF}_6^-$ ), -226.4 (s,  $\text{F}_7$ )

**$^{31}\text{P}\{^1\text{H}\}$  NMR** ( $\text{CD}_2\text{Cl}_2$ , 162 MHz, 295 K): 39.9 (s,  $\text{PPh}_3$ ), -143.9 (septet,  $^1J_{\text{PF}} = 711$  Hz,  $\text{PF}_6^-$ )

**$^{31}\text{P}\{^1\text{H}\}$  NMR** (Solid, 162 MHz, 295 K): 34.9 (s,  $\text{PPh}_3$ ), 40.5 (s,  $\text{PPh}_3$ )

**ESI-MS** ( $m/z$ ): Expected for  $\text{C}_{47}\text{H}_{44}\text{FP}_2\text{Ru}$   $[\text{M}]^+ = 791.1940$ ; Observed = 791.1943  
 $[\text{M}+\text{H}]^+$  (Error = 1.0 mDa).

## 6.15 Synthesis of $[\text{Ru}(\eta^5\text{-C}_5\text{H}_5)(\text{PPh}_3)_2(=\text{C}(\text{CF}_3)\text{Ph})]\text{BF}_4$ [9] $\text{BF}_4$



An oven-dried Schlenk tube was charged with  $[\text{Ru}(\eta^5\text{-C}_5\text{H}_5)(\text{-C}\equiv\text{CPh})(\text{PPh}_3)_2]$  (300 mg, 0.38 mmol) in dichloromethane (12 ml). 5-(trifluoromethyl)dibenzothiophenium tetrafluoroborate (118 mg, 0.35 mmol) was added, and allowed to stir for 4 hours. The mixture was filtered *via* a cannula to remove any residual 5-(trifluoromethyl)dibenzothiophenium tetrafluoroborate, and the volume of solvent was reduced under vacuum to approximately 0.5 ml. An orange solid precipitated on the addition of pentane. The solid was isolated by filtration *via* a cannula and redissolved in minimum dichloromethane and precipitated with pentane. The orange suspension was filtered in air and washed with pentane (25 mL). The orange powder was collected to yield **[9]** $\text{BF}_4$  (332 mg, 92 %).

Red crystals of **[9]** $\text{BF}_4$  were grown by slow diffusion of pentane into a DCM solution of the complex. The red crystals were filtered in air and washed with pentane.

$^1\text{H NMR}$  ( $\text{CD}_2\text{Cl}_2$ , 400 MHz, 295 K): 5.22 (s, 5H,  $\text{H}_1$ ), 6.80 – 6.84 (m, 2H,  $\text{H}_{9/10}$ ), 6.84 – 6.92 (m, 12H,  $\text{H}_{3/4}$ ), 7.23 – 7.31 (m, 12H,  $\text{H}_{3/4}$ ), 7.31 – 7.37 (m, 2H,  $\text{H}_{9/10}$ ), 7.42 (m, 1H,  $\text{H}_{11}$ ), 7.48 (m, 6H,  $\text{H}_5$ )

$^{13}\text{C}\{^1\text{H}\}$  NMR (Solid, 101 MHz, 295 K): 55.5 (s,  $\text{C}_{12}$ ), 98.3 (s,  $\text{C}_1$ ), 116.0 – 147.5 (m,  $\text{C}_{\text{arom}}$ ), 340.7 (s,  $\text{C}_6$ )

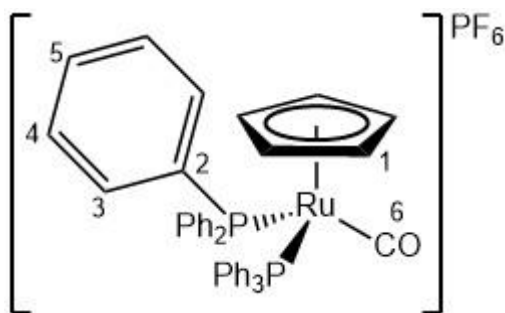
$^{19}\text{F NMR}$  ( $\text{CD}_2\text{Cl}_2$ , 376 MHz, 295 K): -57.6 (s, 3F,  $\text{F}_{12}$ ), -154.1 (s, 4F,  $\text{BF}_4^-$ )

**$^{19}\text{F}$  NMR** (Solid, 376 MHz, 295 K): -65.8 (s,  $\text{F}_{12}$ ), -157.7 (s,  $\text{BF}_4^-$ )

**$^{31}\text{P}\{^1\text{H}\}$  NMR** ( $\text{CD}_2\text{Cl}_2$ , 162 MHz, 295 K): 39.5 (s,  $\text{PPh}_3$ )

**$^{31}\text{P}\{^1\text{H}\}$  NMR** (Solid, 162 MHz, 295 K): 36.9 (s,  $\text{PPh}_3$ ), 38.2 (s,  $\text{PPh}_3$ )

## 6.16 Synthesis of $[\text{Ru}(\eta^5\text{-C}_5\text{H}_5)(\text{PPh}_3)_2(\text{CO})]\text{PF}_6$ [**10**] $\text{PF}_6$



An oven-dried Schlenk tube was charged with a suspension of  $[[\text{Ru}(\text{Cl})(\eta^5\text{-C}_5\text{H}_5)(\text{PPh}_3)_2]$  (400 mg, 0.55 mmol) and  $\text{NH}_4\text{PF}_6$  (179 mg, 1.10 mmol) in methanol (20 mL). The nitrogen atmosphere was removed and replaced with a CO atmosphere and the suspension was stirred for 40 hours. The solvent was removed *in vacuo* to afford a yellow solid. The solid was re-dissolved in dichloromethane (5 mL) and filtered *via* a cannula into stirring diethyl ether (25 mL). The yellow solid was collected by vacuum filtration to yield [**10**] $\text{PF}_6$  (441 mg, 93 %).

$^1\text{H NMR}$  ( $\text{CD}_2\text{Cl}_2$ , 400 MHz, 295 K): 4.98 (s, 5H,  $\text{H}_1$ ), 7.06 – 7.15 (m, 12H,  $\text{H}_{3/4}$ ), 7.29 – 7.35 (m, 12H,  $\text{H}_{3/4}$ ), 7.43 – 7.49 (m, 6H,  $\text{H}_5$ )

$^{13}\text{C}\{^1\text{H}\}$  NMR (Solid, 101 MHz, 295 K): 92.7 (s,  $\text{C}_1$ ), 125.4 – 146.0 (m,  $\text{C}_{\text{arom}}$ ), 202.7 (s,  $\text{C}_6$ )

$^{31}\text{P}\{^1\text{H}\}$  NMR ( $\text{CD}_2\text{Cl}_2$ , 162 MHz, 295 K): 42.4 (s,  $\text{PPh}_3$ )

$^{31}\text{P}\{^1\text{H}\}$  NMR (Solid, 162 MHz, 295 K): 41.0 (s,  $\text{PPh}_3$ ), 43.6 (s,  $\text{PPh}_3$ )

ESI-MS ( $m/z$ ): Expected for  $\text{C}_{42}\text{H}_{35}\text{OP}_2\text{Ru}$   $[\text{M}]^+$  = 719.1201; Observed = 719.01204  $[\text{M}+\text{H}]^+$  (Error = 0.9 mDa).

### 6.17 Synthesis of $[\text{Ru}(\text{Cl})_2(\text{PPh}_3)_3]$

Prepared as described in the literature.<sup>158</sup>

An oven dried Schlenk tube charged with a suspension of  $\text{RuCl}_3 \cdot n\text{H}_2\text{O}$  (1.00 g, 3.83 mmol for  $n = 3$ ) and triphenylphosphine (6.00 g, 22.9 mmol) in methanol (50 mL) was heated at reflux for 4 hours. The brown solid that precipitated was collected by filtration, washed with diethyl ether and dried in air to give  $\text{RuCl}_2(\text{PPh}_3)_3$  as a dark brown powder (3.59 g, 98 %) which was used without further purification.

## 6.18 Synthesis of *trans*-[Ru(Cl)<sub>2</sub>(dppe)<sub>2</sub>]

Prepared as described in the literature.<sup>159</sup>

An oven dried Schlenk tube charged with a suspension of RuCl<sub>2</sub>(PPh<sub>3</sub>)<sub>3</sub> (2.00 g, 2.01 mmol) and dppe (1.75 g, 4.40 mmol) in degassed acetone (40 mL) was sonicated for 15 minutes. The suspension was then stirred for 30 minutes and sonicated for a further 15 minutes. The resulting yellow precipitate was collected by filtration, washed with acetone and diethyl ether and dried in air to afford *trans*-[Ru(Cl)<sub>2</sub>(dppe)<sub>2</sub>] (2.00 g, 99 %) which was used without further purification.

## 6.19 Synthesis of [Ru(Cl)(dppe)<sub>2</sub>]OTf

Prepared as described in the literature.<sup>159</sup>

An oven dried Schlenk tube charged with a suspension of *trans*-[Ru(Cl)<sub>2</sub>(dppe)<sub>2</sub>] (1.41 g, 1.46 mmol) and AgOTf (0.37 g, 1.46 mmol) in dichloromethane (20 ml) was sonicated for 15 minutes. The suspension was then stirred for 30 minutes and sonicated for a further 15 minutes. The resulting dark red solution was filtered through Celite to remove the precipitated AgCl. The solvent was removed *in vacuo*. The red solid was re-dissolved in a minimum of dichloromethane and added dropwise to stirring diethyl ether. [Ru(Cl)(dppe)<sub>2</sub>]OTf was collected by filtration and washed with diethyl ether to afford a dark red solid, which is stable in air and chlorinated solvents (1.36 g, 86 %).

**<sup>1</sup>H NMR** (CD<sub>2</sub>Cl<sub>2</sub>, 400 MHz, 295 K): 1.57 (m, 2H, CH<sub>2</sub>), 2.37 (m, 4H, CH<sub>2</sub>), 2.62 (m, 2H, CH<sub>2</sub>), 6.69 (m, 4H, H<sub>Ar</sub>), 7.02 (m, 12H, H<sub>Ar</sub>), 7.23 (m, 16H, H<sub>Ar</sub>), 7.63 (m, 2H, H<sub>Ar</sub>), 7.56 (m, 2H, H<sub>Ar</sub>), 7.75 (m, 4H, H<sub>Ar</sub>),

**<sup>31</sup>P{<sup>1</sup>H} NMR** (CD<sub>2</sub>Cl<sub>2</sub>, 162 MHz, 295 K): 4.98 (s, 5H, H<sub>1</sub>), 7.06 – 7.15 (m, 12H, H<sub>3/4</sub>), 7.29 – 7.35 (m, 12H, H<sub>3/4</sub>), 7.43 – 7.49 (m, 6H, H<sub>5</sub>)

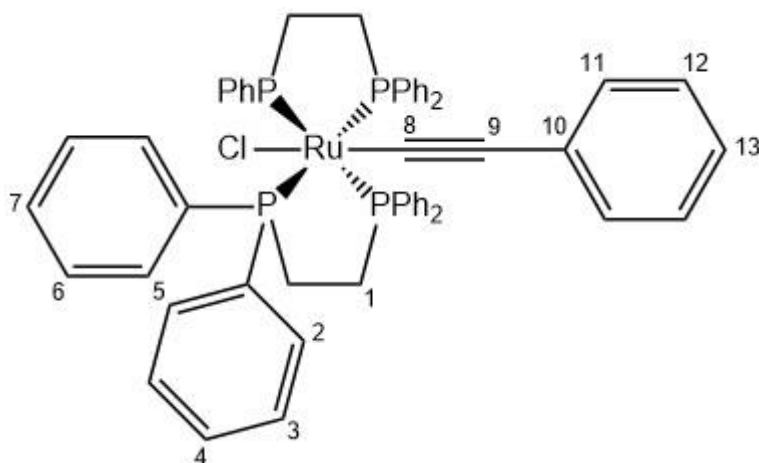
**ESI-MS** (*m/z*): Expected for C<sub>52</sub>H<sub>48</sub>ClP<sub>4</sub>Ru [M]<sup>+</sup> = 933.1433; Observed = 933.1460 [M]<sup>+</sup> (Error = – 1.6 mDa).

## 6.20 Synthesis of $\text{LiN}(\text{SiMe}_3)_2$

Prepared as described in the literature.<sup>160</sup>

A Schlenk tube was charged with hexamethyldisilazane (3.00 g, 3.88 mL, 18.6 mmol) in diethyl ether (50 mL). The solution was cooled to 0 °C and  $^n\text{BuLi}$  (1.6 M in hexanes, 12 mL, 19 mmol) was added dropwise. The solution was allowed to warm to room temperature and was stirred for 3 h. The solvent was removed *in vacuo*. The yellow precipitate was washed with pentane cooled in ice (2 x 20 mL). The solid was dried *in vacuo* yielding a white solid which was used immediately without purification or analysis. Yield = 2.67 g, 90 %.

## 6.21 Synthesis of *trans*-[Ru(Cl)(-C≡C-Ph)(dppe)<sub>2</sub>] [**1a**]'



Prepared as described in the literature.<sup>159</sup>

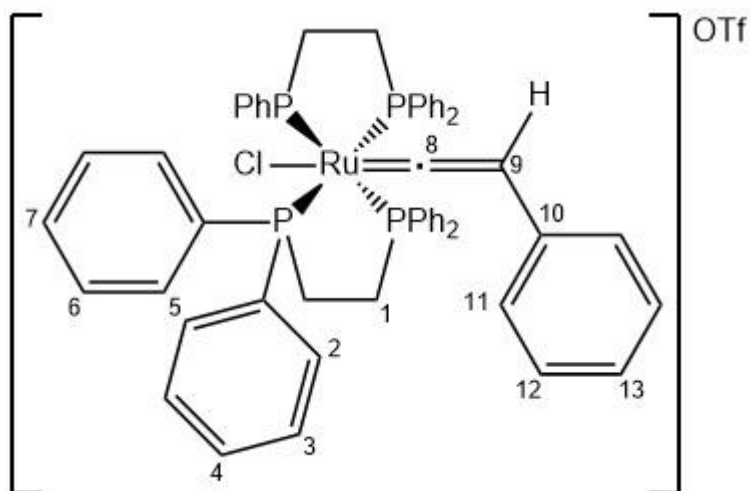
An oven dried Schlenk tube was charged with a solution of [Ru(Cl)(dppe)<sub>2</sub>][OTf] (100 mg, 0.092 mmol) and phenylacetylene (10  $\mu$ L, 0.09 mmol) in dichloromethane (5 mL). The solution was stirred for 2 hours, after which the solvent was removed *in vacuo*. The residue was washed with diethylether (2 x 5 mL) to remove excess alkyne. The residue was redissolved in dichloromethane ( $\sim$  2 mL) and treated with a solution of potassium *tert*-butoxide (35 mg) in methanol (5 mL). The yellow precipitate was isolated immediately by filtration and dried *in vacuo*. The yellow solid was recovered as [**1d**]' . Yield = 75 mg, 79 %.

<sup>1</sup>H NMR (CD<sub>2</sub>Cl<sub>2</sub>, 400 MHz, 295 K): 2.70 (m, 8H, H<sub>1</sub>), 6.67 (d, <sup>3</sup>J<sub>HH</sub> = 8 Hz, 2H, H<sub>11</sub>), 6.90 – 7.00 (m, 9H, H<sub>13+2/5</sub>), 7.02 – 7.08 (m, 8H, H<sub>2/5</sub>), 7.11 (t, <sup>3</sup>J<sub>HH</sub> = 8 Hz, 2H, H<sub>12</sub>), 7.15 – 7.27 (m, 8H, H<sub>4+7</sub>), 7.34 – 7.47 (m, 16H, H<sub>3+6</sub>)

<sup>31</sup>P{<sup>1</sup>H} NMR (CD<sub>2</sub>Cl<sub>2</sub>, 162 MHz, 295 K): 49.5 (s, PPh<sub>3</sub>)

ESI-MS (*m/z*): Expected for C<sub>60</sub>H<sub>53</sub>P<sub>4</sub>Ru [M-Cl]<sup>+</sup> = 999.2136; Observed = 999.2176 [M-Cl]<sup>+</sup> (Error = – 2.4 mDa).

## 6.22 Synthesis of *trans*-[Ru(Cl)(dppe)<sub>2</sub>(=·=CHPh)]OTf [**2a**]'OTf



An oven dried Schlenk tube was charged with a solution of *trans*-[Ru(Cl)(-C≡C-Ph)(dppe)<sub>2</sub>] (200 mg, 0.19 mmol) in dichloromethane (10 mL). The solution was treated with trifluoromethane sulfonic acid (41 mg, 24  $\mu$ L, 0.27 mmol) and stirred. Crystals of [**2a**]'OTf were recovered by slow diffusion of diethyl ether into a dichloromethane solution of [**2a**]'OTf. The crystals were dried *in vacuo*. Yield: 202 mg, 88 %.

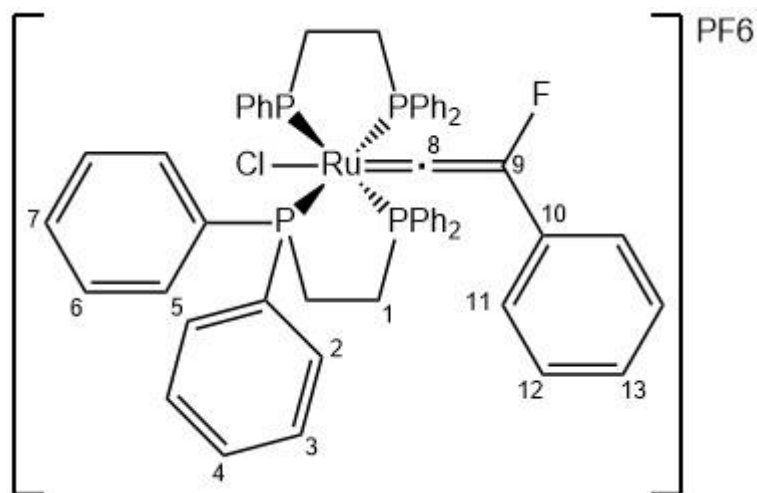
<sup>1</sup>H NMR (CD<sub>2</sub>Cl<sub>2</sub>, 400 MHz, 295 K): 2.68 – 3.05 (m, 8H, H<sub>1</sub>), 6.67 (d, <sup>3</sup>J<sub>HH</sub> = 8 Hz, 2H, H<sub>11</sub>), 6.90 – 7.00 (m, 9H, H<sub>13+2/5</sub>), 7.02 – 7.08 (m, 8H, H<sub>2/5</sub>), 7.11 (t, <sup>3</sup>J<sub>HH</sub> = 8 Hz, 2H, H<sub>12</sub>), 7.15 – 7.27 (m, 8H, H<sub>4+7</sub>), 7.34 – 7.47 (m, 16H, H<sub>3+6</sub>)

<sup>13</sup>C{<sup>1</sup>H} NMR (Solid, 101 MHz, 295 K): 23.0 – 40.9 (s, C<sub>1</sub>), 111.4 (s, C<sub>9</sub>), 119.4 – 147.1 (m, C<sub>arom</sub>), 365.4 (s, C<sub>8</sub>)

<sup>31</sup>P{<sup>1</sup>H} NMR (CD<sub>2</sub>Cl<sub>2</sub>, 162 MHz, 295 K): 40.1 (s, PPh<sub>2</sub>)

<sup>31</sup>P{<sup>1</sup>H} NMR (Solid, 162 MHz, 295 K): 30.0 (m, PPh<sub>2</sub>), 41.0 (m, PPh<sub>3</sub>)

## 6.23 Synthesis of *trans*-[Ru(Cl)(dppe)<sub>2</sub>(=CFPh)]PF<sub>6</sub> [**3a**]'PF<sub>6</sub>



An oven dried Schlenk tube was charged with *trans*-[Ru(Cl)(-C≡C-Ph)(dppe)<sub>2</sub>] (250 mg, 0.24 mmol) in dichloromethane (*ca.* 6 mL). An acetonitrile solution of Selectfluor® (93 mg, 0.26 mmol, in 10 mL) was added slowly, stirred for 15 minutes, and the solvent was removed *in vacuo*. The residue was extracted with dichloromethane (*ca.* 6 mL) and filtered; a green solid precipitated upon addition of pentane (20 mL). The solid was isolated by filtration, washed with diethyl ether (2 x 10 mL), and dried *in vacuo*. The solid was dissolved in dichloromethane (6 mL) and stirred with sodium hexafluorophosphate (800 mg, 4.76 mmol) for 1 h. The solution was filtered via a cannula and layered with pentane (40 mL) to yield green crystals of [**3a**]'PF<sub>6</sub>. Yield = 121 mg, 78 %.

<sup>1</sup>H NMR (CD<sub>2</sub>Cl<sub>2</sub>, 400 MHz, 295 K): 2.52 – 2.99 (m, 8H, H<sub>1</sub>), 5.74 (d, <sup>3</sup>J<sub>HH</sub> = 8 Hz, 2H, H<sub>11</sub>), 6.74 – 6.84 (m, 3H, H<sub>12+13</sub>), 6.99 – 7.17 (m, 32H, H<sub>2+3+5+6</sub>), 7.25 – 7.39 (m, 8H, H<sub>4+7</sub>)

<sup>13</sup>C{<sup>1</sup>H} NMR (Solid, 101 MHz, 295 K): 20.2 – 43.2 (s, C<sub>1</sub>), 116.7 – 148.4 (m, C<sub>arom</sub>), 200.2 (d, <sup>1</sup>J<sub>C-F</sub> = 229 Hz, C<sub>9</sub>), 414.6 (s, C<sub>8</sub>)

<sup>19</sup>F NMR (Solid, 376 MHz, 295 K): -235.3 (s, 1F, F<sub>9</sub>), -73.2 (d, <sup>1</sup>J<sub>FP</sub> = 661 Hz)

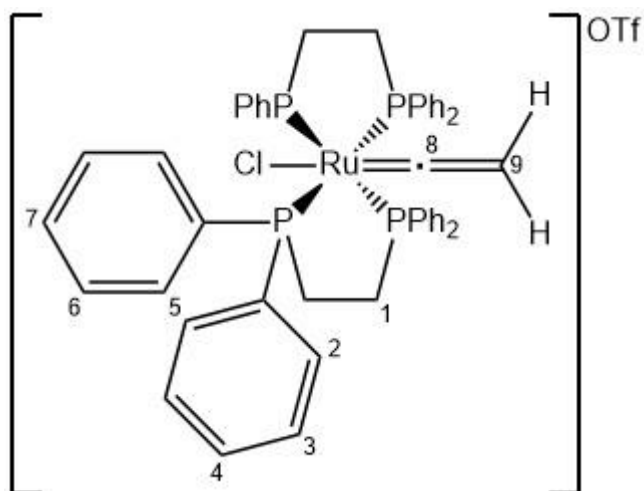
<sup>19</sup>F NMR (CD<sub>2</sub>Cl<sub>2</sub>, 376 MHz, 295 K): -229.7 (s, F<sub>9</sub>), -78.6 (d, <sup>1</sup>J<sub>FP</sub> = Hz)

<sup>31</sup>P{<sup>1</sup>H} NMR (CD<sub>2</sub>Cl<sub>2</sub>, 162 MHz, 295 K): -143.9 (septet, <sup>1</sup>J<sub>FP</sub> = 714 Hz, PF<sub>6</sub><sup>-</sup>), 33.9 (s, PPh<sub>2</sub>)

**$^{31}\text{P}\{^1\text{H}\}$  NMR** (Solid, 162 MHz, 295 K): -142.0 (septet,  $^1J_{\text{FP}} = 719$  Hz,  $\text{PF}_6^-$ ), 25.8 (m,  $\text{PPh}_2$ ), 33.4 (m,  $\text{PPh}_2$ )

**ESI-MS** ( $m/z$ ): Expected for  $\text{C}_{60}\text{H}_{53}\text{ClFP}_4\text{Ru}$   $[\text{M}]^+$  = 1053.1808; Observed = 1053.1829  $[\text{M}]^+$  (Error = - 0.7 mDa).

## 6.24 Synthesis of *trans*-[Ru(Cl)(dppe)<sub>2</sub>(=CH<sub>2</sub>)]OTf [5]'OTf



An oven dried Schlenk tube was charged with a solution of [Ru(Cl)(dppe)<sub>2</sub>][OTf] (500 mg, 0.46 mmol) and ethynyltrimethylsilane (88 mg, 124  $\mu$ L, 0.90 mmol) in dichloromethane (10 mL). The solution was stirred for 48 h after which the solvent was removed *in vacuo*. The residue was washed with diethyl ether (2 x 10 mL) to remove excess alkyne and dried *in vacuo* to afford [5]'OTf as a pale red powder. Yield = 502 mg, 98 %.

<sup>1</sup>H NMR (CD<sub>2</sub>Cl<sub>2</sub>, 400 MHz, 295 K): 2.47 (quintet, <sup>4</sup>J<sub>HP</sub> = 3 Hz, 2H, H<sub>9</sub>), 2.75 – 3.03 (m, 8H, H<sub>1</sub>), 7.02 – 7.49 (m, 40H, H<sub>arom</sub>)

<sup>13</sup>C{<sup>1</sup>H} NMR (Solid, 101 MHz, 295 K): 23.3 – 43.6 (s, C<sub>1</sub>), 91.3 (s, C<sub>9</sub>), 119.8 – 146.5 (m, C<sub>arom</sub>), 354.6 (s, C<sub>8</sub>)

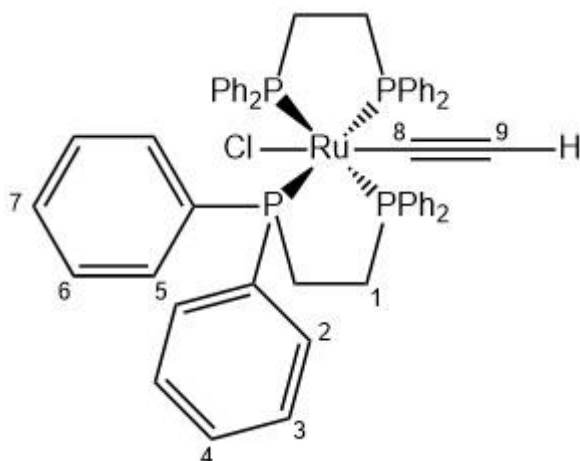
<sup>19</sup>F NMR (CD<sub>2</sub>Cl<sub>2</sub>, 376 MHz, 295 K): -78.8 (s, <sup>-</sup>O<sub>3</sub>SCF<sub>3</sub>)

<sup>31</sup>P{<sup>1</sup>H} NMR (CD<sub>2</sub>Cl<sub>2</sub>, 162 MHz, 295 K): 41.5 (s, PPh<sub>2</sub>)

<sup>31</sup>P{<sup>1</sup>H} NMR (Solid, 162 MHz, 295 K): 22.7 – 60.3 (m, PPh<sub>2</sub>)

ESI-MS (*m/z*): Expected for C<sub>54</sub>H<sub>49</sub>P<sub>4</sub>Ru [M-HCl]<sup>+</sup> = 923.1823; Observed = 923.1826 [M-HCl]<sup>+</sup> (Error = 1.2 mDa). Expected for C<sub>54</sub>H<sub>50</sub>ClP<sub>4</sub>Ru [M]<sup>+</sup> = 959.1590; Observed = 959.1593 [M]<sup>+</sup> (Error = 0.8 mDa).

## 6.25 Synthesis of *trans*-[Ru(Cl)(dppe)<sub>2</sub>(-C≡C-H)] [4]'



An oven dried Schlenk tube charged with *trans*-[Ru(Cl)(dppe)<sub>2</sub>(=CH<sub>2</sub>)](OTf) (400 mg, 0.39 mmol) suspended in tetrahydrofuran (10 mL) was treated with tetrabutylammonium fluoride (390  $\mu$ L, 1 M in THF). The solution was stirred for 10 minutes and the solvent removed *in vacuo*. The residue was washed with diethyl ether and the solvent removed *in vacuo*. The residue was washed with acetonitrile (3 mL) and the thick suspension filtered through a cotton wool plug. The yellow solid was washed further with acetonitrile (2 x 3 mL) and diethyl ether (3 mL). The solid was dissolved in dichloromethane and the solvent removed *in vacuo*. The solution was washed with a minimum of DCM and filtered. The solid was redissolved in DCM and added to stirring diethyl ether. The solid [4]' was recovered by filtration. Yield: 152 mg, 44 %.

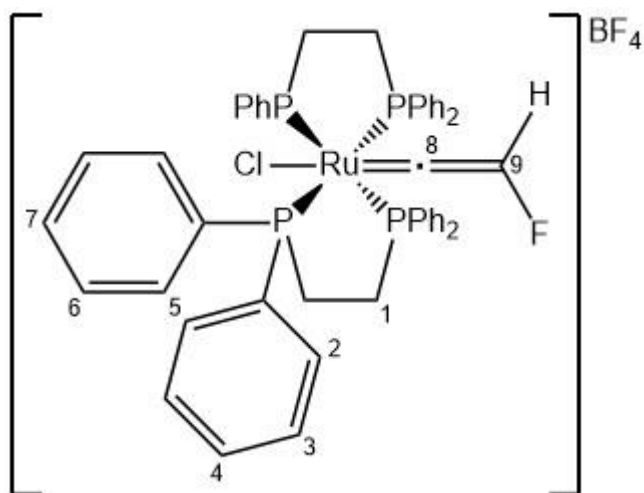
<sup>1</sup>H NMR (CD<sub>2</sub>Cl<sub>2</sub>, 400 MHz, 295 K):  $\delta$  1.32 (quin, <sup>4</sup>J<sub>HP</sub> = 1.5 Hz, 1H, H<sub>9</sub>), 2.58-2.77 (m, 8H, H<sub>3a+b</sub>), 6.93 – 7.04 (m, 16H, H<sub>2+5</sub>), 7.14-7.30 (m, 16H, H<sub>3+6</sub>), 7.46 – 7.45 (m, 8H, H<sub>4+7</sub>).

<sup>13</sup>C{<sup>1</sup>H} NMR (Solid, 101 MHz, 295 K):  $\delta$  33.0 – 43.8 (m, H<sub>1</sub>), 102.1 (s, H<sub>9</sub>), 120.6 (s, H<sub>8</sub>), 123.1 – 147.6 (m, H<sub>arom</sub>)

<sup>31</sup>P{<sup>1</sup>H} NMR (CD<sub>2</sub>Cl<sub>2</sub>, 162 MHz, 295 K):  $\delta$  49.3 (s, PPh<sub>2</sub>).

<sup>31</sup>P{<sup>1</sup>H} NMR (Solid, 162 MHz, 295 K):  $\delta$  36.7 – 52.4 (m, PPh<sub>2</sub>).

## 6.26 Synthesis of *trans*-[Ru(Cl)(dppe)<sub>2</sub>(=CHF)]OTf [6]’BF<sub>4</sub>



An oven dried Schlenk tube was charged with *trans*-[Ru(Cl)(-C≡C-H)(dppe)<sub>2</sub>] (260 mg, 0.30 mmol) in dichloromethane (~ 5 mL). An acetonitrile solution of Selectfluor® (113 mg, 0.32 mmol, in 10 mL) was added slowly and stirred for 30 minutes. The solvent was removed *in vacuo*. The residue was extracted with dichloromethane (*ca.* 6 mL) and filtered; a green solid precipitated upon addition of pentane (20 mL). The solid was isolated by filtration, washed with diethyl ether (2 x 10 mL), and dried *in vacuo*. The product was isolated as a 1:1 mixture of [6]’[BF<sub>4</sub>] and 1-chloromethyl-1,4-diazoniabicyclo[2.2.2]octane [BF<sub>4</sub>]. Yield = 283 mg, 77 %.

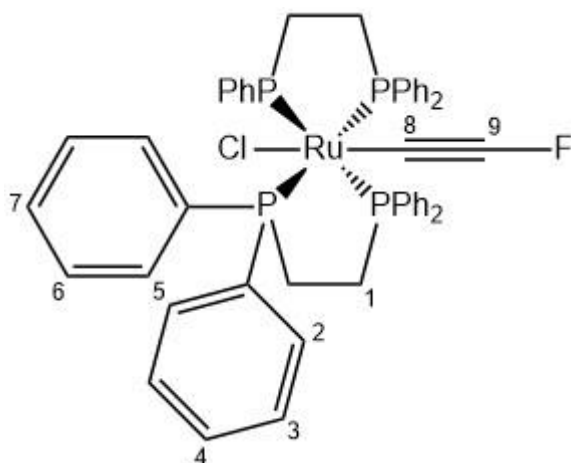
<sup>1</sup>H NMR (CD<sub>2</sub>Cl<sub>2</sub>, 500 MHz, 295 K): δ 2.62 – 2.77 (m, 4H, H<sub>1</sub>), 2.91 – 3.07 (m, 4H, H<sub>1</sub>), 6.14 (d quin, <sup>2</sup>J<sub>HF</sub> = 80 Hz, <sup>4</sup>J<sub>HP</sub> = 2.5 Hz, 1H, H<sub>9</sub>), 7.05 (m, 8H, H<sub>5/9</sub>), 7.12 (t, <sup>3</sup>J<sub>HH</sub> = 7.7 Hz, 8H, H<sub>6/10</sub>), 7.20 (m, 8H, H<sub>9/5</sub>), 7.24 (t, <sup>3</sup>J<sub>HH</sub> = 7.7 Hz, 8H, H<sub>6/10</sub>), 7.38 (t, <sup>3</sup>J<sub>HH</sub> = 7.4 Hz, 4H, H<sub>11/7</sub>) 7.46 (t, <sup>3</sup>J<sub>HH</sub> = 7.4 Hz, 4H, H<sub>4/11</sub>).

<sup>13</sup>C{<sup>1</sup>H} NMR (Solid, 101 MHz, 295 K): δ 26.5 – 41.9 (m, H<sub>1</sub>), 120.6 (s, H<sub>8</sub>), 121.7 – 145.6 (m, H<sub>arom</sub>), 178.6 (br. s, H<sub>9</sub>), 387.5 (br. s, H<sub>8</sub>)

<sup>19</sup>F NMR (CD<sub>2</sub>Cl<sub>2</sub>, 376 MHz, 295 K): δ -242.6 (d, <sup>2</sup>J<sub>HF</sub> = 81 Hz, F<sub>2</sub>).

<sup>31</sup>P{<sup>1</sup>H} NMR (CD<sub>2</sub>Cl<sub>2</sub>, 162 MHz, 295 K): δ 41.8 (s).

## 6.27 Synthesis of *trans*-[Ru(Cl)(-C≡C-F)(dppe)<sub>2</sub>] [7']



An oven dried Schlenk tube charged with a solution of *trans*-[Ru(Cl)(dppe)<sub>2</sub>(=C=CFH)][BF<sub>4</sub>].[C<sub>7</sub>H<sub>14</sub>ClN][BF<sub>4</sub>] (100 mg, 0.076 mmol) in tetrahydrofuran (10 mL) cooled to -78 °C was treated with lithium bis(trimethylsilyl)amide (12.7 mg, 0.076 mmol) in tetrahydrofuran (3 mL). The solution was stirred for 15 mins at -78 °C, allowed to warm up to room temperature and the solvent removed *in vacuo*. A yellow solution was extracted with toluene (2 x 5 mL) and the solvent removed *in vacuo*. The residue was washed with n-pentane (2 x 3 mL) and diethyl ether (3 mL) and dried to afford the product as a yellow powder [7']. Yield = 61 mg, 82 %.

<sup>1</sup>H NMR (CD<sub>2</sub>Cl<sub>2</sub>, 400 MHz, 298 K): δ 2.56 (m, 8H, H<sub>1</sub>), 6.90 (t, <sup>3</sup>J<sub>HH</sub> = 7.6 Hz, 8H, H<sub>2/5</sub>), 6.96 (m, 8H, H<sub>2/5</sub>), 7.01 (m, 8H, H<sub>4+7</sub>), 7.18 (m, 8H, H<sub>3/6</sub>), 7.91 (m, 8H, H<sub>3/6</sub>).

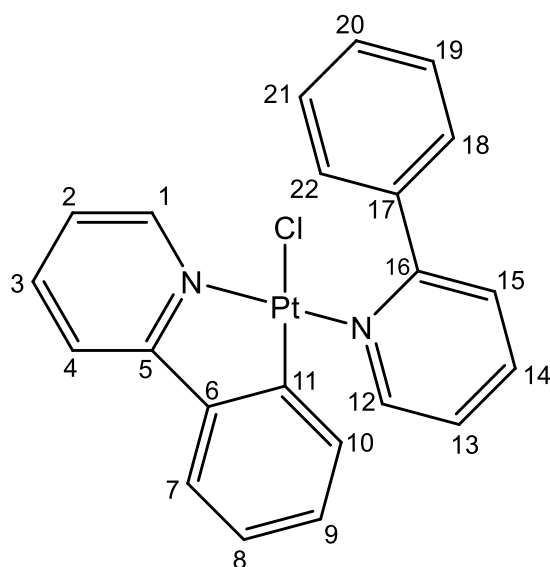
<sup>19</sup>F NMR (CD<sub>2</sub>Cl<sub>2</sub>, 376 MHz, 298 K): δ -182.1 (quin, <sup>4</sup>J<sub>FP</sub> = 4 Hz, F<sub>9</sub>).

<sup>19</sup>F NMR (Solid, 376 MHz, 298 K): δ -184.0 (quin, <sup>4</sup>J<sub>FP</sub> = 4 Hz, F<sub>9</sub>).

<sup>31</sup>P{<sup>1</sup>H} NMR (CD<sub>2</sub>Cl<sub>2</sub>, 162 MHz, 298 K): δ 49.6 (d, <sup>4</sup>J<sub>FP</sub> = 4 Hz, PPh<sub>2</sub>).

<sup>31</sup>P{<sup>1</sup>H} NMR (Solid, 162 MHz, 298 K): δ 35.8 – 55.6 (m, PPh<sub>2</sub>).

## 6.28 Synthesis of [Pt(Cl)(ppy)(ppyH)] [73]

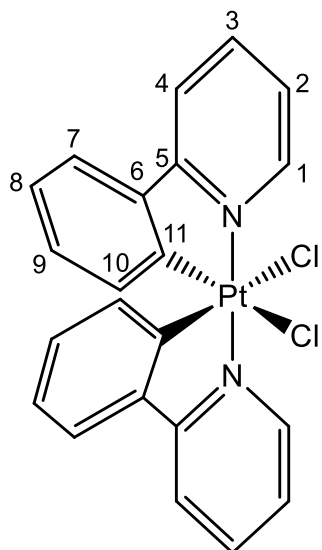


The product was prepared as described in the literature and matched literature data.<sup>150, 161</sup>

2-phenyl pyridine (36  $\mu$ L, 39 mg, 0.25 mmol) and  $K_2[PtCl_4]$  (50 mg, 0.12 mmol) were combined in 1:1 H<sub>2</sub>O:*t*BuOH (2.6 mL total volume) and stirred at 80 °C for 12 h. The reaction was cooled before the yellow precipitate filtered and washed with methanol (8 mL). The yellow solid [73] was recovered. Yield = 42 mg, 66 %.

<sup>1</sup>H NMR (CDCl<sub>3</sub>, 400 MHz, 298 K):  $\delta$  6.20 (m, d, <sup>3</sup>*J*<sub>H-H</sub> = 8 Hz, <sup>3</sup>*J*<sub>H-Pt</sub> = 46 Hz, <sup>4</sup>*J*<sub>H-H</sub> = 1 Hz, 1H, H<sub>10</sub>), 6.88 (dt, <sup>3</sup>*J*<sub>H-H</sub> = 8 Hz, <sup>4</sup>*J*<sub>H-H</sub> = 1 Hz, 1H, H<sub>9</sub>), 7.00 (dt, <sup>3</sup>*J*<sub>H-H</sub> = 8 Hz, <sup>4</sup>*J*<sub>H-H</sub> = 1 Hz, 1H, H<sub>8</sub>), 7.08 (m, <sup>3</sup>*J*<sub>H-H</sub> = 7 Hz, 1H, H<sub>2</sub>) (, 7.31 – 7.36 (m, 4H, H<sub>7,13,19,20</sub>) 7.38 (m, <sup>3</sup>*J*<sub>H-H</sub> = 7 Hz, 1H, H<sub>20</sub>) 7.53 (d, <sup>3</sup>*J*<sub>H-H</sub> = 8 Hz, 1H, H<sub>4</sub>), 7.65 (m, <sup>3</sup>*J*<sub>H-H</sub> = 8 Hz, 1H, H<sub>15</sub>), 7.75 (dt, <sup>3</sup>*J*<sub>H-H</sub> = 8 Hz, <sup>4</sup>*J*<sub>H-H</sub> = 2 Hz, 1H, H<sub>3</sub>), 7.95 (dt, <sup>3</sup>*J*<sub>H-H</sub> = 8 Hz, <sup>4</sup>*J*<sub>H-H</sub> = 2 Hz, 1H, H<sub>14</sub>), 8.10 (m, 2H, H<sub>18,20</sub>), 9.26 (m, d, <sup>3</sup>*J*<sub>H-H</sub> = 6 Hz, <sup>3</sup>*J*<sub>H-Pt</sub> = 41 Hz, 1H, H<sub>12</sub>), 9.62 (m, d, <sup>3</sup>*J*<sub>H-H</sub> = 6 Hz, <sup>3</sup>*J*<sub>H-Pt</sub> = 36 Hz, 1H, H<sub>1</sub>)

## 6.29 Synthesis of [Pt(Cl)<sub>2</sub>(ppy)<sub>2</sub>] [74]

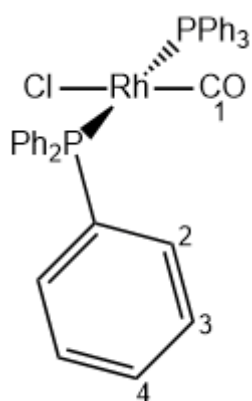


The product was prepared as described in the literature and matched literature data.<sup>150</sup>

[Pt(Cl)(ppy)(ppyH)] (30 mg, 0.06 mmol) and iodobenedichloride (15 mg, 0.06 mmol) were dissolved in dichloromethane (6 mL) and stirred for 24 h. The yellow precipitate **[74]** was recovered which was highly insoluble in *d*<sub>6</sub>-DMSO. Yield 15 mg (47 %).

<sup>1</sup>H NMR (*d*<sub>6</sub>-DMSO, 400 MHz, 298 K): δ 5.93 (m, <sup>3</sup>*J*<sub>H-H</sub> = 8 Hz, <sup>3</sup>*J*<sub>H-Pt</sub> = 32 Hz, <sup>4</sup>*J*<sub>H-H</sub> = 1 Hz, 2H, H<sub>10</sub>), 6.96 (m, <sup>3</sup>*J*<sub>H-H</sub> = 8 Hz, 2H, H<sub>3/8/9</sub>), 7.15 (m, <sup>3</sup>*J*<sub>H-H</sub> = 8 Hz, 2H, H<sub>3/8/9</sub>), 7.80 (m, <sup>3</sup>*J*<sub>H-H</sub> = 6 Hz, 2H, H<sub>2</sub>), 7.95 (m, <sup>3</sup>*J*<sub>H-H</sub> = 8 Hz, 2H, H<sub>7/4</sub>), 8.38 (m, <sup>3</sup>*J*<sub>H-H</sub> = 8 Hz, 2H, H<sub>3/8/9</sub>), 8.47 (m, <sup>3</sup>*J*<sub>H-H</sub> = 8 Hz, 2H, H<sub>7/4</sub>), 9.71 (m, <sup>3</sup>*J*<sub>H-H</sub> = 6 Hz, <sup>3</sup>*J*<sub>H-Pt</sub> = 29 Hz, <sup>4</sup>*J*<sub>H-H</sub> = 1 Hz, 2H, H<sub>1</sub>)

### 6.30 Synthesis of $[\text{Rh}(\text{CO})\text{Cl}(\text{PPh}_3)_2]$ *trans*-[15]



A solution of rhodium(III)chloride trihydrate (500 mg, 1.90 mmol) in ethanol (15 mL) was slowly added to a boiling solution of triphenylphosphine (1.99 g, 7.59 mmol) in ethanol (70 mL). The red suspension was heated at reflux for approximately 5 minutes, until a deep red solution was observed. To this, an excess of 37 % formaldehyde in H<sub>2</sub>O solution (5 mL) was added. The solution underwent an immediate colour change from deep red to pale yellow and a yellow solid precipitated. The solution was cooled and filtered, the yellow solid was washed with ethanol (20 mL) and diethyl ether (20 mL) to yield  $[\text{Rh}(\text{CO})\text{Cl}(\text{PPh}_3)_2]$ . Yield = 880 mg, 67 %.

Selected IR Bands:  $\nu_{\text{CO}} = 1978 \text{ cm}^{-1}$  (in dichloromethane)

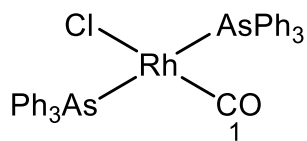
$^{13}\text{C}\{^1\text{H}\}$  NMR (Solid, 101 MHz, 298 K):  $\delta$  124.9 – 145.0 (m, C<sub>arom</sub>), 188.8 (s, C<sub>1</sub>).

$^{31}\text{P}\{^1\text{H}\}$  NMR (CD<sub>2</sub>Cl<sub>2</sub>, 162 MHz, 298 K):  $\delta$  29.8 (d,  $^1J_{\text{RhP}} = 127 \text{ Hz}$ , PPh<sub>3</sub>).

$^{31}\text{P}\{^1\text{H}\}$  NMR (Solid, 162 MHz, 298 K):  $\delta$  32.82 (m, PPh<sub>3</sub>).

ESI-MS (*m/z*): Expected for C<sub>37</sub>H<sub>30</sub>OP<sub>2</sub>Rh [M-Cl]<sup>+</sup> = 655.0821; Observed = 655.0825 [M-HCl]<sup>+</sup> (Error = -0.3 mDa).

### 6.31 Synthesis of [Rh(CO)Cl(AsPh<sub>3</sub>)<sub>2</sub>] [16]

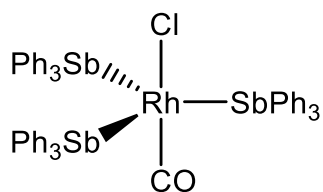


An oven dried Schlenk tube was charged with [Rh(Cl)(COD)]<sub>2</sub> (250 mg, 0.51 mmol) in toluene (20 mL). The solution was bubbled with CO<sub>(g)</sub> and cooled to 0 °C. To this, a solution of AsPh<sub>3</sub> (621 mg, 2.04 mmol) in toluene (5 mL) at 0 °C was added dropwise. The yellow precipitate **[16]** formed, which was recovered by vacuum filtration. Yield 654 mg, 83 %.

Selected IR Bands:  $\nu_{CO} = 1973 \text{ cm}^{-1}$  (in dichloromethane)

<sup>13</sup>C{<sup>1</sup>H} NMR (Solid, 101 MHz, 298 K):  $\delta$  121.4 – 147.1 (m, C<sub>arom</sub>), 188.0 (s, C<sub>1</sub>).

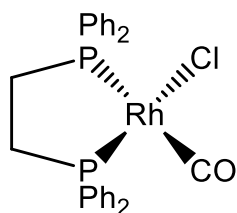
### 6.32 Synthesis of $[\text{Rh}(\text{CO})\text{Cl}(\text{SbPh}_3)_3]$ [70]



An oven dried Schlenk tube was charged with  $[\{\text{Rh}(\text{Cl})(\text{COD})\}_2]$  (250 mg, 0.51 mmol) in toluene (20 mL). The solution was bubbled with  $\text{CO}_{(\text{g})}$  and cooled to 0 °C. To this, a solution of  $\text{SbPh}_3$  (716 mg, 2.04 mmol) in toluene (5 mL) at 0 °C was added dropwise. The red precipitate **[70]** formed, which was recovered by vacuum filtration. Yield 1.12 g, 90 %.

Selected IR Bands:  $\nu_{\text{CO}} = 1968 \text{ cm}^{-1}$  (in dichloromethane), matching *tris*  $\text{SbPh}_3$  coordination.<sup>147</sup>

### 6.33 Synthesis of [Rh(CO)Cl(dppe)] [19]



An oven dried Schlenk tube was charged with  $[\text{Rh}_2(\text{Cl}_2)(\text{CO})_4]$  (245 mg, 0.63 mmol) in toluene (5 mL). A separate Schlenk tube was charged with 1,2-*bis*(diphenylphosphino)ethane (502 mg, 1.26 mmol) in toluene (5 mL). The solutions were combined, vigorous effervescence was observed accompanied by a colour change from orange to yellow. After 5 minutes of stirring, the volume of the solvent was reduced to half *in vacuo* and ethanol (5 mL) added. On addition of ethanol, a yellow solid precipitated, which was isolated by filtration to yield **[19]**. Yield 481 mg, 69 %.

Selected IR Bands:  $\nu_{\text{CO}} = 2015 \text{ cm}^{-1}$  (in dichloromethane).

$^1\text{H NMR}$  ( $\text{CD}_2\text{Cl}_2$ , 101 MHz, 298 K):  $\delta$  2.13 – 2.30 (m, 2H,  $\text{CH}_{2a}$ ), 2.41 – 2.58 (m, 2H,  $\text{CH}_{2b}$ ) 7.37 – 7.54 (m, 12H,  $\text{C}_{\text{arom}}$ ), 7.68 – 7.88 (m, 8H,  $\text{C}_{\text{arom}}$ ).

### 6.34 X-Ray Data for [Ru( $\eta^5$ -C<sub>5</sub>H<sub>5</sub>)(PPh<sub>3</sub>)<sub>2</sub>(=CHPh)]BF<sub>4</sub>·CH<sub>2</sub>Cl<sub>2</sub> [2a]BF<sub>4</sub>

Identification code	jml1808
Empirical formula	C <sub>50</sub> H <sub>43</sub> BCl <sub>2</sub> F <sub>4</sub> P <sub>2</sub> Ru
Formula weight	964.56
Temperature/K	110.05(10)
Crystal system	orthorhombic
Space group	Pbca
a/Å	17.39580(10)
b/Å	19.7461(2)
c/Å	24.8752(2)
$\alpha$ /°	90
$\beta$ /°	90
$\gamma$ /°	90
Volume/Å <sup>3</sup>	8544.61(12)
Z	8
$\rho_{\text{calc}}$ /cm <sup>3</sup>	1.500
$\mu$ /mm <sup>-1</sup>	5.271
F(000)	3936.0
Crystal size/mm <sup>3</sup>	0.224 × 0.179 × 0.166
Radiation	CuK $\alpha$ ( $\lambda$ = 1.54184)
2 $\theta$ range for data collection/°	7.108 to 134.156
Index ranges	-20 ≤ h ≤ 20, -23 ≤ k ≤ 21, -29 ≤ l ≤ 22

Reflections collected 58632  
Independent reflections 7631 [ $R_{\text{int}} = 0.0299$ ,  $R_{\text{sigma}} = 0.0156$ ]  
Data/restraints/parameters 7631/0/541  
Goodness-of-fit on  $F^2$  1.029  
Final R indexes [ $I \geq 2\sigma(I)$ ]  $R_1 = 0.0228$ ,  $wR_2 = 0.0544$   
Final R indexes [all data]  $R_1 = 0.0252$ ,  $wR_2 = 0.0559$   
Largest diff. peak/hole /  $e \text{ \AA}^{-3}$  0.56/-0.51

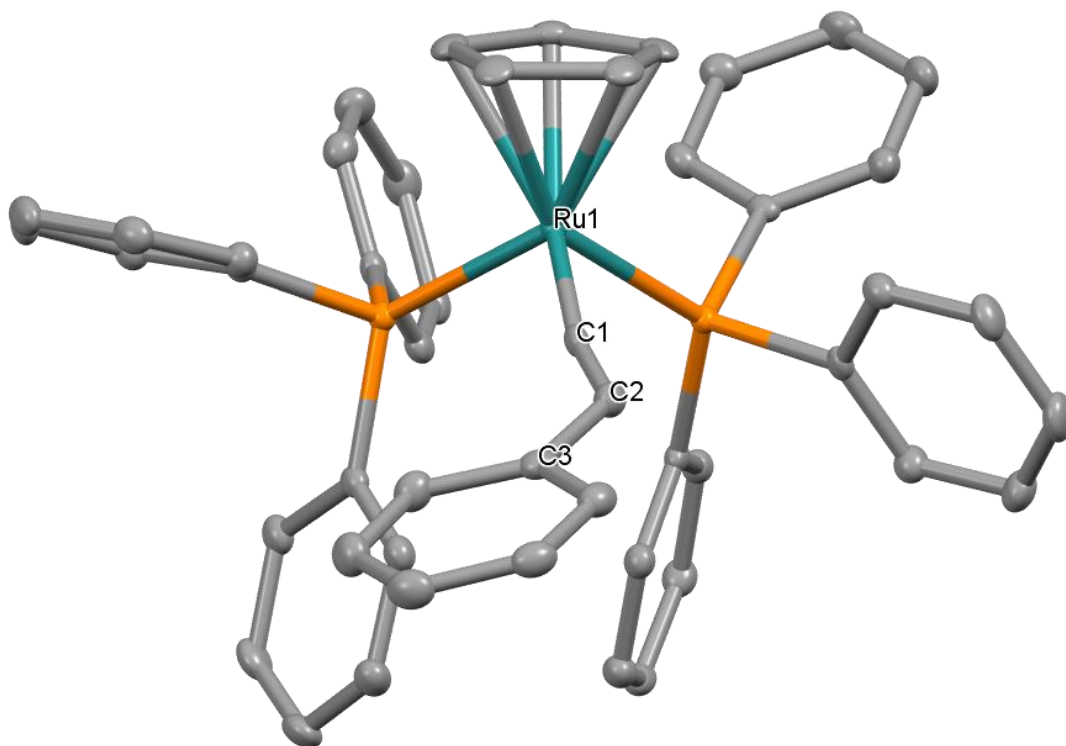


Figure 110. Solid-state structure of **[2a]**BF<sub>4</sub>, hydrogen atoms, solvent of crystallisation, and counter ion omitted for clarity. Selected bond lengths /  $\text{\AA}$  Ru1-C1 1.848, C1-C2 1.314, C2-C3 1.476. Selected bond angles /  $^\circ$  Ru1-C1-C2 165.68, C1-C2-C3 131.74.

**6.35 X-Ray Data for [Ru( $\eta^5$ -C<sub>5</sub>H<sub>5</sub>)(PPh<sub>3</sub>)<sub>2</sub>(=CH(C<sub>6</sub>H<sub>4</sub>-*p*-CF<sub>3</sub>))]OTf·CH<sub>2</sub>Cl<sub>2</sub>  
[2c]OTf**

Identification code jml1824

Empirical formula C<sub>51</sub> H<sub>40</sub> F<sub>6</sub> O<sub>3</sub> P<sub>2</sub> RuS

Formula weight 1009.90

Temperature/K 110.05(10)

Crystal system monoclinic

Space group I2/a

a/Å 21.8270(3)

b/Å 10.10290(10)

c/Å 41.4173(4)

$\alpha$ /° 90

$\beta$ /° 103.5470(10)

$\gamma$ /° 90

Volume/Å<sup>3</sup> 8879.07(18)

Z 8

$\rho$  calc g/cm<sup>3</sup> 1.511

$\mu$ /mm<sup>1</sup> 0.541

F(000) 4112.0

Crystal size/mm<sup>3</sup> 0.242 × 0.164 × 0.073

Radiation MoK $\alpha$  ( $\lambda$  = 0.71073)

2 $\theta$  range for data collection/° 6.76 to 60.162

Index ranges -28 ≤ h ≤ 30, -14 ≤ k ≤ 14, -57 ≤ l ≤ 58

Reflections collected 41336

Independent reflections 13034 [R int = 0.0281, R sigma = 0.0280]

Data/restraints/parameters 13034/0/591

Goodness-of-fit on F 2 1.051

Final R indexes [ $I \geq 2\sigma(I)$ ] R 1 = 0.0289, wR 2 = 0.0680

Final R indexes [all data] R 1 = 0.0340, wR 2 = 0.0708

Largest diff. peak/hole / e Å<sup>-3</sup> 0.45/-0.50

Refinement Special Details.

The fluorines of the CF<sub>3</sub> group were disordered by rotation about the C-CF<sub>3</sub> bond.

They were modelled in two positions with refined occupancies of 0.892:0.108(3). The

ADP of opposite fluorines were constrained to be equal, i.e. F1 and F1A, F2 and F2A, F3 and F3A.

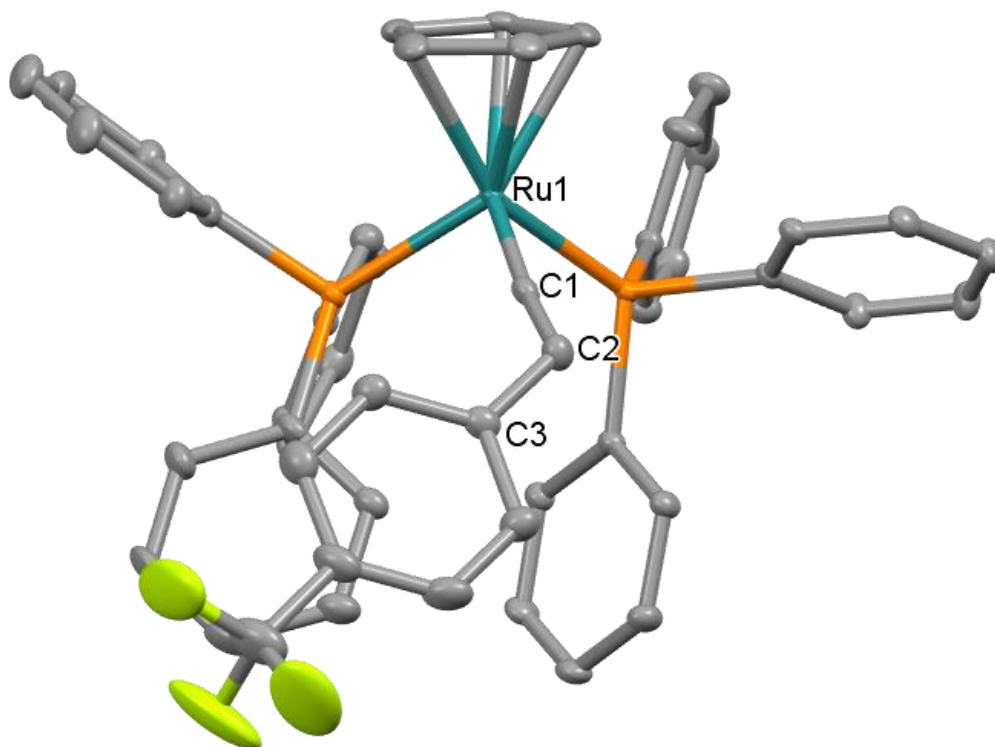


Figure 111. Solid-state structure of **[2c]**OTf, hydrogen atoms and counter ion omitted for clarity. Selected bond lengths / Å Ru1-C1 1.836, C1-C2 1.317, C2-C3 1.470. Selected bond angles / ° Ru1-C1-C2 174.23, C1-C2-C3 124.04.

### 6.36 X-Ray Data for [Ru( $\eta^5$ -C<sub>5</sub>H<sub>5</sub>)(PPh<sub>3</sub>)<sub>2</sub>(=CH(<sup>t</sup>Bu))]OTf [2d]OTf

Identification code	jml2001
Empirical formula	C <sub>48</sub> H <sub>45</sub> F <sub>3</sub> O <sub>3</sub> P <sub>2</sub> RuS
Formula weight	921.91
Temperature/K	110.00(10)
Crystal system	monoclinic
Space group	P2 <sub>1</sub> /c
a/Å	12.61147(14)
b/Å	15.58545(16)
c/Å	22.1604(2)
$\alpha$ /°	90
$\beta$ /°	101.7025(11)
$\gamma$ /°	90
Volume/Å <sup>3</sup>	4265.21(8)
Z	4
$\rho_{\text{calc}}$ /cm <sup>3</sup>	1.436
$\mu$ /mm <sup>-1</sup>	0.546
F(000)	1896.0
Crystal size/mm <sup>3</sup>	0.311 × 0.184 × 0.163
Radiation	Mo K $\alpha$ ( $\lambda$ = 0.71073)
2 $\theta$ range for data collection/°	6.652 to 60.16
Index ranges	-16 ≤ h ≤ 17, -21 ≤ k ≤ 21, -31 ≤ l ≤ 28

Reflections collected 38093

Independent reflections 12512 [ $R_{\text{int}} = 0.0302$ ,  $R_{\text{sigma}} = 0.0349$ ]

Data/restraints/parameters 12512/0/703

Goodness-of-fit on  $F^2$  1.063

Final R indexes [ $I \geq 2\sigma(I)$ ]  $R_1 = 0.0306$ ,  $wR_2 = 0.0648$

Final R indexes [all data]  $R_1 = 0.0412$ ,  $wR_2 = 0.0707$

Largest diff. peak/hole /  $e \text{ \AA}^{-3}$  0.73/-0.79

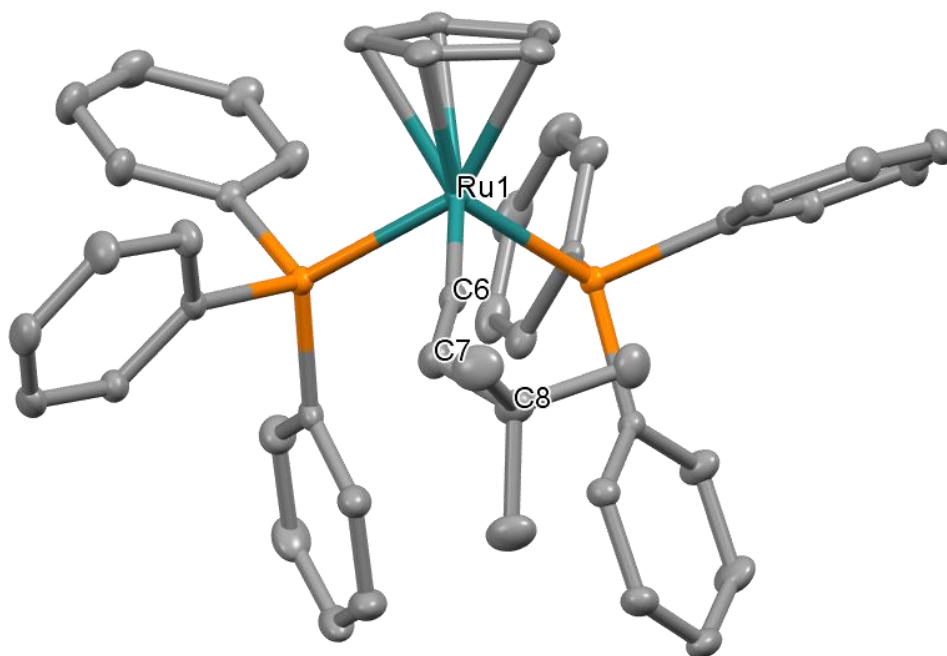


Figure 112. Solid-state structure of **[2d]OTf**, hydrogen atoms and counter ion omitted for clarity. Selected bond lengths /  $\text{\AA}$  Ru1-C6 1.861, C6-C7 1.307, C7-C8 1.521. Selected bond angles /  $^\circ$  Ru1-C6-C7 169.41, C6-C7-C8 130.35.

## Table of Abbreviations

BP86	DFT GGA functional
$\mu\text{L}$	Microlitre, $10^{-6}$ L
$\text{C}_\alpha$	The metal-bound $\alpha$ -carbon
$\text{C}_\beta$	The carbon two bonds away from the metal
$\text{CDCl}_3$	$d_1$ -chloroform
cm	Centimeter, $10^{-1}$ m
COSMO	Conductor-like screening model
CP	Cross-Polarisation
Cp	$\eta^5$ -cyclopentadienyl
D1	Recycle Delay
DBU	1,8-Diazabicyclo[5.4.0]undec-7-ene
DCM	Dichloromethane
$\delta^{\text{dia}}$	Diamagnetic shielding term
def2_SV(P)	A double zeta Karlsruhe basis set
def2_TZVPP	A triple zeta Karlsruhe basis set
DFT	Density functional theory
$\delta^{\text{iso}}$	Isotropic chemical shift
$\delta^{\text{para}}$	Paramagnetic shielding term
dppe	1,2- <i>bis</i> -(diphenylphosphino)ethane
dppm	1,1- <i>bis</i> -(diphenylphosphino)methane
dppp	1,3- <i>bis</i> -(diphenylphosphino)propane
ECP	Effective core potential
ESI	Electrospray ionization
FID	Free induction decay
FMO	Frontier molecular orbital
FTMP	1-Fluoro-2,4,6-trimethylpyridinium tetrafluoroborate
g	Gram
GGA	Generalized gradient approximation
h	Planck constant
HD	High definition
HOMO	Highest occupied molecular orbital
HP DEC	High-power decoupling

IGLOIII	Individual Gauge for Localized Orbital Basis Set
IR	Infrared
K	Kelvin
kHz	Kilohertz, $10^3$ Hz
LUMO	Lowest unoccupied molecular orbital
MAS	Magic-angle Spinning
mDa	MilliDalton, $10^{-3}$ Da
Mesityl	2,4,6-trimethylphenyl
mg	Milligram, $10^{-3}$ g
MHz	Megahertz, $10^6$ Hz
mL	Millilitre, $10^{-3}$ L
mmol	Millimole, $10^{-3}$ mol
MO	Molecular orbital
MS	Mass spectrometry
NFSI	<i>N</i> -fluorobenzenesulfonimide
NHC	<i>N</i> -heterocyclic carbene
NMR	Nuclear magnetic resonance
NOE	Nuclear Overhauser effect
$v_{\text{rot}}$	Rotation speed
Ns	Number of scans
OSEF	Outer-sphere electrophilic fluorination
OTf	Trifluoromethanesulfonate
PBE0	DFT GGA Functional
PCM	Polarizable continuum model
PCy <sub>3</sub>	Tricyclohexylphosphine
PES	Potential energy surface
PET	Positron emission tomography
PF <sub>6</sub>	Hexafluorophosphate anion
Ph	Phenyl
PPh <sub>3</sub>	Triphenylphosphine
ppm	Parts per million
PTFE	Polytetrafluoroethylene
R	An unspecified substituent
rf	Radiofrequency light

SARC	A Scalar relativistic basis set
SCF	Self-consistent field
Selectfluor	1-Chloromethyl-4-fluoro-1,4-diazoniabicyclo[2.2.2]octane bis(tetrafluoroborate)
SOLA	Topspin solids line shape analysis command
SS	Solid state
<sup>t</sup> Bu	<i>Tert</i> -butyl
TD	Time-dependent
TEP	Tolman electronic parameter
TR	Time resolved
Ts	Toluenesulfonyl
UV-vis	Ultraviolet-visible
XRD	X-Ray Diffraction
ZORA	Zero-Order Regular Approximation

## References

1. I. Fleming and D. Williams, *Spectroscopic methods in organic chemistry*, Springer Nature, 2020.
2. M. M. Maricq and J. Waugh, *The Journal of Chemical Physics*, 1979, **70**, 3300-3316.
3. F. Blanc, J.-M. Basset, C. Copéret, A. Sinha, Z. J. Tonzetich, R. R. Schrock, X. Solans-Monfort, E. Clot, O. Eisenstein and A. Lesage, *Journal of the American Chemical Society*, 2008, **130**, 5886-5900.
4. J. Herzfeld and A. E. Berger, *The Journal of Chemical Physics*, 1980, **73**, 6021-6030.
5. J. R. Sachleben, *Journal of Magnetic Resonance*, 2006, **183**, 123-133.
6. D. Alderman, M. S. Solum and D. M. Grant, *The Journal of chemical physics*, 1986, **84**, 3717-3725.
7. G. E. Pake, *The Journal of Chemical Physics*, 1948, **16**, 327-336.
8. F. Jensen, *Introduction to Computational Chemistry*, 2007.
9. E. Schrödinger, *Physical review*, 1926, **28**, 1049.
10. D. J. Griffiths and D. F. Schroeter, *Introduction to quantum mechanics*, Cambridge university press, 2018.

11. R. Van Leeuwen, E. van Lenthe, E.-J. Baerends and J. G. Snijders, *The Journal of chemical physics*, 1994, **101**, 1272-1281.
12. A. D. Becke, *The Journal of chemical physics*, 1993, **98**, 1372-1377.
13. H. Bethe, *Annalen der Physik*, 1929, **395**, 133-208.
14. H. A. Bethe, in *Selected Works Of Hans A Bethe: (With Commentary)*, World Scientific, 1997, pp. 1-72.
15. J. H. Van Vleck, *Physical Review*, 1932, **41**, 208-215.
16. P. George, D. McClure, J. Griffith and L. Orgel, *The Journal of Chemical Physics*, 1956, **24**, 1269-1269.
17. J. Chatt and L. Duncanson, *Journal of the Chemical Society (Resumed)*, 1953, 2939-2947.
18. P. W. Van Leeuwen, *Homogeneous catalysis: understanding the art*, Springer Science & Business Media, 2006.
19. P. Atkins and T. Overton, *Shriver and Atkins' inorganic chemistry*, Oxford University Press, USA, 2010.
20. C. A. Tolman, *Chemical Reviews*, 1977, **77**, 313-348.
21. C. A. Tolman, *Journal of the American Chemical Society*, 1970, **92**, 2956-2965.
22. A. Furstner, O. Guth, A. Duffels, G. Seidel, M. Liebl, B. Gabor and R. Mynott, *Chemistry – A European Journal*, 2001, **7**, 4811-4820.

23. C. A. Tolman, *Journal of the American Chemical Society*, 1970, **92**, 2953-2956.
24. M. Nonnenmacher, D. M. Buck and D. Kunz, *Beilstein journal of organic chemistry*, 2016, **12**, 1884-1896.
25. D. G. Gusev, *Organometallics*, 2009, **28**, 6458-6461.
26. K. Yamamoto, C. P. Gordon, W.-C. Liao, C. Copéret, C. Raynaud and O. Eisenstein, *Angewandte Chemie International Edition*, 2017, **56**, 10127-10131.
27. S. Halbert, C. Copéret, C. Raynaud and O. Eisenstein, *Journal of the American Chemical Society*, 2016, **138**, 2261-2272.
28. X. Solans-Monfort, C. Copéret and O. Eisenstein, *Organometallics*, 2015, **34**, 1668-1680.
29. C. P. Gordon, K. Yamamoto, W.-C. Liao, F. Allouche, R. A. Andersen, C. Copéret, C. Raynaud and O. Eisenstein, *ACS Central Science*, 2017, **3**, 759-768.
30. P. Jean-Louis Hérisson and Y. Chauvin, *Die Makromolekulare Chemie: Macromolecular Chemistry and Physics*, 1971, **141**, 161-176.
31. K. Yamamoto, C. P. Gordon, W.-C. Liao, C. Copéret, C. Raynaud and O. Eisenstein, *Angewandte Chemie*, 2017, **129**, 10261-10265.
32. C. D. Montgomery, *Journal of Chemical Education*, 2015, **92**, 1653-1660.

33. R. H. Grubbs, *Tetrahedron*, 2004, **60**, 7117-7140.
34. F. Blanc, J.-M. Basset, C. Copéret, A. Sinha, Z. J. Tonzetich, R. R. Schrock, X. Solans-Monfort, E. Clot, O. Eisenstein, A. Lesage and L. Emsley, *Journal of the American Chemical Society*, 2008, **130**, 5886-5900.
35. J. C. Mol and E. F. G. Woerlee, *Journal of the Chemical Society, Chemical Communications*, 1979, DOI: 10.1039/c39790000330, 330.
36. M. Valla, R. Wischert, A. Comas-Vives, M. P. Conley, R. Verel, C. Copéret and P. Sautet, *Journal of the American Chemical Society*, 2016, **138**, 6774-6785.
37. J. A. M. Lummiss, F. A. Perras, R. McDonald, D. L. Bryce and D. E. Fogg, *Organometallics*, 2016, **35**, 691-698.
38. D. P. Estes, C. P. Gordon, A. Fedorov, W.-C. Liao, H. Ehrhorn, C. Bittner, M. L. Zier, D. Bockfeld, K. W. Chan, O. Eisenstein, C. Raynaud, M. Tamm and C. Copéret, *Journal of the American Chemical Society*, 2017, **139**, 17597-17607.
39. D. P. Estes, C. Bittner, Ò. Àrias, M. Casey, A. Fedorov, M. Tamm and C. Copéret, *Angewandte Chemie International Edition*, 2016, **55**, 13960-13964.
40. D. P. Estes, C. Bittner, Ò. Àrias, M. Casey, A. Fedorov, M. Tamm and C. Copéret, *Angewandte Chemie*, 2016, **128**, 14166-14170.

41. J. Hillenbrand, M. Leutzsch, E. Yiannakas, C. P. Gordon, C. Wille, N. Nöthling, C. Copéret and A. Fürstner, *Journal of the American Chemical Society*, 2020, **142**, 11279-11294.
42. J. B. Ernst, S. Muratsugu, F. Wang, M. Tada and F. Glorius, *Journal of the American Chemical Society*, 2016, **138**, 10718-10721.
43. J. Xu, Q. Wang and F. Deng, *Accounts of Chemical Research*, 2019, **52**, 2179-2189.
44. T. Blasco, *Chemical Society Reviews*, 2010, **39**, 4685-4702.
45. C. P. Gordon, K. Yamamoto, K. Searles, S. Shirase, R. A. Andersen, O. Eisenstein and C. Copéret, *Chemical Science*, 2018, **9**, 1912-1918.
46. C. P. Gordon, D. B. Culver, M. P. Conley, O. Eisenstein, R. A. Andersen and C. Copéret, *Journal of the American Chemical Society*, 2019, **141**, 648-656.
47. C. P. Gordon, C. Raynaud, R. A. Andersen, C. Copéret and O. Eisenstein, *Accounts of Chemical Research*, 2019, **52**, 2278-2289.
48. L. Foppa, K. Yamamoto, W.-C. Liao, A. Comas-Vives and C. Copéret, *The Journal of Physical Chemistry Letters*, 2018, **9**, 3348-3353.
49. T. Biberger, C. P. Gordon, M. Leutzsch, S. Peil, A. Guthertz, C. Copéret and A. Fürstner, *Angewandte Chemie International Edition*, 2019, **58**, 8845-8850.

50. T. Biberger, C. P. Gordon, M. Leutzsch, S. Peil, A. Guthertz, C. Copéret and A. Fürstner, *Angewandte Chemie*, 2019, **131**, 8937-8942.
51. Z. Wang, S. Patnaik, N. Eedugurala, J. S. Manzano, I. I. Slowing, T. Kobayashi, A. D. Sadow and M. Pruski, *Journal of the American Chemical Society*, 2020, **142**, 2935-2947.
52. H.-P. Jia, E. Gouré, X. Solans-Monfort, J. Llop Castelbou, C. Chow, M. Taoufik, O. Eisenstein and E. A. Quadrelli, *Inorganic Chemistry*, 2015, **54**, 11648-11659.
53. K. E. Johnston, C. A. O'Keefe, R. M. Gauvin, J. Trébosc, L. Delevoye, J. P. Amoureux, N. Popoff, M. Taoufik, K. Oudatchin and R. W. Schurko, *Chemistry—A European Journal*, 2013, **19**, 12396-12414.
54. C. A. O'Keefe, K. E. Johnston, K. Sutter, J. Autschbach, R. Gauvin, J. Trébosc, L. Delevoye, N. Popoff, M. Taoufik, K. Oudatchin and R. W. Schurko, *Inorganic Chemistry*, 2014, **53**, 9581-9597.
55. E. S. Blaakmeer, G. Antinucci, V. Busico, E. R. H. Van Eck and A. P. M. Kentgens, *The Journal of Physical Chemistry C*, 2016, **120**, 6063-6074.
56. A. J. Rossini, I. Hung, S. A. Johnson, C. Slebodnick, M. Mensch, P. A. Deck and R. W. Schurko, *Journal of the American Chemical Society*, 2010, **132**, 18301-18317.

57. W. A. Nugent, D. W. Ovenall and S. J. Holmes, *Organometallics*, 1983, **2**, 161-162.
58. M. G. Clerici and F. Maspero, *Synthesis*, 1980, 2.
59. L. F. Yaacoub, M. A. Aljuhani, A. Jedidi, M. S. Al-Harbi, W. Al Maksoud, W. Wackerow, E. Abou-Hamad, J. D. A. Pelletier, M. El Eter, L. Cavallo and J.-M. Basset, *Organometallics*, 2020, **39**, 2438-2445.
60. E. Pietrasiak, C. P. Gordon, C. Copéret and A. Togni, *Physical Chemistry Chemical Physics*, 2020, **22**, 2319-2326.
61. F. A. Perras, A. L. Paterson and T. Kobayashi, *Solid State Nuclear Magnetic Resonance*, 2021, **111**, 101712.
62. R. C. Weast, M. Astle and W. Beyer, *WH Beyer (Boca Baton, FL: Chemical Rubber Company Press, 1999)*, 1982, 12-192.
63. S. Hartmann and E. Hahn, *Physical Review*, 1962, **128**, 2042.
64. D. J. Wink, *Journal of Chemical Education*, 1989, **66**, 810.
65. C. R. Morcombe and K. W. Zilm, *Journal of Magnetic Resonance*, 2003, **162**, 479-486.
66. M. I. Bruce, F. S. Wong, B. W. Skelton and A. H. White, *Journal of the Chemical Society, Dalton Transactions*, 1981, 1398-1405.
67. M. K. A. Reinhart Ahlrichs, Rafał A. Bachorz, Hilke, A. B. Bahmann, Michael Bär, Hans–Peter Baron, Rüdiger

Bauernschmitt, Florian A. Bischoff, Stephan Böcker, Asbjörn M., N. C. Burow, Peter Deglmann, Fabio Della Sala, Michael, M. E. Diedenhofen, Karin Eichkorn, Simon Elliott, Yannick J., D. F. Franzke, Filipp Furche, Tino Gimon, Andreas Glöß, Nora, L. G. Graf, Frank Haase, Marco Häser, Christof Hättig, Arnim, B. H. Hellweg, Sebastian Höfener, Christof Holzer, Hans, C. H. Horn, Waldemar Hujo, Uwe Huniar, Marco Kattannek, Sascha Klawohn, Wim Klopper, Andreas Köhn, Christoph Kölmel,, K. K. Markus Kollwitz, Michael Kühn, Roman Łazarski,, F. M. Toni M. Maier, Klaus May, Nils Middendorf, Paola Nava,, H. Ö. Christian Ochsenfeld, Mathias Pabst, Holger Patzelt, Patrik, D. R. Pollak, Kevin Reiter, Oliver Rubner, Ansgar Schäfer,, U. S. Gunnar Schmitz, Tobias Schwabe, Marek Sierka, David, O. T. P. Tew, Barbara Unterreiner, Malte von Arnim, Florian and P. W. Weigend, Horst Weiss, Nina Winter, *Journal*, 2007.

68. M. J. Frisch, G. W. Trucks, H. B. Schlegel, G. E. Scuseria, M. A. Robb, J. R. Cheeseman, G. Scalmani, V. Barone, G. A. Petersson, H. Nakatsuji, X. Li, M. Caricato, A. V. Marenich, J. Bloino, B. G. Janesko, R. Gomperts, B. Mennucci, H. P. Hratchian, J. V. Ortiz, A. F. Izmaylov, J. L. Sonnenberg, Williams, F. Ding, F. Lipparini, F. Egidi, J. Goings, B. Peng, A. Petrone, T. Henderson, D. Ranasinghe, V. G. Zakrzewski,

J. Gao, N. Rega, G. Zheng, W. Liang, M. Hada, M. Ehara, K. Toyota, R. Fukuda, J. Hasegawa, M. Ishida, T. Nakajima, Y. Honda, O. Kitao, H. Nakai, T. Vreven, K. Throssell, J. A. Montgomery Jr., J. E. Peralta, F. Ogliaro, M. J. Bearpark, J. J. Heyd, E. N. Brothers, K. N. Kudin, V. N. Staroverov, T. A. Keith, R. Kobayashi, J. Normand, K. Raghavachari, A. P. Rendell, J. C. Burant, S. S. Iyengar, J. Tomasi, M. Cossi, J. M. Millam, M. Klene, C. Adamo, R. Cammi, J. W. Ochterski, R. L. Martin, K. Morokuma, O. Farkas, J. B. Foresman and D. J. Fox, *Journal*, 2016.

69. F. Neese, *Wiley Interdisciplinary Reviews: Computational Molecular Science*, 2012, **2**, 73-78.
70. F. Neese, *Wiley Interdiscip. Rev.: Comput. Mol. Sci.*, 2012, **2**, 73.
71. C. M. Widdifield and R. W. Schurko, *Concepts in Magnetic Resonance Part A: An Educational Journal*, 2009, **34**, 91-123.
72. T. Zuschneid, H. Fischer, T. Handel, K. Albert and G. Häfelinger, *Zeitschrift für Naturforschung B*, 2004, **59**, 1153-1176.
73. E. Zurek, C. J. Pickard and J. Autschbach, *The Journal of Physical Chemistry C*, 2008, **112**, 11744-11750.
74. J. Autschbach, S. Zheng and R. W. Schurko, *Concepts in Magnetic Resonance Part A*, 2010, **36**, 84-126.

75. K. W. Zilm and D. M. Grant, *Journal of the American Chemical Society*, 1981, **103**, 2913-2922.
76. K. B. Wiberg, J. D. Hammer, K. W. Zilm and J. R. Cheeseman, *The Journal of Organic Chemistry*, 1999, **64**, 6394-6400.
77. J. Grutzner, *Recent advances in organic NMR spectroscopy*, 1987, 17-42.
78. L. Ackermann and R. Vicente, *CH Activation*, 2009, 211-229.
79. I. Ojima, *Fluorine in medicinal chemistry and chemical biology*, John Wiley & Sons, 2009.
80. T. Liang, C. N. Neumann and T. Ritter, *Angewandte Chemie International Edition*, 2013, **52**, 8214-8264.
81. J. McMurry, *Organic chemistry*, 8th edn., 2012.
82. N. C. Craig, A. Chen, K. H. Suh, S. Klee, G. C. Mellau, B. P. Winnewisser and M. Winnewisser, *Journal of the American Chemical Society*, 1997, **119**, 4789-4790.
83. L. Goodman, H. Gu and V. Pophristic, *The Journal of Physical Chemistry A*, 2005, **109**, 1223-1229.
84. S. D. Pike, M. R. Crimmin and A. B. Chaplin, *Chemical Communications*, 2017, **53**, 3615-3633.
85. J. Luo, R. Theron, L. J. Sewell, T. N. Hooper, A. S. Weller, A. G. Oliver and J. S. McIndoe, *Organometallics*, 2015, **34**, 3021-3028.

86. R. Dallanegra, A. P. M. Robertson, A. B. Chaplin, I. Manners and A. S. Weller, *Chemical Communications*, 2011, **47**, 3763.
87. T. M. Douglas, A. B. Chaplin, A. S. Weller, X. Yang and M. B. Hall, *Journal of the American Chemical Society*, 2009, **131**, 15440-15456.
88. M. A. Huertos and A. S. Weller, *Chemical Communications*, 2012, **48**, 7185.
89. M. A. Huertos and A. S. Weller, *Chemical Science*, 2013, **4**, 1881.
90. A. Prades, M. Fernández, S. D. Pike, M. C. Willis and A. S. Weller, *Angewandte Chemie International Edition*, 2015, **54**, 8520-8524.
91. I. Pernik, J. F. Hooper, A. B. Chaplin, A. S. Weller and M. C. Willis, *ACS Catalysis*, 2012, **2**, 2779-2786.
92. J. F. Hooper, R. D. Young, I. Pernik, A. S. Weller and M. C. Willis, *Chemical Science*, 2013, **4**, 1568.
93. J. M. Slattery, A. Higelin, T. Bayer and I. Krossing, *Angewandte Chemie*, 2010, **122**, 3297-3301.
94. J. M. Slattery, A. Higelin, T. Bayer and I. Krossing, *Angewandte Chemie International Edition*, 2010, **49**, 3228-3231.

95. S. Welsch, M. Bodensteiner, M. Dušek, M. Sierka and M. Scheer, *Chemistry—A European Journal*, 2010, **16**, 13041-13045.
96. O. Eisenstein, J. Milani and R. N. Perutz, *Chemical Reviews*, 2017, **117**, 8710-8753.
97. M. R. Gyton, A. E. Kynman, B. Leforestier, A. Gallo, J. R. Lewandowski and A. B. Chaplin, *Dalton Transactions*, 2020, **49**, 5791-5793.
98. A. D. Selmeczy, W. D. Jones, M. G. Partridge and R. N. Perutz, *Organometallics*, 1994, **13**, 522-532.
99. W. D. Jones, M. G. Partridge and R. N. Perutz, *J. Chem. Soc., Chem. Commun.*, 1991, **0**, 264-266.
100. L. P. Press, A. J. Kosanovich, B. J. McCulloch and O. V. Ozerov, *Journal of the American Chemical Society*, 2016, **138**, 9487-9497.
101. M. A. Esteruelas, M. Oliván and A. Vélez, *Organometallics*, 2015, **34**, 1911-1924.
102. D. M. Tellers, C. M. Yung, B. A. Arndtsen, D. R. Adamson and R. G. Bergman, *Journal of the American Chemical Society*, 2002, **124**, 1400-1410.
103. E. Clot, M. Besora, F. Maseras, C. Mégret, O. Eisenstein, B. Oelckers and R. N. Perutz, *Chemical Communications*, 2003, DOI: 10.1039/b210036n, 490-491.

104. M. E. Evans, C. L. Burke, S. Yaibuathes, E. Clot, O. Eisenstein and W. D. Jones, *Journal of the American Chemical Society*, 2009, **131**, 13464-13473.
105. E. Clot, C. Mégret, O. Eisenstein and R. N. Perutz, *Journal of the American Chemical Society*, 2009, **131**, 7817-7827.
106. S. D. Taylor, C. C. Kotoris and G. Hum, *Tetrahedron*, 1999, **55**, 12431-12477.
107. R. P. Singh and M. S. Jean'ne, *Tetrahedron*, 2000, **39**, 7613-7632.
108. T. Umemoto and K. Tomita, *Tetrahedron letters*, 1986, **27**, 3271-3274.
109. E. Differding and H. Ofner, *Synlett*, 1991, **1991**, 187-189.
110. R. EricáBanks and G. SankaráLal, *Journal of the Chemical Society, Chemical Communications*, 1992, 595-596.
111. L. M. Milner, N. E. Pridmore, A. C. Whitwood, J. M. Lynam and J. M. Slattery, *Journal of the American Chemical Society*, 2015, **137**, 10753-10759.
112. L. M. Milner, L. M. Hall, N. E. Pridmore, M. K. Skeats, A. C. Whitwood, J. M. Lynam and J. M. Slattery, *Dalton Transactions*, 2016, **45**, 1717-1726.
113. L. M. Hall, D. P. Tew, N. E. Pridmore, A. C. Whitwood, J. M. Lynam and J. M. Slattery, *Angewandte Chemie*, 2017, **129**, 7659-7664.

114. L. M. Hall, D. P. Tew, N. E. Pridmore, A. C. Whitwood, J. M. Lynam and J. M. Slattery, *Angewandte Chemie International Edition*, 2017, **56**, 7551-7556.
115. L. M. Hall, Doctor of philosophy, The University of York, 2018.
116. M. I. Bruce, *Chemical Reviews*, 1991, **91**, 197-257.
117. W. Middleton and W. Sharkey, *Journal of the American Chemical Society*, 1959, **81**, 803-804.
118. H. Bürger and S. Sommer, *J. Chem. Soc., Chem. Commun.*, 1991, DOI: 10.1039/c39910000456, 456-458.
119. R. Banks, M. Barlow, W. Davies, R. Haszeldine, K. Mullen and D. Taylor, *Tetrahedron Letters*, 1968, **9**, 3909-3910.
120. H. G. Viehe, R. Merenyi, J. Oth and P. Valange, *Angewandte Chemie*, 1964, **76**, 888-888.
121. H. Viehe, R. Merényi, J. Oth and P. Valange, *Angewandte Chemie International Edition in English*, 1964, **3**, 746-746.
122. H. G. Viehe and S. Y. Delavarenne, *Chemische Berichte*, 1970, **103**, 1216-1224.
123. M. I. Bruce and R. C. Wallis, *Australian Journal of Chemistry*, 1979, **32**, 1471-1485.
124. M. I. Bruce and A. Swincer, *Australian Journal of Chemistry*, 1980, **33**, 1471-1483.

125. M. J. Cowley, J. M. Lynam, R. S. Money Penny, A. C. Whitwood and A. J. Wilson, *Dalton Transactions*, 2009, 9529-9542.
126. J. Noppers and P. Low, Bachelor of Philosophy (Honours) in Chemistry, The University of Western Australia, 2017.
127. K. Furuta, *Bull. Chem. Soc. Jpn*, 1984, **57**, 2768.
128. D. Lentz, N. Nickelt and S. Willemsen, *Chemistry—A European Journal*, 2002, **8**, 1205-1217.
129. R. Franke, D. Selent and A. Börner, *Chemical reviews*, 2012, **112**, 5675-5732.
130. P. Pino, C. Botteghi, *Organic Syntheses*, 2003, **57**.
131. I. Ojima, C. Y. Tsai, M. Tzamarioudaki and D. Bonafoux, *Organic Reactions*, 2000.
132. R. F. Heck and D. S. Breslow, *Journal of the American Chemical Society*, 1961, **83**, 4023-4027.
133. C. De, R. Saha, S. K. Ghosh, A. Ghosh, K. Mukherjee, S. S. Bhattacharyya and B. Saha, *Research on Chemical Intermediates*, 2013, **39**, 3463-3474.
134. P. W. Van Leeuwen and C. Claver, *Rhodium catalyzed hydroformylation*, Springer Science & Business Media, 2002.
135. D. Evans, J. Osborn and G. Wilkinson, *Journal of the Chemical Society A: Inorganic, Physical, Theoretical*, 1968, 3133-3142.

136. D. Evans, J. Osborn, G. Wilkinson, R. P. Jr and R. Parry, *Inorganic Syntheses: Reagents for Transition Metal Complex and Organometallic Syntheses*, 1990, **28**, 79-80.
137. H.-W. Bohnen and B. Cornils, 2002.
138. B. Heaton, P. C. Kamer, J. N. Reek and P. W. van Leeuwen, *Mechanisms in homogeneous catalysis: a spectroscopic approach*, John Wiley & Sons, 2006.
139. L. A. van der Veen, M. D. Boele, F. R. Bregman, P. C. Kamer, P. W. van Leeuwen, K. Goubitz, J. Fraanje, H. Schenk and C. Bo, *Journal of the American Chemical Society*, 1998, **120**, 11616-11626.
140. M. Kranenburg, Y. E. van der Burgt, P. C. Kamer, P. W. van Leeuwen, K. Goubitz and J. Fraanje, *Organometallics*, 1995, **14**, 3081-3089.
141. R. P. Bronger, P. C. Kamer and P. W. van Leeuwen, *Organometallics*, 2003, **22**, 5358-5369.
142. P. W. Van Leeuwen, P. C. Kamer, L. A. Van der Veen and J. N. Reek, *Chinese Journal of Chemistry*, 2001, **19**, 1-8.
143. S. Hanf, L. Alvarado Rupflin, R. Gläser and S. A. Schunk, *Catalysts*, 2020, **10**, 510.
144. Â. C. Neves, M. J. Calvete, T. M. Pinho e Melo and M. M. Pereira, *European Journal of Organic Chemistry*, 2012, **2012**, 6309.

145. P. W. van Leeuwen, A. J. Sandee, J. N. Reek and P. C. Kamer, *Journal of Molecular Catalysis A: Chemical*, 2002, **182**, 107-123.
146. C. Van Doorslaer, J. Wahlen, P. Mertens, K. Binnemans and D. De Vos, *Dalton Transactions*, 2010, **39**, 8377-8390.
147. S. Otto and A. Roodt, *Inorganica chimica acta*, 2002, **331**, 199-207.
148. J. Grimblot, J. Bonnelle, A. Mortreux and F. Petit, *Inorganica Chimica Acta*, 1979, **34**, 29-36.
149. R. R. Parker, J. P. Sarju, A. C. Whitwood, J. Williams, J. M. Lynam and D. W. Bruce, *Chemistry-a European journal.*, 2018, **24**, 19010-19023.
150. D. M. Jenkins and S. Bernhard, *Inorganic chemistry*, 2010, **49**, 11297-11308.
151. C. Katan, L. Pedesseau, M. Kepenekian, A. Rolland and J. Even, *Journal of Materials Chemistry A*, 2015, **3**, 9232-9240.
152. R. Mais, P. Owston and A. M. Wood, *Acta Crystallographica Section B: Structural Crystallography and Crystal Chemistry*, 1972, **28**, 393-399.
153. T. M. Gilbert and T. Ziegler, *The Journal of Physical Chemistry A*, 1999, **103**, 7535-7543.
154. S. Sparks and P. Ellis, *Journal of the American Chemical Society*, 1986, **108**, 3215-3218.

155. J. M. Ernsting, S. Gaemers and C. J. Elsevier, *Magnetic Resonance in Chemistry*, 2004, **42**, 721-736.
156. J. Ernsting, C. Elsevier, W. De Lange and K. Timmer, *Magnetic resonance in chemistry*, 1991, **29**, S118-S124.
157. R. Fornika, H. Görls, B. Seemann and W. Leitner, *Journal of the Chemical Society, Chemical Communications*, 1995, 1479-1481.
158. M. A. Fox, R. L. Roberts, W. M. Khairul, F. Hartl and P. J. Low, *Journal of organometallic chemistry*, 2007, **692**, 3277-3290.
159. M. A. Fox, J. E. Harris, S. Heider, V. Pérez-Gregorio, M. E. Zakrzewska, J. D. Farmer, D. S. Yufit, J. A. Howard and P. J. Low, *Journal of Organometallic Chemistry*, 2009, **694**, 2350-2358.
160. C. E. Willans, University of York, 2006.
161. F. Niedermair, K. Waich, S. Kappaun, T. Mayr, G. Trimmel, K. Mereiter and C. Slugovc, *Inorganica chimica acta*, 2007, **360**, 2767-2777.